

IMPROVED MONITORING OF ANTARCTIC ICE SHELVES USING THE SENTINEL-1 TOPSAR ACQUISITION MODE



QUENTIN GLAUDE

SUPERVISOR : PROF. F.PATTYN & CO-SUPERVISOR : DR. C.BARBIER

ULB

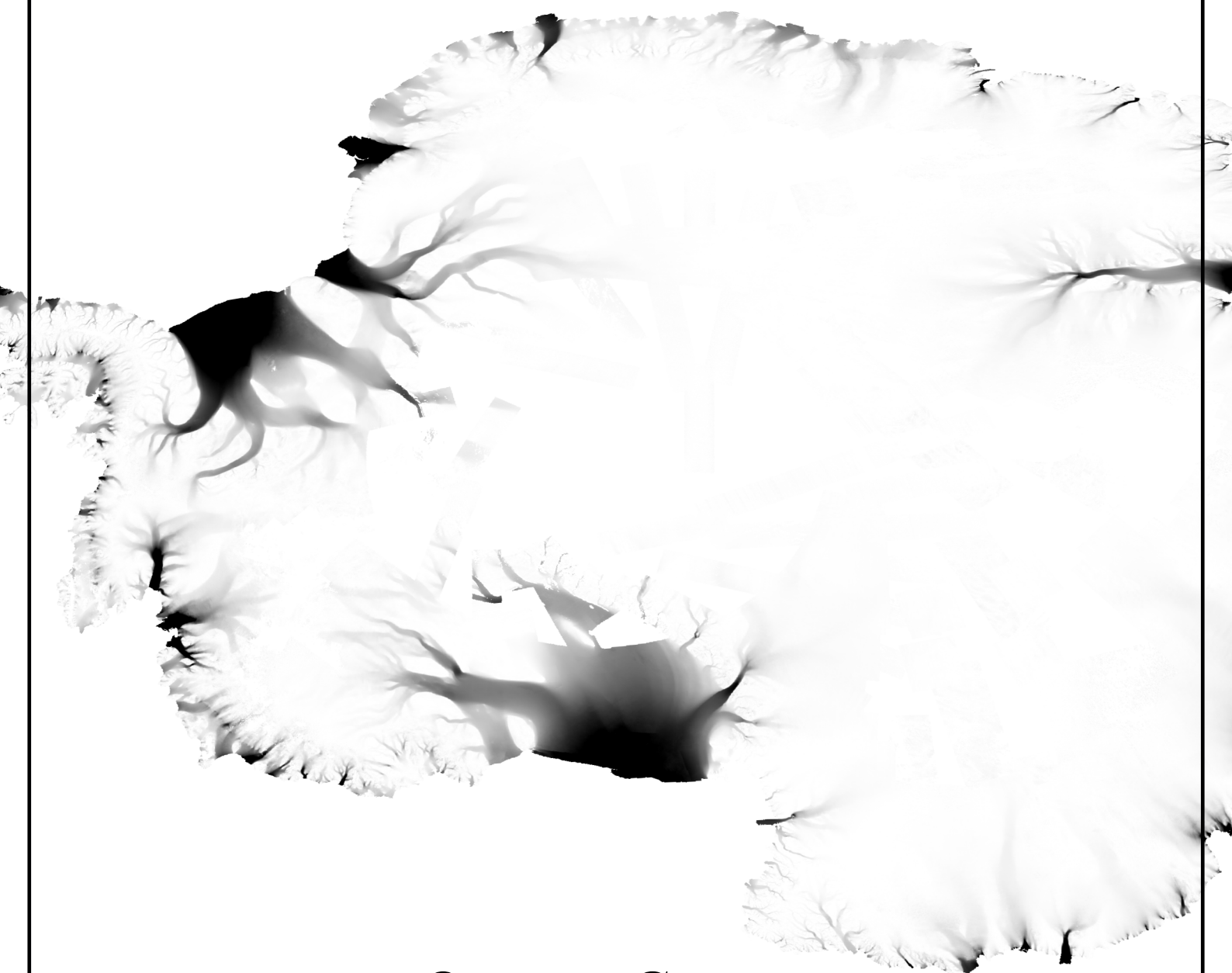


Thesis submitted in fulfilment of the requirements of the PhD Degree in Sciences

A handwritten signature in black ink, which appears to be 'Glaude'.

IMPROVED MONITORING OF ANTARCTIC ICE SHELVES

USING THE SENTINEL-1 TOPSAR ACQUISITION MODE



QUENTIN GLAUDE

SUPERVISOR : PROF. F.PATTYN & CO-SUPERVISOR : DR. C.BARBIER



FACULTÉ
DES SCIENCES

UNIVERSITÉ LIBRE DE BRUXELLES



LIÈGE université
Sciences

Improved Monitoring of Antarctic Ice Shelves Using the Sentinel-1 TOPSAR Acquisition Mode

Thesis submitted by Quentin GLAUDE

in fulfilment of the requirements of the PhD Degree in Sciences (“Docteur en Sciences”)

Academic year 2021-2022

Supervisor: Professor Frank Pattyn

Laboratoire de Glaciologie, Université Libre de Bruxelles

Co-supervisor: Doctor Christian Barbier

Centre Spatial de Liège, Université de Liège

Thesis jury:

Xavier FETTWEIS (Université de Liège, chair)
François FRIPIAT (Université Libre de Bruxelles, secretary)
Frank PATTYN (Université Libre de Bruxelles)
Christian BARBIER (Université de Liège)
Dominique DERAUW (Université de Liège)
Geir MOHOLDT (Norwegian Polar Institute)



Acknowledgments

A Ph.D. thesis is a long journey. On the road, I met incredible people. Some of these encounters were brief, some lasted a couple of months or years, and some never stopped. Before digging into an unfortunately too technical and detailed document, I found it important to take a moment and thank all the people who helped me in a way or another.

First and foremost, I would like to thank my promoters Frank Pattyn and Christian Barbier. Together, they gave me the opportunity to study geophysical processes using remote sensing. Available, positive, knowledgeable, heartwarming, it has been an honor but also a pleasure to work with them.

Second, a special thanks to my mentor, Dominique Derauw, who initiated me to SAR remote sensing during my internship at the Liège Space Center. During the thesis, Dominique never stopped sharing his expertise. I hope he won't be haunted by my thousands of technical questions.

I would also like to thank the Liège Space Center Signal Processing Lab. I met incredible people there, inside or outside the signal processing lab. I already mentioned Dominique Derauw and Christian Barbier. I'd like to thank Anne Orban, who welcomed me in her team, Ludivine Libert, for helping me in the early stages of the Ph.D. project, but also for the infinite discussions about cooking. I'd like to also thank Murielle Kirkove, Denis Defrère, Aikaterina Radioti, Thomas Dethinne, and Romy Schlogel, for all the good times.

Similarly, I would also like to thank the members of the Laboratory of Glaciology of the Université Libre de Bruxelles. My short stays never allowed me to know them as much as I would have liked. The moments shared were special, and I will remember with joy our EGU train travel, the scientific congresses, or the lunches in the Solbosch campus. Violaine, Claire, Konz, Harry, Elise, Veronica, Lars, and other people I forgot: you are truly nice people and I wish you the best.

The external jury of the MIMO project in which I was part, composed of Geir Moholdt, Malcolm McMillan, and Francesco Casu, is also acknowledged for all the precious advice given during the steering committee meetings.

I would like to thank all the students in internship and the master thesis students I supervised. I tried my best to share my knowledge in order to fulfill interesting objectives. Some of these are directly related to my thesis, and the subjects developed helped me experiment different sides of remote sensing of the cryosphere. Valentine Piroton, Vincent Boudard, Damien Stock, Manon Mackels, Stephane Lizin, Christina Broche, Thomas Dethinne: I'm proud of you.

The *Belgian Science Policy Office*, *F.R.S.-FNRS* and *Fondation Jaumotte-Demoulin et Fonds David et Alice Van Buuren* are also acknowledged for the financial support of this Ph.D. thesis, whether for staff costs, equipment, travel expenses, or publications fees.

Finally, I would also like to thank my companion, family, and friends, for their love and support. They helped me become who I am. A special thanks to Bletana Tahiraj, who helped me create

my presentations and figures, and had to support my training sessions before giving talks. A special thanks also to the artist Fatos, for the acrylic cover page, *The Observer*, he gently created after being inspired by one of my wide-audience presentations

A final thanks to all the volunteer reviewers and editors, who help the scientific dissemination of knowledge, often the hidden part of the scientific research. Your job is invaluable.

Abstract

The Antarctic Ice Sheet is the largest mass of ice on Earth. In contact with the ocean, the ice starts to float and forms an ice shelf. These ice shelves have an important role in the stability of the Antarctic Ice Sheet. They are acting as regulators by restraining the upwards ice flow. The thinning or damage of these ice shelves is directly translated into a decrease of their holding capacity and causes an acceleration of the ice flow and a retreat of the grounding line.

In parallel, the European Space Agency developed the Sentinel-1 Synthetic Aperture Radar - SAR satellite, part of the Copernicus program. Sentinel-1 aims at the systematic observation of the Earth in the C-Band radar frequency (5.54 GHz), with a revisit time of 6 to 12 days. This thesis aims to study the ability of Sentinel-1 to improve the monitoring of ice shelves, opening up new opportunities in terms of capturing small-scale events.

To begin with, we studied the ice flow velocity on ice shelves using speckle tracking or differential interferometry. SAR interferometry allows measuring local displacements between two acquisition dates. Classical interferometry allows deriving this velocity component only along the line-of-sight direction. This limitation may be overcome using the specificities of the TOPSAR acquisition mode, allowing a bidimensional estimation of the displacements.

The ice-motion estimation is far from trivial, and the specific case of ice shelves introduces additional problems in repeat-pass SAR studies. First, the rapid changes due to high displacements induce a rapid temporal decorrelation. We present a technique, coherence tracking, that aims to correct interferograms from these surface movements. Second, impacted by ocean tides and the inverse barometer effect, ice shelves are subject to vertical variations, inducing a bias to be removed. In the thesis, we present an empirical method using double interferograms and a climate model that corrects these false signals. These double interferograms can also be exploited to map the grounding line at a high temporal and spatial resolution over the Roi Baudouin Ice Shelf over multiple years.

Finally, focusing on amplitude information, we can analyze spatial patterns to monitor the ice shelves crevasses and calving front, and their evolution. Similarly, time-series analysis of SAR backscattering allows the determination of melt seasons and their spatial variability.

All these techniques participate in the derivation of new information about ice-shelves dynamics. From the results we obtained and the abundant literature, we conclude that the Sentinel-1 mission is a major step towards an improved monitoring of Antarctic ice-shelves dynamics.

Résumé

L'Antarctique contient la plus grande masse continue de glace sur Terre. Au contact de l'océan, la glace se met à flotter et forme une plate-forme de glace. Ces dernières ont un rôle important dans la stabilité de la calotte polaire de l'Antarctique. Elles agissent comme des régulateurs en retenant le flux de glace en amont. L'amincissement ou l'endommagement de ces plates-formes de glace se traduit directement par une diminution de l'effet de retenue, et provoque une accélération de l'écoulement glaciaire et un recul de la ligne d'ancrage.

En parallèle, l'Agence Spatiale Européenne a développé le satellite radar à synthèse d'ouverture (SAR) Sentinel-1, visant l'observation systématique de la Terre en bande C (5.54GHz), avec un temps de revisite de 6 à 12 jours. Cette thèse vise à étudier la capacité de Sentinel-1 à améliorer le suivi des plates-formes de glace, ouvrant de nouvelles opportunités en termes d'analyse d'événements à fine échelle spatio-temporelle.

Pour commencer, nous avons étudié la vitesse d'écoulement de la glace en utilisant le suivi de *speckle* ou l'interférométrie différentielle. Cette dernière permet de mesurer les déplacements locaux entre deux dates d'acquisition. L'interférométrie permet de dériver la composante de vitesse uniquement le long de la ligne de visée. Cette limitation peut être surmontée grâce aux spécificités du mode d'acquisition TOPSAR, permettant une estimation bidimensionnelle du déplacement.

L'estimation du mouvement de la glace est loin d'être triviale, et le cas spécifique des plates-formes de glace introduit des problèmes supplémentaires. Premièrement, les changements rapides dus aux déplacements importants induisent une rapide décorrélation temporelle. Nous présentons une technique, le suivi de cohérence, qui vise à corriger les interférogrammes de ces mouvements de surface. Deuxièmement, impactées par les marées océaniques et l'effet barométrique inverse, les plates-formes de glace sont soumises à d'importants déplacements verticaux, induisant un biais à retirer. Dans la thèse, nous présentons une méthode empirique utilisant des interférogrammes doubles et un modèle climatique qui corrigent ces faux signaux. Ces doubles interférogrammes peuvent également être exploités pour cartographier la ligne d'ancrage à haute résolution temporelle et spatiale de la plate-forme de glace Roi Baudouin sur plusieurs années.

Enfin, en se concentrant sur les informations d'amplitude, nous avons pu analyser les structures spatiales pour surveiller les crevasses des plate-formes de glace et le front de vêlage, et leur évolution. De même, l'analyse des séries temporelles de la rétrodiffusion SAR a permis de déterminer les saisons de fonte et sa variabilité spatiale à haute résolution.

Toutes ces techniques participent à la compréhension sur la dynamique des plateformes de glace. Au regard des résultats obtenus et l'abondante littérature, nous concluons que la mission Sentinel-1 est une étape majeure vers un meilleur monitoring de la dynamique des plates-formes de glace.

Contents

Acknowledgments	i
Abstract	iii
Résumé	v
Table of Contents	viii
List of Figures	xiii
List of Tables	xv
List of Publications and Outreach Activities	xvii
1 Antarctica in a Changing World	1
1.1 The Study of the Ice Sheet: Observations, Mechanisms, Projections	2
1.1.1 The Context of Greenland and Antarctic Ice Sheets	2
1.1.2 Ice Shelves: The Seat Belt of the Antarctic Ice Sheet	4
1.1.3 The Observation of Ice-Shelf Forcing Mechanisms From Space	7
1.1.4 The Specific Case of the Roi Baudouin Ice Shelf	13
1.2 Advances in Data Acquisition Techniques	16
1.3 Research Question: Does the TOPSAR Acquisition Mode of Sentinel-1 Improve the Monitoring of the Antarctic Ice Sheet?	22
2 High-Resolution Observations of Driving Factors of the Antarctic Ice-Flow Dynamics	23
2.1 SAR Remote Sensing: Theoretical Background and Recent Changes in the Global Observation Scheme	24
2.2 Surface Displacements – The Foundations of Ice Shelves Dynamics	39
2.2.1 Determining Displacements from Image Matching Techniques	39
2.2.1.1 Incoherent Speckle Tracking	39

2.2.1.2	Analysis of Velocity Time Series over the Roi Baudouin Ice Shelf – An Ongoing Long Term Stability	47
2.2.1.3	Coherence Tracking, and its Adaptation to the TOPSAR Acquisition Mode	63
2.2.1.4	Computation of Strain Rates over the Roi Baudouin Ice Shelf . .	71
2.2.2	Determining Displacements from Phase-Based Measurements	73
2.2.2.1	Ice Displacements from Differential SAR Interferometry	73
2.2.2.2	The Importance of Tracking Coherence in Ice Shelves Studies . .	79
2.2.2.3	The Influence of Tides and Inverse Barometer Effect on Measurements	103
2.2.2.4	An Observed Stable Grounding Line Around the Roi Baudouin Ice Shelf	119
2.2.2.5	Detection of Landfast Sea Ice Along the Calving Front from Dual Polarimetric SAR Interferometry	120
2.2.2.6	Along-Track Displacement Estimations Using Multiple Aperture Interferometry and Burst Overlapping Interferometry	124
2.3	Damages, Crevasses, and Calving Front Monitoring: the Causes and the Consequences of some Ice Shelves’ Destabilization	146
2.4	Surface Melt Estimation from SAR Remote Sensing – Comparisons with a Regional Climate Model	158
3	Discussions and Conclusion: Towards a Narrower Picture of Antarctica	171
	Bibliography	175
	Glossary	192

List of Figures

- 1.1 Human risks with regards to global mean surface temperature. Purple indicates a very high impact, with a very high likelihood, while yellow indicates a moderate impact. Global warming affects an important number of topics. Illustration from IPCC (2014), with modifications. 2
- 1.2 Spatial distribution of people at risk of a 100-Year flood following the RCP4.5 scenario. South Asia is the main victim of the SLR. Illustration from Haasnoot et al. (2021), with modifications. 3
- 1.3 Marine Ice Sheet Instability. In the case of retrograde bed slope, a retreat of the grounding line is followed by an ice flux increase, and an increase of mode 1 and 3 basal melt, further enhancing the grounding line retreat. A positive feedback loop is settled. Illustration from Pattyn et al. (2018), with modifications. 5
- 1.4 Buttressing of individual Antarctic ice shelves. Blue areas are representing the passive portions of the ice shelf. Illustration from Fürst et al. (2016), with modifications. 6
- 1.5 Main forcing mechanisms behind ice flow dynamics at an ocean-terminating outlet glacier in Antarctica. Illustration from Dirscherl, Dietz, Dech, and Kuenzer (2020), with modifications. 7
- 1.6 Frequency of local and regional ice motion investigations on the main Antarctic ice shelves. Illustration recreated from Dirscherl et al. (2020). 9
- 1.7 Temporal resolution of Antarctic ice velocity studies over time. Data from Dirscherl et al. (2020). Only a small fraction of studies analyzes the intra-annual velocity variations. 10
- 1.8 Tidally-induced velocity changes. Near the grounding line, the ice-shelf bending creates a horizontal displacement of the ice shelf. The influence can extend further upstream when grounding line short-scale migrations influence the water drainage under the ice shelf, lubricating the bed and modifying the basal drag. Figure recreated from Rosier, Gudmundsson, and Green (2015). 12
- 1.9 Double DInSAR allows the determination of vertical variations of the displacement vector. This characteristic allows the delineation of the boundary between the grounded ice and the floating ice shelf. Additional topographic structures, such as ice rises and ephemeral pinning points are also distinguishable. Illustration reworked from (Schmeltz, Rignot, & MacAyeal, 2001). 13
- 1.10 Location of the Roi Baudouin Ice Shelf. 14

1.11	Ice rises and ice rumples over the RBIS and the associated buttressing effect. illustration from Goel et al. (2020), with modifications.	14
1.12	Ice-shelf channels start at the grounding line. Illustration from Drews (2015), with modifications.	15
1.13	High-resolution basal mass balance over the RBIS. Illustration from Berger, Drews, Helm, Sun, and Pattyn (2017), with modifications.	16
1.14	Acquisition geometry of a TOPSAR image. The image is composed of sub-swaths and bursts with overlapping areas.	19
1.15	Time-frequency diagram of SLC TOPSAR images.	19
1.16	Azimuth shifts removal from an external azimuthal displacement map. Illustration from Andersen, Kusk, Boncori, Hvidberg, and Grinsted (2020) with modifications.	20
1.17	Combination of ascending and descending paths, where across- and along-track displacement are retrieved using DInSAR (left), and MAI and BOI (right). Illustration from Grandin, Klein, Métois, and Vigny (2016).	21
2.1	Horizontal and vertical Sobel filters.	39
2.2	Unprojected velocity map determination. Due to the image acquisition, the area is flipped upside-down, with the ocean at the bottom of the image. The large gap in the bottom of the image is the Ocean.	41
2.3	Unprojected velocity gradients computation. On the RBIS itself, we see that the settings are very important in terms of velocity gradient.	41
2.4	Local physical entities (red circles) that significantly reduce the ice-shelve velocity and that are smoothed in #2 settings but not in #3. The location corresponds to the dotted rectangle in Fig. 2.2.	42
2.5	Influence of the oversampling factor on the velocity estimated at grid locations (in order: 2, 4, 8, 16, 32, and 64).	43
2.6	Influence of the oversampling factor on the estimated azimuthal velocity at grid locations (in order: 2, 4, 8, 16, 32, and 64).	44
2.7	Effect of the hole filling and spatial filtering.	45
2.8	Effect of post-processing on velocity distribution, using an oversampling factor of 32 (left = grid, right = interpolated as image resolution).	45
2.9	Spatial distribution of Sentinel-1 acquisitions over the Dronning Maud Land region. Basemap: U.S. Geological Survey (2020).	46
2.10	Change of the orbit acquisition footprint.	46
2.11	Dronning Maud Land merged velocity map (2016), with ice shelves delimited in solid black line.	47
2.12	Quicklook of the Sentinel-1 images used for the velocity time series. Left: track 78 (2016), right: track 59 (from 2017).	48
2.13	2D displacements maps are produced by minimizing the temporal decorrelation, linking SAR images to their closest acquisition.	48
2.14	Good and poor results of velocity field estimation on RBIS from incoherent speckle tracking.	49
2.15	Comparison between 16/12/2017 and 28/12/2017 sigma0 (HH polarization).	49
2.16	Time distribution of selected pairs. We can notice a systematic gap in the first half of each year (March-June period).	50

2.17	Average velocity field. The profile in purple consists in a 160 km curve along the West Ragnhild Glacier (EPSG:3031).	51
2.18	Subset of the RBIS velocity fields time series.	52
2.19	Velocity profiles. Each line corresponds to an estimated velocity for one pair of SAR images. The effect of buttressing is clearly represented by the strong reduction of velocity at 40km.	52
2.20	Average azimuthal velocity.	53
2.21	Subset of the RBIS surface azimuthal velocity fields time series (top). Azimuthal velocity anomalies (bottom).	54
2.22	Average range velocity field.	55
2.23	Subset of RBIS surface range velocity fields time series (top). Range velocity anomalies (bottom).	56
2.24	Comparison between azimuthal (left) and range (right) velocity time series. . . .	57
2.25	Comparison between range velocity time series over the ice shelf (left) and over grounded ice (right). On grounded ice, the range variability is similar to the azimuthal one.	57
2.26	Linear trends of surface displacements at given coordinates. Zones A, B, C, D, and E are represented in Fig. 2.17.	58
2.27	Important calving event due to the collision between the Roi Baudouin Ice Shelf's "Dog head" and the D28 iceberg in June 2021.	58
2.28	Velocity difference between our Sentinel-1 2017-2018 dataset and ERS 1/2 (1996).	60
2.29	Velocity difference between our Sentinel-1 2017-2018 dataset and RADARSAT (2000).	60
2.30	Velocity difference between our Sentinel-1 2017-2018 dataset and ALOS PALSAR (2010-2011).	61
2.32	Velocity difference between the ALOS PALSAR dataset and the Rignot 2010 dataset.	61
2.31	Velocity difference between our Sentinel-1 2017-2018 dataset and the Rignot data collection (years 2007, 2009, 2010, 2013, 2014, 2015, 2016, and 2017).	62
2.33	Effects of the deramping operation. Left: real part of the original TOPSAR master signal. Right: the deramped image of the same location.	63
2.34	From top left to bottom right: range shifts (green = leftwards and blue = rightwards), azimuth shifts (blue to red = [0-1 meter per day]), tracked coherence, and tracked interferogram.	64
2.35	Left = original coherence using classical full resolution interferometry. Center = Coherence after retrieving the scatterers. Right = coherence gain from classical interferometry to coherence tracking (white representing a 0.5 gain).	64
2.36	Examples of strain rates from temporally-aggregated results.	72
2.37	RBIS DEM extracted from TanDEM-X data.	73
2.38	DML DEM extracted from TanDEM-X data.	74
2.39	Interferogram and coherence maps of a 12-day Sentinel-1 pair in Extended Wideswath mode (track 88). In the Western part of the RBIS, surface velocity of around 300 meters per year is observed, reducing the interferometric coherence. The large round-shaped dark element is the Derwael ice rise. A low signal is recorded in that place, compromising interferometric studies.	75

2.40	Sentinel-1 DInSAR mass processing flowchart.	76
2.41	Examples of coherence loss due to an increase of the temporal baseline (from left to right: 12, 24, and 36-day interferograms).	77
2.42	Difference in fringe rates between a 12-day interferogram (left) and a 6-day interferogram (right).	78
2.43	Difference in coherence between a 12-day interferogram (left, mean coherence = 0.39) and a 6-day interferogram (right, mean coherence = 0.61).	79
2.44	Surface atmospheric pressure (hPa) from MAR for October 5 and 17, 2017, and their difference (right).	103
2.45	Double Difference Interferogram, revealing the grounded and floating ice, separating by the hinge zone, represented by a high fringe rate.	104
2.46	Processing Scheme of Double Difference Interferometry for grounding line extraction.	119
2.47	Grounding line migration over the RBIS (2018 to 2020).	120
2.48	Comparison between HV and HH coherence. Top = HV ; Bottom = HH. Dark areas in the bottom of the images represent the ocean. However, near the ice-shelf, HH polarization enables the recognition of stable sea ice.	121
2.49	Process of the stable sea ice detection algorithm. The area cover the left square of Fig. 2.48. Top-left = difference between HH and HV coherence. Top-right = average filter output (5x5). Center-left = classification by thresholding. Center-right = classification enhancement by mathematical morphology. Bottom = classification overlay (red) on HV coherence image.	122
2.50	Process of the stable sea ice detection algorithm. The area cover the right rectangle of Fig. 2.48. Top-left = difference between HH and HV coherence. Top-right = average filter output (5x5). Center-left = classification by thresholding. Center-right = classification enhancement by mathematical morphology. Bottom = classification overlay (red) on HV coherence image.	123
2.51	Azimuth time-frequency diagram of a single burst acquired in TOPS before and after deramping.	125
2.52	Doppler band filtering. Backward and forward filters are displayed in green and blue.	126
2.53	Block-diagram of Doppler band splitting for MAI.	127
2.54	(top left) Initial spectrum of azimuth line at mid-range. (top right) Spectrum of azimuth line at mid-range after de-apodization. (bottom left) Spectrum of azimuth line at mid-range after band splitting (rounded rectangle filter in blue). (bottom right) Spectrum of azimuth line at mid-range (after apodization). In bottom figures, both forward and backward spectra are represented, but corresponds to two different signals.	129
2.55	Forward, Backward, and Multiple Aperture Interferograms (zoomed-in).	130
2.56	Comparison between Multiple Aperture Interferogram and Azimuth shifts estimated from coherence tracking.	131
2.57	Acquisition geometry of a TOPSAR image. The image is composed of sub-swaths and bursts with overlapping areas.	136
2.58	Block diagram of Burst Overlapping Interferometry - BOI.	137

2.59	On the left side, we present the concept of the BOI-adapted Goldstein phase filtering. The filter is applied iteratively through a moving window that generates the output phase column-by-column. On the right side, we can see the result of the filter applied to the BOI phase.	138
2.60	(Top) Intensity of the master image (left) and BOI coherence before filtering (right). (Bottom) Intensity, BOI coherence and BOI phase	140
2.61	BOI phase of the third burst of Fig. 2.60.	140
2.62	Over time, the number of cracks increased drastically where the shear stress is relatively important. This crack propagation participates in the destabilization of an ice shelf, calving events, and retreat of the ice front towards the continent. In parallel, we can observe a retreat of the hinge line of several kilometers in some cases. The first two lines cover 2 different parts of the Pine Island Glacier. Illustration reworked from Lhermitte et al. (2020), with authorizations.	146
2.63	Processing scheme of the crevasses and calving front monitoring. The bottom images illustrate the input and output images of the preprocessing step (colored in chart).	147
2.64	Edge detection by first and second derivatives analysis, using the location of the peak or the zero-crossing (resp.).	147
2.65	Edge detection of the filtered signal by gaussian-2nd-derivative, using one property of the convolution product.	148
2.66	(left) subset of the calibrated Radar Cross Section of the SAR image. Center: result of the Sato filtered SAR image. (right) edges extraction by thresholding. Acquisition date: 31st of October 2018.	149
2.67	Comparison between June 2017 (blue) and June 2020 (red).	149
2.68	Time series of crack propagation and calving front products over Pine Island Glacier.	151
2.69	Selection of crack propagation and calving front products over Brunt Ice Shelf. We displayed the important calving event of February 2021	152
2.70	South chasm propagation observed using the Sato conditional probability criterion. The region corresponds to the bounding box visible in Fig. 2.69.	152
2.71	(left) Number of melt days (i.e. when the daily meltwater production is greater than 1 mmWE/day) from the 01 Nov 2019 to 28 Feb 2020. (right) Number of melt days with respect to the 1981-2010 average from 01 Nov 2019 to 28 Feb 2020. Figure obtained by Xavier Fettweis, using MARv3.10.	158
2.72	Calibrated Radar Cross Section of Synthetic Aperture Radar Sentinel-1 Acquisitions. Left figure represents a dry condition with the calving front of the ice shelf easily distinguishable from the ocean. Right figure represents an intense melting event, where we observe a strong decrease in the radar cross section.	159
2.73	Radar backscattering, in blue, in comparison with MAR variables, in orange. (a) Melt, expressed in kilogram per m ² and per day. (b) Rainfall, expressed in kilogram per m ² and per day. (c) First-meter liquid water content, expressed as the ratio between the mass of liquid by the total mass. (d) Albedo in the visible spectrum [%]. (e) Surface temperature, expressed in degrees Celsius. (f) Air temperature, expressed in degrees Celsius.	160

List of Tables

- 2.1 Four parametrization settings are tested, balancing the spatial fineness and high frequency noise 40
- 2.2 Oversampling factor - Computation time dependency. 42
- 2.3 Number of images and pairs for each orbit. The quality of each pair is *a priori* estimated, and candidates are finally selected for fine velocity estimation. 47
- 2.4 Velocity [m.a⁻¹] evolution based on yearly averages estimates. 57
- 2.5 Estimation of the phase standard deviation (in degree) according to the coherence (columns) and the number of looks (rows). 141

List of Publications and Outreach Activities

Articles :

- **Glaude, Q.**, Amory, C., Berger, S., Derauw, D., Pattyn, F., Barbier, C., & Orban, A. (2020). Empirical Removal of Tides and Inverse Barometer Effect on DInSAR From Double DInSAR and a Regional Climate Model. *IEEE Journal of Selected Topics in Applied Earth Observations and Remote Sensing*, vol. 13, pp. 4085-4094, 2020, doi: 10.1109/JS-TARS.2020.3008497.
- (Accepted) **Glaude, Q.**, & Orban, A. (2022). The Dark Side of Remote Sensing: Current SAR Remote Sensing Missions and Applications. *Bulletin de la Société Géographique de Liège*, vol. 76.
- (Accepted) Dethinne, T., **Glaude, Q.**, Amory, C., Kittel, C., & Fettweis, X. (2022). Comparison Between Surface Melt Estimation from Sentinel-1 Synthetic Aperture Radar and a Regional Climate Model: Case Study Over the Roi Baudouin Ice Shelf, East Antarctica. *Bulletin de la Société Géographique de Liège*, vol. 76.
- (In Preparation) **Glaude, Q.**, Derauw, D., Barbier, C., Pattyn, F., & Orban, A. (2022). The Importance of Tracking Coherence for Interferometric Studies over Ice Shelves. In preparation for *Remote Sensing*.

Conference Papers:

- **Glaude, Q.**, Berger, S., Amory, C., Derauw, D., Pattyn, F., Barbier, C., & Orban, A. (2019). Empirical Correction of Tides and Inverse Barometer Effect Phase Components from Double Dinsar and Regional Models. *IGARSS 2019 - 2019 IEEE International Geoscience and Remote Sensing Symposium*, Yokohama, Japan, 2019, pp. 2034-2037, doi: 10.1109/IGARSS.2019.8899171.
- **Glaude, Q.**, Lizin, S., Pattyn, F., Barbier, C., & Orban, A. (2021). Crack Propagation and Calving Front Monitoring Using Sato Filter. *IGARSS 2021 - 2021 IEEE International Geoscience and Remote Sensing Symposium*, Brussels, Belgium.
- Kirkove, M., **Glaude, Q.**, Derauw, D., Pattyn, F., Barbier, C., & Orban, A. (2021). Sentinel-1 Azimuth Subbanding for Multiple Aperture Interferometry - test case over the Roi Baudouin Ice Shelf, East Antarctica. *IGARSS 2021 - 2021 IEEE International Geoscience and Remote Sensing Symposium*, Brussels, Belgium.
- **Glaude, Q.**, Derauw, D., Barbier, C., & Pattyn, F. (2021). The Added-Value of TOPSAR Coherence Tracking for Sentinel-1 Interferometry Over Ice Shelves. *EUSAR 2021 - 2021 European Conference on Synthetic Aperture Radar*, Leipzig, Germany.

- **Glaude, Q.**, Derauw, D., Barbier, C., & Pattyn, F. (2021). Fast Azimuthal Displacement Retrieval from TOPSAR Burst Overlapping Interferometry: Application in Dronning Maud Land (Antarctica). *EUSAR 2021 - 2021 European Conference on Synthetic Aperture Radar*, Leipzig, Germany.

Oral Interventions :

- **Glaude, Q.**, Berger, S., Amory, C., Derauw, D., Pattyn, F., Barbier, C., & Orban, A. (2019). Empirical Correction of Tides and Inverse Barometer Effect Phase Components from Double Dinsar and Regional Models. *IGARSS 2019 - 2019 IEEE International Geoscience and Remote Sensing Symposium*, Yokohama, Japan.
- **Glaude, Q.**, Berger, S., Amory, C., Derauw, D., Pattyn, F., Barbier, C., & Orban, A. (2019). Removing Tides and Inverse Barometer Effect on DInSAR of Antarctic Ice Shelves. *EGU General Assembly 2019*, 7–12 April 2019, Vienna.
- **Glaude, Q.**, Lizin, S., Pattyn, F., Barbier, C., & Orban, A. (2021). Crack Propagation and Calving Front Monitoring Using Sato Filter'. *IGARSS 2021 - 2021 IEEE International Geoscience and Remote Sensing Symposium*, Brussels, Belgium.
- Kirkove, M., **Glaude, Q.**, Derauw, D., Pattyn, F., Barbier, C., & Orban, A. (2021). Sentinel-1 Azimuth Subbanding for Multiple Aperture Interferometry - test case over the Roi Baudouin Ice Shelf, East Antarctica. *IGARSS 2021 - 2021 IEEE International Geoscience and Remote Sensing Symposium*, Brussels, Belgium, 2021
- **Glaude, Q.**, Derauw, D., Barbier, C., & Pattyn, F. (2021). The Added-Value of TOPSAR Coherence Tracking for Sentinel-1 Interferometry Over Ice Shelves. *EUSAR 2021 - 2021 European Conference on Synthetic Aperture Radar*, Leipzig, Germany, 2021
- **Glaude, Q.**, Derauw, D., Barbier, C., & Pattyn, F. (2021). Fast Azimuthal Displacement Retrieval from TOPSAR Burst Overlapping Interferometry: Application in Dronning Maud Land (Antarctica). *EUSAR 2021 - 2021 European Conference on Synthetic Aperture Radar*, Leipzig, Germany, 2021
- **Glaude, Q.**, Lizin, S., Pattyn, F., Barbier, C., & Orban, A. (2021). Automation of ice fractures and calving events monitoring using medical imaging ridge detection algorithm. *vEGU 2021*. 19 – 30 April 2021.
- **Glaude, Q.**, Derauw, D., Barbier, C., & Pattyn, F. (2021). Coherence Tracking and its Adaptation to TOPSAR Acquisition Mode - Study case over Antarctic Ice Shelves. *FRINGE 2021*.

Posters :

- **Glaude, Q.**, & Kittel, C. Comparison Between Surface Melt Days Estimation from a Regional Climate Model and Near-Daily Synthetic Aperture Radar Backscattering. *EGU Sharing Geosciences Online 2020*. 3-8 May 2020, Vienna.
- **Glaude, Q.**, Berger, S., Amory, C., Derauw, D., Pattyn, F., Barbier, C., & Orban, A. (2019). *IGARSS 2019 - 2019 IEEE International Geoscience and Remote Sensing Symposium*, Yokohama, Japan.

Note: national and smaller events were not considered in this list.

Antarctica in a Changing World

The invention of the steam engine in the early XIXth century and the rapid move through the industrial era marks the beginning of the Anthropocene (Mohajan, 2019). Coal was found to possess incredible properties. A considerable amount of disposable energy is hidden in this condensed sedimentary rock. Until 2010, coal was the fastest-growing energy source, ahead of gas and oil. After the two World Wars, the use of petroleum from military to civil purposes brought Humankind into a new era, where the liquid property of oil made transportation almost free, in comparison to the pre-industrial period.

We generally separate energy sources into two categories: fossil and non-fossil fuels. The fossil fuels comprised coal, oil, and gas, while non-fossil fuels include wood, hydropower, nuclear, wind turbines, solar panels, or other synthesized fuels (hydrogen, oil, gas). Fossil fuels encompass more than 70% of the world's energy consumption: coal for electricity and industry, oil for transport, and gas for heat and electricity production (Díaz, Marrero, Puch, & Rodríguez, 2019).

This energy brought Humankind into the Anthropocene. Energy allowed us to travel the way we travel, to eat the way we eat, to work the way we work, to consume the way we consume, but also to benefit from limited work hours, paid days off, or even paid retirement. In addition, this general trend occurs with a growing population, whose life expectancy globally never ceased increasing.

This energy comes from more than 70% of fossil fuels, emitting in its combustion GreenHouse Gases - GHG. From Arrhenius (1897), the effects of greenhouse gases were already known, and discussions about the consequences of the industrial era in terms of global warming emerged. IPCC (2019) underlines the indisputable influence of humans on warming the planet. This global warming is even amplified in polar regions. With a population getting closer to 8.000.000.000 inhabitants (still growing) and CO₂ annual emission (or equivalent) around 6-7 tons per capita (stable since 1970), Humankind is leaving an important footprint of its presence. The IPCC presents evidence-based human threats with regards to emission scenarios (IPCC, 2019). Anthropogenic global warming can take different aspects. The warming of the atmosphere increases the rate and length of heatwaves. Extreme weather events, in general, are and will become even more frequent. As an example, we observe in Fig. 1.1 that 3° above the pre-industrial period, global access to food supplies are highly compromised. In an experiment, Power and Delage (2019) investigated the occurrence, amplitudes, and duration of future extreme temperature records in relation to global warming. In high emission scenarios, the number of new monthly temperature records per decade is above 5 everywhere on the Earth.

One of the most visible and direct impacts of global warming is the Sea-Level Rise - SLR, due to ocean thermal expansion and unbalanced ice discharge from the Antarctic and Greenland ice

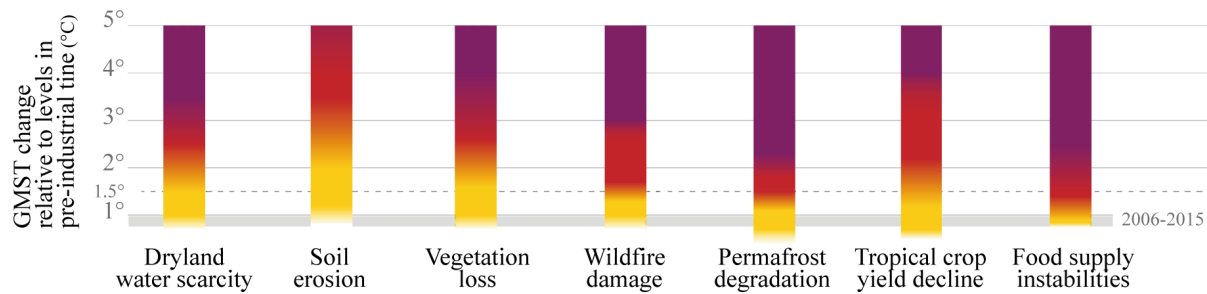


Figure 1.1: Human risks with regards to global mean surface temperature. Purple indicates a very high impact, with a very high likelihood, while yellow indicates a moderate impact. Global warming affects an important number of topics. Illustration from IPCC (2014), with modifications.

sheets and glaciers (IPCC, 2014). In a world where the majority of the largest cities are located in coastal areas, the problem of increased flood events is critical.

Rintoul et al. (2018) present a story-driven analysis of two potential futures for Antarctica. In one scenario, the 1.5° warming adopted in Paris Agreements is respected. In comparison, he studied a business-as-usual scenario leading to 2.9° global air temperature. If the difference between those two values seems small, the consequences of the high emission scenario are drastically increased for 2100. For example, the Antarctic contribution to sea-level increases by a factor of 4 to 5, and the volume of ice shelves is reduced from 8% to 23%, in comparison to the 1.5° scenario. Technical solutions for mitigating the causes and consequences are being studied. As an example, Wolovick and Moore (2018) investigated the role of artificial pinning points to reinforce ice shelves. These types of last-chance solutions are nevertheless extremely expensive, with low success rates.

1.1 The Study of the Ice Sheet: Observations, Mechanisms, Projections

1.1.1 The Context of Greenland and Antarctic Ice Sheets

The factors responsible for the SLR mainly include thermal expansion and ice loss (Frederikse et al., 2020). The ice loss comes primarily from glaciers and the Greenland Ice Sheet. The ratio between the contributors are varying throughout the time. For example, the role of the Antarctica Ice Sheet - AIS quadrupled throughout the last century. With a potential of 58 meters sea-level rise if completely melted, Antarctica is still the major potential absolute contributor, with important uncertainties (Fyke, Sergienko, Löfverström, Price, & Lenaerts, 2018). While glaciers have an important role for local populations, their ice content only represents an SLR equivalent of 32 centimeters (Farinotti et al., 2019).

To compute the mass balance of the Antarctic and Greenland Ice Sheets, there exists three independent methods: the input-output method, the altimetry method, and the gravimetry method. The input-output methods rely on the modeling of the balance between what goes into the AIS (precipitations, refreezing), and what goes out (based on ice thickness and velocity) (Shepherd, Fricker, & Farrell, 2018). Altimetry is based on the direct measurement of ice surface elevations. The computation of ice thickness difference measured at different times from spaceborne or airborne altimeters allows a reconstruction of the mass balance. Gravimetry relies on temporal Earth gravitational variations. These variations are observed using the GRACE satellite constellation (Tapley et al., 2019). GRACE satellites' relative positions are known with extreme precision, and slight variation of the Earth-mass distribution will induce a variable gravity field

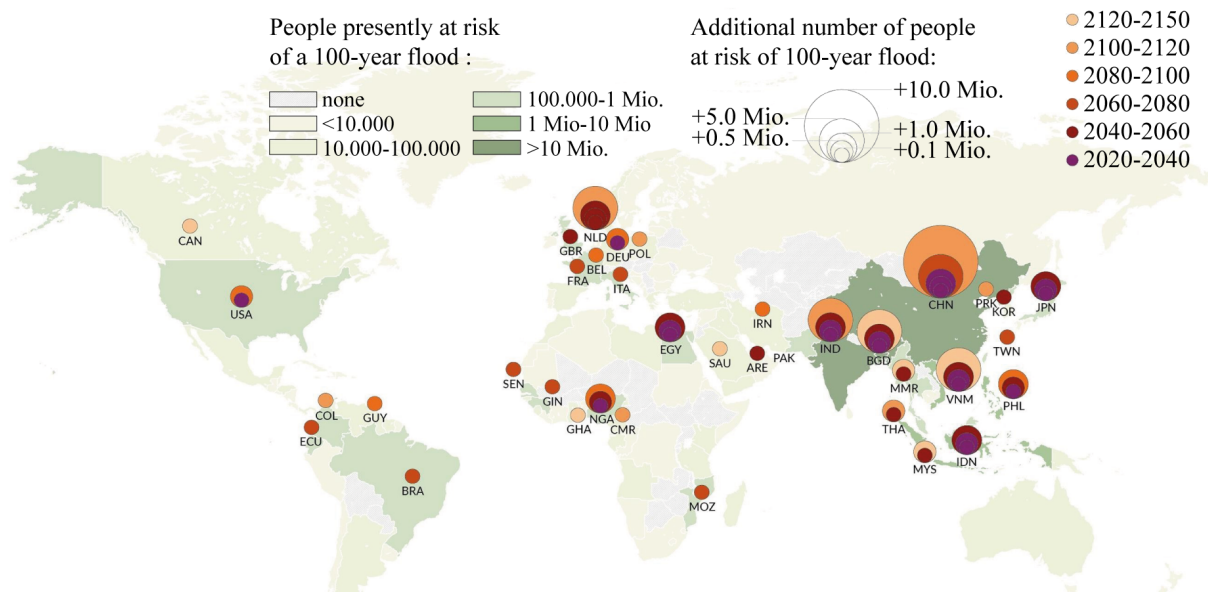


Figure 1.2: Spatial distribution of people at risk of a 100-Year flood following the RCP4.5 scenario. South Asia is the main victim of the SLR. Illustration from Haasnoot et al. (2021), with modifications.

and so a variable distance between the two satellites. Using inverse problem and taking into account isostatic measurements (Larour et al., 2019; Steig, 2019), we can compute the mass balance.

Antarctic and Greenland ice mass losses in recent decades are very important (Paolo, Fricker, & Padman, 2015), following worst-case scenarios from IPCC AR5 reports (Slater et al., 2021). Even in the case of 1.5 global warming Paris Agreement, both Greenland and Antarctic Ice Sheets will face long-term mass losses (Pattyn et al., 2018). This ice mass loss comes with a decrease in sea ice extent, and a reduction of the snow cover, affecting the sea level, and Earth global albedo (IPCC, 2019). After thermal expansion, Greenland is the main contributor to SLR and its ice discharge is accelerating (M. D. King et al., 2020). The danger of global warming is that the effects are far from linear, and passing tipping points leads to long-term consequences (Ritchie, Clarke, Cox, & Huntingford, 2021). The potential total disintegration of the Greenland Ice Sheet is one example. As elevation decreases due to ice melt and runoff, the air temperature rises because of the elevation-related thermal gradient, and so further melt is produced. In this particular example, a tipping point is the temperature rise leading to this long-term irreversible event. In Antarctica, several important basins in West Antarctica are under threat too. Globally, the SLR has never stopped increasing since the 1960s (Dangendorf et al., 2019).

As the SLR increases, the need for adaptation also increases. Currently, we estimate 68 million the number of people who are at risk for a 100-year flood, to be doubled by the end of the century (Haasnoot et al., 2021) (Fig. 1.2). Even drastic and rapid GHG emissions cutoffs will require important adaptation strategies. Using updated coastal Digital Elevation Models - DEMs, the impacts of SLR on coastal areas are even further increased (Kulp & Strauss, 2019). In high-emissions scenarios, the important SLR would compromise the coastal adaptation, leading to a forced tactical retreat (Edwards et al., 2021).

The mass losses of glaciers, ice sheets, and ice shelves find different causes. Glaciers and Greenland ice losses are mainly due to increased air temperature while basal melt is the main contributor for antarctic ice shelves (Dirscherl et al., 2020). One reason is the amplified temperature anomalies in polar regions. In Antarctica, the spatial pattern of mass loss is highly variable among the three main regions (Dirscherl et al., 2020). Schröder et al. (2019) studied the eleva-

tion change of the AIS from all available altimetry missions, representing 4 decades of records. The study highlights the important mass losses near the Amundsen sea sector and the Wilkes Land. The main increase in ice discharge is attributed to West Antarctica, while East Antarctica remains overall stable over the last decades (Gardner et al., 2018). At finer scales, parts of the Eastern AIS are also losing mass. This is particularly the case with the Totten ice shelf.

In the decade 1972-1980 to 1980-1990, the Greenland Ice Sheet mass balance switched from a mass gain regime to a mass loss regime (Mouginot, Rignot, Bjørk, et al., 2019). Then, this mass loss never stopped decreasing, from -51 Gt per year in the 80s to -286 Gt per year in the decade 2010-2018. In this study, Mouginot, Rignot, Bjørk, et al. studied the ice discharge of the drainage basins. During the 46 years of the survey, 50% of Greenland's SLR contribution occurred in the last 8 years.

The AIS lost 1365 Gt of ice between 1992 and 2011. Together with the Greenland Ice Sheet, this represents a total of 1.1 cm of SLR (Shepherd et al., 2012). The ice losses in the Antarctic have increased by a factor of 5 in 25 years (Shepherd et al., 2019) and there is evidence of long-term Antarctic decline (Shepherd et al., 2018). Future projections of SLR from Antarctica are rather uncertain, and ranges from -0.75 to +1.6 meters depending on Representative Concentration Pathway - RCP scenarios (Slater & Shepherd, 2018). In particular, in scenario RCP8.5, it is not excluded that Antarctica alone contributes to one-meter SLR in 2100 (Seroussi, 2019). The high uncertainties in Antarctica make long-term projections extremely difficult (Ritz et al., 2015). Nevertheless, the modeling of the ice sheet is evolving, and while it remains many uncertainties, future projections are getting refined (Moon, Ahlstrøm, Goelzer, Lipscomb, & Nowicki, 2018). Bulthuis, Arnst, Sun, and Pattyn (2019) determined the influence of uncertainty sources. Errors in the inputs are translated into errors in the projections, that are based on a great number of feedback processes. All in all, these uncertainties make the long-term projection a non-trivial problem.

1.1.2 Ice Shelves: The Seat Belt of the Antarctic Ice Sheet

Ice shelves are the floating extensions of the AIS, at the interface between the ocean, the atmosphere, and the grounded ice sheet (Pritchard et al., 2012; Paolo et al., 2015). Ice-shelves' mass comes from the continental ice streams and snow accumulations, and they lose ice by calving, basal and surface melting (Dinniman et al., 2016). In some cases, ice shelves can gain mass from basal refreezing. Ice shelves are crucial gatekeepers of the AIS because they restrain ice flow as they are often laterally constrained by embayments or locally grounded on rigid obstacles in the bathymetry (Favier & Pattyn, 2015; Dupont & Alley, 2005). Thinning of Antarctic ice shelves and the corresponding decrease in the restraint experienced by inland ice flow (Payne, Vieli, Shepherd, Wingham, & Rignot, 2004; Pritchard, Arthern, Vaughan, & Edwards, 2009) are recognized as major drivers of current Antarctic ice loss (IPCC, 2014; Shepherd et al., 2018). Ice-shelf thinning causes an instantaneous acceleration and a retreat of the grounding line, i.e. the limit between the grounded ice sheet and the floating ice-shelf (D. Goldberg, Holland, & Schoof, 2009), an increase in grounded ice loss hence a sea-level rise (Gudmundsson, Paolo, Adusumilli, & Fricker, 2019). This is particularly concerning as ice shelves are thinning in many areas in Antarctica due mainly to increased basal melting.

The AIS was initially thought to be a slow-response system to atmospheric and oceanic changes (Pattyn, 2018). This is not verified for the Antarctic boundaries, near the ice shelves, where many destabilization processes are occurring. These have a direct impact on the upstream ice flow and thus the entire AIS. The f.ETISH model demonstrated the role of the ice shelves and the consequences due to their disintegration (Pattyn, 2017). Marine Ice Sheet Instability - MISI is one of these destabilization processes (Fig. 1.3). The idea behind MISI is that, if the ice shelf is or becomes unbuttressed, the retreat of the grounding line set in a retrograde bed slope will

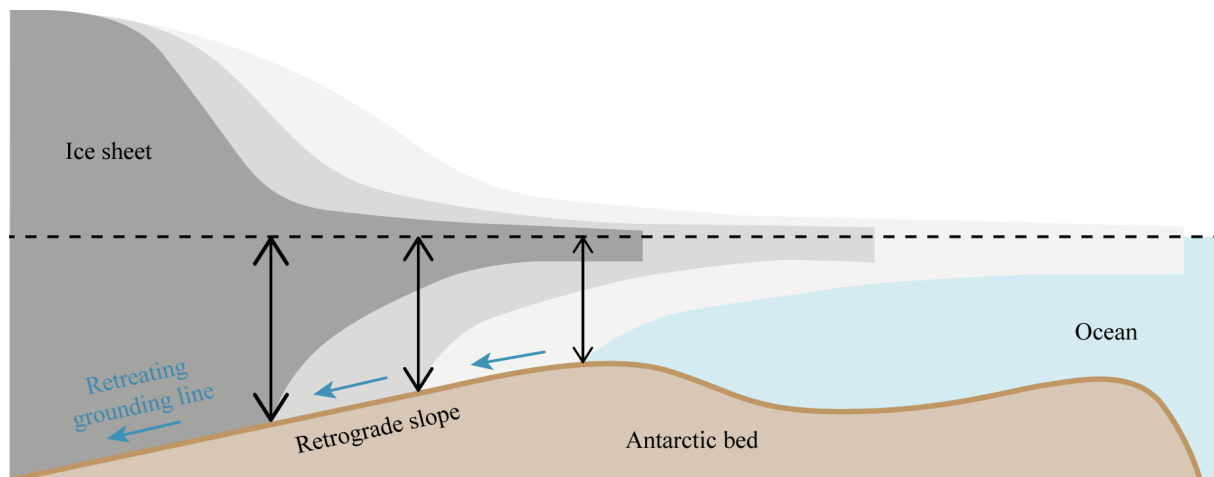


Figure 1.3: Marine Ice Sheet Instability. In the case of retrograde bed slope, a retreat of the grounding line is followed by an ice flux increase, and an increase of mode 1 and 3 basal melt, further enhancing the grounding line retreat. A positive feedback loop is settled. Illustration from Pattyn et al. (2018), with modifications.

induce an increased subshelf ocean current, and an increase in ice flux toward the ocean, further enhancing the grounding line retreat (Pattyn, 2018). Using numerical modeling, Schoof (2007) confirmed the hypothesis of MISI by studying the dynamics at the grounding line.

Ice shelves' main contributor to mass loss is the basal melt from ice-ocean interaction (Adusumilli, Fricker, Medley, Padman, & Siegfried, 2020; Reese, Albrecht, Mengel, Asay-Davis, & Winkelmann, 2018). This basal melt varies strongly spatially and temporally. Berger et al. (2017) studied the spatial variations of these melt rates in Dronning Maud Land - DML. The ocean is the main heat sink of anthropogenic global warming. Its energy intakes results in a global ocean warming (Swart, Gille, Fyfe, & Gillett, 2018). Around the Bellingshausen Sea, warm waters directly communicate with ice shelves, producing important basal melt rates. The basal melt rates vary from 0 to 10 meters per year from a given place depending on the season. In its research, Adusumilli et al. (2020) developed a global map of Antarctic melt rates at high spatial resolution. In Antarctic Peninsula and East Antarctica, warm winds are inducing surface melting, and ocean wind stresses cause ice flow acceleration (Dirscherl et al., 2020; Greene, Blankenship, Gwyther, Silvano, & van Wijk, 2017). While the spatial resolution is key information, bathymetry below ice shelves needs to be improved for better understanding the melt rates determination (D. N. Goldberg, Gourmelen, Kimura, Millan, & Snow, 2019). In addition, the understanding of mechanisms under ice-shelf thinning requires long time measurements using remote sensing and in situ from ApRES data (Sun et al., 2019).

The grounding-line location is also an important parameter because the stresses applied to the ice sheet and the ice shelf are fundamentally different. In the grounded part, basal dragging is the main brake of the ice sheet. In the ice shelf, buttressing effects are produced mainly because of shear stresses due to embayments or geographical configurations (Rignot, Mouginot, & Scheuchl, 2011a). Buttressing is computed from stress fields, which are then converted into a normal upstream force reducing the flow to the ocean. Using these information, *active* and *passive* regions within ice shelves are delineated. Concretely, if a region of low-buttressing capabilities collapses, dynamics of the upstream ice flow remain unchanged, and the region can be considered as *passive*. Fürst et al. (2016) computed the continent-wide measurement of ice-shelf buttressing (Fig. 1.4).

Scambos, Hulbe, and Fahnestock (2003) tried to explain the collapse of Larsen B in 2002. The important melt seasons are found to be responsible for the rapid disintegration through fracturing

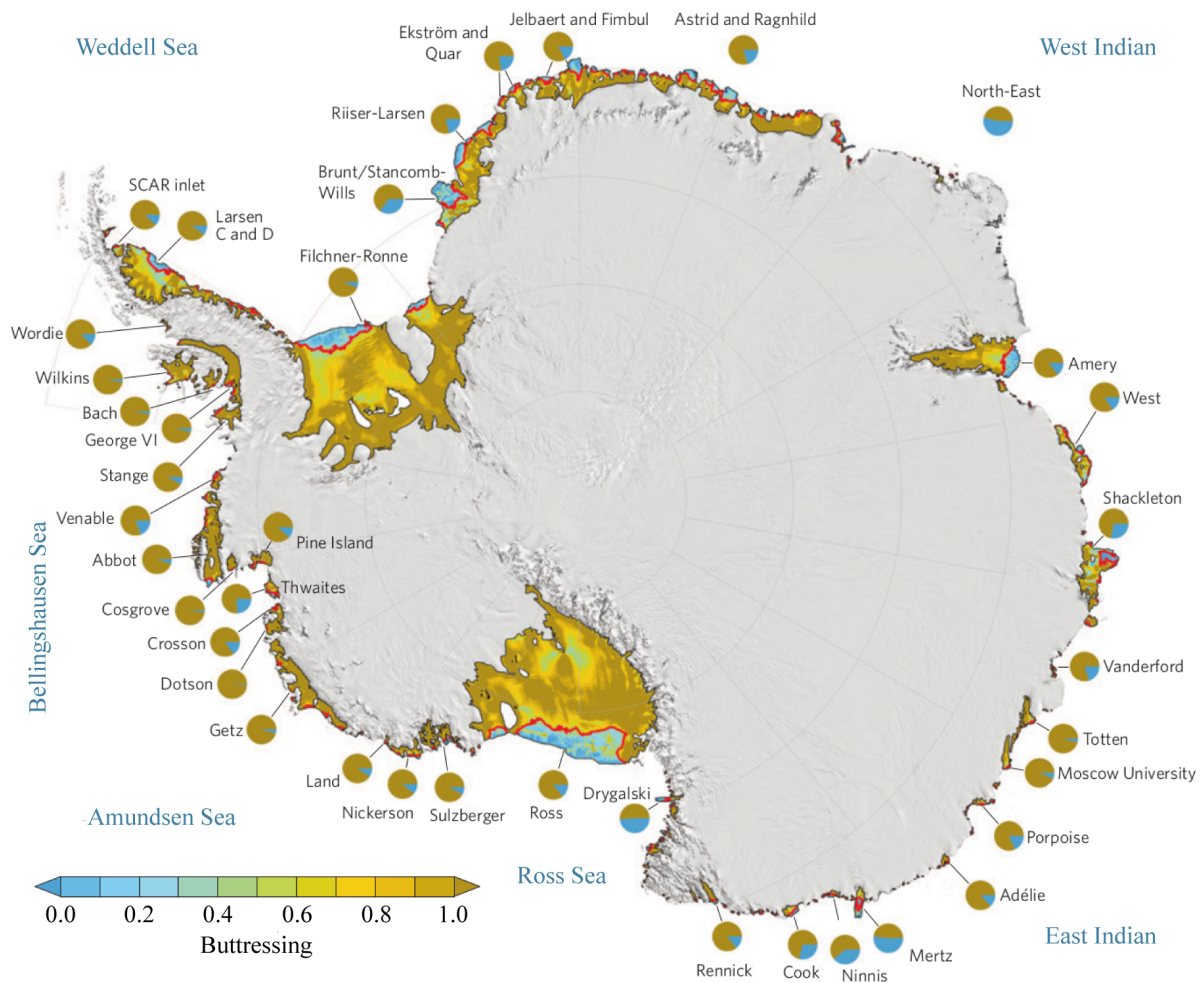
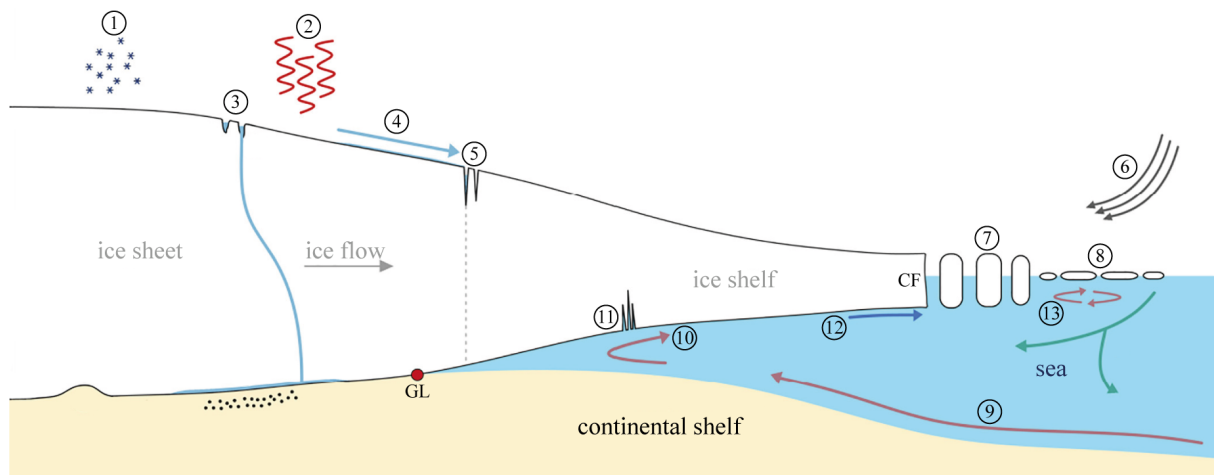


Figure 1.4: Buttressing of individual Antarctic ice shelves. Blue areas are representing the passive portions of the ice shelf. Illustration from Fürst et al. (2016), with modifications.



Processes and features of an ocean-terminating outlet glacier system

- | | | | |
|-----------------------|--------------------|--------------------|---------------------|
| ① Snow accumulation | ⑤ Hydrofracturing | ⑨ CDW upwelling | ⑬ Tidal mixing |
| ② Atmospheric warming | ⑥ Wind conditions | ⑩ Basal melting | GL = Grounding line |
| ③ Supraglacial lakes | ⑦ Iceberg presence | ⑪ Basal crevassing | CF = Calving front |
| ④ Surface melting | ⑧ Sea ice presence | ⑫ Basal refreezing | |

Figure 1.5: Main forcing mechanisms behind ice flow dynamics at an ocean-terminating outlet glacier in Antarctica. Illustration from Dirscherl et al. (2020), with modifications.

mechanisms, due to the presence of water ponds at the surface. The collapse of the Larsen B ice shelf in 2002 is one prime example of the role of the ice-shelves regulators of ice streams (Rignot et al., 2004). The recent Larsen C calving event raises questions about the potential long-term impacts in the region. The event already showed a reduction of the ice-shelf's surface by 10% (Hogg & Gudmundsson, 2017). Fortunately, the resulting A78 iceberg was part of the passive region of the Larsen C ice shelf.

An overview of main forcing mechanisms behind ice flow dynamics at an ocean-terminating outlet glacier in Antarctica is illustrated schematically in Fig. 1.5, and include: ice flow velocity, sea ice presence, calving, surface melt, tidal influence, or even grounding line migration. Observations of these phenomena will be discussed in the next section.

1.1.3 The Observation of Ice-Shelf Forcing Mechanisms From Space

Point-based velocity measurements are unrepresentative of the reality of AIS and are time-consuming. In that sense, remote sensing appeared as a revolution for geophysical research (Bindschadler, 1998). Satellite remote sensing is an essential tool in monitoring ice-shelf health by deriving ice flow fields, strain rates, and tracking grounding line positions over time, among others. In that domain, Synthetic Aperture Radar - SAR remote sensing became the first-choice solution for the computation of ice velocity, thanks to its day-and-night and cloud-free capabilities (see section 2.1). The usefulness of SAR interferometry has already been demonstrated for the study of ice motion and grounding line location in Antarctica, with the Rutford ice stream as an example (Goldstein, Engelhardt, Kamb, & Frolich, 1993). SAR remote sensing occupies more than 60% of the ice velocity studies (Dirscherl et al., 2020), but the long-term Landsat archives make optical data good candidates too.

We separate different techniques to determine displacements from SAR remote sensing. Offset-based techniques are based on image matching algorithms. This coarse determination of range and azimuth offsets employs incoherent or coherent complex correlation between small tiles of two coregistered images. Phase-based techniques are based on the idea that, if a displacement

occurred between two dates, a phase shift will be visible in an interferogram. Range displacement from phase-based measurements are determined using Differential SAR Interferometry - DInSAR. Azimuth displacements, on the other hand, are determined from Multiple Aperture Interferometry - MAI, and recent developments exploiting new acquisition modes are studied (H. Jiang, Feng, Wang, & Bürgmann, 2017).

DInSAR has the advantage of being more precise, but the rapid changes over the AIS create important temporal decorrelation factors due to the relatively fast displacements of the ice streams, the snow precipitations, or the melt events. In consequence, offset tracking is generally considered as more simple to use, and the majority of SAR-based ice motion techniques are using offset tracking techniques (Dirscherl et al., 2020). For DInSAR studies to progress, future SAR missions will require a shorter revisit time to increase the potential of phase-based measurements (see chapter 3).

Offset- and phased-based techniques allowed the determination of the continental-wide mapping of the mean Antarctic velocity field (Rignot, Mouginot, & Scheuchl, 2011b) as well as establishing grounding-line products (Rignot et al., 2011a), which form the base for all major ice-sheet model predictions (Favier et al., 2014). Rignot et al. (2011a) provides 15 years of grounding line mapping using double differential SAR interferometry using ERS, RADARSAT, and ALOS data from 1994 to 2009. Both products are also essential in determining the current state of the ice sheet by determining its basin-wise mass balance through the input-output method, in combination with atmospheric modeling (Shepherd et al., 2018). In addition, the spatio-temporal analysis of ice displacements helps in understanding the driving mechanisms of ice-flow variations. Over the Ross Ice shelf, for example, Siegfried, Fricker, Carter, and Tulaczyk (2016) observed ice velocity variations were due to basal conditions.

Similarly, in 2012, Mouginot, Scheuchl, and Rignot (2012) computed a global surface velocity mapping of Antarctica using SAR data, using ASAR, ERS-1 and -2, ALOS, and both RADARSAT satellites. In 2017, Mouginot, Rignot, Scheuchl, and Millan (2017) updated the annual velocity maps of Antarctica by including optical (Landsat-8) on top of SAR data (Sentinel-1 and Radarsat-2). While SAR images produce better results, the amount of optical data greatly helps in the determination of surface displacements. RADARSAT is found particularly useful thanks to its left-looking acquisition geometry, allowing observations closer to the South Pole.

In 2019, Mouginot, Rignot, and Scheuchl (2019) went a step further by drastically improving the accuracy of Antarctic Velocity fields by providing a continent-wide estimate of the annual velocity from DInSAR. Nevertheless, the velocity determination is limited in ice shelves areas or along important ice streams, where the high temporal decorrelation does not allow the phased-based displacement measurements. In 2017, the European Space Agency funded the Climate Change Initiative, responsible for the creation of SAR-based surface velocity products. These products were computed from DInSAR, MAI, and offset tracking. The choice of the technique is region dependant. Once computed, the different products were assessed by GNSS measurements. In total, 6 international groups developed velocity products (Merryman Boncori et al., 2018).

The grounding line is also a critical component of ice shelves' health (Friedl, Weiser, Fluhrer, & Braun, 2020). Their retreat is an important sign of glacier mass imbalance, and many Antarctic ice shelves are retreating. Between 2010 and 2016, 22% of West Antarctic ice shelves are retreating at a rate of 25 meters per year or higher (Konrad et al., 2018). Consequently, the surface of grounded ice also diminished at the same time. Unfortunately, the detection of grounding line from Double DInSAR presented in Rignot et al. (2011a) is not always possible due to high temporal decorrelation and large temporal gap between acquisitions. Using 1-day COSMO-Skymed data and Double DInSAR, Brancato et al. (2020) determined grounding line retreat of Denman Glacier, East Antarctic, of around 5 kilometers in the last 20 years, but the availability of this type of product is scarce.

Overall, we observed strong variations regarding the spatial and temporal distribution of studies

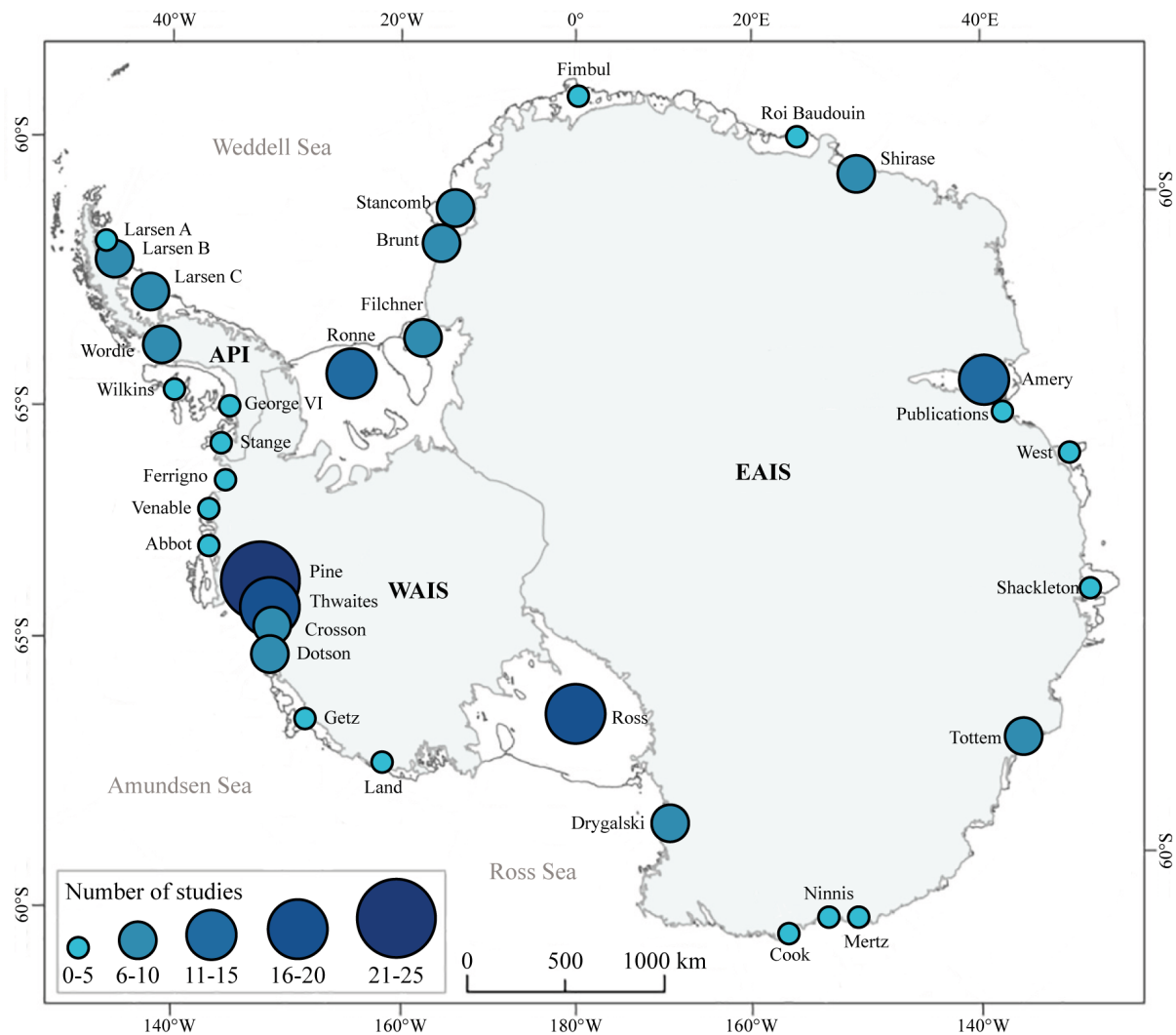


Figure 1.6: Frequency of local and regional ice motion investigations on the main Antarctic ice shelves. Illustration recreated from Dirscherl et al. (2020).

(Fig. 1.6 and 1.7), and a special attention should be taken with regards to the East Antarctica (Dirscherl et al., 2020). While East Antarctic Ice Sheet represents the vast majority of the total AIS mass, it also encompasses a minority of all studies. The main interest is about the West AIS, in the Amundsen Sea Sector, and especially over the fast-flowing Pine Island and Thwaites glaciers, motivated by the recent ice shelf's grounding line retreat and mass loss (Scambos et al., 2017). In the late 20's century, recent increases in ice discharge over Pine Island glacier were observed (Joughin, Rignot, Rosanova, Lucchitta, & Bohlander, 2003). In the same sector, Crosson and Dutson Ice-Shelves' grounding lines are retreating at 2km per year and thinning at 6.3 meters per year, inducing an increase in surface velocities (D. N. Goldberg et al., 2019). This contrasts with Dronning Maud Land, East Antarctica, where individual ice shelves are poorly covered in the scientific literature. While it was modeled and observed that the Antarctic Peninsula and West Antarctica are facing important mass losses, East Antarctica was expected to remain relatively stable. Recent observations in Wilkes Land are questioning this assumption (Shen et al., 2018). Indeed, unexpected acceleration is observed, and the intrusion of modified Circumpolar Deep Water - mCDW has been discovered in several regions around the Totten ice shelf, producing important basal melt (Rich et al., 2021).

On top of ice motion determination, other dynamics of ice shelves can be studied. This is the case

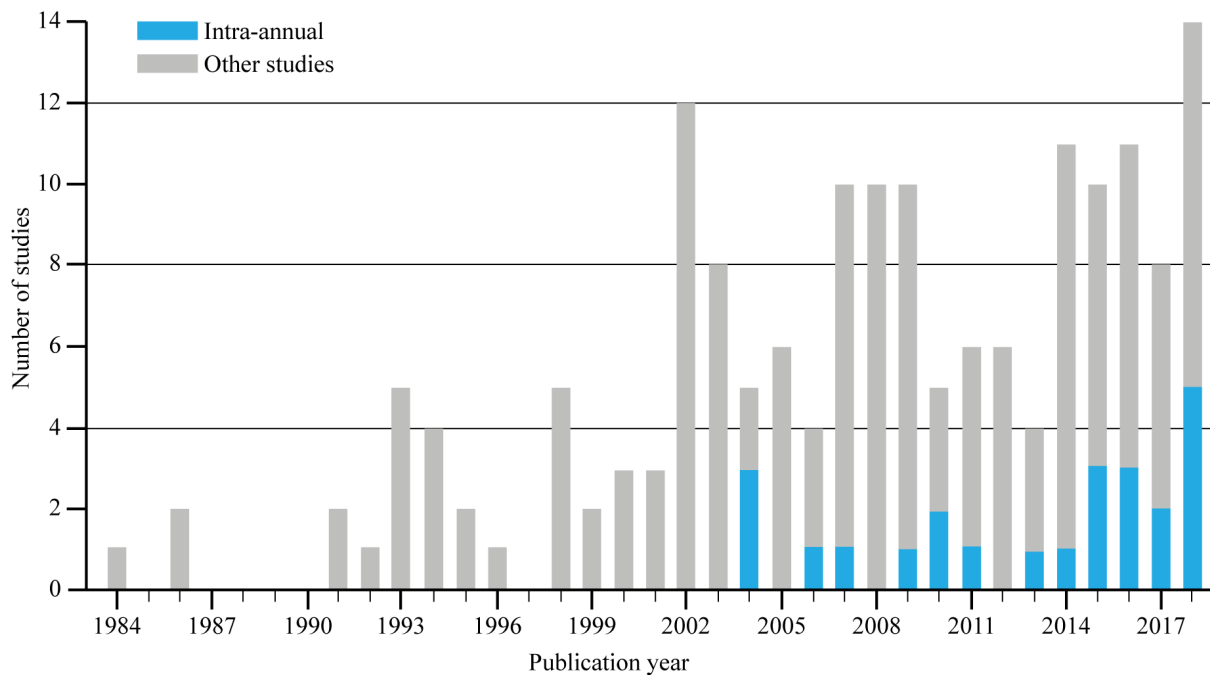


Figure 1.7: Temporal resolution of Antarctic ice velocity studies over time. Data from Dirscherl et al. (2020). Only a small fraction of studies analyzes the intra-annual velocity variations.

of sea ice and ice-mélange presence, participating in a partial stabilization of ice shelves (Robel, 2017; Dirscherl et al., 2020). Using TerraSAR-X data, Rott et al. (2018) noticed a decrease in surface velocities of Larsen A and B embayments due to the presence of stable sea ice and ice mélange. Unfortunately, the Arctic sea ice extent decreased by 3.5–4.1% per decade (Dirscherl et al., 2020). In addition, sea ice has an important role in the energy balance of the Earth, through albedo processes.

Among ice-shelves processes, we can also mention the case of calving. Calving is a natural phenomenon occurring at the front of ice shelves. When the ice sheet is in equilibrium, the amount of received mass is equal to the losses (Benn, Warren, & Mottram, 2007). The mechanisms behind losses include surface melt, basal melt, and calving. This balance is compromised if the outputs are greater than the input. Calving mechanisms greatly amplify ice-flow acceleration, or glacier retreat (Choi, Morlighem, Wood, & Bondzio, 2018). Different mechanisms explain calving, such as the spatial variation of velocity fields, observed in strain rates products. In particular, analyzing these stresses gives clues on the passive and active parts of the ice shelves (Alley et al., 2018). Pattyn and Derauw (2002) determined strain rates over the Shirase glacier from velocity fields determined by using coherence tracking on ERS data. The other calving source is related to the propagation of fractures and crevasses (see section 2.3). Calving is also enhanced by the intrusion of liquid water through the ice shelf (Cook, Galton-Fenzi, Ligtenberg, & Coleman, 2018).

The damages around Pine Island Glaciers and Thwaites evolve in a positive feedback process where damages are causing more damages, witnesses of future disintegration of the ice shelf (Lhermitte et al., 2020). The strain around the sides of Pine Island is high, tearing apart the ice shelf. The rifts become unstable when the ice shelf weakens due to thinning or lateral constraints unpinning (Lipovsky, 2020). When calving impacts active parts of outlets glaciers or ice shelves, an immediate response occurs. This is the case for the Petermann Glacier, Greenland, where 10% velocity increase is observed (Rückamp, Neckel, Berger, Humbert, & Helm, 2019). Rifts instability and damages are caused by an ice-shelf weakening due to different processes such as ice-shelf thinning from sub-shelf melting, glacier acceleration, and grounding line retreat.

Surface melting is another ice-shelf mechanism, as a precursor for hydrofracturing (Kuipers Munneke et al., 2018). It is generally produced during the austral summer, where temperatures rise above the melting point. The evaluation of melt from remote sensing was already performed using low-resolution passive microwave satellites (Johnson, Fahnestock, & Hock, 2020). However, surface melt has also strong signatures in SAR images. The detection of melt is based on the observed decrease in the backscattering coefficient, i.e. the ratio between the power of the signal emitted by a ground surface and the incident power of the signal illuminating this area (Small, 2011). The decrease in backscatter is related to the increase of liquid water content in the snowpack. A first study was performed in 1997 by Koskinen, Pulliainen, and Hallikainen (1997) in Finland. Using Sentinel-1 time series analysis, Buchelt, Skov, and Ullmann (2021) describe the snow processes that occur in Greenland areas. Temporal variations of the backscattering coefficient and its first derivatives can be used to identify the states of the snow (dry, wet, or snow-free) and ongoing processes (moisturizing, ripening, runoff). Nagler, Rott, Ripper, Bippus, and Hetzenecker (2016) also developed a melt detection algorithm from Sentinel-1 SAR satellites. The potential of SAR to detect melt at high resolution was found very promising. Time series of surface melt detection using Sentinel-1 has also been performed in Antarctica (D. Liang et al., 2021). In this study, continent-wide melt detection was performed using a large number of Sentinel-1 data in Extended Wideswath mode.

Another mechanism, oceanic tides, also have important consequences on processes such as sub-shelf ocean mixing (Padman, Siegfried, & Fricker, 2018). Initially, tidally-induced ice-shelf deformations were observed from tiltmeters placed near the grounding line (Smith, 1991). From there, elastic beam models were built. Wild, Marsh, and Rack (2017) analyzed the difference between elastic and viscous models for the interpretation of ice-shelf deformation due to tides. One major observation was that the choice of the model depends on the tides' amplitude. In the case of low tides, elastic models were used, while viscous models better represent high-tides-related bending. The largest difference between the two models is the time delay introduced by viscous models before the bending occurs. Padman, Fricker, Coleman, Howard, and Erofeeva (2002) developed a regional tide model around Antarctica, named CATS2008.

Padman, King, Goring, Corr, and Coleman (2003) studied next the ice-shelf elevation changes due to changes in atmospheric pressure, a phenomenon called inverse barometer effect - IBE. Indeed, variations of the atmospheric pressure induce an isostatic response of one centimeter per hPa. This rate has been readjusted in several studies and varies between 0.95 and 1.01 cm hPa⁻¹, but still gives a very good approximation of the rebound. Both IBE and tides need to be corrected for interferometric studies over ice shelves (Glaude et al., 2020). The accuracy of tide models was performed in the Amundsen Sea (McMillan, Shepherd, Nienow, & Leeson, 2011). The three most famous tide models, CAT2008, TPX07.1, and FES2004, were assessed. Errors between models are similar, at around 9 cm. The accuracy of the models can be increased by taking into account the inverse barometer effect.

Tides can control the flow of Antarctic ice streams (Fig 1.8). This is the case of Rutford Ice Stream, where 10% and 20% of the velocity are attributed to tidal motion depending on studies (Rosier et al., 2015; Rosier & Gudmundsson, 2016; Gudmundsson, 2006; Minchew, Simons, Riel, & Milillo, 2017). There are ways to integrate tides and IBE effects into the models but the tidal influence is not always linear, due to the viscoelastic properties of the ice (M. A. King, Murray, & Smith, 2010). Similar observations are met on the Filchner-Ronne Ice shelf (Rosier & Gudmundsson, 2020), and Beardmore Glacier (Marsh, Rack, Floricioiu, Gollledge, & Lawson, 2013). These velocity variations can be observed from DInSAR or offset tracking (if the resolution allows it). Rack, King, Marsh, Wild, and Floricioiu (2017) analyzed the tidal motion of the McMurdo ice shelf using InSAR and GNSS data. They conclude that the interferograms are key observations to understand the bending processes. On the contrary, Wild, Marsh, and Rack (2019) used DInSAR to locally correct tides estimations and improve small scale events by using finite-element modeling. Baessler, Rosenau, Dietrich, Shibuya, and Doi (2012) analyzed the

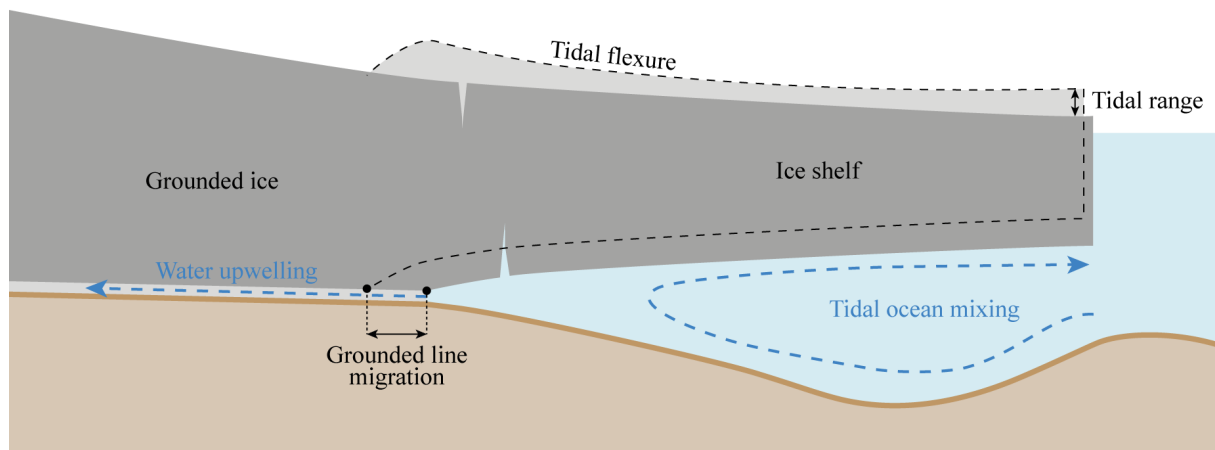


Figure 1.8: Tidally-induced velocity changes. Near the grounding line, the ice-shelf bending creates a horizontal displacement of the ice shelf. The influence can extend further upstream when grounding line short-scale migrations influence the water drainage under the ice shelf, lubricating the bed and modifying the basal drag. Figure recreated from Rosier et al. (2015).

vertical tidal component of DInSAR by removing the horizontal velocity acquired using speckle tracking. One important use of tidal flexure is its capacity to detect the grounding-line position (Rosier et al., 2017; Friedl et al., 2020).

More classical DInSAR also highlights topographic structures such as ice rises, ice rumples, ice front, ephemeral grounding, the grounding line, and so forth (Joughin, Smith, & Abdalati, 2010). Ice rises and ice rumples are locally grounded elements. They act as pinning points and participate in the buttressing capabilities of the ice shelf and thus the stabilization of the AIS (Matsuoka et al., 2015). Ice rises are important topographic structures that completely block the ice flow. In these areas, shear stresses are maximum, and so the ability to restrain the ice flow. Ice rumples, on the contrary, are located below the ice shelf, but in contact with it. The ice flow is mitigated from basal drag, but generally not deviated.

More subtle topographic features can also be present. In their article, Schmelz et al. (2001) presents the influence of ephemeral pinning points over the Thwaites glacier, where the decrease of surface velocity can reach 0.5 to 2% locally. These topographic features can be detected using Double Differential SAR Interferometry (Fig. 1.9).

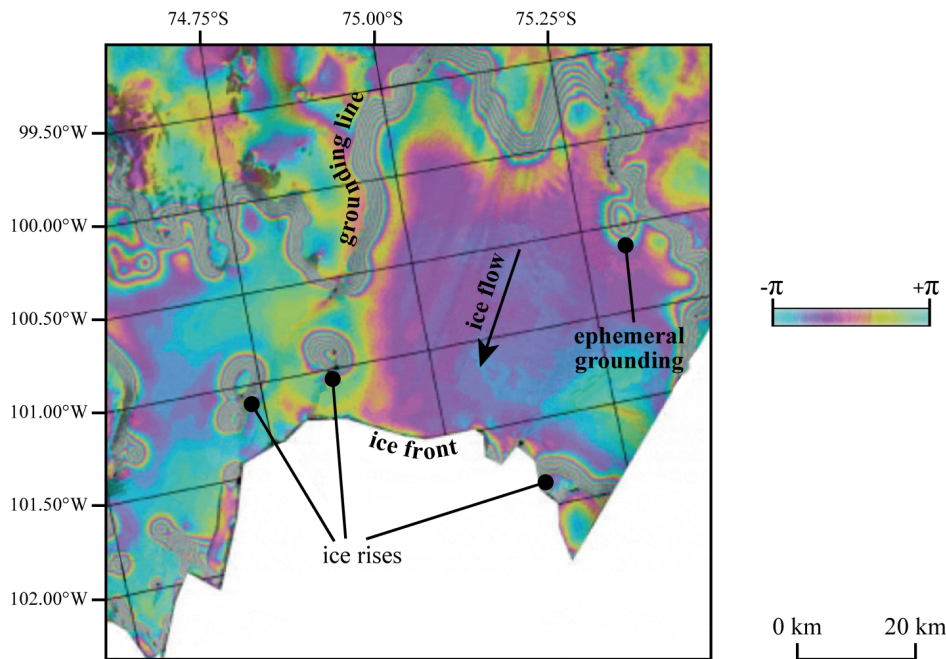


Figure 1.9: Double DInSAR allows the determination of vertical variations of the displacement vector. This characteristic allows the delineation of the boundary between the grounded ice and the floating ice shelf. Additional topographic structures, such as ice rises and ephemeral pinning points are also distinguishable. Illustration reworked from (Schmeltz et al., 2001).

1.1.4 The Specific Case of the Roi Baudouin Ice Shelf

The Roi Baudouin Ice Shelf - RBIS is the second-largest ice shelf of Dronning Maud Land - DML (Fig. 1.10). With around 350 kilometers length, the RBIS is covered by a single Sentinel-1 acquisition in Extra Wideswath mode.

The ice shelf is fed by the Ragnhild glacier, and surface displacements up to 300 meters are recorded on the Western part of the ice shelf. The ice shelf is constrained on its sides by two promontories, and an important structural element, the Derwael Ice Rise. With an elevation of a couple of hundred meters, it acts as an important regulator of ice-flow amplitudes and directions.

Goel et al. (2020) studied the ice rises and ice rumples in Dronning Maud Land (DML). In the specific case of the Eastern part of the RBIS, a series of ice rumples are present (Fig. 1.11), easily distinguishable in velocity maps. The Derwael Ice Rise, situated on the RBIS, is one of them, and strongly impacts the flow direction of the Western Ragnhild glacier (Drews et al., 2015). DML is particular by its abundance of these features, partly explaining the number of ice shelves surrounding the DML coast. These ice shelves are rather small in comparison to other regions in Antarctica. Nevertheless, they are important regulators of the major part of the AIS. Concerning the RBIS, these topographic structures are located near the calving front of the ice shelf. The high buttressing role of a small but important pinning point was studied in (Berger et al., 2017). If these elements protect the ice shelf, it makes RBIS particularly sensitive to unpinning of ice rumples in case of important basal melt RBIS, although Goel et al. (2020) testified the stability of DML.

Important katabatic winds over RBIS are responsible for a higher temperature than neighboring ice shelves, especially in the Eastern part of the shelf. This specificity makes RBIS subject to important surface melt periods. The winds also change the surface structure, removing the low-density snow deposits and exposing the surface to blue ice areas near the grounding line. This observation is confirmed by looking at SAR backscattering coefficient. Lenaerts et al. (2017) put

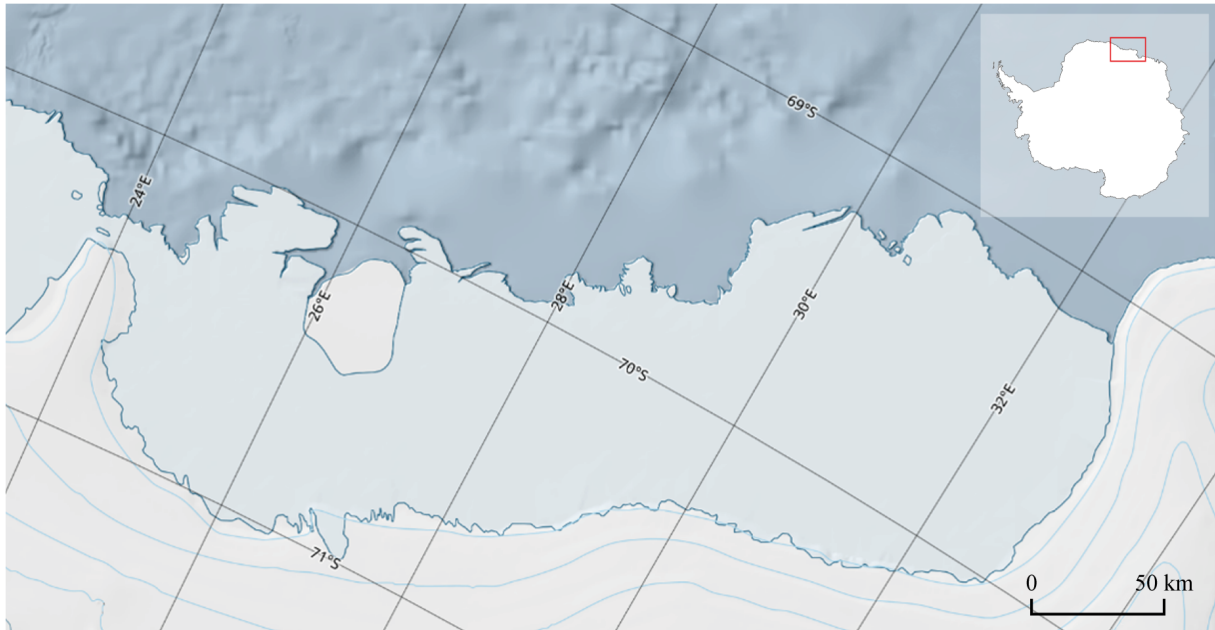


Figure 1.10: Location of the Roi Baudouin Ice Shelf.

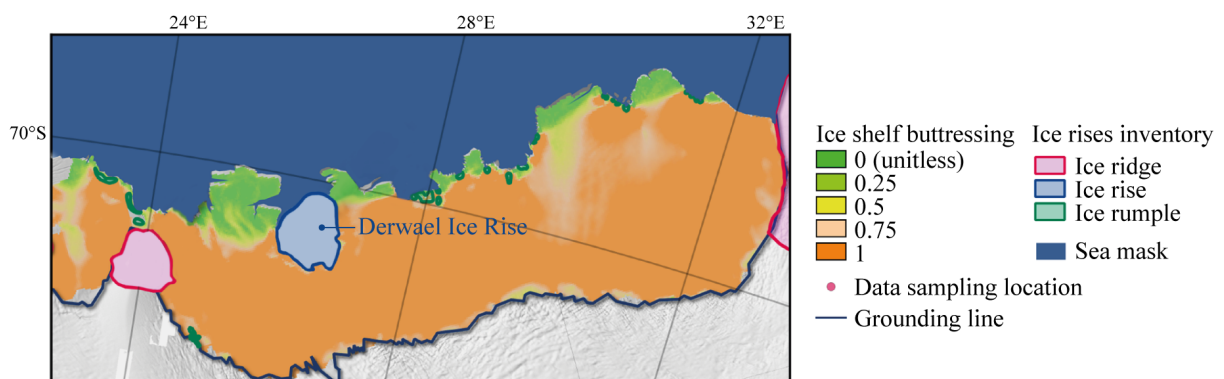


Figure 1.11: Ice rises and ice rumples over the RBIS and the associated buttressing effect. illustration from Goel et al. (2020), with modifications.

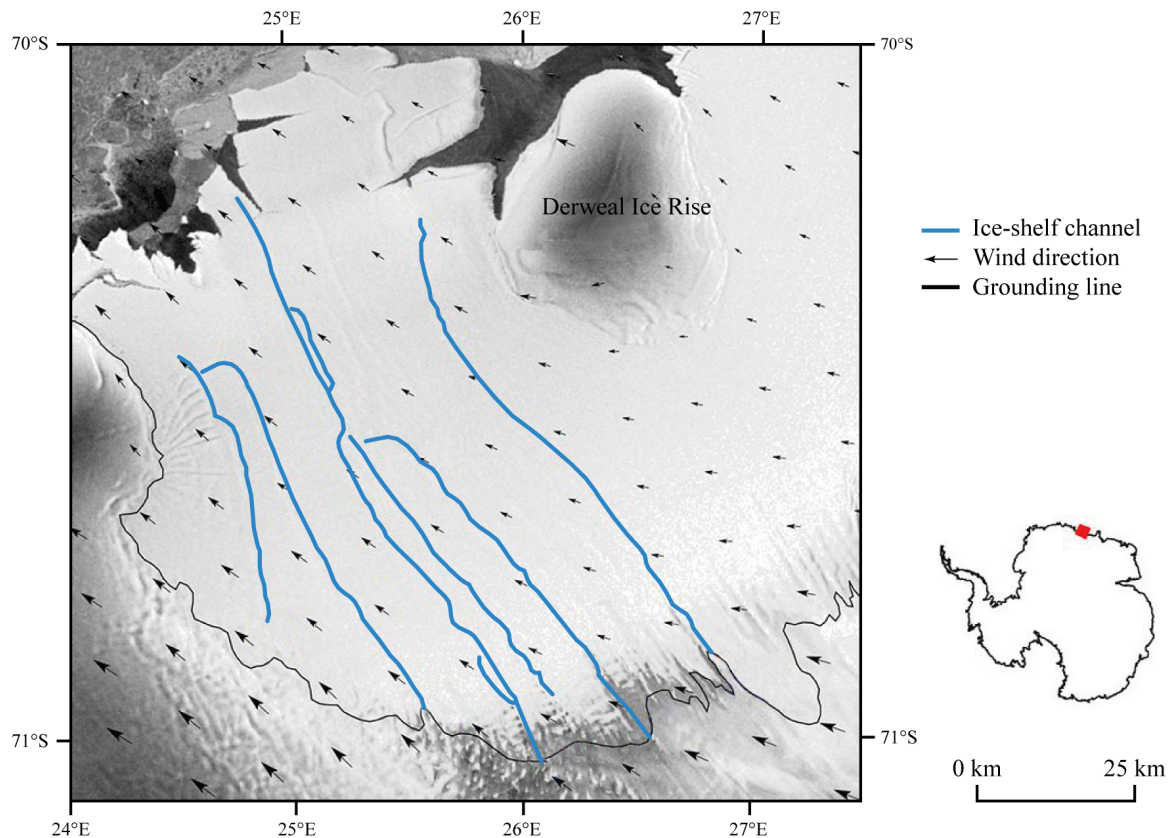


Figure 1.12: Ice-shelf channels start at the grounding line. Illustration from Drews (2015), with modifications.

evidence of the interaction of warm katabatic winds in the productions of surface meltwater.

The RBIS is composed of several longitudinal channels. These channels start near the grounding line, and extend toward the calving front (Drews et al., 2020). These channels are particularly sensitive to atmospheric and oceanic geophysical processes. They are also marked by enhanced basal melt (Drews, 2015; Berger et al., 2017).

Compared to previous satellite systems, Sentinel-1's high repeat pass cycle (6-12 days) now allows evaluating changes between velocity fields, while previously only a mean state could be determined. This has already allowed for determining sub-shelf melt rates over periods of 1-2 years using Lagrangian techniques (Marsh et al., 2016; Berger et al., 2017) (Fig. 1.13). This constitutes a drastic change from previous studies, largely focused on single velocity maps or only inter-annual studies (Fig. 1.7). With its 300 meters per year velocity, the RBIS is a good candidate for both speckle tracking and interferometry, considering the Sentinel-1 spatial resolution, wavelength, and revisit time.

Considering all the discussed information, the specifications of Sentinel-1, and changes in its acquisition geometry, the fine analysis of the RBIS case seems a pertinent study case for the thesis project. In addition, this answers the lack of research in DML observed by Dirscherl et al. (2020) (Fig. 1.6).

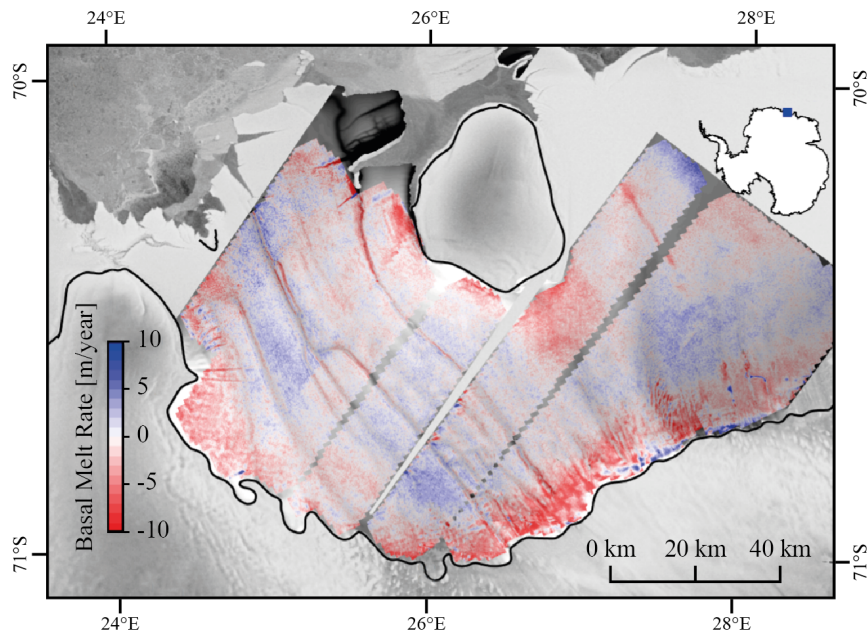


Figure 1.13: High-resolution basal mass balance over the RBIS. Illustration from Berger et al. (2017), with modifications.

1.2 Advances in Data Acquisition Techniques

The comprehension of geophysical processes is tied to the evolution of acquisition techniques and methods. In this section, we summarize the major breakthroughs that are guiding the understanding of ice shelves, and are setting the foundations on which the thesis is built.

Using a pair of coregistered SAR acquisitions taken at different times and slightly different positions, we can compute an interferogram based on the phase difference of SAR images¹. The coregistration is currently generally performed using precise orbits and DEM-assisted SAR coregistration algorithms (Sansosti, Berardino, Manunta, Serafino, & Fornaro, 2006; Nitti, Hanssen, Refice, Bovenga, & Nutricato, 2011; Frey, Santoro, Werner, & Wegmuller, 2013). Topography, Surface displacements, and atmospheric changes will introduce a phase shift in an interferogram.

Using a DEM, we can remove the phase term related to the topography, and exploit the phase shifts to infer ground displacements (Pepe & Calò, 2017; Bamler & Hartl, 1998). In Antarctica, the availability of precise DEM is more complicated. The SRTM is the most commonly used global DEM for DInSAR studies. This DEM was created by using Space Shuttle Endeavour in a bistatic configuration with two SAR sensors distant by a mechanical arm of 60 meters. The height accuracy of SRTM is a few meters. The issue is that the orbital geometry of the spaceship made the DEM limited to areas between 60 and -56 °latitude. In response, we can use the ACE (Altimeter Corrected Elevations), a 30-second resolution global DEM, released in 2001 (Berry, Pinnock, Hilton, & Johnson, 2000). The first major breakthrough came with the Bedmap2 dataset which includes a revised global Antarctic DEM (Fretwell et al., 2013). Then, the CryoSat-2 spaceborne radar altimeter allowed in 2017 the creation of a new Antarctic DEM at 1-km resolution. Thanks to its acquisition geometry, the vast majority of Antarctica could be sampled. CryoSat-2 DEM became the new reference for Antarctica (Slater et al., 2018). Compared to previous altimeters, CryoSat-2 has interferometric SAR capabilities, which greatly enhance the spatial resolution compared to the last sensors (Gourmelen et al., 2018). The determination of surface height from this new technique improved by 35% the root mean square

¹For more details, an entire section of chapter 2 is dedicated to the comprehension of SAR remote sensing, its basic concepts, and the recent and future changes in the SAR satellites fleet.

error (McMillan et al., 2018). REMA - the Reference Elevation Model of Antarctica, is the most recent DEM of Antarctica (Howat, Porter, Smith, Noh, & Morin, 2019). It is characterized by very high spatial resolution (up to 2 meters in Antarctic Peninsula) and elevation errors are generally below one meter. REMA was built from ultra-fine resolution optical satellites (GeoEye-1 and WorldView-1 to -3), with a ground sample distance of less than half a meter. The DEM was created from stereophotogrammetry, and elevation corrected from current spaceborne altimeters.

Changes in the atmosphere have a direct impact on interferograms. These changes will induce a variation of the refractive index and so a change in the optical path difference. To study atmospheric effects, we generally separate the ionosphere and the troposphere. The ionosphere is a dispersive medium, with influence on the chosen wavelength. Larger wavelengths, such as L-bands SAR systems from ALOS or SAOCOM, are particularly sensitive to variations of the ionosphere (Ding, Li, Zhu, Feng, & Long, 2008). The tropospheric effects depend on the atmospheric pressure, temperature, and water vapor. It will affect the small wavelengths more deeply. These effects can be corrected from meteorological data or by stacking different interferograms. Other ionospheric corrections were also proposed, based on split-spectrum approaches (Liao et al., 2018; C. Liang, Agram, Simons, & Fielding, 2019; Gomba, Parizzi, De Zan, Eineder, & Bamler, 2016).

When topographic and atmospheric influence has been removed, we can derive ground displacements according to the line-of-sight - LOS direction by differential SAR interferometry - DInSAR (Massonnet et al., 1993; Moreira et al., 2013; Richards, 2007; Ferretti, Monti-Guarnieri, Prati, Rocca, & Massonnet, 2007; Derauw, 1999b; Ouchi, 2013). Nonetheless, interferograms are tainted with errors; Zebker and Villasenor (1992) analyzes the different sources of decorrelation. He developed the temporal, spatial, and thermal components of decorrelation. An additional important deterministic noise is the speckle, resulting from interferences from the many scatterers in the resolution element. Multilooking is an important processing step during the analyses of SAR or InSAR products to reduce the deterministic noise, inherent in SAR imagery (Huang & van Genderen, 1997; Rosen et al., 2000). Finally, the phased-based information is known between $-\pi$ and $+\pi$. To translate an interferogram into a displacement, a prior phase unwrapping operation is required. An example of an unwrapping algorithm was developed in a study of Herráez, Burton, Lalor, and Gdeisat (2002). This phase unwrapping step generally depends on phase quality, and thus the need for a phase filtering algorithm. Goldstein and Werner (1998) developed a very efficient phase filtering algorithm. Further refinements of Goldstein's algorithm were made, taking into account the coherence information (Baran, Stewart, Kampes, Perski, & Lilly, 2003; Mestre-Quereda, Lopez-Sanchez, Selva, & Gonzalez, 2018).

In the specific case of Antarctic Ice Shelves, an additional phase term in DInSAR is introduced by the vertical variations of the elevation due to tides. The correction of tides comes from the reconstruction of the tidally induced bias in your DInSAR measurements. This is performed first by the computation of tide-deflection ratio over the area of interest (Han & Lee, 2014), then by the computation of the IBE-corrected tidal phase component (Han & Lee, 2015). This empirical correction method showed impressive results. A similar approach is developed in (Glaude et al., 2020) in section 2.2.2.3. One other possible correction of tides and IBE relies on the interferograms stacking (McMillan et al., 2012).

While DInSAR allows the computation of precise line-of-sight displacement measurement, many geophysical processes need at least 2D velocity components in their models. By combining ascending and descending passes, it is possible to determine 2D displacement maps (Wright, Parsons, & Lu, 2004). Unfortunately, ascending and descending orbits are not available everywhere on Earth. Other techniques use local correlation of images to extract 2D displacements (Euillades et al., 2016; Pattyn & Derauw, 2002; Scheiber, Jäger, Prats-Iraola, De Zan, & Geudtner, 2015; Casu, Manconi, Pepe, & Lanari, 2011; Lütting, Neckel, & Humbert, 2017). However, the accuracy of these pixel-based approaches is generally low.

Berardino, Fornaro, Lanari, and Sansosti (2002) developed in 2002 a method to analyze and follow non-linear deformations from a connected network of interferograms in a technique that will become famous: SBAS (Small BAseline Subset). The technique will create pairs of SAR images that minimize the geometrical and temporal baselines. All the interferograms are connected all together to monitor displacements through time, with high coherence. A similar time-series approach was developed two years before, called Persistent Scatterer Interferometry - PSI (Ferretti, Prati, & Rocca, 2000) where an important review paper has been published in 2016 (Crosetto, Monserrat, Cuevas-González, Devanthéry, & Crippa, 2016). The technique will seek for points in the images that remain highly coherent in time. A high density of these points allows an accurate measurement of displacements time series. When data gaps remain, geostatistical simulation models and regression algorithms are partially able to recover these missing information (Zakeri & Mariethoz, 2021).

Recent satellites launched by the European Space Agency (ESA) through the Copernicus program bring a new added value in the world of DInSAR. In this program, the Sentinels form a constellation of satellites designed to systematically and routinely observe the Earth. Sentinel-1 is a high-resolution SAR system with a large coverage obtained through a new acquisition mode, called Terrain Observation by Progressive Scans (TOPS or TOPSAR) (De Zan & Monti Guarnieri, 2006). Contrary to the ScanSAR mode which steers its sensor from close to far range, the TOPSAR acquisition steers its sensor from back to front when acquiring a burst, sparing time to acquire different parallel subswaths. TOPSAR mode can be used in Interferometric Wide-swath mode (IW), with a coverage of 250km or, in Extended Wide-swath (EW), with a coverage of 400km at coarser spatial resolution. Currently, two Sentinel-1 satellites are operational, reducing the revisit time up to 6 days, which opens the door to numerous applications and new techniques, some still to be discovered. Nevertheless, while remote sensing has drastically improved our understanding of many geophysical elements, the minimum requirements for studying hydrogeological processes in Antarctica has been assessed to 5 days, meaning that even the highly acclaimed Sentinel-1 SAR satellites do not fulfill these requirements (Tsai, Dietz, Oppelt, & Kuenzer, 2019). A situation that might change with the next Sentinel-1 C, to be launched in early 2023 (see chapter 3).

The performance of the TOPSAR imaging mode was assessed using TerraSAR-X data by re-configuring the acquisition geometry of the sensor (Yagüe-Martínez et al., 2016). From there, special requirements about the azimuth coregistration accuracy are being established. Indeed, the TOPSAR acquisition mode requires extremely fine coregistration. A number of techniques to coregister TOPSAR images were developed (Yague-Martinez, De Zan, & Prats-Iraola, 2017; Grandin, 2015). In addition, the interferometric process of TOPSAR data is slightly different from conventional interferometry. Due to the burst-by-burst imaging mode, A TOPSAR image is composed of multiple bursts and swaths with overlapping areas (Fig. 1.14). Points located in the intersection of two consecutive bursts are observed twice; once with a beam steered forward and secondly with a beam steered backward. In terms of signal characteristics, this leads to observations at different Doppler Centroid - DC due to time-varying DC within bursts (Fig. 1.15) (Rodriguez-Cassola et al., 2015; Yagüe-Martínez et al., 2016), inducing an additional phase ramp in the azimuth direction. This phase ramp needs to be removed in the coregistration process for proper image resampling, using the procedure developed by Miranda and Hajduch (2017).

When joining the burst-level interferograms, one may notice a phase jump in the overlapping regions. In the case of stationary scenarios, the method to be applied is an extension of the spectral diversity approach (Scheiber & Moreira, 2000) for the coregistration of SAR interferograms. It uses phase information at a pixel-by-pixel basis to infer misregistration and correct it. This technique, adapted to burst overlapping regions for TOPSAR acquisition mode, removes phase shift between bursts. That technique is called Enhanced Spectral Diversity - ESD.

On the contrary, in the case of non-stationary scenarios in bursts overlapping areas, the dis-

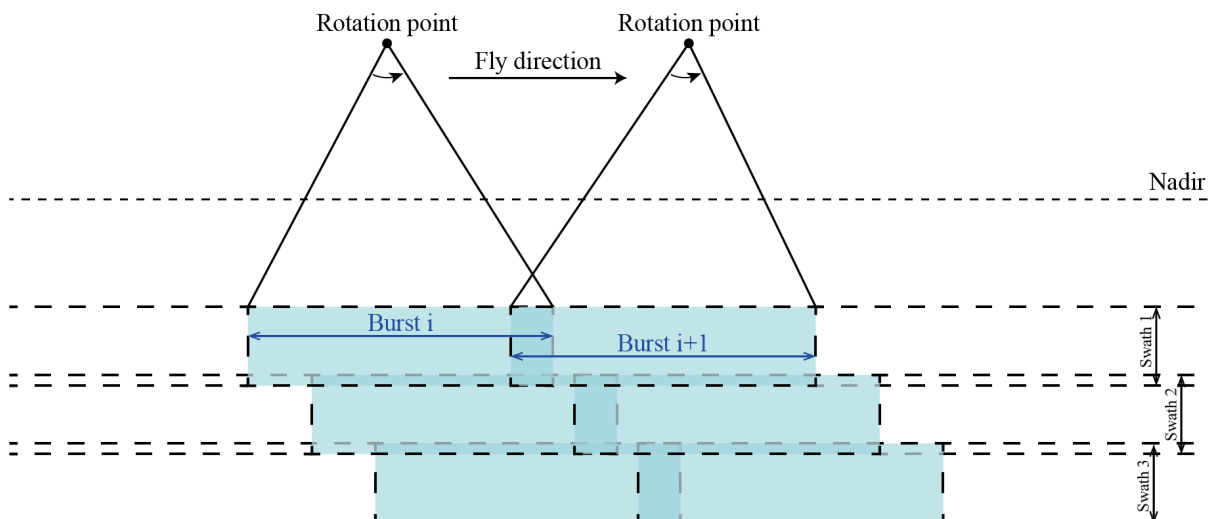


Figure 1.14: Acquisition geometry of a TOPSAR image. The image is composed of sub-swaths and bursts with overlapping areas.

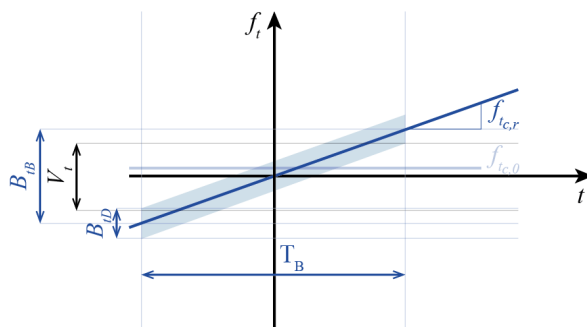


Figure 1.15: Time-frequency diagram of SLC TOPSAR images.

placement component along the azimuth direction will induce an additional and opposite phase term in consecutive bursts due to the opposite steering angle along which points are observed (De Zan, Prats-Iraola, Scheiber, & Rucci, 2014; Scheiber et al., 2015). In these cases, phase jumps between bursts will be present in TOPSAR images. These effects can be estimated from external velocity map and removed, and late residuals can be estimated from burst overlapping interferometry (Fig. 1.16) (Andersen et al., 2020).

The phase shifts in overlapping areas can also be used to estimate azimuthal displacements, using Burst Overlapping Interferometry (Yague-Martinez, Prats-Iraola, Pinheiro, & Jaeger, 2019). From two interferograms in the overlapping regions, it is possible to link the phase difference of these interferograms into an azimuth shift. The concepts of Burst Overlapping Interferometry are also applicable on the superposition areas between the different subswaths, where spectral diversity techniques are also applicable with lower spectral separation (Mancon, Guarnieri, Giudici, & Tebaldini, 2017). This has already been employed by H. Jiang et al. (2017) to study the azimuthal component of a land displacement triggered by an earthquake in Nepal. Their approach will be further developed and adapted in glaciology contexts, where higher displacements are observed. The heliosynchronism of the orbits and the main North-South component of the velocity make these effects are particularly important in Antarctica.

The computation of azimuthal shifts can also be determined from another spectral diversity technique called Multiple Aperture Interferometry - MAI (Mastro, Serio, Masiello, & Pepe,

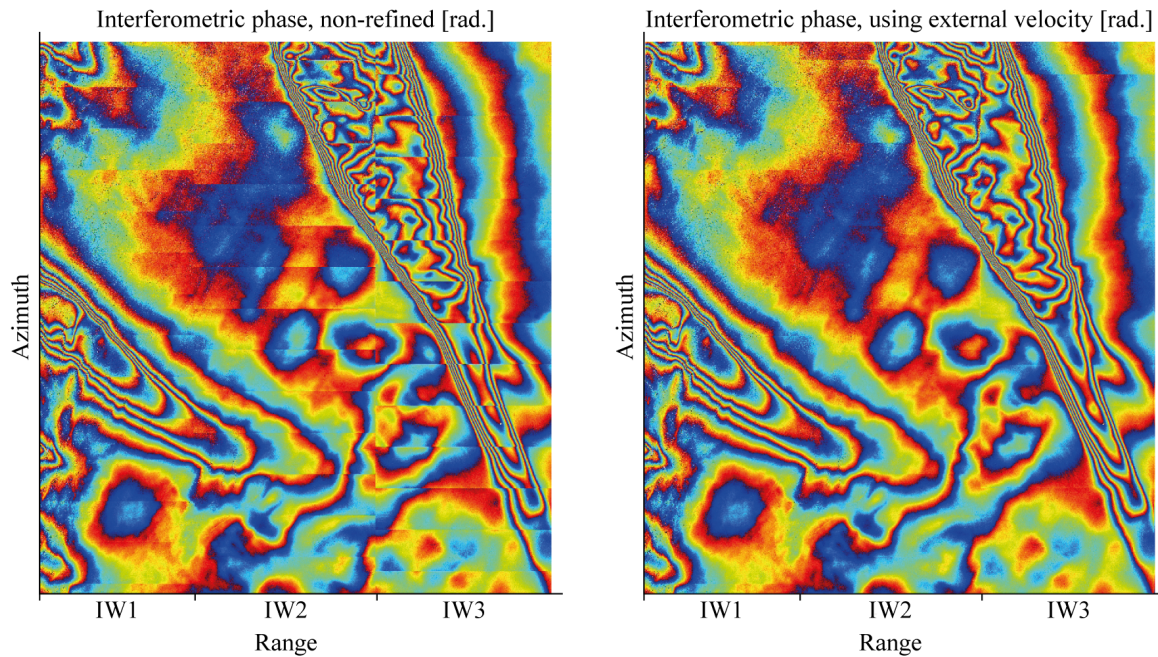


Figure 1.16: Azimuth shifts removal from an external azimuthal displacement map. Illustration from Andersen et al. (2020) with modifications.

2020). MAI was first introduced by Bechor and Zebker (2006). The principle of MAI relies on the creation of sub-aperture SAR images to create forward- and backward-looking SLC images. This is made possible either by adapting the Doppler Centroid during the focusing operation, or by applying an azimuthal splitband filter. In both cases, the reduced bandwidth implies an important decrease of the azimuthal resolution. Using two SAR images taken at two different times, the phase difference between interferograms created from forward- and backward-looking SLC images are witnesses of an azimuthal displacement. Jung, Won, and Kim (2009) will refine the technique by taking into account other geometrical artifacts.

Jung, Lu, and Zhang (2013) analyzed the *a priori* expected performance of MAI applied to Sentinel-1. Compared to ERS, Sentinel-1 azimuth resolution is 4 times coarser, due to the reduced azimuthal sampling of the TOPSAR acquisition mode. When coherence is high, the expected accuracy of MAI for Sentinel-1 of around 27 centimeters (Jung, Lee, & Zhang, 2014). The error estimation is based on Cramér-Rao bound and variance propagation through the MAI process. If MAI has proved useful to infer bidimensional displacements from a single SAR pair, the process of azimuthal subbanding further decreases the azimuthal direction. This drawback was limited for the case of ERS, because the azimuthal resolution was finer than the range resolution. This is not the case for TOPSAR acquisitions, with MAI creating highly asymmetrical spatial sampling of the observed scene. The consequence is a reduced along-track displacement accuracy. Due to the increased spectral separation, BOI is expected to be 20 times more sensitive than MAI (H. J. Jiang, Pei, & Li, 2017).

Using the principles of MAI and BOI, Yague-Martinez, Prats-Iraola, and Wollstadt (2018) proposed a variation of the TOPSAR acquisition mode such that burst overlapping areas cover the entire scene. Said in other words, each resolution element is observed twice by the sensor, explaining the acquisition name: the 2-Looks TOPS mode.

Using burst overlapping interferometry and multiple aperture interferometry in combination with classical DInSAR, Grandin et al. (2016) retrieved the full three-dimensional displacement fields of an Earthquake event in Chile (Fig. 1.17). A similar approach was used in He, Wen, Xu, and Chen (2019) for the 2017 Iranian Earthquake in Ezgeleh. There, the authors also use DInSAR,

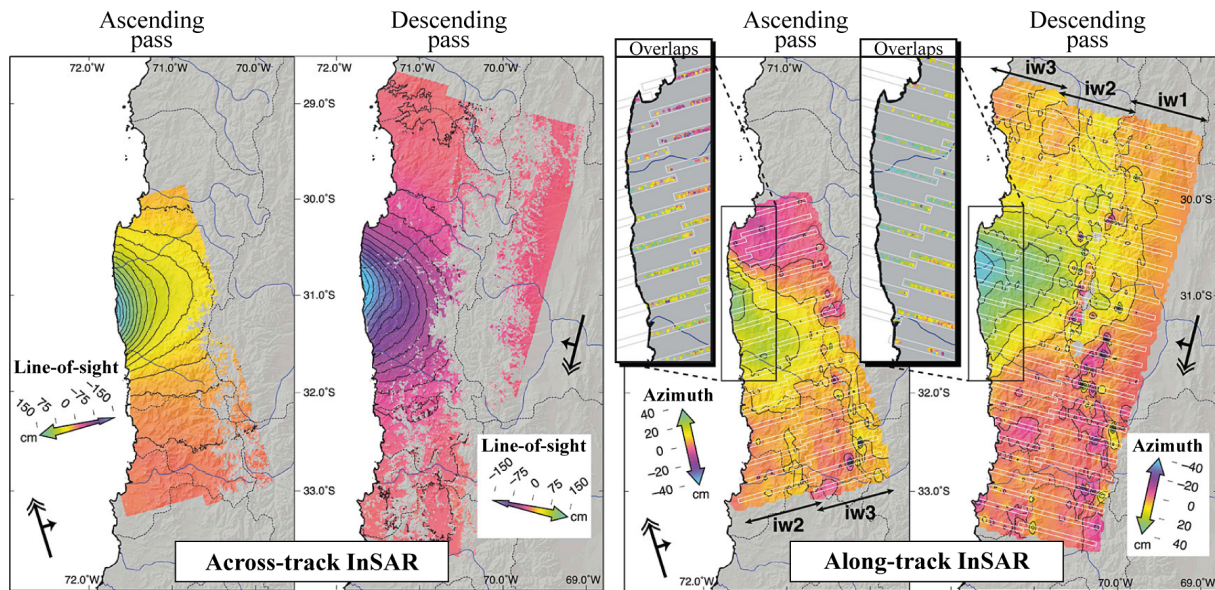


Figure 1.17: Combination of ascending and descending paths, where across- and along-track displacement are retrieved using DInSAR (left), and MAI and BOI (right). Illustration from Grandin et al. (2016).

MAI, BOI, but also a more classical offset tracking approach. From all measurements, it is finally possible to get the 3D displacement model from matrix inversion and least-squares approaches. Finally, H. Jiang et al. (2017) also used the combined four techniques for the 2016 Kumamoto Earthquake (Japan).

Despite all these advances, the use of phase-based measurement for the estimation of glacier and ice sheet displacements is limited, encouraging the use of speckle tracking techniques (Strozzi, Luckman, Murray, Wegmuller, & Werner, 2002). This is often the case in Antarctica, where the temporal baseline of repeat-pass interferometry is too large. In 1999, Derauw (1999a) developed the coherence tracking technique. Coherence tracking is based on local coregistration using coherence as maximization criteria. Doing so, coherence tracking gives an estimation of bidimensional displacements from misfit determination, and an interferogram corrected from geometrical decorrelation. Bidimensional displacements from tracking algorithms are tainted with statistical errors and false detections. Lüttig et al. (2017) developed filtering algorithms that are responsible for the removal of false detection related to speckle noise, but still preserving structures.

Sánchez-Gómez and Navarro (2017) use a combination of offset tracking and DInSAR from Sentinel-1 data to extract surface velocities, depending on the local temporal decorrelation. Because of the low azimuth resolution, (Sánchez-Gómez & Navarro, 2017) compute only range shifts, and use ascending and descending paths to retrieve the full vector of displacements.

In addition to the displacement retrieval, the open-data policy of the Copernicus program enables us to have free access to Sentinel-1 data every 6-12 days. This with the high resolution of Sentinel-1 products brings a paradigm shift in interferometry: the opportunity to monitor and address rapid and local changes. The number of wide swath acquisitions of Antarctica and Greenland is huge, with a high revisit rate. This allows the computation of frequent and precise velocity fields (Nagler, Rott, Hetzenecker, Wuite, & Potin, 2015). In addition, Sentinel-1 has a long-term commitment, and the new Sentinel-1 C and D will be launched in the next years.

1.3 Research Question: Does the TOPSAR Acquisition Mode of Sentinel-1 Improve the Monitoring of the Antarctic Ice Sheet?

The objectives of the Ph.D. thesis are to investigate short time-scale dynamics of the Antarctic ice sheet and its ice shelves by taking advantage of the high spatial and temporal resolution offered by the Sentinel-1 Synthetic Aperture Radar (SAR) satellite. Moreover, the Sentinel-1 particular acquisition mode, Terrain Observation by Progressive Scan (TOPSAR), opens up new opportunities for SAR applications in dynamic glaciology.

The main hypothesis of the thesis is built around how ice-shelves influence inland Antarctic ice dynamics on different (monthly-yearly-decadal) time scales. This hypothesis is driven by the fact that Antarctic ice-sheet models used for predicting future ice mass changes (hence sea-level contribution) need initial conditions that currently stem from coarse-resolution products. Furthermore, these products represent a temporal aggregation of time-series without considering the short-scale temporal variability. In order to reach the necessary precision, we will take advantage of the TOPSAR mode peculiarities on burst superposition areas to infer precise bi-dimensional displacement maps. Furthermore, we will adapt coherence tracking methods to Sentinel-1 TOPSAR mode for spatially continuous determination of coarse bi-dimensional velocity fields. This way, time series of ice-shelf flow and grounding line variability measurements can be derived.

Data will mainly consist of Sentinel-1 SAR images in IW and EW acquisition modes. The proposed methods will be applied to several areas in the Antarctic for which additional datasets are available, either at ULB or through collaborations with international partners. The major area of application is the RBIS in Dronning Maud Land for the reasons exposed in section 1.1.4. Indeed, a major lack of studies in Antarctica is present (Dirscherl et al., 2020). This is particularly the case for the ice shelves along Dronning Maud Land, in Eastern Antarctica.

The project structure consists in the determination of main drivings mechanisms (chapter 2). We will start by demonstrating the use of Sentinel-1 on the ice velocity determination using offset- and phased-based techniques, and associated strain rates. Particular attention is drawn to the effects of tides and IBE. Using Double Differential Interferometry, we also studied the location and evolution of grounding line positions. Then, the presence of sea ice is investigated too. After that, the study of hydrofracturing, icebergs presence, and calving front locations has also been monitored. Finally, the surface melt will be investigated and compared with regional climate models.

In chapter 3, we take a step back on our results, and try to answer the question: *Does the TOPSAR Acquisition Mode of Sentinel-1 Improve the Monitoring of the Antarctic Ice Sheet?*

High-Resolution Observations of Driving Factors of the Antarctic Ice-Flow Dynamics

In this chapter, we focus on methods that allow us to extract from SAR images information on driving factors of Antarctic Ice Shelves. Among them, ice velocity is of key importance, with a large portion of the chapter dedicated to it. We separate offset- and phased-based methods, as they are significantly different in their concepts, implementations, issues, and results. In each case, we develop how Sentinel-1 can be exploited, by discussing the parametrization and the limitations, and how to react to it. This thought process is valid for offset tracking which is highly parameter-dependent, as well as SAR Interferometry, which, by its high sensitivity, has a large number of external influences to take into account. In the chapter, some of these external factors have received particular attention. This is the case for tides and atmospheric pressure changes, as well as displacement-induced decorrelation. From these results, the temporal evolution of the velocity is studied, and spatial variations of ice motion are derived into strain rates.

In addition, SAR Interferometry allows the study of the grounding line migration, which is an important signal of the (de)stabilization of the ice shelf. Using SAR Interferometry and the dual-polarization of Sentinel-1 images, we can also have a look beyond the calving front, and observe the presence of stable sea ice.

To conclude with phase-based techniques, we investigate two methods to determine along-track displacements, using spectral diversity. If these two techniques are based on the same principle, they differ significantly in their approach. While the first one, Multiple Aperture Interferometry, requires special care because of the particular TOPSAR acquisition mode, the second one, Burst Overlapping Interferometry, on the contrary, exploits the specificities of this mode to extract azimuthal displacements.

Finally, two other subjects retain our attention. First, we are interested in the retrieval of surface features on SAR images. In particular, we focus our analysis on the extraction of crevasses, the calving front, and icebergs formation. This section brings us back to some fundamentals of computer vision. Secondly, we look at strong melt events, which appear to have strong signatures in SAR images. The results are then compared to a regional climate model, with spatio-temporal analysis of their residuals.

2.1 SAR Remote Sensing: Theoretical Background and Recent Changes in the Global Observation Scheme

In an article to be published in BSGlG (volume 77, 2022), we introduce in a couple of pages the concepts of Synthetic Aperture Radar and Interferometry, and some of its applications. What follows is a long detailed photograph of the current situation of the various major space institutions (NASA, JAXA, ESA, and so forth). To our knowledge, the article presents the most up-to-date situation of the SAR Earth Observation acquisition scheme.

We believe the article is appropriate to start with, as it provides the necessary prerequisites to understand the developments of the next sections. In addition, it situates the Sentinel-1 mission within the other SAR satellites orbiting the Earth. Some SAR concepts will be further developed in the next sections. This is particularly the case for offset tracking, Multiple Aperture Interferometry, or Burst Overlapping Interferometry, which are important parts of the thesis.

THE DARK SIDE OF REMOTE SENSING: CURRENT SAR REMOTE SENSING MISSIONS AND APPLICATIONS

Quentin GLAUDE & Anne ORBAN

Abstract

The present paper provides an overview of Synthetic Aperture Radar (SAR) remote sensing concepts. SAR remote sensing is a coherent active imaging technique, where the spaceborne sensor emits an electromagnetic wave and captures its backscattered signal. Each pixel contains amplitude information, witness of the ground properties to reflect the signal back to the sensor, and a phase component, which is related to the distance from the sensor to the ground target. Firstly, we will focus on SAR and SAR interferometry concepts. The acquisition geometry, the different wavelengths, the issue of spatial resolution, the polarization; SAR has a number of differences compared to optical remote sensing. In addition, the coherent imaging technique allows the exploitation of the phase information, with applications such as DEM generation or surface displacements retrieval. In a second part, we will discuss the current and future SAR constellations as well as recent advances in applications coming from the deep learning field. The domain of SAR remote sensing is a rapidly evolving field, where more and more satellites are being set up and where the private sector is investing massively. Service-oriented market using small X-Band SAR satellites is getting more and more present. In parallel, public institutions already have several important SAR satellites and are currently preparing the next generation, with improved technical specifications.

Keywords

SAR, InSAR Sentinel-1, ESA, JAXA, NASA, DLR, Newspace

Résumé

Ce papier présente un aperçu des concepts liés au radar à synthèse d'ouverture (SAR en anglais). La télédétection SAR est une technique d'imagerie cohérente où le senseur émet un rayonnement électromagnétique, et enregistre le signal rétrodiffusé. Chaque pixel de l'image contient une information sur la capacité de la cible au sol à rétrodiffuser le signal, et une information sur la distance satellite – cible au sol. Dans un premier temps, nous passerons en revue les concepts du SAR et de l'interférométrie SAR. Nous verrons qu'il existe un grand nombre de différences par rapport à la télédétection optique : la géométrie d'acquisition, les longueurs d'ondes employées, les soucis de la résolution spatiale, la polarisation, etc. De plus, nous nous intéresserons aux applications employant l'information de phase, comme l'extraction de modèles numériques de terrain (MNT) ou de cartes de déplacements. Dans un second temps, nous discuterons des missions SAR actuelles et futures, ainsi qu'un nombre d'applications provenant du monde de l'apprentissage en profondeur. Le domaine du SAR évolue rapidement, et de plus en plus de satellites sont en développement. Le secteur privé investit massivement, s'attaquant à un marché orienté services. En parallèle, les grandes institutions publiques disposent déjà de satellites SAR importants, et précisent les spécifications techniques des nouvelles générations.

Mots-clés

SAR, InSAR, Sentinel-1, ESA, JAXA, NASA, DLR, Newspace

INTRODUCTION

The term dark in *dark side of remote sensing* refers to two elements of Synthetic Aperture Radar (SAR) remote sensing.

First, as we will see, SAR is an active imaging technique. It is not the only one, as altimeters are also active spaceborne sensors. Nevertheless, SAR produces images that share visual similarities with more classical remote sensing, such as images produced by optical

satellites (Landsat 8, Sentinel-2, or Pléiades). SAR sensors emit pulsed electromagnetic waves in the radio frequencies and capture the echoed signal. Contrary to optical remote sensing, SAR does not capture the reflected solar radiation. SAR is therefore completely independent of the Sun illumination, and is perfectly capable of working in *dark* conditions such as during the night. This is particularly useful in polar regions, where areas of interest are subject to multi-month length nights, where optical sensors become unusable.

The *dark* side also refers to the relative quietness of SAR remote sensing in the classes in environmental sciences studies. This is understandable, in the sense that remote sensing is already a highly transverse field that merges physics, mathematics and computer science. Depending on the objectives, we will also need backgrounds in biology, chemistry, and geosciences. In remote sensing lessons, the student will encounter topics such as optics, celestial mechanics, radiative transfer, and digital signal processing. With a focus on methods, the students will also face subjects related to computer vision, such as data visualization, multivariate statistics, machine learning and so forth. In a user-oriented approach, the students will finally need additional specificities related to its application; crop yield estimation requires biology / agronomy backgrounds; cryosphere monitoring requires glaciology; atmosphere composition requires chemistry and climatology. In this ocean of possibilities, and limited hours to give a proper remote sensing class, professors have to purposely omit branches of remote sensing. SAR remote sensing is often one of them, especially the deeper SAR interferometry domain. Nevertheless, we are observing a shift in this trend, as SAR was the first priority of the European Space Agency Copernicus program, and we now occasionally see SAR content in general remote sensing courses.

I. SAR AND INSAR CONCEPTS

In optical remote sensing, the Sun illuminates the Earth surface in its entire wavelength spectrum. The ground backscatters a part of the energy received. The satellite picks up the backscattered signal and records the light intensity according to the sensitive spectrum of the sensor (Elachi & IEEE, 1987).

Unlike optical remote sensing, SAR sensors generate their own radiation, with a given frequency and polarization, which is then backscattered by the ground and received by the sensor (Elachi & van Zyl, 2006). Moreover, radar authorizes work day and night, through clouds, and to study geophysical processes at a given frequency. For instance in Belgium, due to cloud coverage, it allows increasing the number of potential usable acquisitions by one order of magnitude.

Radar remote sensing includes a series of bands between 1 and 40 GHz (Table 1), each frequency having specific properties. In general, a signal reacts strongly with geometries of size comparable to the wavelength used, determining the range of applications (topography, cryosphere, biomass, and so on). For the example of forestry, small wavelengths (X band) will be stopped by the canopy while long wavelengths (L to P bands) pass through the canopy and interact with the soil, trunks, or large branches.

Radar Band	Frequency (GHz)	Wavelength (cm)
Ka	26.5–40	1.1–0.75
K	18–26.5	1.7–1.1
Ku	12.5–18	2.4–1.7
X	8–12.5	3.75–2.4
C	4–8	7.5–3.75
S	2–4	15–7.5
L	1–2	30–15
P	0.3–1	100–30

Table 1. Common radar frequencies employed in SAR remote sensing (Parker, 2010)

The satellite moves by illuminating one of its sides. SAR sensors are said to be side-looking. In a SAR image, one dimension of the image corresponds to the flight direction, called the azimuth direction, and the other to the range, meaning the distance from the sensors to the target. Contrary to optical images, the pixel location in a SAR image does not correspond to the sight-angle of the sensor, but to a distance, here called the slant range.

In terms of spatial resolution, radar wavelengths do not allow to reach fine pixel spacing. Resolution is linearly dependent on the distance and the wavelength, and inversely linearly dependent on the antenna size. Using typical C-band SAR sensors, a kilometric resolution in the range direction is obtained. It is possible to narrow the beam and achieve the metric spatial resolution using Synthetic Aperture Radar (SAR), by combining the different echoes emitted by the sensor. This is called the focusing operation. From this, the image is said to go from RAW (LO) to Single-Look-Complex, or SLC (L1).

The choice of the acquisition strategy also has an influence on the spatial resolution. We generally separate them into three modes: Stripmap, Spotlight and ScanSAR/TOPSAR. In Stripmap mode, the satellite is illuminating the scene at a fixed look angle. Spotlight, in contrary, is focusing on a more restraint area by increasing the aperture time. It allows the sensor to drastically increase the spatial resolution in this specific region. In TOPSAR and ScanSAR modes, SAR sensors electronically steer their antenna on a wider region to increase spatial coverage at a cost of spatial resolution. In the end, the balance between spatial resolution and coverage is application dependent, and determines the acquisition mode.

II. AMPLITUDE INFORMATION

A SAR image is a complex image, made up of phase information and amplitude information (Eckardt *et al.*, 2013).

The amplitude depends on the backscattering mechanisms of the target. Typically, the amplitude of the backscattered signal is linked to a couple of parameters specific to the object: rugosity and moisture. In addition, it is affected by the acquisition geometry, in particular the angle between the normal to the slope and the sight-direction of the sensor. One example is the double bounce effect. When the electromagnetic wave meets two perpendicular smooth surfaces, the beam is reflected back to the sensor with maximum amplitude (Figure 1). This effect is very common in urban areas. Radar amplitude has a range of important applications in oceanography, land use, urban planning or ecology.



Figure 1. Double bounce effect, revealing anthropogenic structures: buildings, offshore wind turbines and boats (illustration from Sentinel-1 over the Belgian coast)

Unlike optical imaging, the position of a pixel in SAR depends on the distance from the sensor. A consequence is that topography influences the distance between an object on the ground and the sensor, inducing geometric distortions. We generally distinguish three types of geometric distortions: foreshortening, layover and shadowing.

Foreshortening occurs when higher altitudes are closer to the sensor; therefore, they appear at an inadequate place within the image. An extreme case of foreshortening is layover, where the summit of a target (e.g. mountain, building) is seen before the base of the element, shifting the pixel location of the summit and creating ghost artefacts. Topography can obstruct parts of the observed scene, creating a shadow area in the image, and hence a shadowing effect. Hidden pixels appear black since, for a given distance, no backscatter is recorded.

SAR images are characterized by an additive deterministic noise called speckle. The return signal of a pixel contains each of the contributions of the ground diffusers, the variability of which creates a speckle effect. The speckle has a statistical distribution centered around zero, and can therefore be reduced by spatial or temporal aggregation. This technique is called multilooking (spatial or temporal – Figure 2).



Figure 2. Speckle noise reduction using temporal multilooking (illustration from Ferreti *et al.*, 2007)

The satellite sends out a pulsed electromagnetic wave, containing an electric field and, perpendicular, a magnetic field. The sensor can control the direction of polarization of the sent signal and the return signal. Examples:

- VV: vertical transmit, vertical receive;
- VH: vertical transmit, horizontal receive.

The ground material is capable of depolarizing the received signal. The combination of signals with different polarizations provides information, and so the difference in intensity between the received signals of different polarizations makes it possible to discriminate between classes on the ground. For example, anthropogenic elements tend to return a signal that is not depolarized while vegetated structures tend to depolarize the signal (Figure 3).

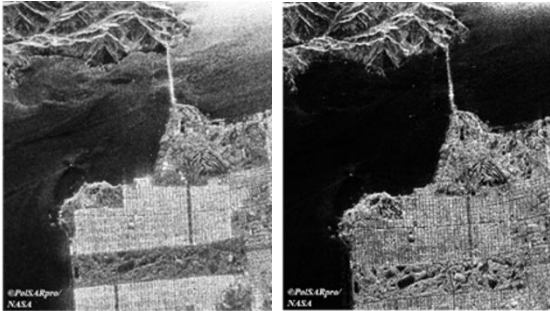


Figure 3. VV and VH images of San Francisco
Anthropogenic elements tend to return a signal that is not

depolarized; on the contrary, vegetated structures tend to depolarize the signal (illustration from NASA)

III. PHASE INFORMATION

The phase information is proportional to the distance between the satellite and the target on the ground, traveled by the electromagnetic wave. Based on two SAR images taken from two similar points of view, it is possible to reconstruct the topography of the place. The first image is at a distance r from the target. The second is at a distance $r + \delta r$ (Figure 4).

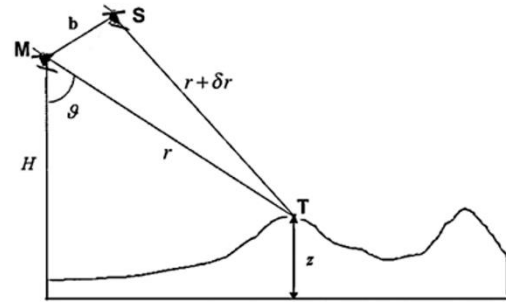


Figure 4. Interferogram formation based on two sensors M and S, separated by a distance b ; M is at a distance r from the target, S is at a distance $r + \delta r$ (illustration from Pepe & Calò, 2017)

An interferogram consists in the combination of signals to reveal the phase difference between the two images (Pepe & Calò, 2017). This phase difference is called the interferometric phase and is proportional to the distance difference δr between the two images.

$$\varphi_{intf} = \varphi_2 - \varphi_1 = \frac{4\pi}{\lambda} \delta r \quad (1)$$

The phase difference varies continuously with δr . Even without topography, the interferometric phase has a component that depends on the viewing angle and the sensor positions. At the same time, the topography also modifies the path difference between the target and the sensors. There are a large number of terms to consider in SAR interferometry, some of which can be calculated and removed. In order, we can enumerate the orbital phase, the topographic phase, the displacement phase, the atmospheric phase screen, and finally a component that comprises the residual noise (Equation 2).

$$\varphi_{intf} =$$

$$\varphi_{orb} + \varphi_{topo} + \varphi_{displ} + \varphi_{atm} + \varphi_{noise} \quad (2)$$

One important note is that the interferometric phase is known modulo 2π , which implies a phase unwrapping operation to determine the absolute phase. The fringe sensitivity is determined by two parameters: the wavelength and the baseline. Larger baselines increase sensitivity to height, while longer wavelengths decrease the sensitivity to topography and displacements. Once unwrapped, the topographic phase can be translated into a digital terrain model (Figure 5).

Several missions allowed the creation of digital terrain models via SAR interferometry. The Shuttle Radar Topography Mission (SRTM) was a mission conducted by performing SAR interferometry by taking two simultaneous acquisitions at each end of a 60 meters mechanical arm attached to the NASA Space Shuttle. In this bistatic configuration, it is possible to neglect the effect of displacements and the atmospheric phase screen. The SRTM allowed the creation of a global Digital Elevation Model (DEM) of the Earth (from -60 to +60 degrees latitude).

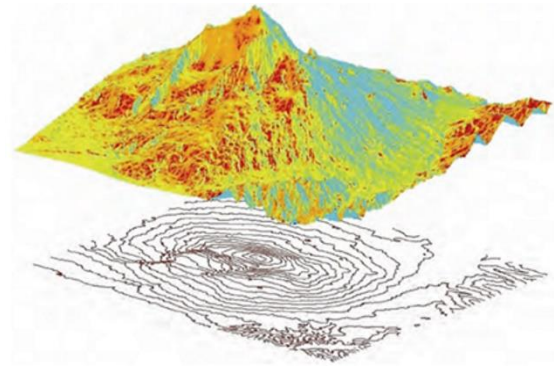
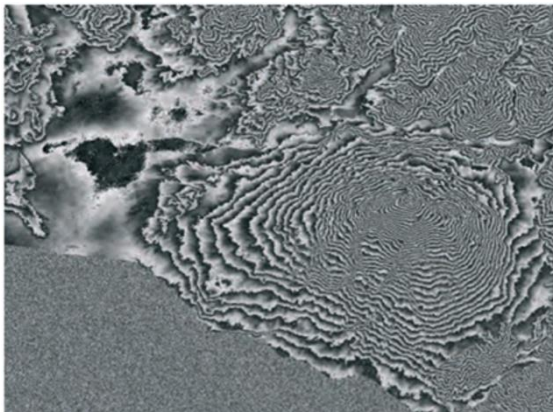


Figure 5. Topographic phase component (top) and DEM extraction from the unwrapped phase (bottom) (illustration from Ferretti *et al.*, 2007)

The quality of an interferogram can vary greatly; coherence is a local measure of quality. It is defined by the complex correlation between the master image and the slave image. A correlation value of 1 means perfect consistency between the images, with perfectly distinguishable and unwrappable fringes. A 0 correlation means a change in the arrangement of ground scatterers, a witness of changes in the ground conditions between the two acquisitions, resulting in a loss of coherence. This type of signal cannot be used for SAR interferometry.

One of the sources of decorrelation is the time that separates the two acquisitions, creating a temporal decorrelation. Another source of decorrelation is related to acquisition geometry, which influences the fringe sensitivity. Thermal noise also induces an additional decorrelation pattern in the interferogram. More importantly, a sudden loss of coherence between successive dates is also a sign of land cover change.

Finally, one very important branch of SAR is Differential SAR Interferometry (DInSAR). By using two images taken at different times, it is possible to determine the movement of a target on the ground. If we know the topography (by using a DEM for example), it is also possible to determine a movement along the line of sight of the satellite. To achieve this, we can remove the topographic phase component from the interferometric phase. As long as the atmospheric influence is negligible (or correctable), this residual phase term can be translated into movement (Ferretti *et al.*, 2007).

Differential interferometry is very sensitive to displacements and is able to determine sub-centimetric movements. Similar to topography, the fringes can be unrolled and converted to a displacement map. One very famous example of displacement estimation is the Landers Earthquake event, making the cover page of the *Nature* journal (Massonet *et al.*, 1993).

IV. CURRENT AND FUTURE SAR MISSIONS

In the early 2000s, the European Space Agency developed its strategic plan in their Earth Observation department. Rapidly, three pillars emerged: Copernicus, Meteorology and Earth Explorer. The Copernicus program includes well-known techniques with a particular focus on user-oriented applications. Copernicus is composed of a set of Sentinels, decomposed into Sentinel-1 to Sentinel-6, each having their particular sensors and objectives.

Sentinel-1 is the workhorse of the SAR part of the Copernicus program (Torres *et al.*, 2012). Currently, two Sentinel-1 are orbiting the Earth (S-1A and S-1B), and are positioned to reduce the revisit time by half (6 days). Sentinel-1 aims at the systematic observation of the Earth in the C-Band radar frequency (5.45 GHz), with low latency. To obtain this small revisit time, Sentinel-1 is characterized by a specific acquisition mode, called TOSPAR, allowing large swath width, ranging from 250 to 400 km, with a decametric resolution.

Sentinel-1 data is accessible free-of-charge by the Open Access Hub, or by mirror data facilities (Operating platform Sentinel products – PEPS, Alaska Satellite Facility, etc.). Sentinel's derived products are available through the different services offered by the Copernicus program (atmosphere, climate change, emergency, land, marine, security) through the Copernicus Service Hub. The Copernicus program brought about 500 000 users, that have access to petabytes of data. In the end, Copernicus is an ambitious program that provides remote sensing data fluxes to the public (Figure 6). It is the user's responsibility to create added value from operational

services. Started in 2014 with S-1A, long time series are already available.

To encourage user developments and education, the European Space Agency funded open-source toolboxes through the SentiNel-Application Platform – SNAP (Brockmann Consult, 2020). SNAP is a multi-mission remote sensing software originally designed for the different Sentinel products but now updated for other sensors (ALOS, TerraSAR, CosmoSkymed, etc.). All source codes are available online in a DevOps environment. Users are allowed to download and commit changes to the project. SNAP has more than 800 000 downloads and is currently the most popular remote sensing software. SNAP functionalities are varied, and enable data calibration, speckle filtering, co-registration, interferometry, multilooking, terrain correction, and so on. SNAP is also linked with other popular routines or software such as STAMPS (Mancini *et al.*, 2021) for permanent scatterer interferometry, or PolSARPro (Pottier *et al.*, 2009) for advanced polarimetric techniques. SNAP is using the BEAM-DIMAP image format, easy to combine with GIS software such as QGIS. For advanced operational services, SNAP allows the development of processing frameworks, thanks to graph processing tools and batch processing operations. Finally, it has a large user support material, with tutorials on various subjects such as SAR interferometry or flood mapping.

Since the launch of Sentinel-1, the number of Earth observation users drastically increased, with limited experience in SAR and SAR interferometry. In particular, SAR is inherently a non-trivial field of remote sensing, with a specific acquisition scheme, synthetic aperture or coherent imaging representation. In response, the National Aeronautics and Space Administration (NASA) developed the openSARLab, a cloud-based SAR training tool environment, using Amazon Web Services (AWS) and Jupyter Notebooks. It also contains a number of books and materials available. Among these books, we recommend the very exhaustive and practical SAR Handbook: *Comprehensive Methodologies for Forest*

Monitoring and Biomass Estimation (Flores *et al.*, 2019).

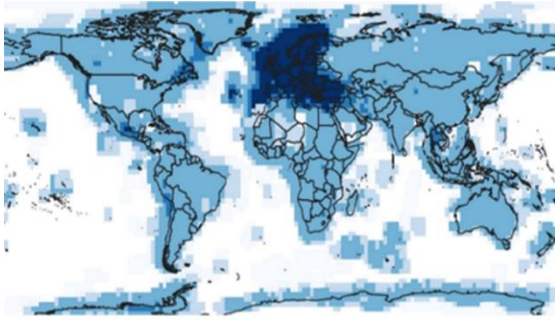


Figure 6. Heatmap of Sentinel-1 SLC products published from the start of operations to the end of 2019 (Hajduch *et al.*, 2020)

Sentinel-1 A and B were launched in 2014 and 2016. They were designed for a 7-year mission, with 5 years of additional consumables. As there are currently approaching the end of their lifetime, their successors, Sentinel-1 C and D, are being prepared, with minor modifications compared to their predecessors (Torres *et al.*, 2021). S-1C is scheduled to be launched in 2022. The question about the acquisition geometry of the Sentinel-1 remains. Currently, each Sentinel-1 satellite has a 12 day revisit time. Coupled, S-1A and B reduce it to 6 days. By repositioning S1-B to a new orbit, it is possible to use S1-A, B, and C, with a revisit time down to 4 days (4/4/4 formation). Another option is to keep the current Sentinel-1 constellation unchanged, and place S1-C 1, 2 or 3 days after Sentinel-1 A (1/5/6, 2/4/6, or 3/3/6 formation scenario). Historically, the ERS mission, in the 1990s, brought a similar acquisition scheme during the TANDEM mission, with two ERS satellites separated by 1 day. This type of configuration is extremely beneficial to study highly dynamic patterns, such as present in the cryosphere domain.

Originally, 6 Sentinel families were planned. Due to the success of the program, 6 additional missions were added as part of the Copernicus Expansion Program. Among them, an additional SAR mission, called ROSE-L, was defined (Davidson & Furnell, 2021). In parallel to the Sentinel-1 mission, the future ROSE-L mission comes as complementary information in the L-band SAR frequencies and fills the observation gaps described in scientific

literature (Lancheros *et al.*, 2018). ROSE-L is in preparation and is scheduled for launch around 2028. ROSE-L will contain up to 3 satellites, each having 12 days revisit time. Acquisition geometry and mission objectives are similar to the Sentinel-1 mission, but the larger wavelength is an important added value to produce deformation maps, sea ice classification, forest monitoring, as well as food security assessment. L-Band is also less impacted by temporal decorrelation.

Finally, SING (Sentinel-1 Next Generation), is in preparation. SING is part of a long-term scenario that ensures the continuity of the C-band SAR acquisition at least up to 2037 (Torres *et al.*, 2021). Sentinel-1 Next Generation brings important enhancements in their specifications: better spatial resolution, larger swath, better radar sensitivity, decreased revisit time, increased duty cycle and so on. In addition, the multichannel SAR system will allow onboard along-track interferometry.

The Japan Aerospace Exploration Agency (JAXA) also developed spaceborne SAR sensors. They rapidly specialized in the L band frequencies with first the JERS1 satellite in 1992, then ALOS in 2006, and ALOS2 in 2014. JAXA is currently preparing ALOS4, which is also a phased array-type L-band SAR sensor (Shibata *et al.*, 2021). With land observation as a key target, ALOS and ALOS2 participated in the development of wide swath imaging sensors. Objectives of their sensor range from land deformation monitoring to environmental monitoring in general. The next sensor ALOS4 is planned to have a 700 km swath in ScanSAR mode with a pixel spacing of 25 meters. In Stripmap acquisition mode, the new onboard digital beamforming unit will allow the acquisition of 200 km swaths at 3 meters resolution.

The German Aerospace Center (DLR) is part of the official partner institution of the European Space Agency. In 2007, they launched the TerraSAR-X satellite, operating – as the name suggests – in the X-band SAR frequencies and providing high-resolution products (Zink *et al.*, 2006). In 2010, a second X-band SAR satellite, similar to the first, was

launched with the objective of flying in bistatic configuration with the first TerraSAR-X (Krieger *et al.*, 2007). The formation – called TanDEM-X – has the ability to perform SAR interferometry without temporal decorrelation. A global DEM was computed from data ranging from 2010 to 2015 with 12 meters posting. A revision using data from 2017 to 2020 is in preparation. Moreover, the TanDEM-X mission was also a laboratory for new acquisition modes. It allowed the development of the TOPSAR acquisition mode, which is the default mode in the Sentinel-1 satellites.

The TanDEM-X mission largely overpassed its mission life expectancy. DLR is preparing the future of the German SAR Earth observation throughout the HRWS for High Resolution – Wide Swath, satellite (Nuncio Quiroz & Bartusch, 2019). HRWS offers a resolution of up to 25 cm and wide swath acquisition modes. The specificity of HRWS is a formation flying mode, with one active sensor and three passive companions (receive-only satellites). The technology is based on a mirror-SAR system, allowing a very large bandwidth (1 200 MHz). The different acquisition modes can balance spatial resolution, polarization and coverage, with spotlight and Stripmap modes for sub-metric resolution for urban applications, and ScanSAR modes for a coverage up to 1 000 km. In the end, a 4 meters posting global DEM is planned during the lifespan of the mission. A similar concept is also in preparation as part of the Earth Explorer pillar of the ESA Earth observation. Indeed, the Harmony mission is studying the added value of lightweight passive companions to Sentinel-1. Finally, the mission aims at resolving Line-Of-Sight diversity issues and providing 3D-DInSAR.

Spain also has an important Earth observation program, which includes the PAZ satellite (Alonso-Gonzalez *et al.*, 2021). PAZ is an X-Band SAR satellite based on the German

TerraSAR-X. Both are almost identical and can be used together. By doing so, it is possible to reduce the revisit time from 11 days to 4 or 7 days. This allows important coherence gains and the study of dynamic events.

The Agenzia Spaziale Italiana (ASI) presents a future roadmap of their Earth observation strategy (Formaro *et al.*, 2021). ASI has a long legacy of SAR products, thanks to their Cosmo-SkyMed constellation consisting of 4 X-Band SAR spaceborne sensors. With the first satellite launched in 2007, ASI is preparing the second generation of Cosmo-SkyMed (called CSG) constellation. The first two new satellites were launched in 2019 and 2021. The third and fourth are in preparation. In parallel, the ASI is pursuing developments in geosynchronous SAR, airborne L and P band SAR (experiments before space developments), SAR minisatellites (Platino-1). Finally, ASI is designing their specifications for a future generation of Cosmo-SkyMed, following the CSG program.

NASA is among the precursors in SAR, with the SIR and SRTM missions. Since then, NASA has been quite silent in terms of spaceborne SAR sensors. In collaboration with the Indian Space Research Organization (ISRO), NASA is developing the NASA ISRO SAR (NISAR) mission to answer the *National Imperatives for the Next Decade and Beyond* (National Research Council, 2007). The NISAR mission aims at providing global, free, and open SAR data, in a mindset similar to what Sentinel-1 is doing. The specificity of NISAR is that the satellite is equipped with a dual-frequency sensor, operating in S- and L-bands simultaneously (Kellogg *et al.*, 2020). The applications are varied, including surface deformation (faults, volcanoes, landslides, subsidence, uplifts), soil moisture, vegetation, ice sheet / ice shelves, sea ice, etc. The launch is currently scheduled for January 2023.

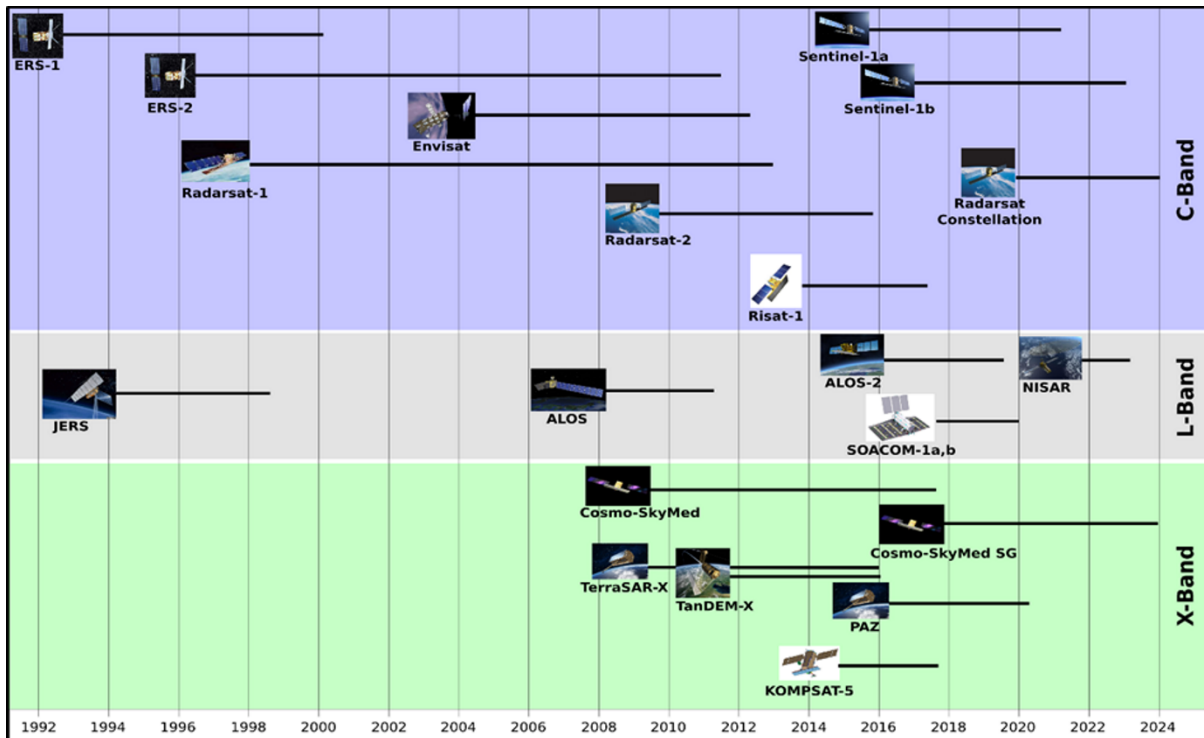


Figure 7. Timeline of current and future popular SAR missions (UNAVCO, 2019)

There are many SAR satellites from other important institutions. It is worth mentioning RADARSAT, from the Canadian Space Agency (CSA). RADARSAT is a C-band SAR spaceborne sensor. With the successful RADARSAT and RADARSAT-2 missions (launched in 1995 and 2007, respectively), CSA launched in 2019 the RADARSAT Constellation, a set of three C-band SAR satellites which, coupled, have a revisit time of 4 days. One must also mention KompSAT-5, a Korean satellite launched in 2013 providing high-resolution X-Band SAR data. It is finally difficult not to talk about the SAOCOM mission, in which the Liège Space Center participated. SAOCOM-1A and 1B are full-polarization L-Band SAR satellites respectively launched in October 2018 and August 2020 by the Argentinian National Space Activities Commission (CONAE).

Finally, the private sector increasingly enters the space industry. With the emergence of *Newspace*, a number of commercial applications appeared. *Newspace* is characterized by a drastic reduction of development costs, allowing non-institutional services to enter the market. Recently,

Newspace also includes SAR remote sensing. Six private companies are already present in this sector, with more coming. Among them, Capella, Synspective or predaSAR can be mentioned. The first SAR satellite belonging to this trend is ICEYE X1, a SAR satellite of 85 kilograms launched in 2018 (Ignatenko *et al.*, 2020). In July 2021, 13 micro SAR satellites are orbiting the Earth. To this day, several hundreds of satellites are being developed.

The goal of this *Newspace* trend is to develop SAR in space at a low cost. To put in perspective, small SAR satellites cost around 10 M\$, while important projects led by ESA, NASA, or JAXA largely overpass the 100 M\$ price tag. These low-cost satellites encourage the formation of mini-satellite constellations, which drastically enhance the revisit time. As an example, the 30 satellites of ICEYE-X1 can reduce the revisit time to less than 1 day. In the end, these types of SAR constellations greatly decrease the latency and allow operability 24/7.

Capella is typical example of this *Newspace* industry. The company is producing small SAR satellites in X-Band. Using spotlight acquisition mode and large bandwidth, the

images can reach the 50 cm spatial resolution (Stringham *et al.*, 2019). The commercial activities are ensured by on-demand self-service requests. In three months, the satellite produced 3 000 images.

The Japanese company Synspective also joined the race of small SAR satellites with its recently launched StriX- α X-band SAR satellite (Obata *et al.*, 2020). StriX- α aims at a sub-daily revisit time, at one meter spatial resolution. A constellation of 6 satellites is scheduled for 2022, with a final objective of 30 satellites.

Finally, Airbus is also developing active, responsive, and reconfigurable spaceborne sensors. Launched in 2018, the NOVASAR satellite is an S-band SAR sensor with large bandwidth (Zhou *et al.*, 2020).

Small satellites are also more accessible to governments or smaller public institutions. The Portugal government developed the Atlantis project, a constellation of very small 16U X-band SAR satellites (less than 30 kilograms), with the objectives of monitoring oil spills, surface currents, sea ice or iceberg calving (Portuguese Space Agency, 2020). One key limitation of small SAR satellites is the coverage. Capella limits its coverage to 5 x 10 kilometers. ICEYE is one exception in this category in the sense that the engineers implemented a TOPSAR acquisition mode to increase the swath of the image. This is balanced by the relative low resolution of the sensor. International agencies, such as ESA, are well aware of the exponential growth of the small satellite market. These agencies need to position themselves in this dynamic trend.

V. DEEP LEARNING ADVANCES

The amount of available data also brings new technical developments that come from the big data world and artificial intelligence (AI). With the growing data flux, these types of techniques are becoming mandatory to filter information from multi-petaoctets datacubes.

Andrew Ng, in an interview, wrote “*AI is the electricity of the XXI's century*” (Graduate School of Stanford Business, 2017). AI indeed

invaded multiple scientific domains. Though AI has been an important part of the computer vision world for a long time, it is only recently that machine and deep learning algorithms are an everyday component of remote sensing applications (Zhu *et al.*, 2017).

Remote sensing is still facing a series of challenges in terms of deep learning. The first problem arose because of the size of SAR acquisitions. Each Sentinel-1 SLC image is several gigaoctets, on temporal scales of several years and a potential large coverage. Remote sensing combined with deep learning automatically requires important processing infrastructures. Nevertheless, popular deep learning networks emerged in remote sensing: FCN, PCANet, U-net, DeepUnet, YOLOv3 or HRnet are now frequently cited in the literature (Gao *et al.*, 2016; Gong *et al.*, 2016; Li *et al.*, 2018; Baumhoer *et al.*, 2019; Chang *et al.*, 2019; Liu *et al.*, 2019; Wang *et al.*, 2019; Dalsasso *et al.*, 2020). Solutions generally require the creation of superposed sub-images to reduce the complexity or temporal clustering of image sets into mini-stacks (Gaddes *et al.*, 2019; Ho *et al.*, 2021).

A second problem comes from the lack of training data. In computer vision, large datasets of images with associated labels exist. This took a long time for remote sensing to have access to this type of data. Still nowadays, the problem of labels availability is present in remote sensing applications. Data augmentation techniques exist to artificially increase the number of training samples. Rotation and mirror operations are such examples. In addition, remote sensing has weak labels issues. In the computer science domain, it is common to have a 1 – to – 1 correspondence between the image and the label (Chen *et al.*, 2019). In remote sensing, the correspondence is much more debatable. This is particularly the case in SAR remote sensing where speckle noise introduces a lot of variety, making the image features difficult to extract.

The inclusion of artificial intelligence in remote sensing needs to deal with a very

limited number of weak labels, on powerful computing stations.

CONCLUSION

Synthetic Aperture Radar is a unique branch of remote sensing. The specificities of radar wavelength make its acquisition geometry and processing quite particular. More specifically, a prior focusing operation is mandatory, contrary to optical remote sensing. SAR images also have uncommon properties. Due to the wavelength employed, radar is able to penetrate through clouds and with the absence of solar illumination. In addition, radar brings new information about the characteristics of the ground. In this paper, we summarized the basic concepts of SAR and SAR interferometry. We also presented a series of applications.

In a second part, we presented the different sensors that are used nowadays and a schedule on the ongoing SAR activities. Important public institutions are present, but the recent *Newspace* era makes the entry of the private sector into the space domain, with service-oriented low-cost satellite constellations.

ACKNOWLEDGEMENTS

Christian Barbier is acknowledged for providing advice and support. This research is supported by the French Community of Belgium in the funding context of a FRIA grant, and carried out in the framework of the MIMO (Monitoring melt where Ice Meets Ocean) project funded by the Belgian Science Policy contract No. SR/00/336.

REFERENCES

- Alonso-Gonzalez, A., Hajnsek, I., Grigorov, C., Roth, A., Marschalk, U., Gimeno Martinez, N., Cifuentes Revenga, P., Gonzalez Bonilla, M. J., Casal Vazquez, N., Cuerda, J. M. & Gracia Rodriguez, M. (2021). Joint PAZ and TanDEM-X Missions Interferometric Performance. In Davidson, M.W.J. & Furnell, R. (eds), *IGARSS 2021 - 2021 IEEE International Geoscience and Remote Sensing Symposium*, Brussels, 792–795.
- Baumhoer, C. A., Dietz, A. J., Kneisel, C. & Kuenzer, C. (2019). Automated extraction of antarctic glacier and ice shelf fronts from Sentinel-1 imagery using deep learning. *Remote Sensing*, 11 (21), 1–22. <https://doi.org/10.3390/rs11212529>
- Brockmann Consult (2020). *Skywatch, Sensar and C-S. SNAP - ESA Sentinel Application Platform v8.0.3* (Computer Software). <http://step.esa.int/>. Retrieved 14 October 2021.
- Chang, Y. L., Anagaw, A., Chang, L., Wang, Y. C., Hsiao, C. Y. & Lee, W. H. (2019). Ship detection based on YOLOv2 for SAR imagery. *Remote Sensing*, 11 (7). <https://doi.org/10.3390/rs11070786>
- Chen, W. Y., Wang, Y. C. F., Liu, Y. C., Kira, Z. & Huang, J. B. (2019). A closer look at few-shot classification. *7th International Conference on Learning Representations (ICLR 2019, 2018)*, 1–17.
- Dalsasso, E., Yang, X., Denis, L., Tupin, F. & Yang, W. (2020). SAR image despeckling by deep neural networks: From a pre-trained model to an end-to-end training strategy. *Remote Sensing*, 12 (16), 1–19. <https://doi.org/10.3390/RS12162636>
- Davidson, M. & Furnell, R. (2021). ROSE-L : Copernicus I-band SAR mission. In Davidson, M.W.J. & Furnell, R. (eds), *IGARSS 2021 - 2021 IEEE International Geoscience and Remote Sensing Symposium*, Brussels, 872–873.
- Eckardt, R., Richter, N., Auer, S., Eineder, M., Roth, A., Hajnsek, I., Walter, D., Braun, M., Motagh, M., Pathe, C., Pleskachevsky, A., Thiel, C. & Schmullius, C. (2013). SAR-EDU - An education initiative for applied Synthetic Aperture Radar remote sensing. In *2012 IEEE International Geoscience and Remote Sensing Symposium*, 5315-5317. <https://doi.org/10.1109/IGARSS.2012.6352408>
- Elachi, C. & IEEE Geoscience and Remote Sensing Society (1987). *Spaceborne radar remote sensing: Applications and techniques*. New York: IEEE Press, 11-50.
- Elachi, C. & van Zyl, J. (2006). Nature and Properties of Electromagnetic Waves. In Kong,

J.A., Elachi, C. & van Zyl, J. (eds), *Introduction to the Physics and Techniques of Remote Sensing*, 23-50.
<https://doi.org/10.1002/0471783390.ch2>.

Ferretti, A., Monti-Guarnieri, A., Prati, C., Rocca, F. & Massonnet, D. (2007). *InSAR Principles: Guidelines for SAR Interferometry Processing and Interpretation (ESA TM-19)*. ESA Publications, A9-B71.

Flores, A., Herndon, K., Thapa, R. & Cherrington, E. (2019). *The SAR Handbook: Comprehensive Methodologies for Forest Monitoring and Biomass Estimation*.
<https://doi.org/10.25966/nr2c-s697>. Retrieved 14 October 2021.

Formaro, R., Longo, F., Varacalli, G., Fasano, L. & Pulcino, V. (2021). ASI roadmap in technology and programmes for earth advanced monitoring and assessment of hazards. In Davidson, M.W.J. & Furnell, R. (eds), *IGARSS 2021 - 2021 IEEE International Geoscience and Remote Sensing Symposium*, Brussels, 1875–1878.

Gaddes, M. E., Hooper, A. & Bagnardi, M. (2019). Using Machine Learning to Automatically Detect Volcanic Unrest in a Time Series of Interferograms. *Journal of Geophysical Research: Solid Earth*, 124 (11), 12304–12322.
<https://doi.org/10.1029/2019JB017519>

Gao, F., Dong, J., Li, B. & Xu, Q. (2016). Automatic Change Detection in Synthetic Aperture Radar Images Based on PCANet. *IEEE Geoscience and Remote Sensing Letters*, 13 (12), 1792–1796.
<https://doi.org/10.1109/LGRS.2016.2611001>

Gong, M., Zhao, J., Liu, J., Miao, Q. & Jiao, L. (2016). Change Detection in Synthetic Aperture Radar Images Based on Deep Neural Networks. *IEEE Transactions on Neural Networks and Learning Systems*, 27 (1), 125-138, doi: 10.1109/TNNLS.2015.2435783.

Graduate School of Stanford Business (2017). Andrew Ng: *Why AI Is the New Electricity* (Press Release, March 11, 2017).
<http://stanford.io/2mwODQU>. Retrieved 14 October 2021.

Hajduch, G., Vincent, P., Meadows, P., Small, D., Pilgrim, A., Schubert, A., Piantanida, R., Recchia, A., Franceschi, N., Mouche, A., Grouazel, A. & Husson, R. (2020). *Sentinel-1 Annual-Performance-Report-2019*. Sentinel-1 Mission Performance Centre, Report DI-MPC-APR / MPC-0460, version 1.1.
<https://doi.org/10.13140/RG.2.2.28472.16646>

Ho, D., Minh, T. & Ngo, Y. (2021). ComSAR: a new algorithm for processing Big Data SAR Interferometry. In Davidson, M.W.J. & Furnell, R. (eds), *2021 IGARSS 2021 - IEEE International Geoscience and Remote Sensing Symposium*, Brussels, 820–823.

Ignatenko, V., Laurila, P., Radius, A., Lamentowski, L., Antropov, O. & Muff, D. (2020). ICEYE Microsatellite SAR Constellation Status Update: Evaluation of First Commercial Imaging Modes. In *IGARSS 2020 - 2020 IEEE International Geoscience and Remote Sensing Symposium*, Waikoloa, (HI), 3581–3584.
<https://doi.org/10.1109/IGARSS39084.2020.9324531>

Kellogg, K., Rosen, P., Barela, P., Hoffman, P., Edelstein, W., Standley, S., Dunn, C., Guerrero, A. M., Harinath, N., Shaffer, S., Baker, C. & Xaypraseuth, P. (2020). NASA-ISRO Synthetic Aperture Radar (NISAR) Mission. In *2020 IEEE Aerospace Conference*, Big Sky (MT), 1-21.
<https://doi.org/10.1109/AERO47225.2020.9172638>

Krieger, G., Moreira, A., Fiedler, H., Hajnsek, I., Werner, M., Younis, M. & Zink, M. (2007). TanDEM-X: A Satellite Formation for High-Resolution SAR Interferometry. *IEEE Transactions on Geoscience and Remote Sensing*, 45 (11), 3317-3341.

Lancheros, E., Camps, A., Park, H., Sicard, P., Mangin, A., Matevosyan, H. & Lluch, I. (2018). Gaps analysis and requirements specification for the evolution of copernicus system for polar regions monitoring: Addressing the challenges in the horizon 2020-2030. *Remote Sensing*, 10 (7), 1–17.
<https://doi.org/10.3390/rs10071098>

- Leinss, S., Li, S., Bernhard, P., & Frey, O. (2020). Temporal Multi-Looking of SAR Image Series for Glacier Velocity Determination and Speckle Reduction, *EGU General Assembly 2020*, Online, 4–8 May 2020, EGU2020-3643. <https://doi.org/10.5194/egusphere-egu2020-3643>
- Li, R., Liu, W., Yang, L., Sun, S., Hu, W., Zhang, F. & Li, W. (2018). DeepUNet: A Deep Fully Convolutional Network for Pixel-Level Sea-Land Segmentation. *IEEE Journal of Selected Topics in Applied Earth Observations and Remote Sensing*, 11 (11), 3954–3962. <https://doi.org/10.1109/JSTARS.2018.2833382>
- Liu, B., Li, X. & Zheng, G. (2019). Coastal Inundation Mapping from Bitemporal and Dual-Polarization SAR Imagery Based on Deep Convolutional Neural Networks. *Journal of Geophysical Research: Oceans*, 124 (12), 9101–9113. <https://doi.org/10.1029/2019JC015577>
- Mancini, F., Grassi, F. & Cenni, N. (2021). A Workflow Based on SNAP–StaMPS Open-Source Tools and GNSS Data for PSI-Based Ground Deformation Using Dual-Orbit Sentinel-1 Data: Accuracy Assessment with Error Propagation Analysis. *Remote Sensing*, 13 (4), 753. MDPI AG. <http://dx.doi.org/10.3390/rs13040753>
- Massonnet, D., Rossi, M., Carmona-Moreno, C., Adragna, F., Peltzer, G., Feigl, K. & Rabaute, T. (1993). The displacement field of the Landers earthquake mapped by Radar interferometry. *Nature*, 364, 138-142. 10.1038/364138a0.
- National Research Council (2007). *Earth Science and Applications from Space: National Imperatives for the Next Decade and Beyond*. Washington D.C.: The National Academies Press, 454 p. <https://doi.org/10.17226/11820>.
- Nuncio Quiroz, A. E. & Bartusch, M. (2019). *Next Generation of the German X-Band SAR: The Multi-static High-Resolution Wide-Swath Mission*. ESA Living Planet Symposium (LPS), Milan.
- Obata, T., Arai, M., Asada, S., Imaizumi, T., Saito, H. & Shirasaka, S. (2020). The Latest Status of Our Commercial Small Synthetic Aperture Radar Satellite Constellation. In *IGARSS 2020 - 2020 IEEE International Geoscience and Remote Sensing Symposium*, Waikoloa (HI), 3578-3580. <https://doi.org/10.1109/IGARSS39084.2020.9323284>
- Parker, M. (2010). *Digital Signal Processing*, Newnes, 101, 191-200, ISBN 9781856179218, <https://doi.org/10.1016/B978-1-85617-921-8.00020-1>.
- Pepe, A. & Calò, F. (2017). A Review of Interferometric Synthetic Aperture RADAR (InSAR) Multi-Track Approaches for the Retrieval of Earth’s Surface Displacements. *Applied Sciences*, 7 (12), 1264. MDPI AG, <http://dx.doi.org/10.3390/app7121264>. Retrieved 14 October 2021.
- Pottier, E., Ferro-Famil, L., Allain, S., Cloude, S., Hajnsek, I., Papathanassiou, K., Moreira, A., Williams, M., Minchella, A., Lavallo, M. & Desnos, Y.L. (2009). Overview of the PolSARpro V4.0 software. the open source toolbox for polarimetric and interferometric polarimetric SAR data processing. In *2009 IEEE International Geoscience and Remote Sensing Symposium*, Cape Town, IV-936-IV-939. <https://doi.org/10.1109/IGARSS.2009.5417532>
- Portuguese Space Agency (2020). *Portugal Space sets major programmatic challenges* (Press Release September 23, 2020). <https://ptspace.pt/portugal-space-sets-major-programmatic-challenges/> Retrieved 14 October 2021.
- Shibata, M., Kuriyama, T., Hoshino, T., Nakamura, S., Kankaku, Y., Motohka, T. & Suzuki, S. (2021). System Performance and Flight Model Evaluation of Palsar-3 Onboard Alos-4. In Davidson, M.W.J. & Furnell, R. (eds), *IGARSS 2021 - 2021 IEEE International Geoscience and Remote Sensing Symposium*, Brussels, 3–6.
- Stringham, C., Farquharson, G., Castelletti, D., Quist, E., Riggi, L., Eddy, D. & Soenen, S. (2019). The Capella X-band SAR Constellation for Rapid Imaging. In *IGARSS*

2019 - 2019 *IEEE International Geoscience and Remote Sensing Symposium*, Yokohama, 9248-9251.
<https://doi.org/10.1109/IGARSS.2019.8900410>

Torres, R., Davidson, M., Geudtner, D. & Furnell, R. (2021). Copernicus Sar Missions (C and L-Band). In Davidson, M.W.J. & Furnell, R. (eds), *IGARSS 2021 - 2021 IEEE International Geoscience and Remote Sensing Symposium*, Brussels, 868–871.

Torres, R., Snoeij, P., Geudtner, D., Bibby, D., Davidson, M., Attema, E., Potin, P., Rommen, B. Ö., Floury, N., Brown, M., Traver, I. N., Deghaye, P., Duesmann, B., Rosich, B., Miranda, N., Bruno, C., L'Abbate, M., Croci, R., Pietropaolo, A. & Rostan, F. (2012). GMES Sentinel-1 mission. *Remote Sensing of Environment*, 120, 9–24.
<https://doi.org/10.1016/j.rse.2011.05.028>

UNAVCO (2019). Synthetic Aperture Radar (SAR) Satellites. UNAVCO.
<https://www.unavco.org/instrumentation/geophysical/imaging/sar-satellites/sar-satellites.html>

Wang, R., Zhang, J., Chen, J., Jiao, L. & Wang, M. (2019). Imbalanced Learning-Based Automatic SAR Images Change Detection by Morphologically Supervised PCA-Net. *IEEE Geoscience and Remote Sensing Letters*, 16(4), 554–558.
<https://doi.org/10.1109/LGRS.2018.2878420>

Zhou, Z.S., Parker, A., Brindle, L., Rosenqvist, A., Caccetta, P. & Held, A. (2020). Initial NovaSAR-1 Data Processing and Imagery Evaluation. In *IGARSS 2020 - 2020 IEEE International Geoscience and Remote Sensing Symposium*, Waikoloa (HI), 6154-6157.
<https://doi.org/10.1109/IGARSS39084.2020.9323291>

Zhu, X., Tuia, D., Mou, L., Xia, G.S., Zhang, L., Xu, F., & Fraundorfer, F. (2017). Deep Learning in Remote Sensing: A Comprehensive Review and List of Resources. *IEEE Geoscience and Remote Sensing Magazine*, 5 (4), 8-36.

Zink, M., Fiedler, H., Hajnsek, I., Krieger, G., Moreira, A. & Werner, M. (2006). The TanDEM-X Mission Concept. In *2006 IEEE*

International Symposium on Geoscience and Remote Sensing, Denver (CO), 1938-1941.
<https://doi.org/10.1109/IGARSS.2006.501>

Authors affiliation :

Quentin GLAUDE
PhD student
Laboratory of Glaciology (ULB)
Centre Spatial de Liège (ULiège)
quentin.glaude@ulb.be

Anne ORBAN
Head of Signal Laboratory
Centre Spatial de Liège (ULiège)
aorban@uliege.be

Corresponding author: Quentin GLAUDE
quentin.glaude@ulb.be

2.2 Surface Displacements – The Foundations of Ice Shelves Dynamics

As discussed in section 1.1, the surface displacements and their spatial and temporal variations are of key importance in the study of ice shelves. In this section, we will monitor the surface displacements thanks to offset- and phase-based measurements. These two methods are not independent, as coherent offset tracking techniques can be used to correct artifacts in interferometric studies (section 2.2.2.2).

2.2.1 Determining Displacements from Image Matching Techniques

Offset tracking is an image matching technique that can be divided into incoherent or coherent speckle tracking, depending on whether we use amplitude or complex SAR images. Both techniques will be used in the chapter, and intra- and inter-annual velocity fields will be analyzed.

2.2.1.1 Incoherent Speckle Tracking

Using multi-temporal remote sensing images, it is possible to follow the movement of determined objects between two scenes. We do a so-called *feature tracking*.

Working with two coregistered images, a feature’s displacement is located by computing a local correlation in a buffer window surrounding the feature position in the first image. The displacement corresponds to the distance to the pixel maximizing the local correlation. The result consists in a shift value in rows and columns in the image coordinate system.

In SAR applications, it is possible to use the peculiarities of the speckle to determine displacements. As the speckle behaves as a determined noise, each image location can be a feature.

As an exhaustive pixel-by-pixel displacement determination is numerically expensive, a solution consists in finding pixel displacements according to a regular grid. This grid is then interpolated to the input image dimensions.

Offset Tracking Parametrization

In addition to the velocity determination, it is necessary to study the velocity gradients according to the different directions :

$$\frac{\partial v_x}{\partial x} \quad , \quad \frac{\partial v_y}{\partial y} \tag{2.1}$$

In a 2D discrete space, partial derivatives are estimated by the discrete convolution product of the velocity map and Sobel filters, whose kernels are defined in Fig. 2.1.

-1	0	+1	x filter	+1	+2	+1	y filter
-2	0	+2		0	0	0	
-1	0	+1		-1	-2	-1	

Figure 2.1: Horizontal and vertical Sobel filters.

Then, we compute the estimated discrete gradient:

$$\widehat{\nabla}v = \sqrt{\left(\widehat{\frac{\partial v_x}{\partial x}}\right)^2 + \left(\widehat{\frac{\partial v_y}{\partial y}}\right)^2} \quad (2.2)$$

However, a bad parameterization of the pixel offset tracking can lead to very noisy velocity estimation. The noise is represented by an additive high-frequency random pattern. Methods to decrease this noise are thus based on low-pass filtering, performed after the computation or within the computation. In the latter case, we set the parameters of the method such that it avoids introducing high-frequency biases. This parameterization is important because the offset tracking process is computationally expensive, especially on long series of SAR pairs. In addition, the protocol has to be clearly defined and fixed on each SAR pair.

We explored four different parameterizations. The images come from Sentinel-1 in Interferometric Wide-swath mode in Ascending orbit on track 59. The images are from September the 23rd and October the 5th, 2017 (temporal baseline of 12 days).

The different parameters used are described as follows :

- **Grid Interleave** (in azimuth/range) : The grid azimuthal/range spacing in pixels.
- **Registration Window**: The window's width and height for cross-correlation.
- **Correlation Threshold**: Threshold for normalized cross-correlation - NCC value. If the cross-correlation value is greater than the threshold, then the estimated offset is considered valid, otherwise invalid, resulting in a gap in our grid.
- **Grid Filtering**: Size of the sliding window for averaging offsets computed for valid offsets.
- **Radius for Hole Filling**: It defines the size of the window for hole filling. For invalid offsets, a window with a given radius centered at the grid coordinates is defined. Offsets from valid neighbors within the window are used by interpolating the offset for the current grid coordinates.

The four test cases' parametrization is presented in Table 2.1.

	#1	#2	#3	#4
Grid Interleave	40x40	200x200	40x40	20x20
Registration Window	128x128	128x128	128x128	32x32
NCC Threshold	0.1	0.1	0.15	0.1
Average Box Size	5	5	9	9
Hole Filling Radius	5	5	5	7

Table 2.1: Four parametrization settings are tested, balancing the spatial fineness and high frequency noise

A velocity gradient is the witness of an ice stream spatial divergence. However, we must separate process-based velocity gradients and true velocity gradients. On the visual interpretation (Fig. 2.2), we see that the velocity variance is highly dependant on the settings. Parametrization #2 is an excellent candidate, by computing velocities on a sparser grid. Nevertheless, we might need to work at a finer scale to capture local perturbations (Fig. 2.4). In parametrization #3, we work at 400m by 400m but with a higher threshold. To avoid high frequencies, we set a high average box size. Parametrization #3 is still a big enhancement compared to #1 when looking at the gradients (Fig. 2.3).

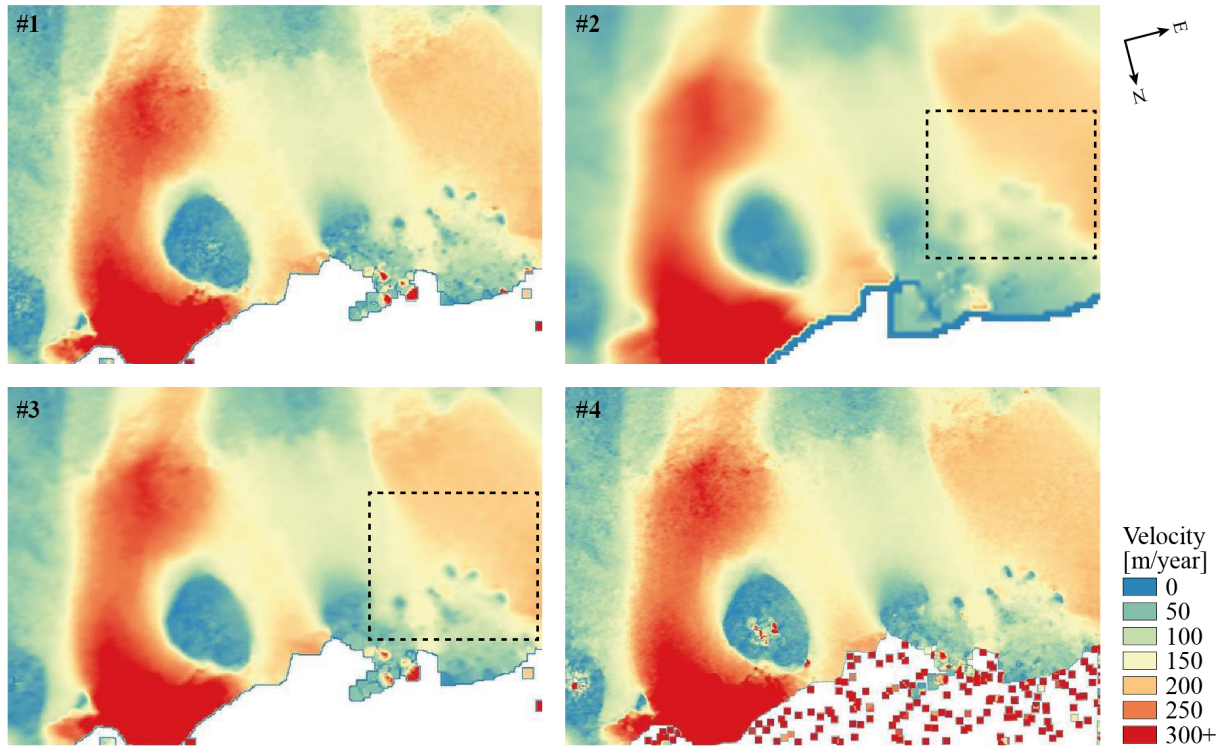


Figure 2.2: Unprojected velocity map determination. Due to the image acquisition, the area is flipped upside-down, with the ocean at the bottom of the image. The large gap in the bottom of the image is the Ocean.

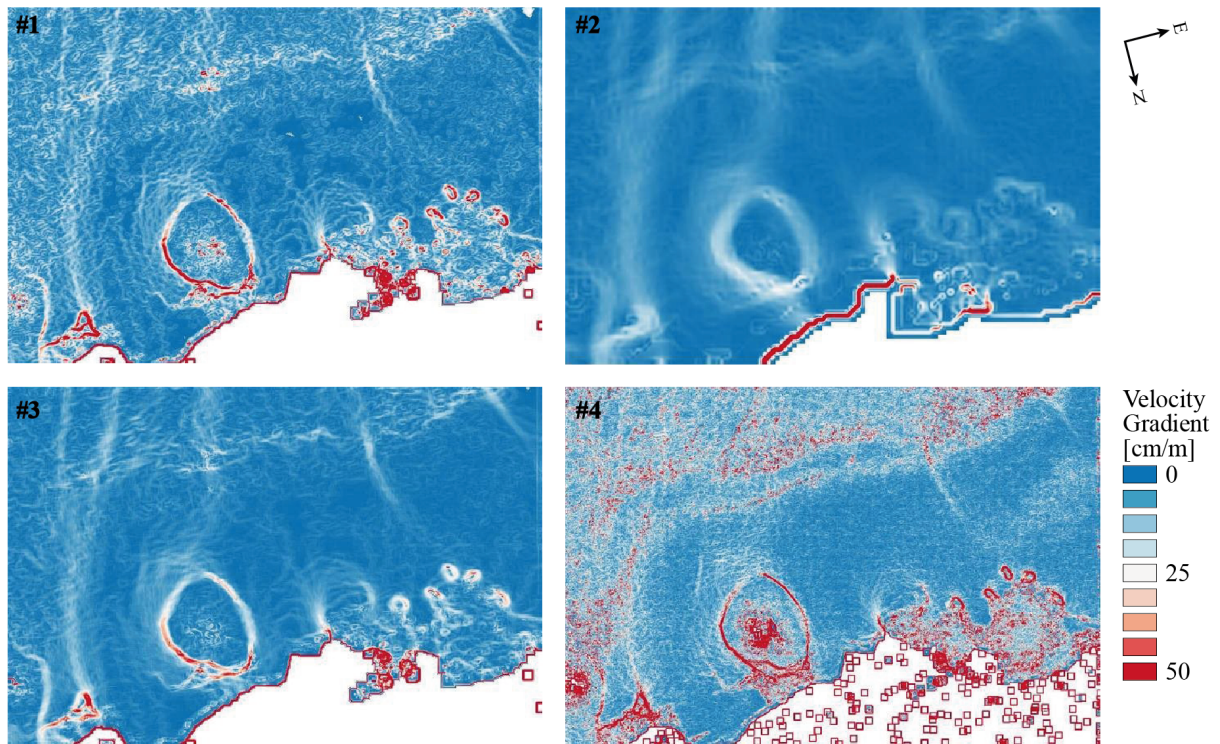


Figure 2.3: Unprojected velocity gradients computation. On the RBIS itself, we see that the settings are very important in terms of velocity gradient.

The estimation of bias and variance of the models are based on the computation order 1 and 2 statistics on stationary areas. We chose the Derwael ice rise which is proven to be stable from DGPS measurements (Pattyn et al., 2012).

A bias is a constant offset. In our case, we considered the mean velocity measurement, being a mean deviation of the *a priori* null displacement. Then, we compute the standard deviation in this stationary area, representing the intra-variability of the model.

	#1	#2
<i>bias</i> [m/yr]	36.8	18.97
$\sqrt{\text{variance}}$ [m/yr]	23.6	4.28

From #1 to #2, we observe a decrease of 48% of the bias and more than 80% of the standard deviation.

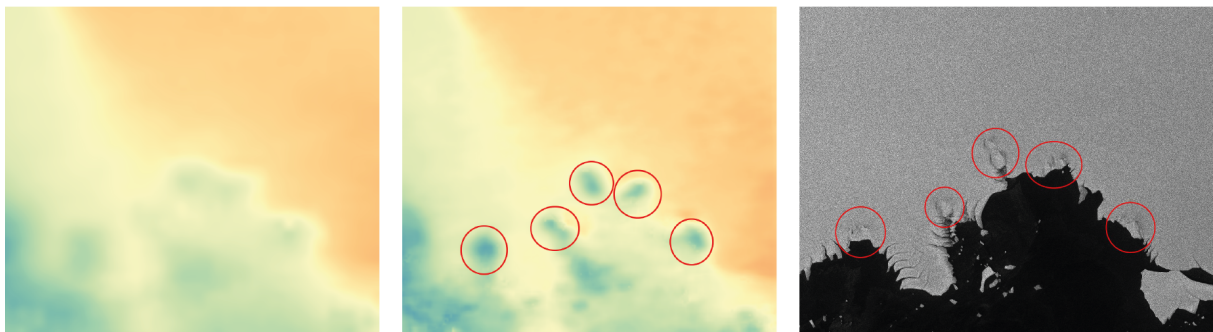


Figure 2.4: Local physical entities (red circles) that significantly reduce the ice-shelve velocity and that are smoothed in #2 settings but not in #3. The location corresponds to the dotted rectangle in Fig. 2.2.

The parametrization is a balance between our willingness to observe the local deformations, while also reducing the noisy offset determinations.

The Role of Pixel Offset Oversampling

In order to get a better estimate of the 2D shift, the search window is oversampled. With an oversampling factor of 16 in each image direction, the smallest shift is a sixteenth of a pixel. Using Sentinel-1 Ground Range Detected - GRD images with a pixel spacing of 10 by 10 meters, it means a 0.625 meter shift in azimuth or range direction. Using a revisit time of 12 days, it means that the smallest detectable velocity is about 19 meters per year. When resampling the grid of displacements estimates to the input image resolution, pixels will be interpolated between this discrete set of values. However, areas of small displacements suffer from small oversampling. The algorithm is not able to detect the rich fineness of the ice flux, crucial for locating precisely the ice divides.

It is important to note that if setting an oversampling factor to 64 allows detecting displacements of fewer than 5 meters per year, it is also much more computationally expensive. This computation time increases strongly passing the oversampling factor of 16 (Table 2.2).

Oversampling factor	2	4	8	16	32	64
Execution Time [min]	8'	8'	9'	16'	43'	183'

Table 2.2: Oversampling factor - Computation time dependency.

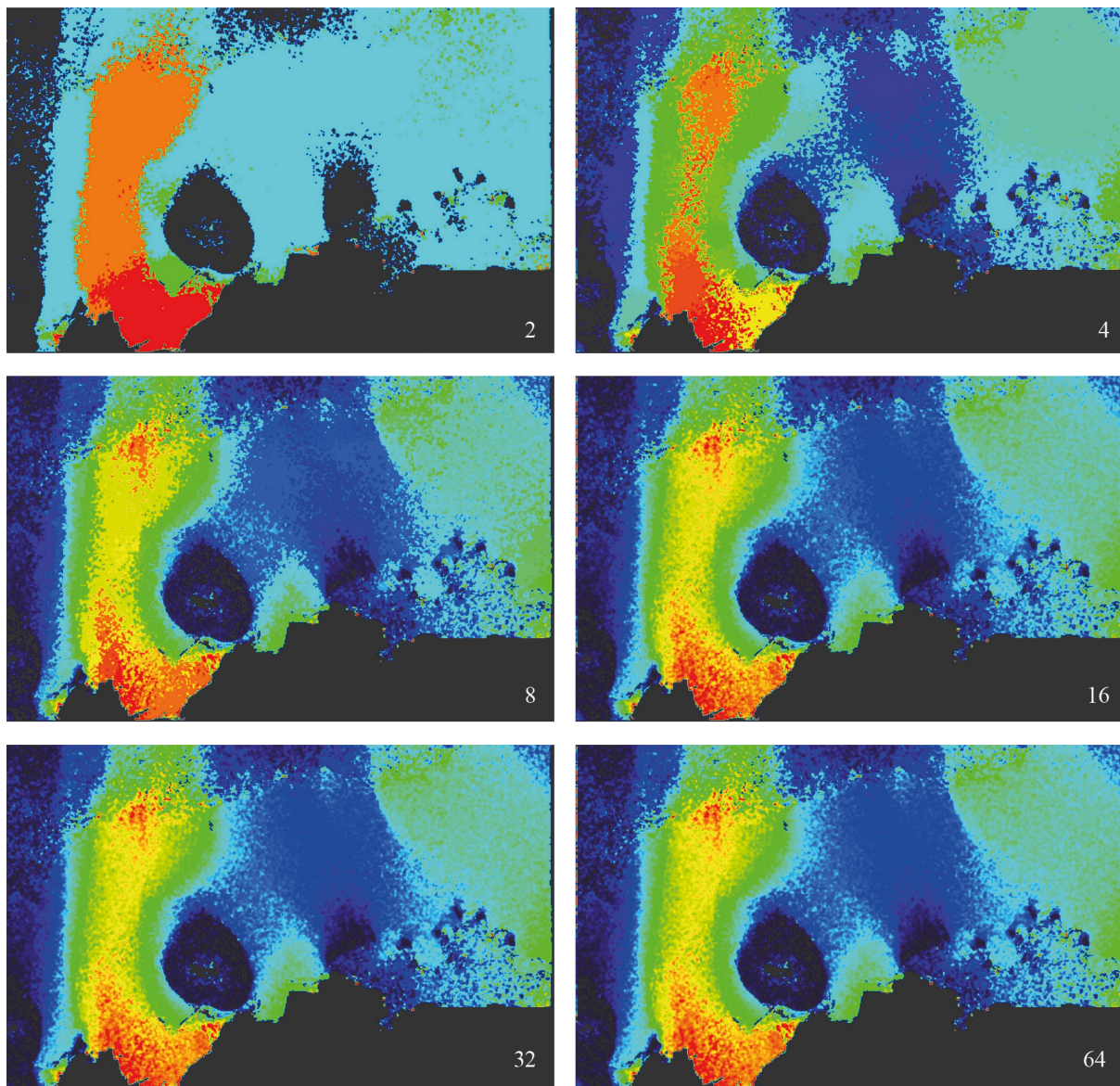


Figure 2.5: Influence of the oversampling factor on the velocity estimated at grid locations (in order: 2, 4, 8, 16, 32, and 64).

From figure 2.5, we can observe that the oversampling highly increases the fineness of the displacement detection.

Figure 2.6 shows how the oversampling factor discretizes the range of detectable displacements. Our study area is moving at a maximum of about 300 meters per year, mostly in an azimuth direction. Using 12 days pairs, we can expect a maximum displacement of about 10 meters, i.e. the image resolution of Sentinel-1 Ground Range Detected acquisitions. That explains why, with an oversampling factor of 2, only the velocity of 0, 150, and 300 meters per year are obtained. With an oversampling factor of 4, the detection of 75 and 225 velocity meters per year displacements becomes possible. Increasing the oversampling factor allows the detection of more subtle changes. Using the oversampling factor of 16, we retrieve the integer multiples of 19 meters per year velocity.

The interpolation between these values is performed using a low pass filter over the grid and a spatial bilinear interpolation between the grid nodes. When the correlation between master and

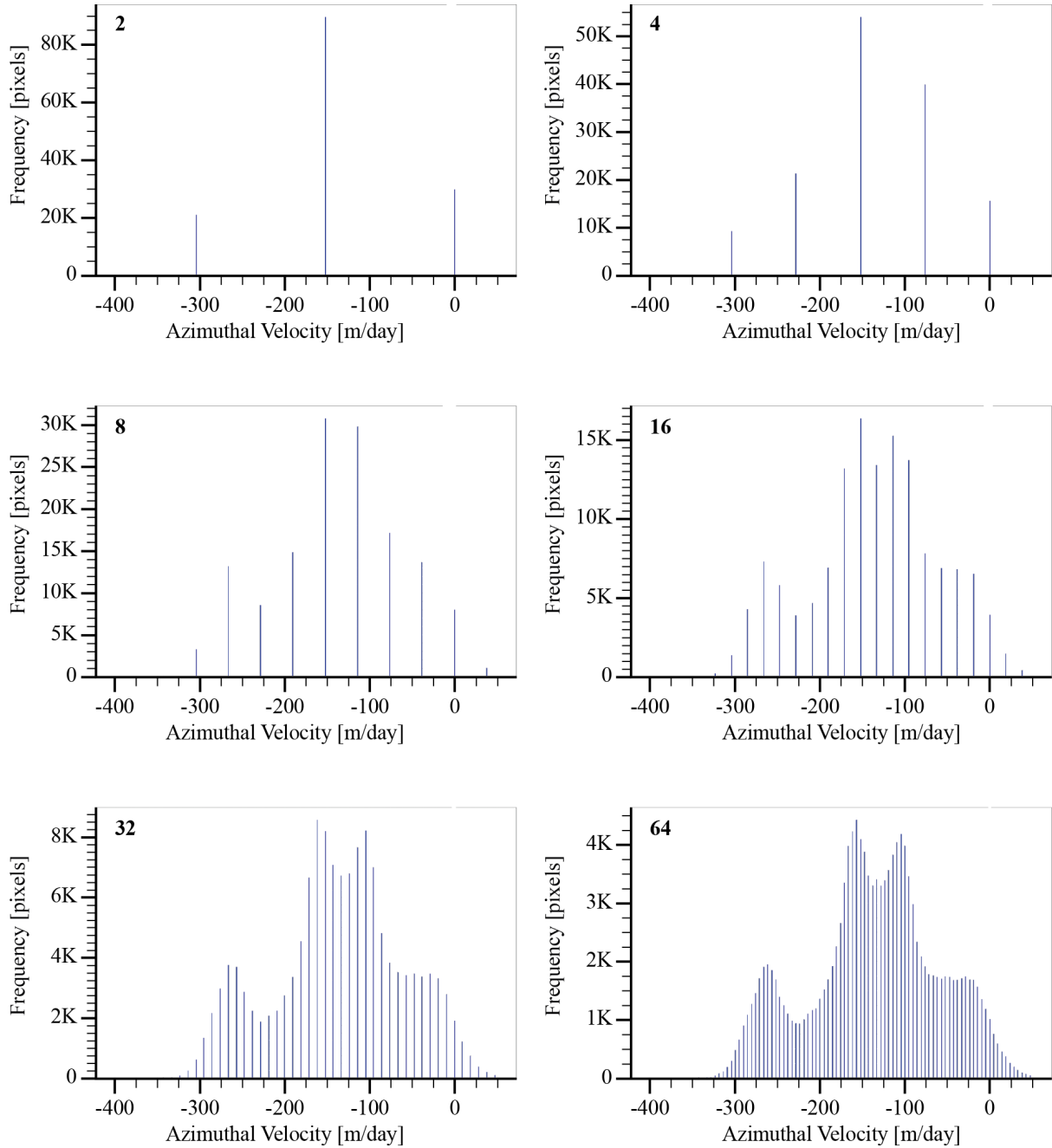


Figure 2.6: Influence of the oversampling factor on the estimated azimuthal velocity at grid locations (in order: 2, 4, 8, 16, 32, and 64).

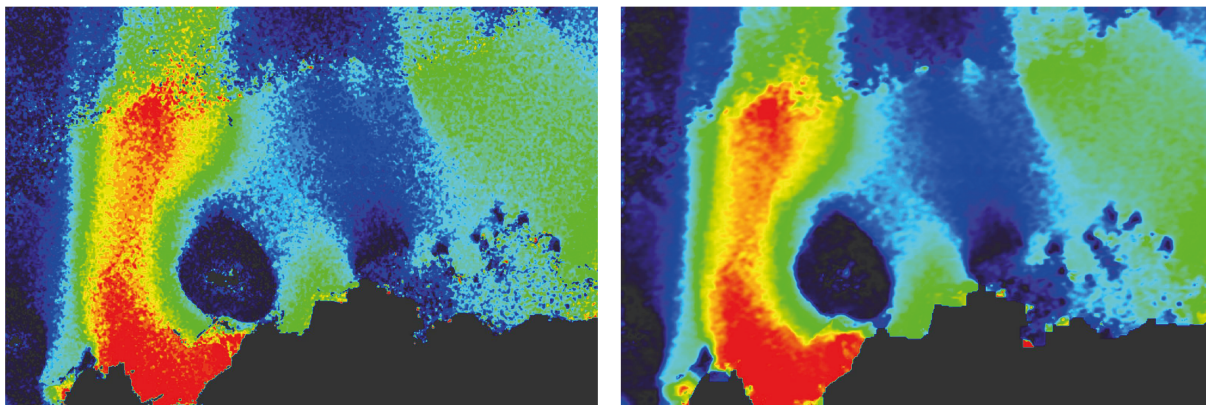


Figure 2.7: Effect of the hole filling and spatial filtering.

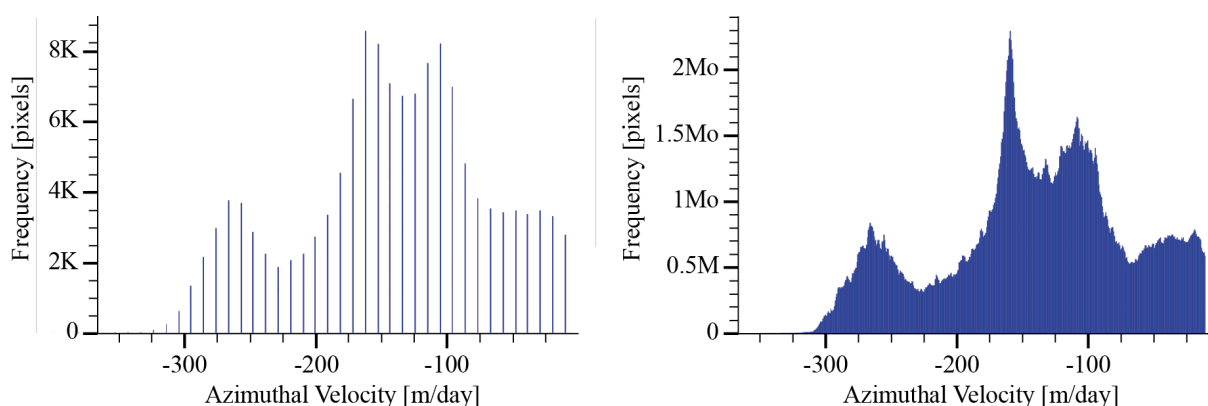


Figure 2.8: Effect of post-processing on velocity distribution, using an oversampling factor of 32 (left = grid, right = interpolated as image resolution).

slave patches is too low, the shift found is considered unreliable and dismissed. It results in a gap in the grid. Using inverse weighted distance around the gap, the algorithm performs data gap filling. The effects of interpolation can be seen in Fig. 2.7 (map) and 2.8 (histogram).

Dronning Maud Land Velocity Merged Product

From the parametrization study, we can now perform offset tracking over the Dronning Maud Land - DML. The Dronning Maud Land requires merging data from a large number of different orbits and dates. Limiting the study to 2016, 255 Sentinel-1 acquisitions in Interferometric Wideswath mode were used, distributed over 14 different orbits, representing more than 1 To of input data. Sentinel-1 acquisitions' footprint over DML can be seen in Fig. 2.9.

Among the 255 acquisitions, some must be discarded. This is the case for pairs with a large temporal baseline (greater than 12 days). In addition, the acquisition geometry of an orbit can change, making some images' footprint incoherent (Fig. 2.10).

This coregistration process represents 114 hours of computation time. Based on the coregistered pairs, intensity offset tracking is performed.

Surface melt, katabatic wind, snowfall and other geophysical processes can rapidly create temporal decorrelation. To avoid unnecessary computations, we selected only the relevant SAR pairs that are inclined to produce good results. This was performed by a prior coarse estimation of surface velocities at low resolution. Then we selected the SAR pairs that provided accurate

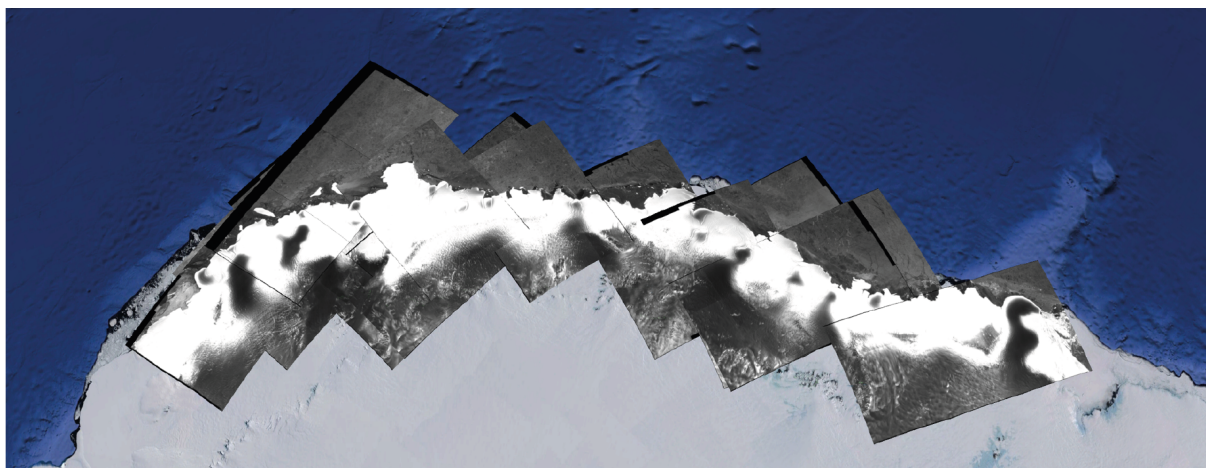


Figure 2.9: Spatial distribution of Sentinel-1 acquisitions over the Dronning Maud Land region. Basemap: U.S. Geological Survey (2020).

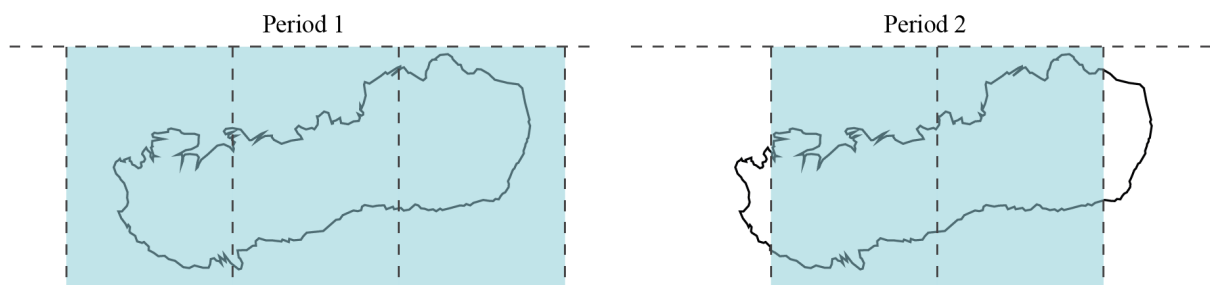


Figure 2.10: Change of the orbit acquisition footprint.

measurements. On a total of 152 potential pairs, 42 are selected. These are reprocessed with finer parametrization (45 minutes per pair - 30 hours in total):

- **Grid Interleave** : 100x100 pixels
- **Registration Window** : 128x128 pixels
- **Oversampling Factor** : 64
- **Correlation Threshold** : 0.15
- **Grid Filtering Size** : 9

Table 2.3 summarizes the orbits, pairs, and the number of reprocessed velocity fields.

The global Dronning Maud Land velocity field in Figure 2.11 is coherent with scientific literature. We can observe the main ice flows and the ice rises. The variety of ice shelves in DML is impressive. The Western part of the Fimbul ice shelf has by far the largest ice discharge of the DML. The Eastern part, on contrary, is completely buttressed due to large and numerous ice rises and embayments. West of Fimbul, we have the Jelbart ice shelf, with velocities that can reach 500 meters per year. Then, we can notice the Borchgrevink ice shelf, which is the fastest of a chain of buttressed ice shelves. The RBIS is the second-largest ice shelf of the DML, after the Fimbul ice shelf. Overall, ice shelves in DML never exceed 100 kilometers long. Though relatively small, these ice shelves surround the vast majority of DML, and are highly buttressed. These ice shelves highly participate in the overall stability of the Northern part of the East AIS. Some relatively stable icebergs can also be noticed in the figure, where the algorithm manages to estimate a displacement.

Orbit	# Images	# Pairs	# Selected for Velocity
2	22	15	3
35	21	15	6
45	21	16	4
46	9	4	2
49	7	4	2
50	40	31	8
74	18	10	2
78	21	13	2
89	24	14	3
90	8	4	2
133	20	14	4
136	27	18	4
165	12	0	0
167	5	0	0

Table 2.3: Number of images and pairs for each orbit. The quality of each pair is *a priori* estimated, and candidates are finally selected for fine velocity estimation.

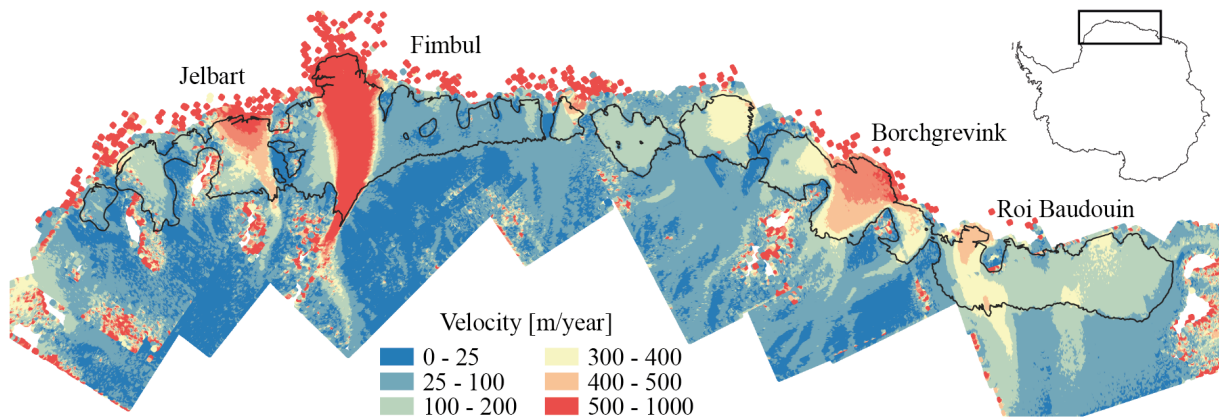


Figure 2.11: Dronning Maud Land merged velocity map (2016), with ice shelves delimited in solid black line.

2.2.1.2 Analysis of Velocity Time Series over the Roi Baudouin Ice Shelf – An Ongoing Long Term Stability

The goal in this section is to analyze the velocity fields in the Roi Baudouin Ice Shelf - RBIS in order to observe short time-scale dynamics of the Antarctic ice sheet and ice shelves. Displacements are determined using incoherent speckle tracking using the parameters defined in section 2.2.1.1.

Sentinel-1 images in Interferometric Wide-swath - IW in 2016 come from a descending pass on track 78. From 2017, images come from the ascending pass on track 59. Track 59 covers most parts of the RBIS. Track 78 (2016) only covers the fastest part of the area. The Extended Wide-swath - EW mode covers a larger coverage. Nevertheless, the coarser-resolution is unusable for offset tracking studies.

To minimize temporal decorrelation, we limit the analysis to SAR pairs with a temporal baseline of 12 days. From these pairs, 2D-displacements maps are produced in a chaining process (Fig. 2.13).

The ability of offset tracking to find homologous points between two images is not guaranteed for

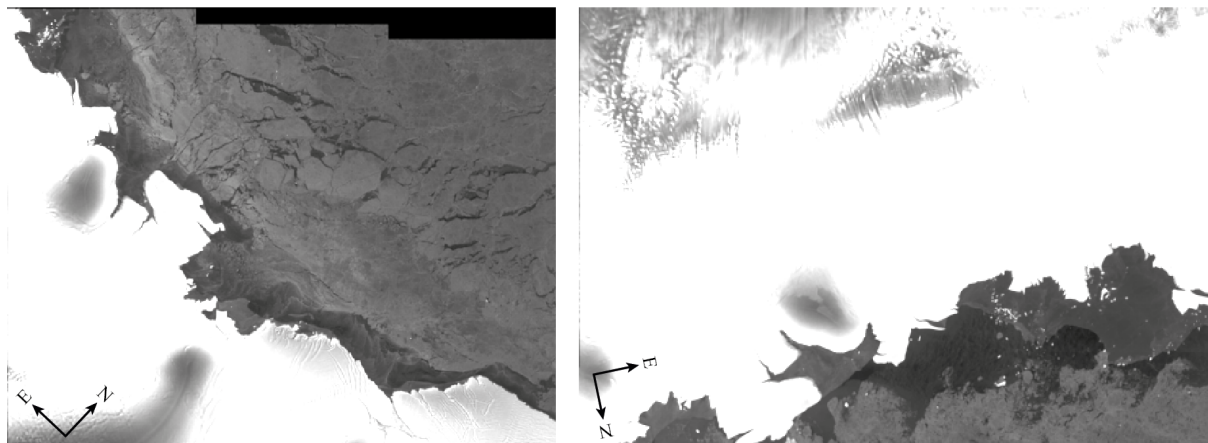


Figure 2.12: Quicklook of the Sentinel-1 images used for the velocity time series. Left: track 78 (2016), right: track 59 (from 2017).

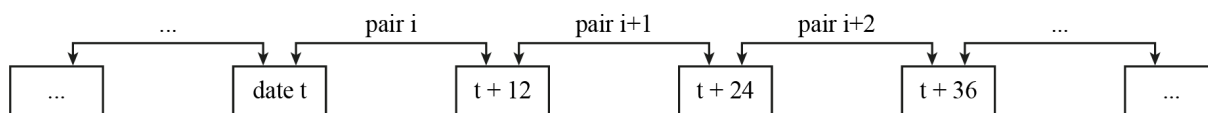


Figure 2.13: 2D displacements maps are produced by minimizing the temporal decorrelation, linking SAR images to their closest acquisition.

each single SAR pair. In response, we rely on the computation of large amounts of SAR images to determine a sufficient number of velocity fields (Fig. 2.14).

The cause of strong decorrelation can be due to particular geophysical areas, such as blue ice, where the exposed ice has very low backscattering. Abrupt changes between two dates can also cause important decorrelations. These can be due to new snow deposits from precipitations, wind, or strong melting events. This latter effect can be verified by looking at the input images where we observe a change in their radiometrically calibrated backscatter (Fig 2.15). The study of surface melting detection using Sentinel-1 will be studied in section 2.4.

Results of 4-Years Velocity Time Series

During the thesis, we used all available Sentinel-1 IW acquisitions on the Roi Baudouin Ice Shelf. Due to data availability, we only use the relative orbit #59. Acquisition dates range from July 25 2017 to August 21, 2021, with a revisit time of 12 days. In this time series, a few acquisitions are missing due to spaceborne acquisition issues, archived in the ESA Sentinel-1 data logger.

Initial parametrization of the Offset Tracking is similar to the Dronning Maud Land merged velocity map:

- **Grid Interleave** : 100x100 pixels
- **Registration Window** : 128x128 pixels
- **Oversampling Factor** : 64
- **Correlation Threshold** : 0.15
- **Grid Filtering Size** : 9

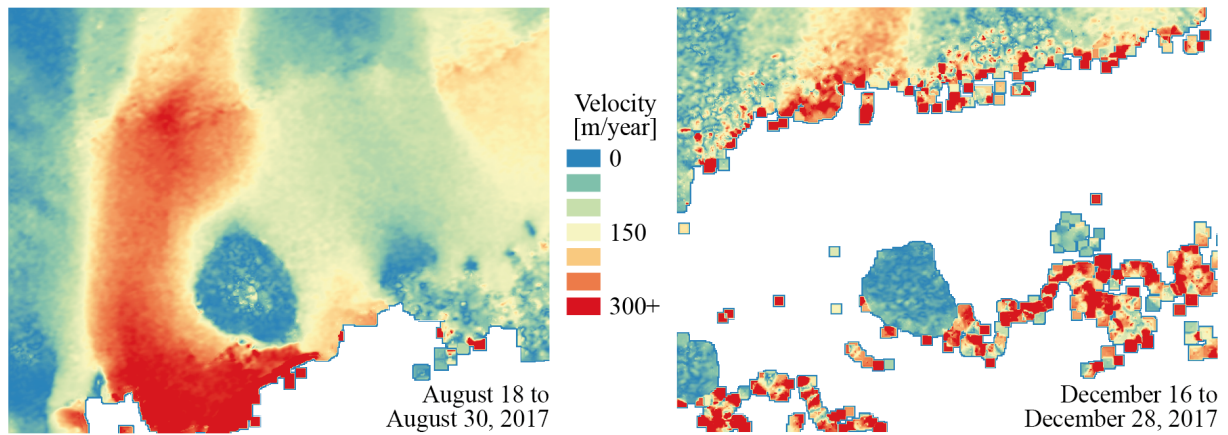


Figure 2.14: Good and poor results of velocity field estimation on RBIS from incoherent speckle tracking.

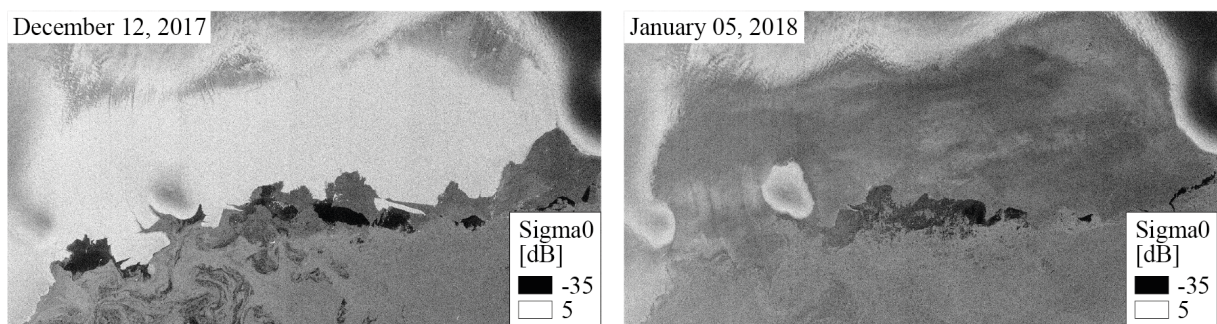


Figure 2.15: Comparison between 16/12/2017 and 28/12/2017 sigma0 (HH polarization).



Figure 2.16: Time distribution of selected pairs. We can notice a systematic gap in the first half of each year (March-June period).

The processing pipeline is divided in three steps: a *coregistration* process, a *rough estimates* of surface velocity, and a *finer estimation* of the displacements for satisfactory SAR pairs. Then, the results are projected on the Antarctic Polar Stereographic reference coordinates system (EPSG:3031). This pipeline is performed for each SAR pair. The SAR pairs are constituted by minimizing temporal decorrelation (here 12 days).

We cannot expect every SAR pair to produce high-quality velocity products. Indeed, surface melt, katabatic wind, snowfall, and other geophysical processes can rapidly create temporal decorrelation. To avoid unnecessary computations, we applied the selection strategy developed in section 2.2.1.1. On a total of 121 pairs, 28 are retained. The selection takes into account the temporal distribution of the acquisition time range (Fig. 2.16). The formed pairs are:

- 2017-08-18 to 2017-08-30
- 2017-09-23 to 2017-10-05
- 2017-10-17 to 2017-10-29
- 2017-12-04 to 2017-12-16
- 2018-02-14 to 2018-02-26
- 2018-08-01 to 2018-08-13
- 2018-08-13 to 2018-08-25
- 2018-09-30 to 2018-10-12
- 2018-11-29 to 2018-12-11
- 2019-02-21 to 2019-03-05
- 2019-07-27 to 2019-08-08
- 2019-09-01 to 2019-09-13
- 2019-10-19 to 2019-10-31
- 2019-10-31 to 2019-11-12
- 2019-11-12 to 2019-11-24
- 2020-02-04 to 2020-02-16
- 2020-06-27 to 2020-07-09
- 2020-09-19 to 2020-10-01
- 2020-10-01 to 2020-10-13
- 2020-12-24 to 2021-01-05
- 2021-01-05 to 2021-01-17
- 2021-01-29 to 2021-02-10
- 2021-02-10 to 2021-02-22
- 2021-02-22 to 2021-03-06
- 2021-07-04 to 2021-07-16
- 2021-08-09 to 2021-08-21

The average 4-year RBIS velocity field can be seen in Fig. 2.17. The ice-shelf velocity shows the different characteristics of the RBIS. The main attraction comes directly to the West Ragnhild glacier terminus, with a velocity higher than 300 meters per year. We can also see the Derwael Ice Rise, a promontory that is the main regulator of the ice flow, with the contribution of the FranKenny ice rise at the West. Note that on ice promontories, the SAR signal is low, affecting the quality of detected displacements. On the East of the RBIS, the velocity is lower with, at the calving front, a great number of smaller ice rises, limiting the ice rise extension and regulating the flow rate. Further East, the East Ragnhild Glacier can move up to more than 200 meters per year. Finally, Fig. 2.18 shows a subset of individual results.

We can make a profile along the West Ragnhild Glacier and its floating termination (Fig. 2.17

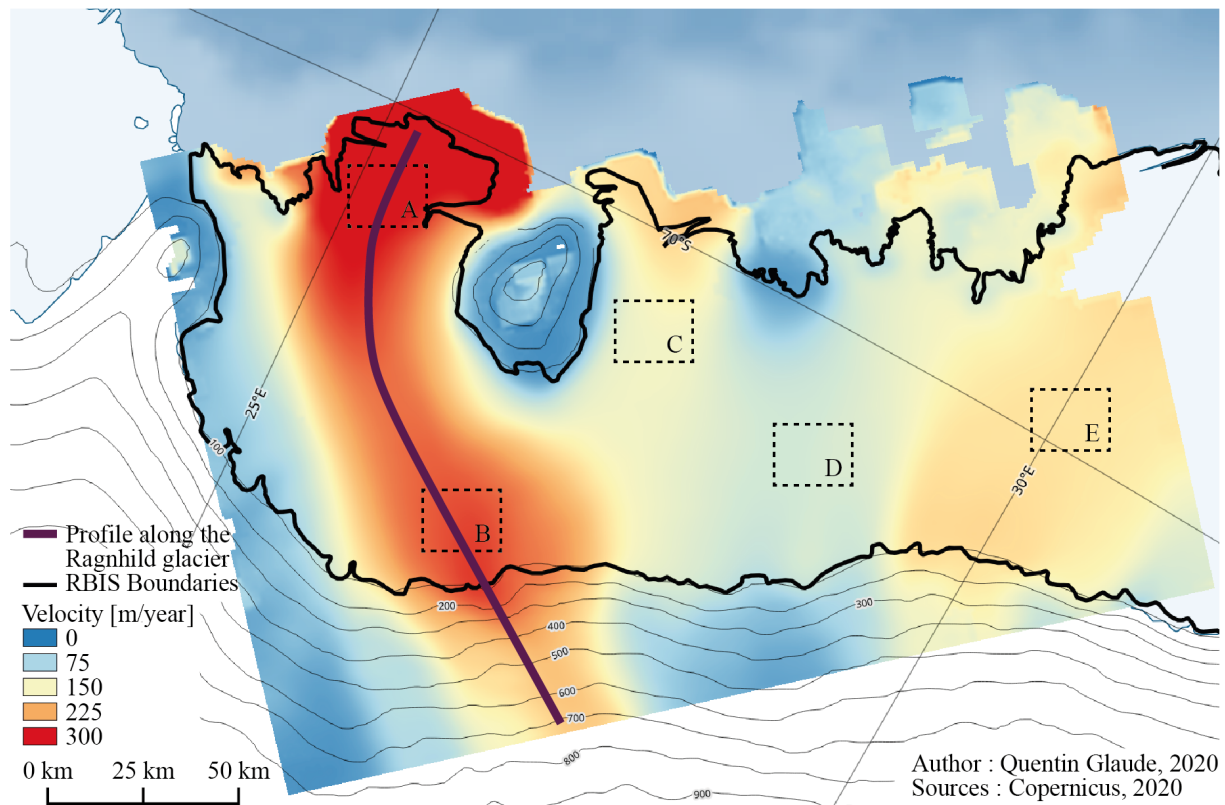


Figure 2.17: Average velocity field. The profile in purple consists in a 160 km curve along the West Ragnhild Glacier (EPSG:3031).

and 2.19). The strong decrease in velocity at the Derwael ice rise level is a good indicator of the ice-shelf's buttressing effect.

The analysis of individual velocity components shows that the azimuthal velocity is the main component of the RBIS displacements. This high North-South component partly explains the limit of SAR interferometry in the region for velocity studies. Fig. 2.20 represents the 4-year azimuthal velocity average velocity. Fig. 2.21 (top) shows a subset of individual results.

The range contribution of the velocity is lower, with a main component toward the East direction. In addition, the range velocity estimation is geometrically affected by vertical variations of the sea level, induced by tides and the inverse barometer effect. These variations are far from negligible, as they can lead to 50 meters per year bias. These effects are zero-centered, and consequently small in aggregated results (Fig. 2.22), but highly visible in individual results (Fig 2.23, top).

To understand these variations, we compared each component (azimuth and range) for each individual date to their corresponding average. Fig. 2.21 (bottom) and 2.23 (bottom) represent the azimuth and range deviations from their average component.

The azimuthal deviations from the azimuthal average (Fig. 2.21, bottom) show that they are related to geophysical components located in the area of interest. It can be the West Ragnhild ice stream, but also the surroundings of the main ice rise. These deviations have a physical interpretation in terms of ice fluxes.

The range deviations from the range average (Fig. 2.23, bottom) are higher than the azimuthal one. Also, the spatial distribution of the range deviations is quite different. On the ice shelf, the shift is more constant, translating an overall shift. Moreover, in the 1st, 7th, 8th, and 9th, the distinction grounded/floating is clearly visible. These observations are in concordance with a potential tidal influence (Glaude et al., 2020).

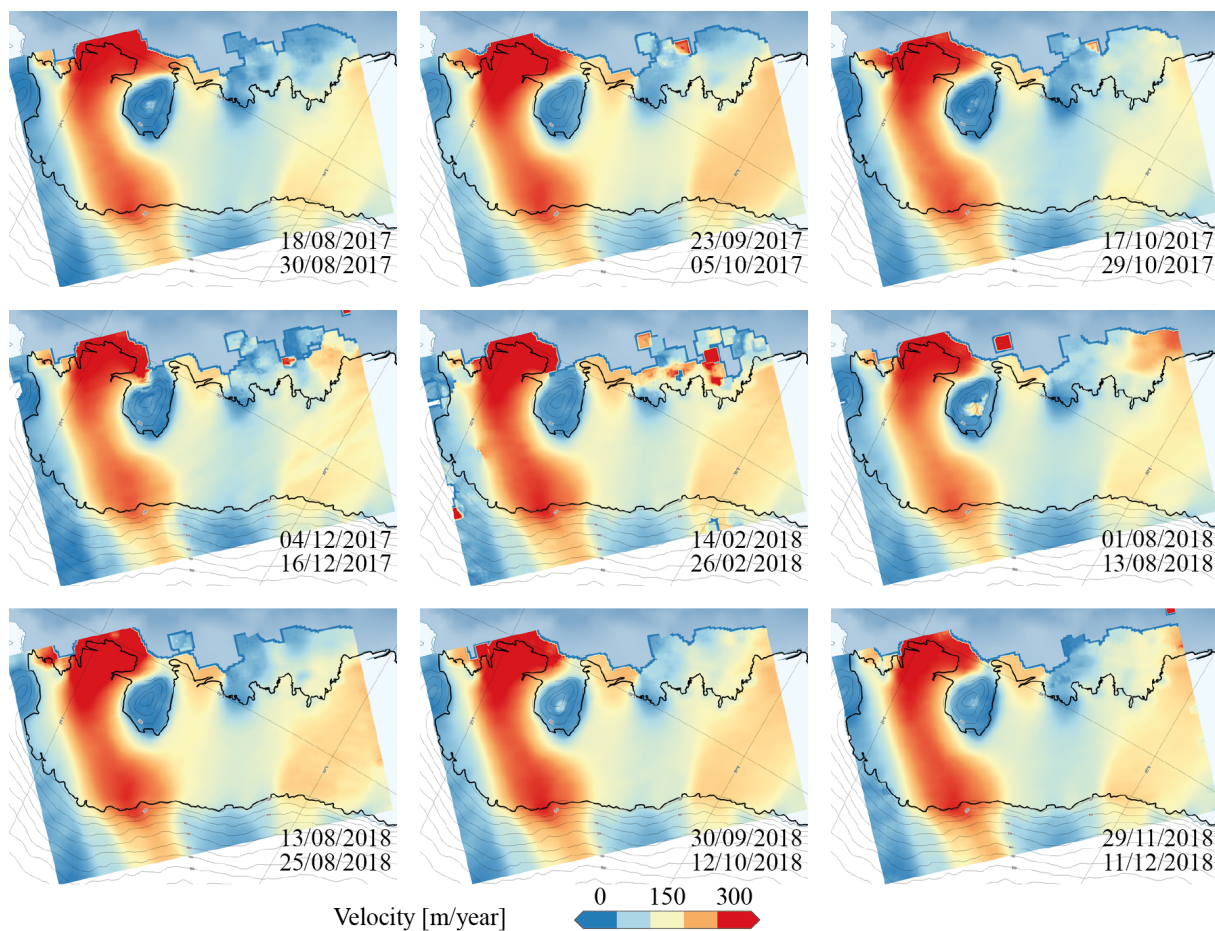


Figure 2.18: Subset of the RBIS velocity fields time series.

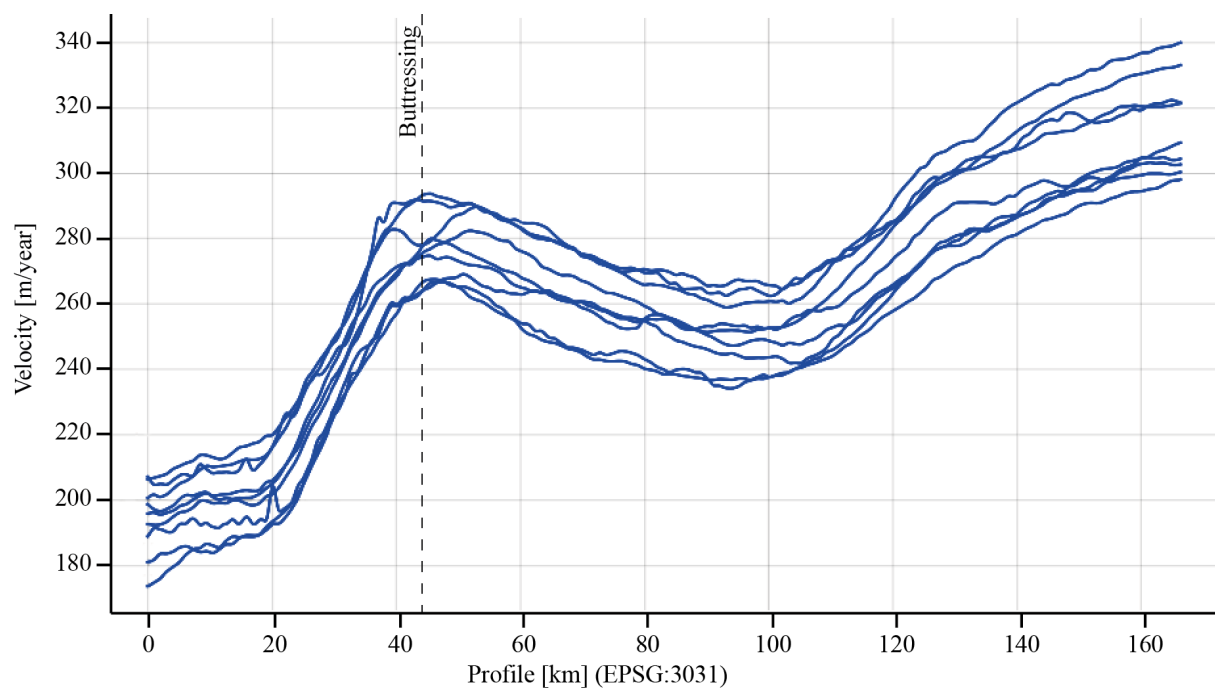


Figure 2.19: Velocity profiles. Each line corresponds to an estimated velocity for one pair of SAR images. The effect of buttressing is clearly represented by the strong reduction of velocity at 40km.

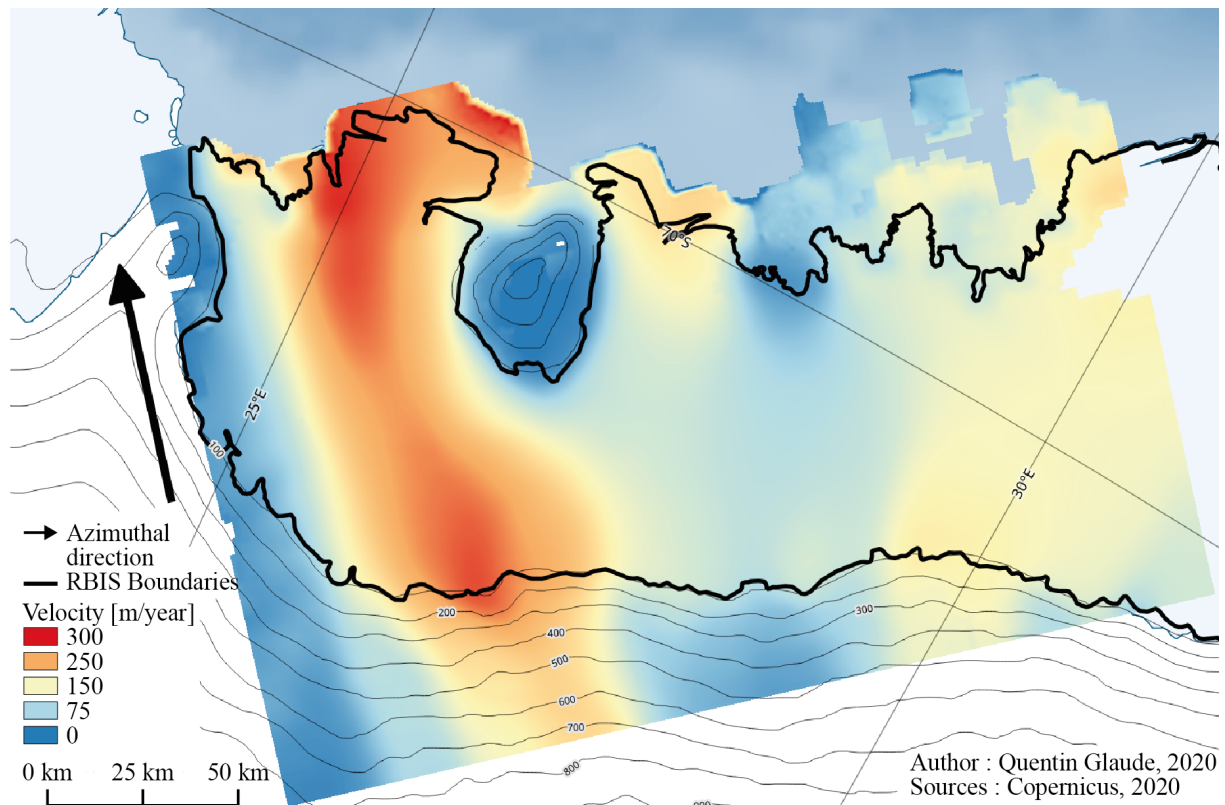


Figure 2.20: Average azimuthal velocity.

Time series of range and azimuthal velocities over coordinates 70°S , 30°E are displayed in Figure 2.24. The vertical axis has been set to an equal velocity range for both components, to facilitate comparisons. We observe a larger uncertainty of the range offsets, where we observe that the dispersion of range velocity is more pronounced than the azimuthal velocity (standard deviation 17.3 versus 12.1 m/year).

The influence of tides/IBE is particularly visible when comparing results between the ice shelf and the grounded ice (Figure 2.25). On grounded ice, the variability goes from 17.3 to 13.2 meters per year).

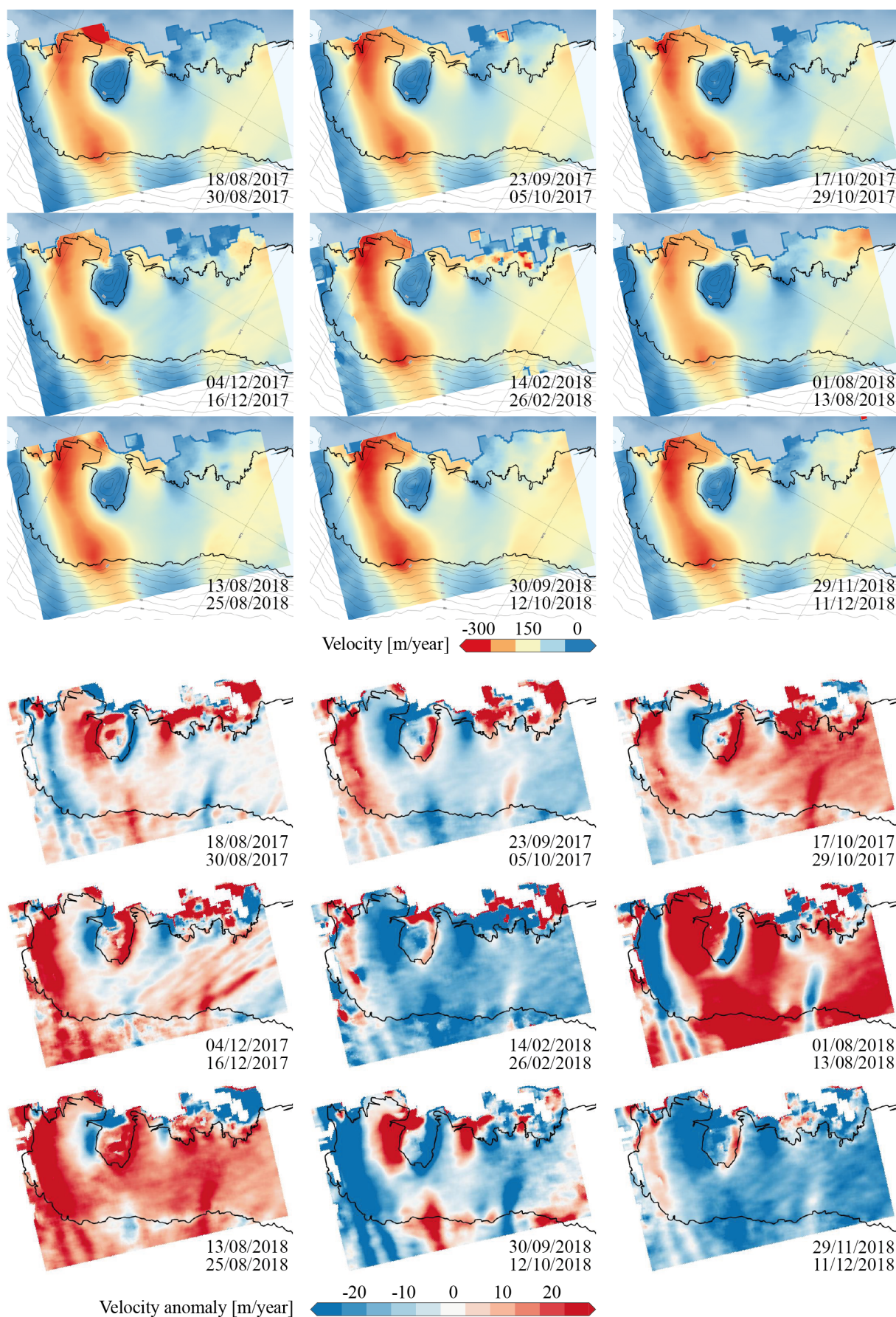


Figure 2.21: Subset of the RBIS surface azimuthal velocity fields time series (top). Azimuthal velocity anomalies (bottom).

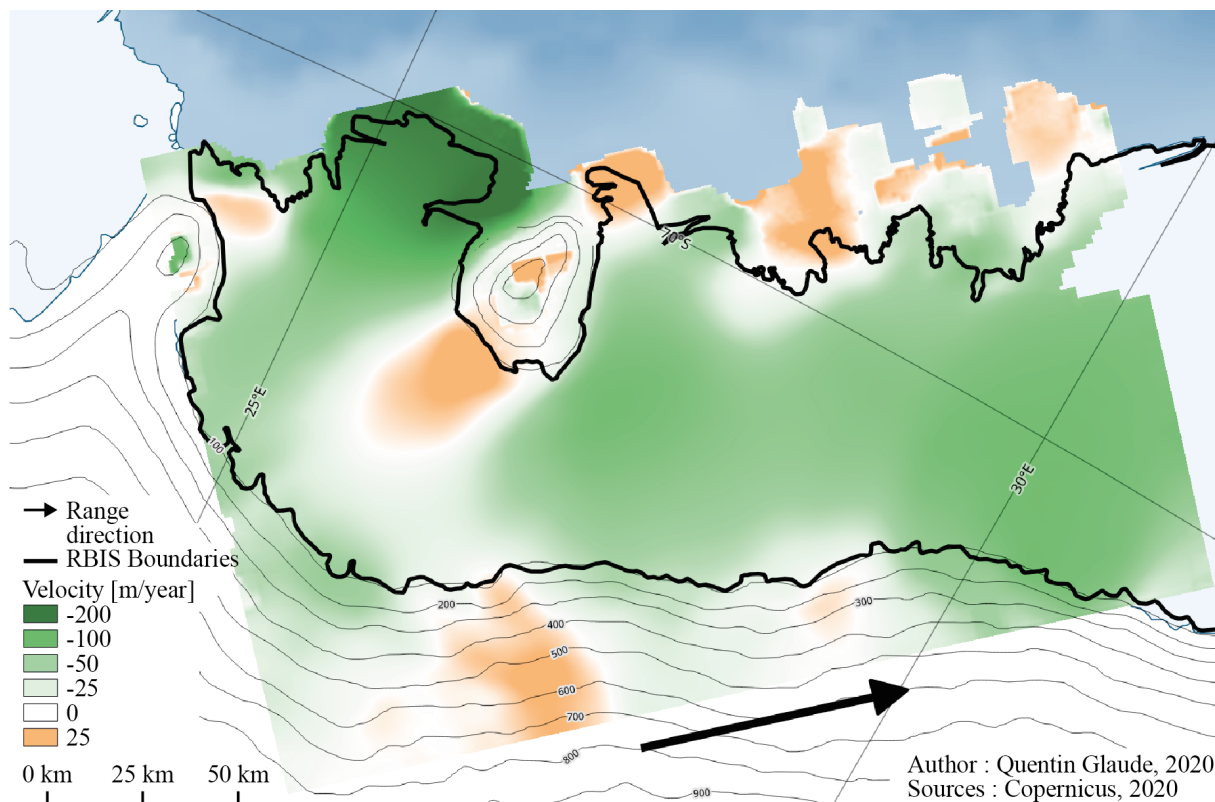


Figure 2.22: Average range velocity field.

Velocity Trends over the Roi Baudouin Ice Shelf

By defining regions of interest (Fig. 2.17, A to E rectangles), we can extract the evolution the velocity (Table 2.4). Linear regression shows a systematic acceleration for all the regions (Fig. 2.26). However, these trend lines are never significant ($p\text{-value} \gg 0.05$). While the analysis of individual results shows important variations from pair to pairs (up to 50 meters/year), the comparison between yearly averages in Table 2.4 confirms the remarkable ongoing stable behavior of the RBIS.

The analyses of trend lines in Fig. 2.26 are the witnesses of the limits of Sentinel-1 to precisely capture individual displacements, due to a relatively low azimuthal resolution, and a range direction that suffers from high-frequency vertical variations due to tidal effects. This limitation is balanced by a relative abundance of data. When omitting data gaps, we counted 121 SAR pairs in our 4-year time range. Nevertheless, the important temporal baseline of high-resolution Sentinel-1 products (12 days) allows us to only use a fraction of the total number of pairs (28).

The recent important calving due to the collision between the Roi Baudouin Ice Shelf and the D28 iceberg in June 2021 (Fig. 2.27) is not visible in recent velocity results. While the lost region was considered passive, such large and rapid changes in the ice shelf's geometry might have impacts on the internal dynamics, motivating us to continue the monitoring.

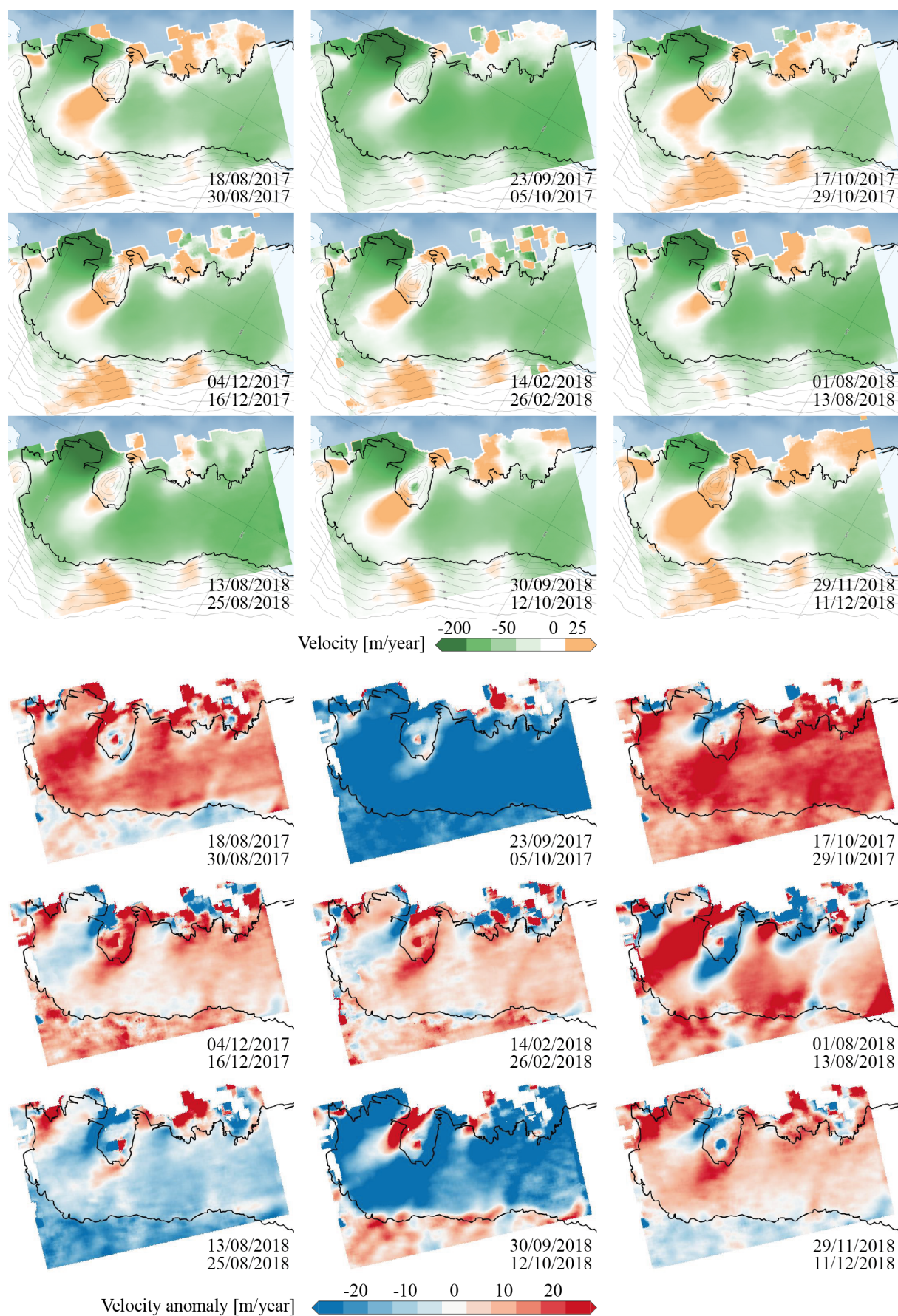


Figure 2.23: Subset of RBIS surface range velocity fields time series (top). Range velocity anomalies (bottom).

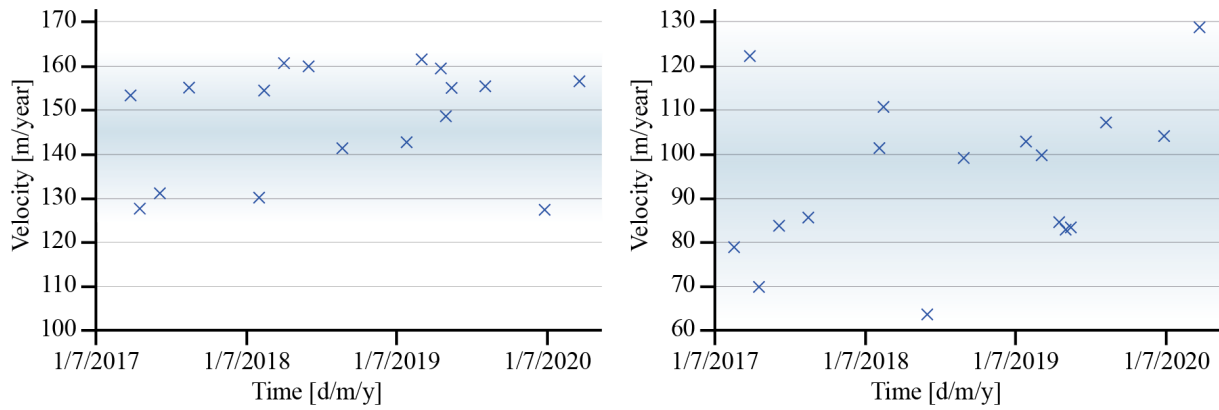


Figure 2.24: Comparison between azimuthal (left) and range (right) velocity time series.

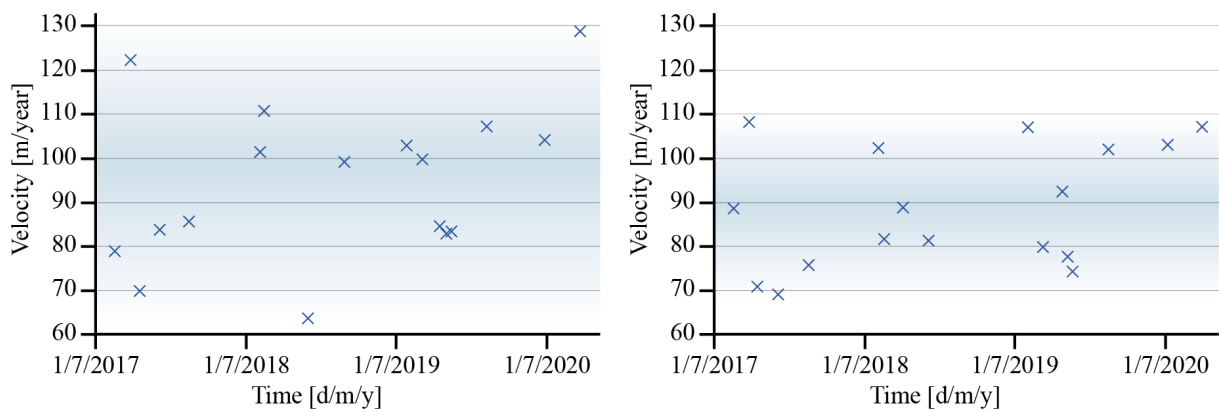


Figure 2.25: Comparison between range velocity time series over the ice shelf (left) and over grounded ice (right). On grounded ice, the range variability is similar to the azimuthal one.

	2017	2018	2019	2020	2021	
A	265	271	275	275	268	(+1.1%)
B	274	280	283	279	277	(+1.1%)
C	134	138	144	152	136	(+1.5%)
D	101	107	114	119	104	(+3.0%)
E	167	172	177	180	169	(+1.2%)

Table 2.4: Velocity [$\text{m}\cdot\text{a}^{-1}$] evolution based on yearly averages estimates.

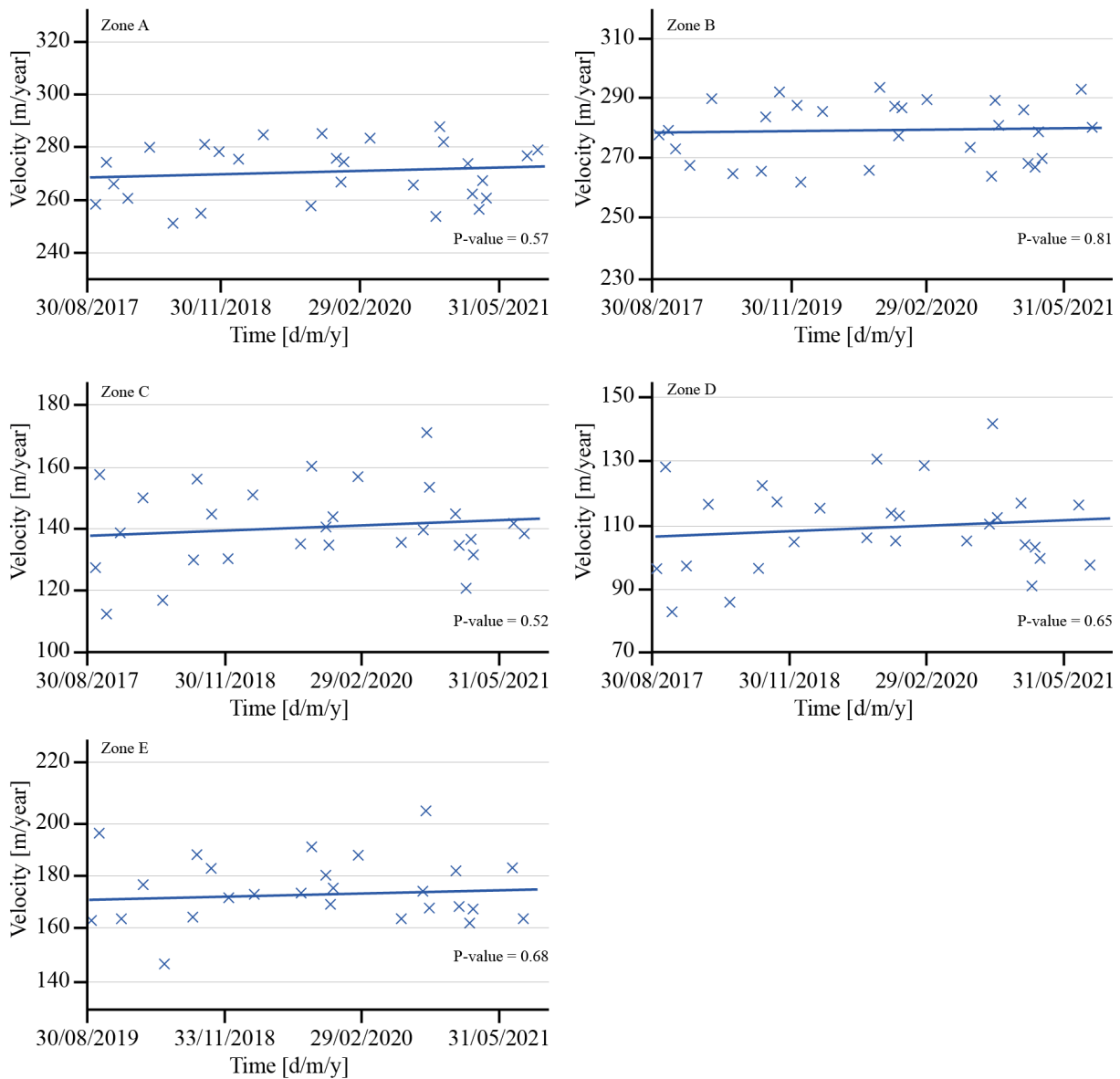


Figure 2.26: Linear trends of surface displacements at given coordinates. Zones A, B, C, D, and E are represented in Fig. 2.17.

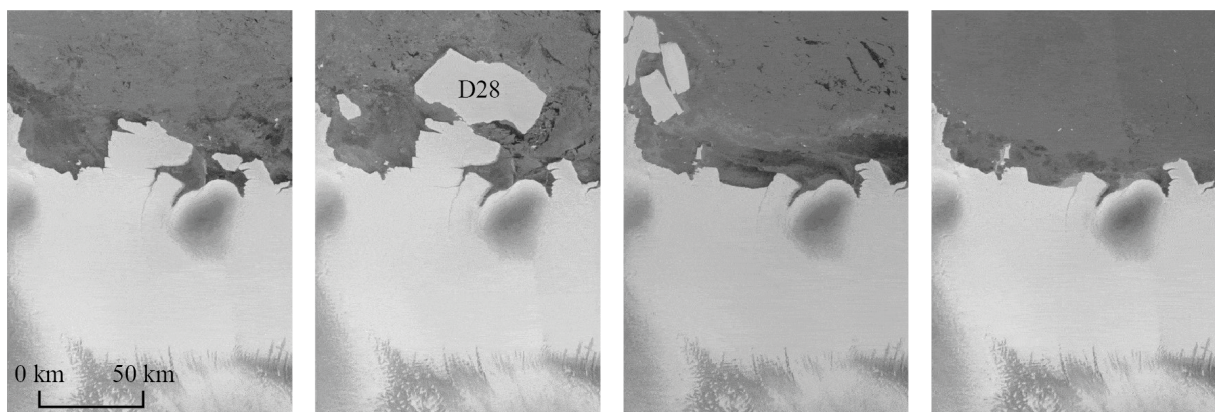


Figure 2.27: Important calving event due to the collision between the Roi Baudouin Ice Shelf's "Dog head" and the D28 iceberg in June 2021.

Surface Velocity Comparison Between Sentinel-1 (2017-2018) and Previous RS Studies

We investigate the potential velocity difference with previous records (up to 1996 with ERS SAR satellite). Several velocity products are available over the RBIS. They are all from SAR remote sensing, with the exception of Rignot's datasets which additionally use optical sensors. All these results are produced using image matching procedures, such as speckle tracking for SAR images. From the Rignot's data collection, gaps over RBIS can be present. In these cases, we discarded the dataset. From the whole series, we retain *2007*, *2009*, *2010*, *2013*, *2014*, *2015* and *2016*. Ordering by acquisition time, we have :

- 1996 : ERS 1/2 (Berger et al., 2017)
- 2000 : RADARSAT 1 (Pattyn et al., 2012)
- 2007-2008 : RADARSAT 1 / ALOS PALSAR / ENVISAT (Rignot et al., 2011a)
- 2009-2010 : ALOS PALSAR / ENVISAT (Rignot et al., 2011a)
- 2010-2011 : RADARSAT 1 / ALOS PALSAR (Rignot et al., 2011a)
- 2010-2011 : ALOS PALSAR (Berger et al., 2017)
- 2013-2014 : RADARSAT 2 / TANDEM-X / LANDSAT 8 (Rignot et al., 2011a)
- 2014-2015 : SENTINEL-1 A / RADARSAT 2 / LANDSAT 8 (Rignot et al., 2011a)
- 2015-2016 : SENTINEL-1 A / RADARSAT 2 / LANDSAT 8 (Rignot et al., 2011a)
- 2016-2017 : SENTINEL-1 A / B / RADARSAT 2 / LANDSAT 8 (Rignot et al., 2011a)

This velocity data collection is compared to our results from 2017-2018 produced with Sentinel-1 A, by computing the velocity difference as

$$\Delta V_i = | \vec{V}_{qq} | - | \vec{V}_i | \quad (2.3)$$

with \vec{V}_{qq} our dataset, and \vec{V}_i the dataset to be compared. A positive ΔV_i means that our dataset estimates a higher velocity. Then we mask out areas that are not covered by the two products, using the boolean expression $\vec{V}_{qq} \cap \vec{V}_i$. Velocity difference maps are displayed from figures 2.28 to 2.31.

When analyzing single velocity maps, we observed that compared to 1996, the velocity on the area covered decreased by about 10%. This observation is inverted when looking at 2000 RADARSAT data. Again, we have a velocity decrease in 2010 according to 2010-2011 ALOS products. This analysis confirms the danger of using a single pair to produce velocity maps. These types of products capture well the displacements on a limited time range, but are rather inefficient when extrapolated to a yearly average.

This interpretation is confirmed when looking at differences between ALOS data and Rignot's dataset, which produce highly different estimates while studying the same period (Fig. 2.32).

Focusing only on Rignot results, we observe a general decrease in velocity near the Derwael Ice Rise, and a global acceleration in the Eastern part of the RBIS.

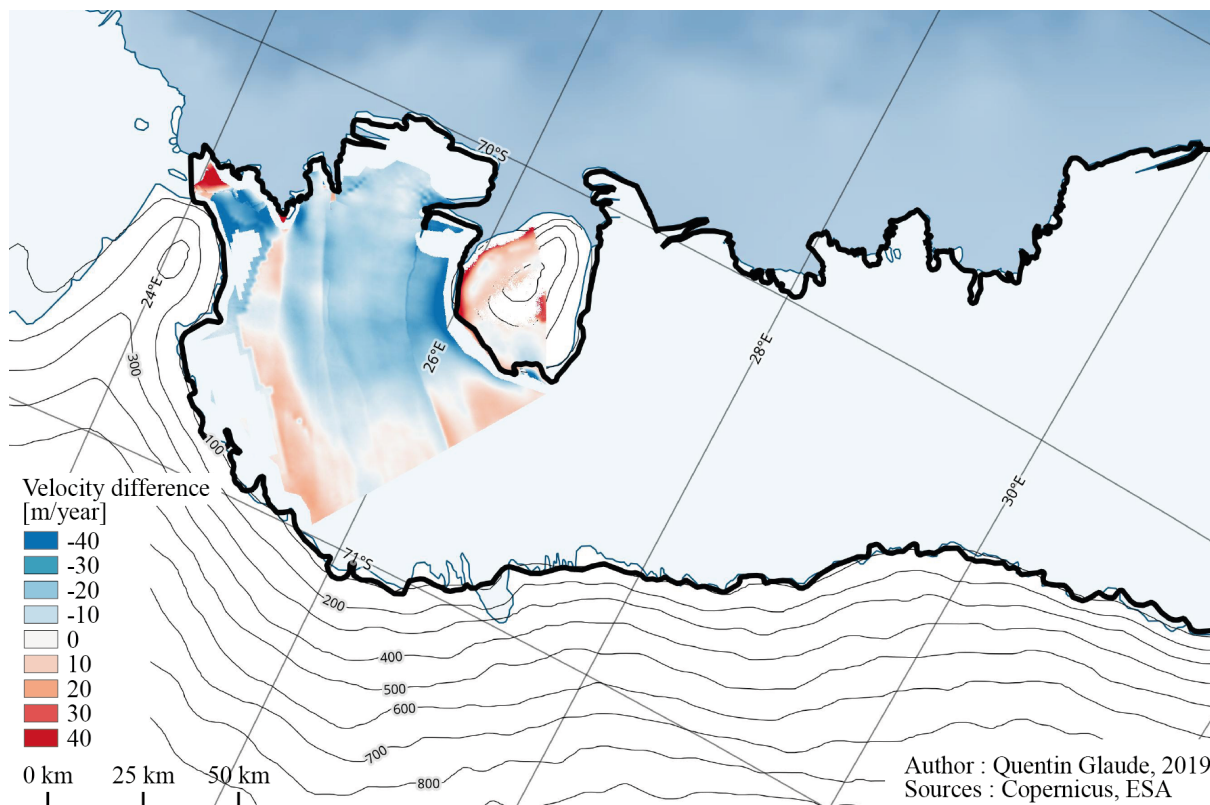


Figure 2.28: Velocity difference between our Sentinel-1 2017-2018 dataset and ERS 1/2 (1996).

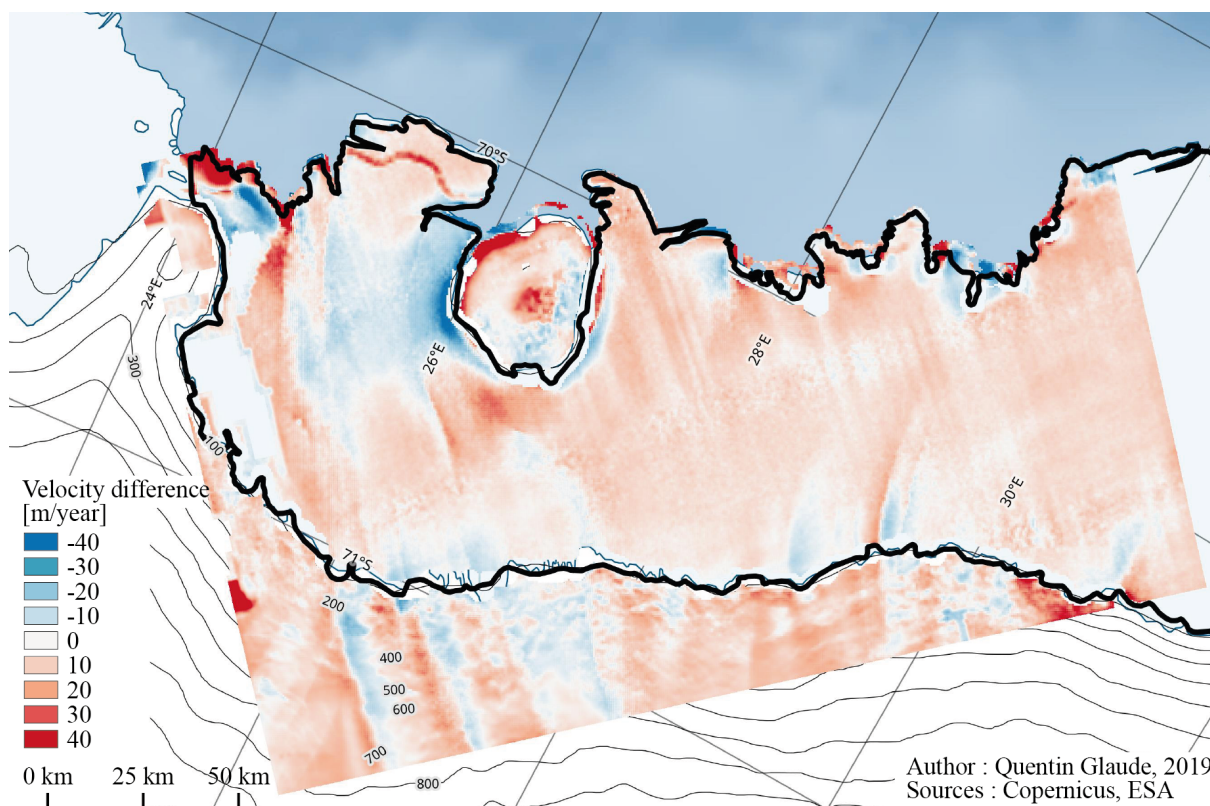


Figure 2.29: Velocity difference between our Sentinel-1 2017-2018 dataset and RADARSAT (2000).

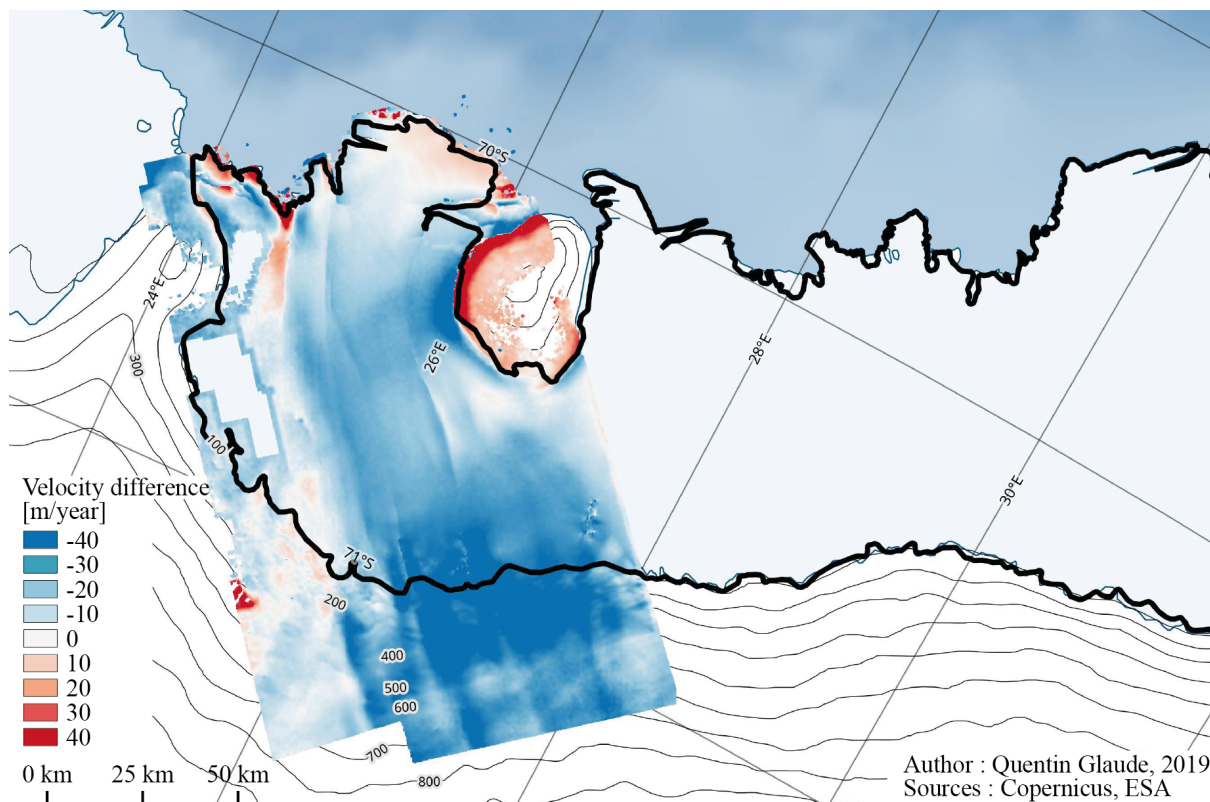


Figure 2.30: Velocity difference between our Sentinel-1 2017-2018 dataset and ALOS PALSAR (2010-2011).

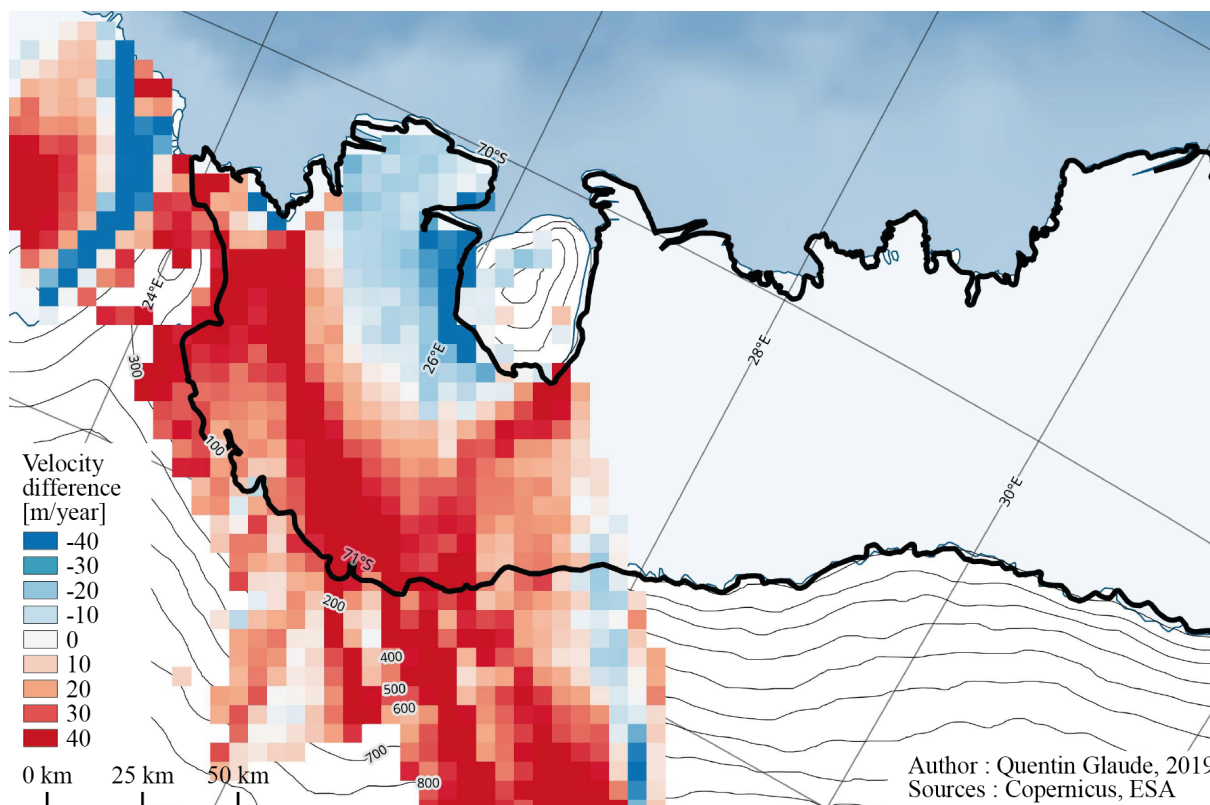


Figure 2.32: Velocity difference between the ALOS PALSAR dataset and the Rignot 2010 dataset.

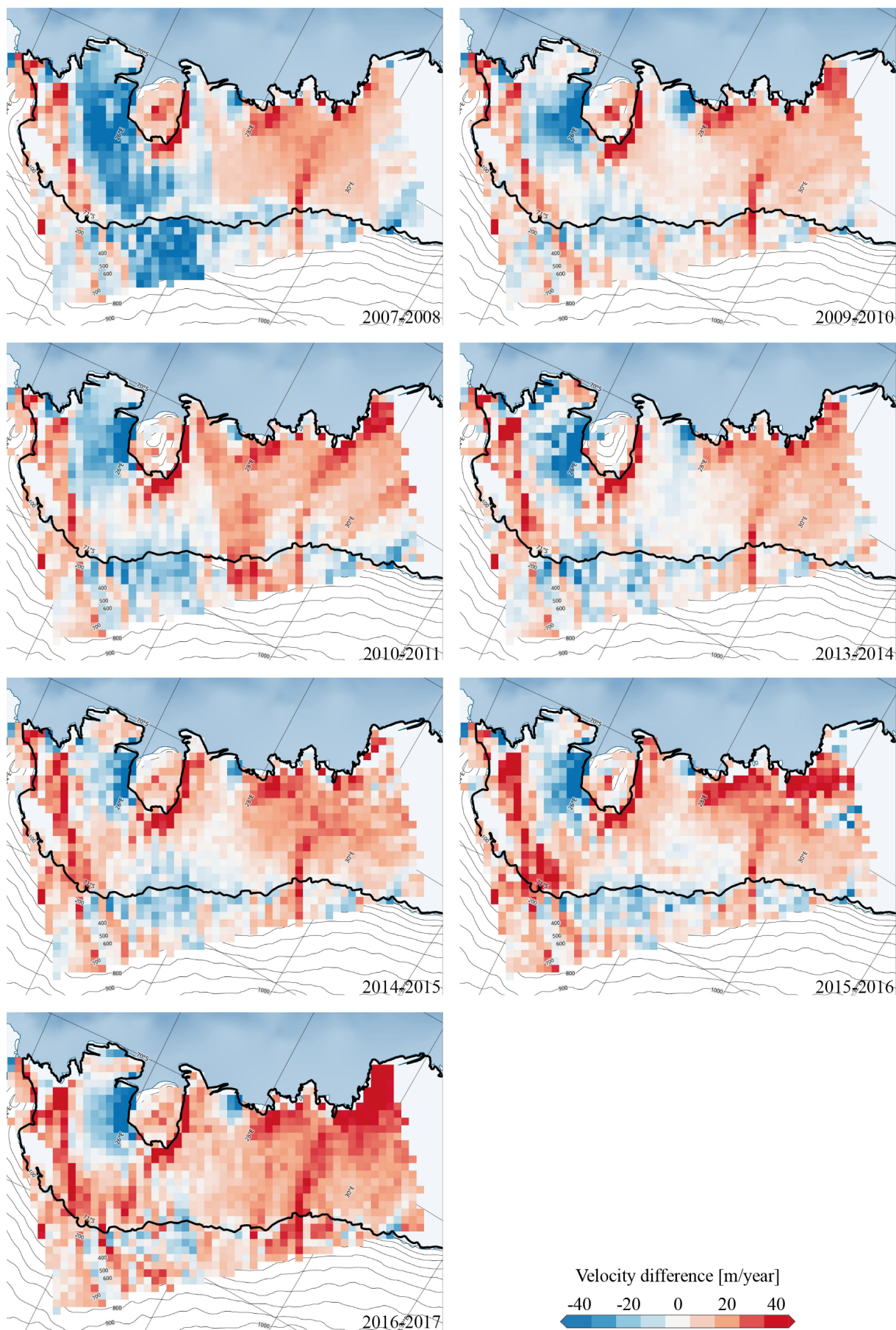


Figure 2.31: Velocity difference between our Sentinel-1 2017-2018 dataset and the Rignot data collection (years 2007, 2009, 2010, 2013, 2014, 2015, 2016, and 2017).

2.2.1.3 Coherence Tracking, and its Adaptation to the TOPSAR Acquisition Mode

Incoherent speckle tracking presented in previous sections relies on the maximization of the local cross-correlation between SAR amplitude images to find azimuthal and range displacements. One may also employ the full complex signal of SAR images to perform the image matching algorithm. This is what is performed through coherent speckle tracking techniques.

Here we present a coherent speckle tracking technique, called coherence tracking, that is both able to retrieve bidimensional displacement maps but also *recorrelate* the 2 signals to produce interferograms for precise estimations of slant-range displacements. The idea of coherence tracking is that large surface displacement will create artificial coherence loss.

Indeed, as we develop in section 2.2.2, DInSAR is a well-established technique that is using phase measurement difference between two SAR images acquired at two different dates to infer a displacement along the line-of-sight direction. However, in Antarctica, we have the problem that large ice displacements lead to locally uncoregistered scatterers, meaning that between two dates, the scatterers moved. The consequences are important decorrelation in strong non-stationary scenarios.

With coherence tracking, we try to find where scatterers moved by performing fine coregistration using maximization of the coherence. Not only it allows us to find directly a bidimensional displacement, but it also allows to retrieval of the misaligned scatterers for interferometry. Results of interferogram corrections were originally applied to Shirase glacier (Derauw, 1999a).

The direct application of coherence tracking on Sentinel-1 data is not possible. The TOPSAR acquisition mode introduces a strong aliased phase bias in the azimuthal direction. This phase ramp can be removed from TOPSAR images (Fig. 2.33) using the protocol defined in Miranda and Hajduch (2017) before applying the coherence tracking technique.

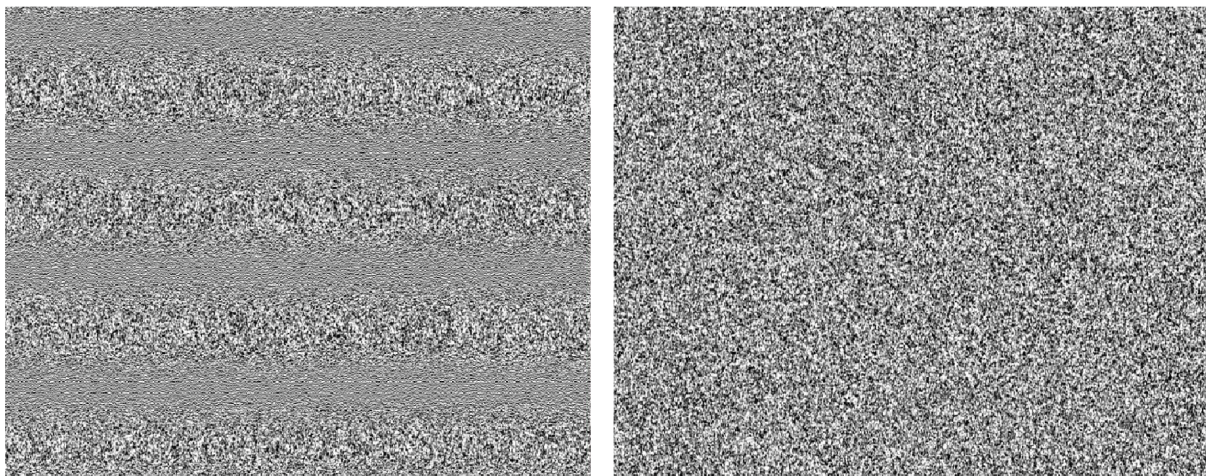


Figure 2.33: Effects of the deramping operation. Left: real part of the original TOPSAR master signal. Right: the deramped image of the same location.

We are here using a single SAR pair in IW mode from the 23rd of September 2017 to the 5th of October 2017 on orbit 59 in the Roi Baudouin Ice Shelf, in Dronning Maud Land (Antarctica). The important results obtained are the azimuth and range shifts, the coherence after tracking, and the tracked interferogram (figure 2.34). These 4 products are resampled to input resolution.

Coherence tracking is able to find the positions of the moving scatterers and produce coherent interferometry. This is well verified in figure 2.35 where we can see that the coherence gain is maximized where the ice is moving fast (both in azimuth and coherence), that is to say in the ice-front location.

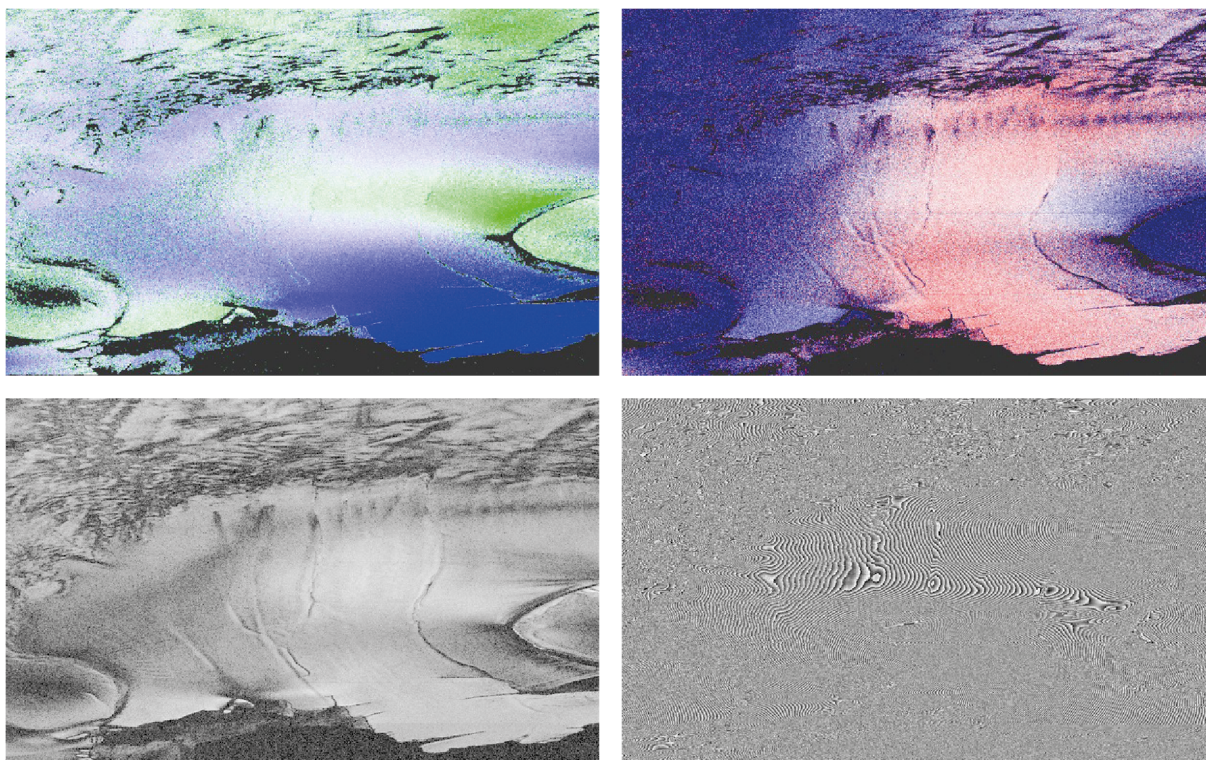


Figure 2.34: From top left to bottom right: range shifts (green = leftwards and blue = rightwards), azimuth shifts (blue to red = [0-1 meter per day]), tracked coherence, and tracked interferogram.

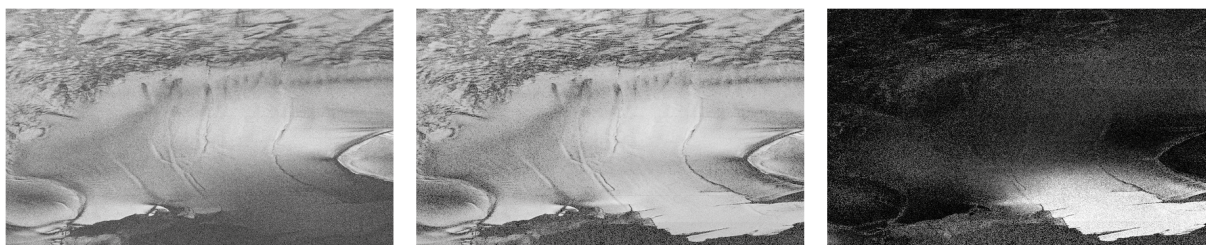


Figure 2.35: Left = original coherence using classical full resolution interferometry. Center = Coherence after retrieving the scatterers. Right = coherence gain from classical interferometry to coherence tracking (white representing a 0.5 gain).

The results are impressive and give valuable information about the 2D-shift at coarse level but also the corrected interferogram for highly accurate range displacements. Moreover, these two products are computed where classical methods do not allow the use of interferometry, because of the fast-moving nature of the surface.

The methods and results were presented during the EUSAR 2021 scientific congress, where a proceeding was written and reviewed. In there, more details about mathematical development, processing parameters, or illustrations, are present. The article is available here-after, and can be cited as

Glaude, Q., Derauw, D., Barbier, C., & Pattyn, F. (2021). The Added-Value of TOPSAR Coherence Tracking for Sentinel-1 Interferometry Over Ice Shelves. *EUSAR 2021 - 2021 European Conference on Synthetic Aperture Radar*, Leipzig, Germany.

Later, in section 2.2.2 about SAR Interferometry, we present the importance of tracking coherence in ice-shelves studies.

The Added-Value of TOPSAR Coherence Tracking for Sentinel-1 Interferometry Over Ice Shelves

Quentin Glaude^{a,b}, Dominique Derauw^{b,c}, Christian Barbier^b, and Frank Pattyn^a

^aLaboratoire de Glaciologie, Université Libre de Bruxelles, Bruxelles, Belgium

^bCentre Spatial de Liège, Université de Liège, Angleur, Belgium

^cInstituto de Investigación en Paleobiología y Geología, Universidad Nacional De Rio Negro, General Roca, Argentina

Abstract

Feature tracking has long been used as a technique to infer bidimensional displacement maps by locally maximizing the incoherent or coherent cross correlation of coregistered SAR images. Coherence tracking is based on the latter technique. Exploiting the phase information, the method tends to find local shifts that maximize the coherence information aiming at enhancing the interferometric signal while also bringing an estimation of bidimensional displacements. This is particularly important in fast-moving areas since it allows recovering an interferometric signal loss due to displacement-induced decorrelations. Here, we present the adaptation of the technique to TOPSAR acquisition mode and results in Antarctica.

1 Introduction

Differential SAR Interferometry (DInSAR) is a well-established technique that takes advantage of phase measurement difference between two SAR images acquired at two different dates to infer line of sight displacements [1]. SAR Earth observation satellites are using polar heliosynchronous orbits. Consequently, DInSAR allows getting primarily the East-West displacement component of horizontal displacements.

In Antarctica however, we observe that the main component of the ice flow goes Northward, following mainly the azimuth direction of SAR observations. Therefore, using DInSAR, displacements in this direction are poorly captured. Another problem concerns local misregistrations due to non-stationary scenarios in which local displacement may prevent global coregistration, leading to artificial local losses of coherence. This is particularly true in the case of ice streams or ice shelves where pixel-size misregistrations are common. To solve the first issue and estimate azimuth displacements one can use image matching techniques such as feature tracking. As an example, [2] used feature tracking to obtain velocity maps on the whole Antarctica.

Feature tracking comes in complement or in replacement to differential SAR interferometry to get an estimation of azimuth displacements and/or to get an estimate of range displacements when coherence losses do not allow to generate a usable interferometric signal. When feature tracking is performed using only the amplitude of SAR images, we talk about incoherent speckle tracking. In that case, we consider the feature to be tracked from one image to another. Feature tracking can be based on fringe visibility or maximization of local coherence, in which case it is called coherent speckle tracking [3].

We can go one step further when estimating and optimiz-

ing the local complex coherence, by directly exploiting the phase information, in order to also get the optimized tracked interferometric phase information at the given position [4, 5]. In this approach, using directly coherence estimation as the tracking criterion, we can retrieve bidimensional displacement maps, similar to coherent speckle tracking, but also recover the interferometric signal for precise estimations of slant-range displacements. Considering the high temporal decorrelation rate over fast-moving areas, tracking the ground scatterers are crucial for interferometric studies. In addition, range shifts can also help in assisting the phase unwrapping of the tracked interferometric signal for fine estimation of range displacements. The estimation of bidimensional displacements does not require special care for the TOPSAR acquisition mode. However, the reconstructed interferometric signal requires a special attention to the azimuthal phase ramp inherent to this particular acquisition mode.

In the following, we present coherence tracking technique adapted to the Sentinel-1 TOPSAR acquisition mode and show the results obtained in the context of ice-shelves displacement measurements in East Antarctica.

2 Method

2.1 TOPSAR Mode Specificity

If coherence tracking was demonstrated using Stripmap SAR acquisition mode such as ERS data [4, 5], Terrain Observation by Progressive Scans (TOPSAR) mode requires some preliminary steps to make coherence tracking applicable.

TOPSAR uses reverse beam steering to decrease aperture synthesis time for a given on-ground azimuth distance. The image formed on this distance is called a burst. Decreasing the required acquisition time, it allows to switch the

beam to consecutive swaths and globally extend the observed cross track at the expense of azimuth resolution loss [6].

This reverse beam steering induces a variable Doppler centroid frequency along the azimuth dimension of the burst. Consequently, each burst contains an azimuth phase ramp that must be considered all along the interferometric processing [7].

Summarizing, slave image bursts must be moved to azimuth base-band (deramping) to allow interpolation of the data in the coregistration process. Following [8], this deramping process must be followed by a reramping process after burst interpolation in such a way that master and slave burst phase ramps coincide in order to cancel out in the interferometric process.

These deramping and reramping operations are applied as such in any TOPSAR interferometric processor. Consequently, after the coregistration process, one has coregistered master and slave images, still bearing this typical TOPSAR phase ramp.

If willing to fully exploit the interferometric signal, coherence tracking applied to a TOPSAR coregistered interferometric pair requires a full removal of this phase ramp from both the master and slave bursts [9]. While this step is not necessary for bidimensional displacement estimation [11], not removing this phase ramp produce a phase bias in the tracked interferogram. Indeed the additional azimuth shifts we are tracking lead to a misregistration of TOPSAR phase ramps that do not fully cancel out in the interferometric process, inducing an additional azimuthal phase difference between the master and slave images that depends on the additional azimuth shift amplitude.

2.2 Coherence Tracking

Coherence tracking is an original adaptation of the coherent speckle tracking method [5]. The basic idea is that large surface displacements will create an artificial coherence loss. Consequently, tracking coherence at pixel level allows recovering the interferometric phase information, while also determining an estimation of the bidimensional velocity field.

Similar to coherent speckle tracking, the goal of coherence tracking is to find where scatterers moved by locally performing fine coregistration using coherence maximization criteria. The local coherence is classically estimated using equation

$$\hat{\gamma}(s_1(x,y), s_2(x,y)) = \frac{\left| \sum_{(x,y) \in n} s_1(x,y) \cdot s_2^*(x,y) \right|}{\sqrt{\sum_{(x,y) \in n} |s_1(x,y)|^2 \cdot \sum_{(x,y) \in n} |s_2(x,y)|^2}} \quad (1)$$

where n is a neighborhood around the (x,y) target location. We find the (i,j) pixel shift that maximizes local coherence by

$$(i,j) = \arg \max_{(i,j)} \{ \hat{\gamma}(s_1(x,y), s_2(x+i,y+j)) \} \quad (2)$$

Around this pixel shift position, we take the estimated coherence at the four-connected neighbors with which we perform a Gaussian fitting. Its maximum gives us a sub-pixel estimate of the local bidimensional displacement.

This simple technique enables us to find directly a bidimensional displacement (in terms of sub-pixels shifts) but also to retrieve the misregistered pixel for interferometry.

In fast-moving areas, we can use this shift to find in the slave image the *true* corresponding scatterers for interferometry. Such interferogram correction was originally applied to the Shirase glacier to infer the surface velocity field [4].

In addition, the estimation of range shifts from equation 2 helps in the unwrapping process, by giving a prior information of the integer phase cycle shift determination for each pixel in the interferometric phase, but also giving the global phase shift to match range displacement determined by range offset tracking.

3 Results

In the frame of the MIMO project (Monitoring melt where Ice Meets Ocean), we are re-developing and adapting the coherence tracking technique to the Sentinel-1 TOPSAR to perform surface velocity field measurements on the Roi Baudouin Ice Shelf, in Dronning Maud Land, Antarctica (figure 1).

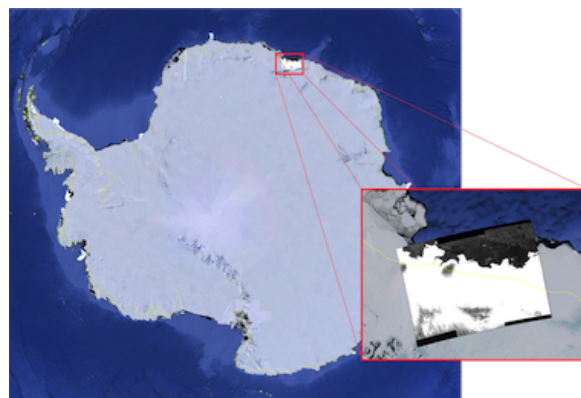


Figure 1 Roi Baudouin Ice Shelf, Dronning Maud land, Antarctica. The vignette represents a scaled-up illustration of the SAR amplitude image.

We present here preliminary coherence tracking results obtained using a Sentinel-1 TOPSAR pair in Interferometric Wide swath mode acquired on September 23 and October 5, 2017, along the relative orbit 59 over our area of interest. Both Sentinel-1 images were first coregistered using precise orbits and a DEM. At the end of the coregistration process, both the master and the slave images are deramped before debursting, leading finally to two stripmap-like images.

Coherence tracking was performed using 7×7 pixels windows on a 2×6 (azimuth \times range) grid of anchor points for local coherence estimation. Tracking is performed from -3 to +3 pixels from the initial coregistration values in both

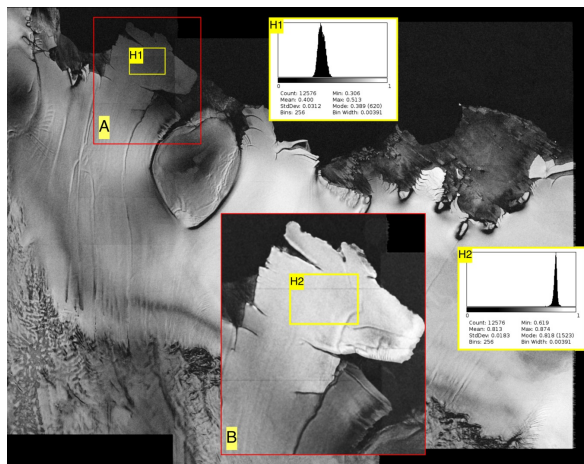


Figure 2 Coherence tracking results:
 Background: Coherence image obtained after global images coregistration.
 A & B: coherence before and after tracking on sub-zone delineating fast-flowing ice stream
 H1 & H2 coherence histograms before and after tracking on a limited zone on fast-flowing ice stream. The coherence on this fast-moving ice stream is greatly improved, from 0.4 on average before tracking, to 0.8 after coherence tracking.

range and azimuth to map the local coherence.
 Optimum coherence is found through a Gaussian fitting of the obtained coherence mapping.
 Four main products are generated:

- the tracked coherence;
- the tracked interferogram;
- the range local displacements (with respect to initial coregistration);
- the azimuth local displacements (with respect to initial coregistration).

Figure 2 illustrates coherence improvements. The background image is the coherence obtained classically, coregistering the Sentinel-1 pair based on precise orbits calculation. Red rectangles A and B show ice stream coherence before and after tracking. The histograms of sub-zones H1 and H2 are shown on the right. This shows clearly that coherence losses were due to local misregistration in this fast-moving area.

Improvement of fringes visibility on the fast-flowing ice stream is clearly shown on full resolution samples interferograms before and after tracking in figure 3. The signal was originally barely distinguishable whereas the tracked interferogram one enables us to infer precise displacement fields at the fastest parts of the shelf. This gain is visible through the coherence in figure 4.

The two last products derived from coherence tracking, i.e., range and azimuth local displacements with respect to global registration, may be represented as such in pixel unit (figure 5) or as vectorial representation (figure 6). Figure

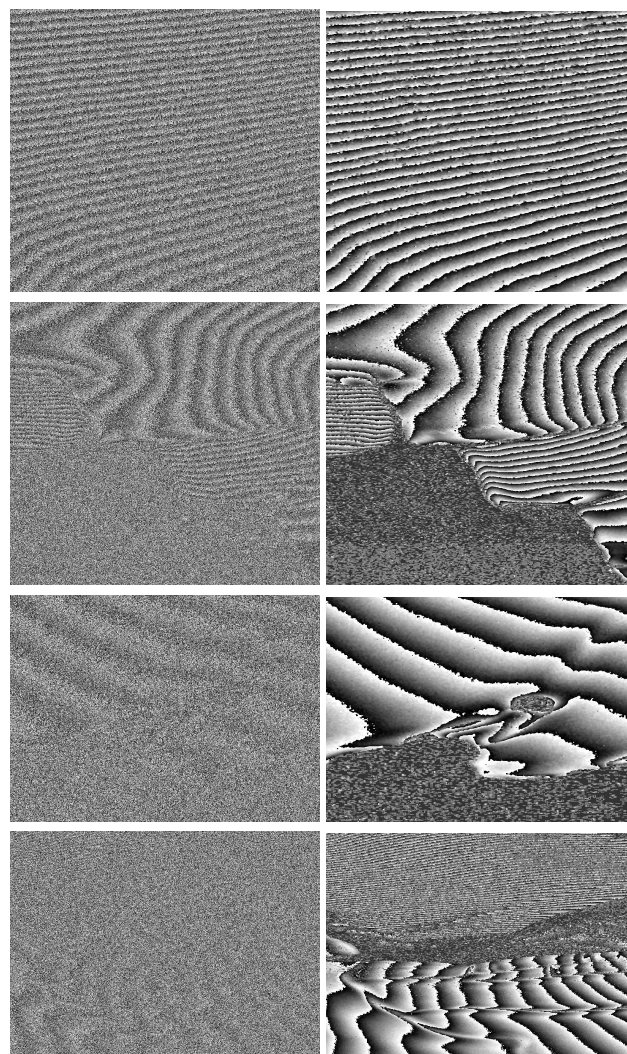


Figure 3 Full resolution, slant-range / azimuth geometry, sample interferograms before (left) and after tracking (right).

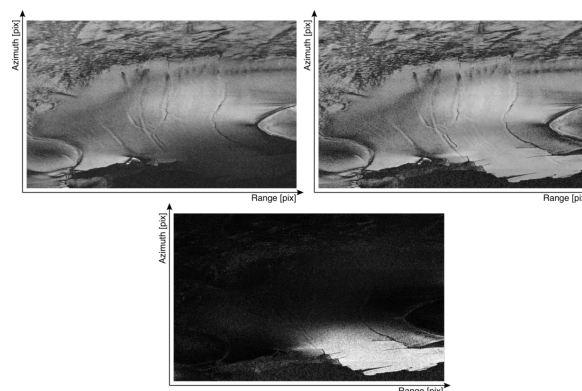


Figure 4 Full resolution, slant-range / azimuth geometry, coherence samples. Left = original coherence. Right = Coherence derived after tracking. Bottom = coherence gain/recovery (white represents a 0.5 gain).

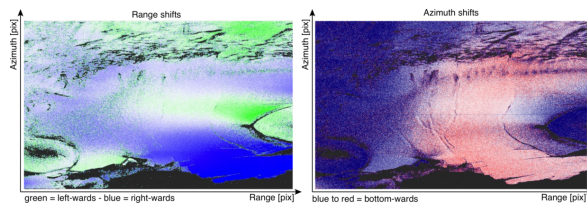


Figure 5 Full resolution, slant-range / azimuth geometry, range (left) and azimuth (right) shifts.

6 is an HSI-like representation of the tracked results with superimposed vectorial representation. The amplitude of the computed displacement, in meters, is used for the Hue channel, which is associated with the lookup table shown on the figure. The tracked coherence is used for the Saturation channel and the log of the amplitude of the master image is used for the Intensity channel. In this representation, the full surface velocity field is well delineated. We observe the Ragnhild ice stream deviates and passes on the left side of the Derwael Ice Rise. A smaller part of the ice stream is passing on the right side. The maximum displacement amplitude as measured by tracking is about 12 meters while the time lapse between acquisitions is 12 days.

4 Conclusion

Coherence tracking is shown to be applicable to Sentinel-1 TOPSAR acquisition mode. The results are impressive in terms of coherence gain, as well as in interferometric signal recovery. On the one hand, similar to coherent speckle tracking techniques, coherence tracking is able to retrieve the 2D-shifts at coarse level and, on the other hand, it also corrects the interferogram to get highly accurate range displacements.

Moreover, these products are computed where classical methods do not allow to use interferometry, because of the fast-moving nature of the surface. The 6-days revisit time of Sentinel-1 pairs is often considered too large for interferometry in the boundaries of the Antarctic Ice Sheet. Over these ice shelves, coherence tracking may offer a promising solution, pushing forward the boundary between the applicability of offset tracking techniques to SAR interferometry.

5 Acknowledgment

This research is supported by the French Community of Belgium in the funding context of a FRIA grant, and carried out in the framework of the MIMO (Monitoring melt where Ice Meets Ocean) project funded by the Belgian Science Policy contract Nos. SR/00/336.

6 Literature

[1] Massonnet, D.: Rossi, M.: Carmona, C.: Adragna, F.: Peltzer, G.: Feigl, K.: Rabaute, T.: The displacement

field of the Landers earthquake mapped by radar interferometry. *Nature*, 364(6433), 1993, pp. 138–142

- [2] Mouginot, J.: Rignot, E.: Scheuchl, B.: & Millan, R.: Comprehensive annual ice sheet velocity mapping using Landsat-8, Sentinel-1, and RADARSAT-2 data. *Remote Sensing*, 9(4), 2017, pp. 1–20
- [3] Werner, C.: Strozzi, T.: Wiesmann, A.: Wegmuller, U.: Murray, T.: Pritchard, L.: Luckman, A.: Complimentary measurement of geophysical deformation using repeat-pass SAR. In *Proceedings of the IEEE 2001 International Geoscience and Remote Sensing Symposium*, Sydney, NSW, Australia, 9–13 July 2001; pp. 3255–3258.
- [4] Pattyn, F.: Derauw, D.: Ice-dynamic conditions of Shirase Glacier, Antarctica, inferred from ERS SAR interferometry. *Journal of Glaciology*, 48(163), 2002, pp. 559–565
- [5] Derauw, D.: DInSAR and coherence tracking applied to glaciology: The example of Shirase Glacier, in *Proc. FRINGE'99*, Liège, Belgium, 1999
- [6] De Zan, F.: Guarnieri, A. M.: TOPSAR: Terrain observation by progressive scans. *IEEE Transactions on Geoscience and Remote Sensing*, 44(9), 2006, pp. 2352–2360
- [7] Yague-martinez, N.: Gonzalez, F. R.: Brcic, R.: Shau, R.: De Zan, F.: Gomba, G.: Interferometric Processing of Sentinel-1A TOPS data. *IEEE Transactions on Geoscience and Remote Sensing*, 54(4), 2015, pp. 2–5
- [8] Miranda, N.: Definition of the TOPS SLC deramping function for products generated by the S-1 IPF, 2015, pp. 1–15
- [9] Grandin, R.: Interferometric Processing of SLC Sentinel-1 TOPS Data Principle of deramping. *Proceedings of ESA Fringe 2015 Workshop*, (1), 2015, pp. 1–14
- [10] Sanchez-Gamez, P.: Navarro, F. J.: Glacier surface velocity retrieval using D-InSAR and offset tracking techniques applied to ascending and descending passes of sentinel-1 data for southern ellesmere ice caps, Canadian Arctic. *Remote Sensing*, 9(5), 2017, 1–17.
- [11] Scheiber, R.: Prats-Iraola, P.: De Zan, F.: Geudtner, D.: Speckle Tracking and Interferometric Processing of TerraSAR-X TOPS Data for Mapping Nonstationary Scenarios. *IEEE Journal of Selected Topics in Applied Earth Observations and Remote Sensing*, 8(4), 2015, pp. 1709–1720.

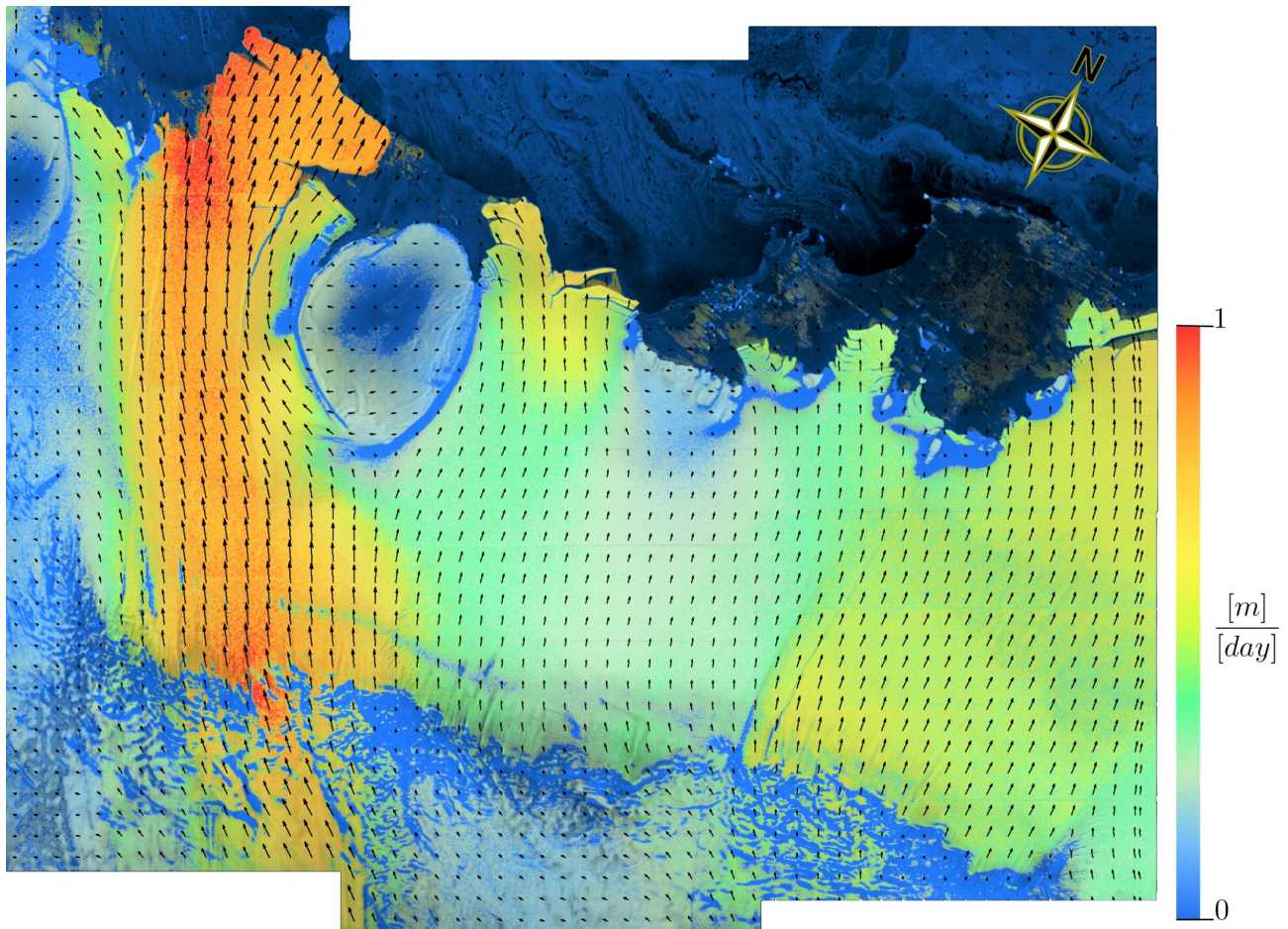


Figure 6 Combine representation of coherence tracking results. Hue = Displacement amplitude - Saturation = Tracked coherence - Intensity = log of master amplitude.

2.2.1.4 Computation of Strain Rates over the Roi Baudouin Ice Shelf

Studying the spatial distribution of ice flow fields (called strain rates) is an important aspect to understand the internal forces that govern the ice shelves' behaviors.

We based our analysis on the work of *Continental-wide estimate of Antarctic strain rates from Landsat 8 velocity grids* (Alley et al., 2018), but applied on coherence tracking results from the Sentinel-1 SAR satellites instead of the optical Landsat satellite.

In physics, strain refers to the deformation of an object. Strain rates are the derivative of this deformation. Strain tensor is a 3D representation of internal forces that govern ice behavior.

$$\tau = \begin{bmatrix} \tau_{xx} & \tau_{xy} & \tau_{xz} \\ \tau_{xy} & \tau_{yy} & \tau_{yz} \\ \tau_{zx} & \tau_{yz} & \tau_{zz} \end{bmatrix} \quad (2.4)$$

In remote sensing and SAR in particular, the 3D deformation cannot be obtained directly. Instead, we focus here on the horizontal strains (Eq. 2.4, in red). In glaciology, we are mainly interested in the spatial variation of these deformations, testifying to the stresses applied within the ice shelf. Strain is thus studied spatially (not temporally). Using u and v the two components of the bidimensional velocity in the horizontal space, we can define the strain rate tensor as :

$$\dot{\epsilon} = \begin{bmatrix} \frac{\partial u}{\partial x} & \frac{1}{2} \left(\frac{\partial v}{\partial x} + \frac{\partial u}{\partial y} \right) \\ \frac{1}{2} \left(\frac{\partial v}{\partial x} + \frac{\partial u}{\partial y} \right) & \frac{\partial v}{\partial y} \end{bmatrix} = \begin{bmatrix} \dot{\epsilon}_x & \dot{\epsilon}_{xy} \\ \dot{\epsilon}_{xy} & \dot{\epsilon}_y \end{bmatrix} \quad (2.5)$$

The $\dot{\epsilon}_x$, $\dot{\epsilon}_{xy}$, and $\dot{\epsilon}_y$ are defined according to the x and y axes, also referred to as range and azimuth directions. Computing the vector orientation α for each point using u and v values, we define the longitudinal, transverse, and shear strains:

$$\begin{aligned} \dot{\epsilon}_{\text{lon}} &= \dot{\epsilon}_x \cos^2 \alpha + 2\dot{\epsilon}_{xy} \cos \alpha \sin \alpha + \dot{\epsilon}_y \sin^2 \alpha \\ \dot{\epsilon}_{\text{trans}} &= \dot{\epsilon}_x \sin^2 \alpha - 2\dot{\epsilon}_{xy} \cos \alpha \sin \alpha + \dot{\epsilon}_y \cos^2 \alpha \\ \dot{\epsilon}_{\text{shear}} &= (\dot{\epsilon}_y - \dot{\epsilon}_x) \cos \alpha \sin \alpha + \dot{\epsilon}_{xy} (\cos^2 \alpha - \sin^2 \alpha) \end{aligned} \quad (2.6)$$

This flow direction α is computed pixel-wise using the arctan formula.

The longitudinal strain rate $\dot{\epsilon}_{\text{lon}}$ describes how the velocity changes toward the flow direction. If it is positive, it means that the ice flow is accelerating. The transverse strain rate $\dot{\epsilon}_{\text{trans}}$ explains how the flow is dividing. Finally, the shear strain rate $\dot{\epsilon}_{\text{shear}}$ explains the cross deformations. The latter is important because it explains mainly the buttressing effect.

The implementation of the strain rates $\dot{\epsilon}$ is defined by dividing velocity differences over short distances. If we take $\dot{\epsilon}_x$ as an example, its practical computation is as follows :

$$\frac{du}{dx} = \frac{u_2 - u_1}{\Delta x} \quad (2.7)$$

A logarithmic definition of the strain rates is also possible and recommended if the strain rates are large.

The distance parameter Δx is important. Short distances allow the computation of fine strain rates but can also be quite noisy. Enlarging this distance allows a better macro-view of the situation.

The first step consists in translating the azimuthal and range shifts into velocity:

$$u = \frac{\text{RangeShift} \times \text{RangePixelSpacing}}{\text{TemporalBaseline}} \quad (2.8)$$

$$v = \frac{\text{AzimuthShift} \times \text{AzimuthPixelSpacing}}{\text{TemporalBaseline}} \quad (2.9)$$

, with RangePixelSpacing and AzimuthPixelSpacing equal to 2.33 and 14.1 meters respectively using Sentinel-1 IW images, and a temporal baseline of 12 days.

We considered using temporal aggregation of coherence tracking results to compute strain rates. The five pairs are: 01-08-18 to 13-08-18, 27-07-19 to 08-08-19, 01-09-2019 to 13-09-2019, 19-10-19 to 31-10-19, and 31-10-19 to 12-11-19.

The sampling of the velocity and coherence has been set to 250 meters. From u and v , we computed the flow direction. Then, we used Sobel filters to compute the spatial derivatives $\frac{du}{dx}$, $\frac{du}{dy}$, $\frac{dv}{dx}$, and $\frac{dv}{dy}$ with a 500 meters neighborhood. Then, the strain rates are computed (Fig. 2.36). The shear strain rates is witness of strong right (red) and left (blue) lateral deformations. For transverse strain rates, positive and negative values indicate lateral expansion and compression regimes.

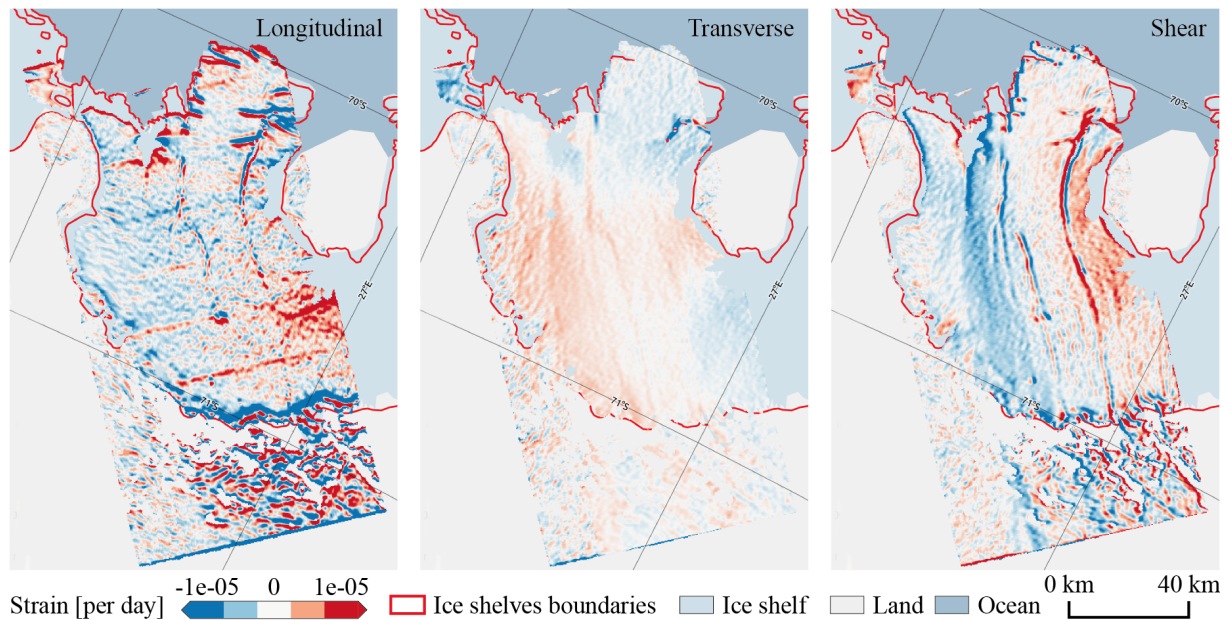


Figure 2.36: Examples of strain rates from temporally-aggregated results.

2.2.2 Determining Displacements from Phase-Based Measurements

Phase-based determination of ice velocity is much more precise than offset tracking techniques, and is resolution-independent. In return, it implies the consideration of a series of perturbation factors, especially in ice-shelves studies, due to meteorological conditions, tidal effects, or geometric and important temporal decorrelations.

Traditionally, phase-based techniques were focused on the measurements of *across-track* displacements, through the Differential SAR Interferometry - DInSAR and derived techniques (Small BAseline Subset - SBAS, and Persistent Scatterer Interferometry - PSI), but recent developments based on spectral diversity allows the determination of *along-track* displacements (Multiple Aperture Interferometry, and Burst Overlapping Interferometry).

In this large section, across- and along-track techniques are developed. We investigate the potential issues, and how to mitigate them. The specific case of Sentinel-1, its pros and cons, are discussed throughout the section.

2.2.2.1 Ice Displacements from Differential SAR Interferometry

The topographic phase removal necessary in DInSAR studies were performed using TanDEM-X's DEM. The Alfred-Wegener-Institut Helmholtz-Zentrum für Polar-und Meeresforschung - AWI produced highly precised DEMs. In 2013, the AWI built DEM over the RBIS (Fig. 2.37). In 2016, an update covering the entire Dronning Maud Land was computed (Fig. 2.38). In order to do that, AWI used Tandem-X images. TanDEM-X is the name of the mission implying two TerraSAR twin satellites working in a bi-static configuration. The advantage is that the DEM extraction is not affected by many artifacts or unwanted terms present in repeat-pass interferograms (mainly atmosphere and displacements) and to focus only on topographic elements. Thus, TanDEM-X is the preferable choice when the area of interest is not covered by SRTM products or when we need a recent DEM. Produced DEMs can have a resolution below 30 meters per pixel. Nevertheless, TerraSAR images have a rather small footprint. The RBIS topography is thus produced by mosaicking multiple acquisitions.

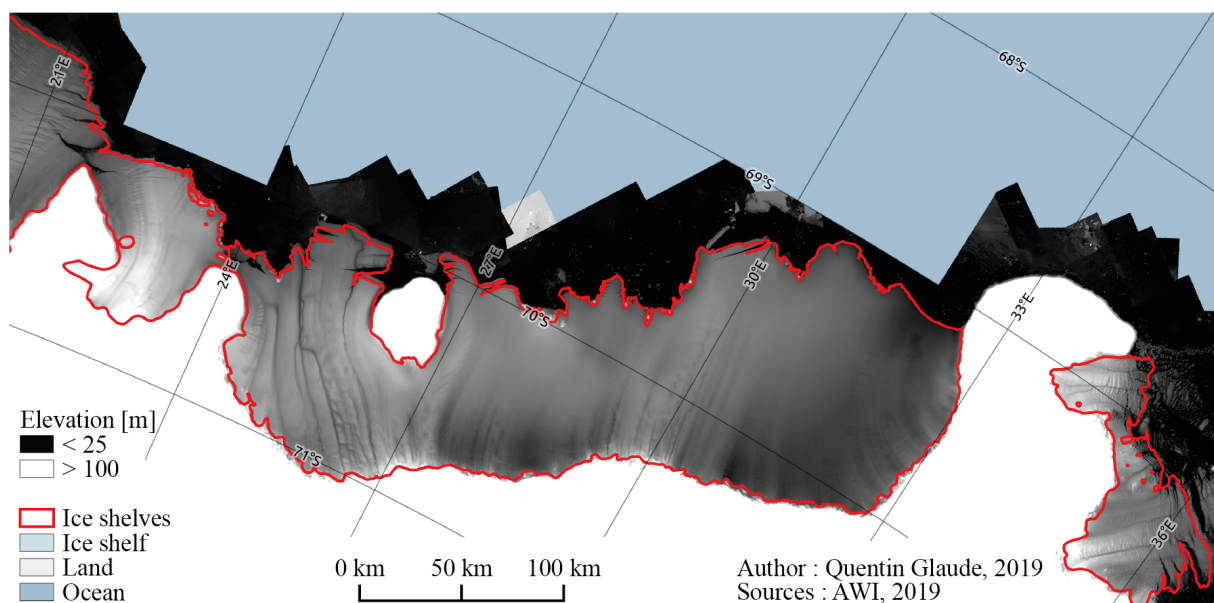


Figure 2.37: RBIS DEM extracted from TanDEM-X data.

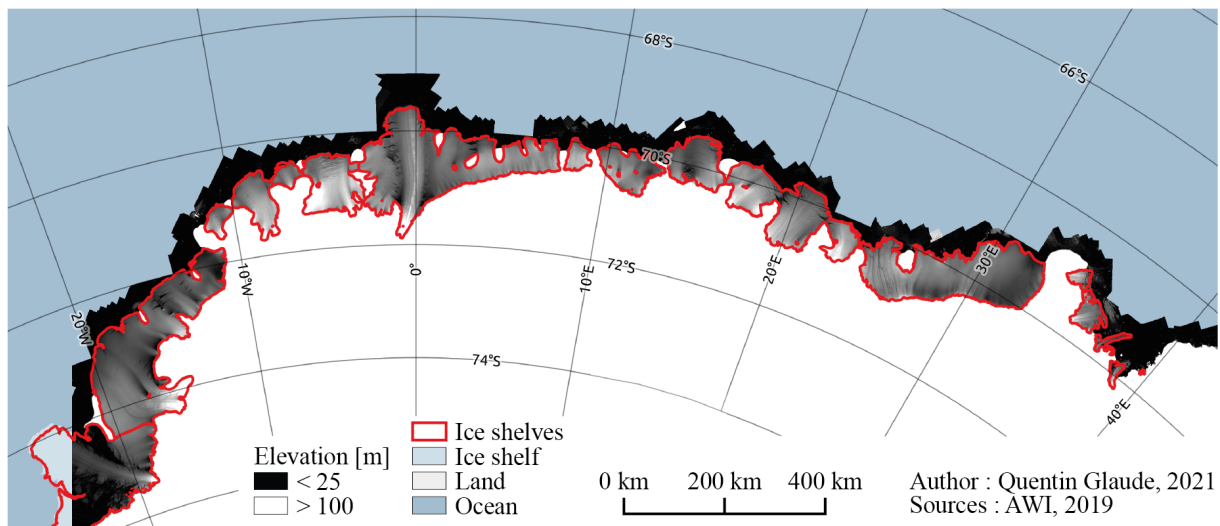


Figure 2.38: DML DEM extracted from TanDEM-X data.

For InSAR studies over the RBIS, we mainly used Extended Wide-swath - EW Sentinel-1 images. The entire RBIS is visible on a single scene on the relative orbit #88 on one single pair. Using two SAR images with a temporal baseline of 12 days, we found a perpendicular baseline is 53.39 m (resulting in a height ambiguity of 269m), we can produce an interferogram and remove the topographic phase component from the TanDEM-X DEM (Fig. 2.39). The interferogram is overall good quality excepted in the fast-moving areas where strong coherence loss is present, or over the Derwael ice rise, where the returned signal is naturally low.

DInSAR Mass Processing Using the SentiNel Application Platform and Bash Scripting

Thanks to the Sentinel-1 free-access policies, an important amount of satellites data became available. Hence, it is of great interest to automatize the complete process of Differential SAR Interferometry. In addition, increasing the mass processing allows to limit human-related errors.

During the thesis, we developed a rather simple mass processing codes that uses free access data and open access codes (SentiNel Application Platform and snaphu). Given a set of SAR images, the script will take consecutive pairs and apply the flowchart displayed at Fig. 2.40.

The process begins by extracting the bursts-of-interest of the two images. Then, we update the orbit information by downloading the precise orbits computed by the Copernicus Precise Orbit Determination - CPOD Service. These orbits are necessary for the next step: the DEM-Assisted coregistration. We can create our interferogram from our coregistered SAR pair. Then, we remove the orbital and topographic phase components from the external DEM developed earlier. The interferometric phase is filtered and reduced using the common Goldstein Phase Filtering algorithm and a multilooking operation. All bursts can now be merged. The phase information is unwrapped using the snaphu software. Finally, the results are converted into a metric line-of-sight displacement map.

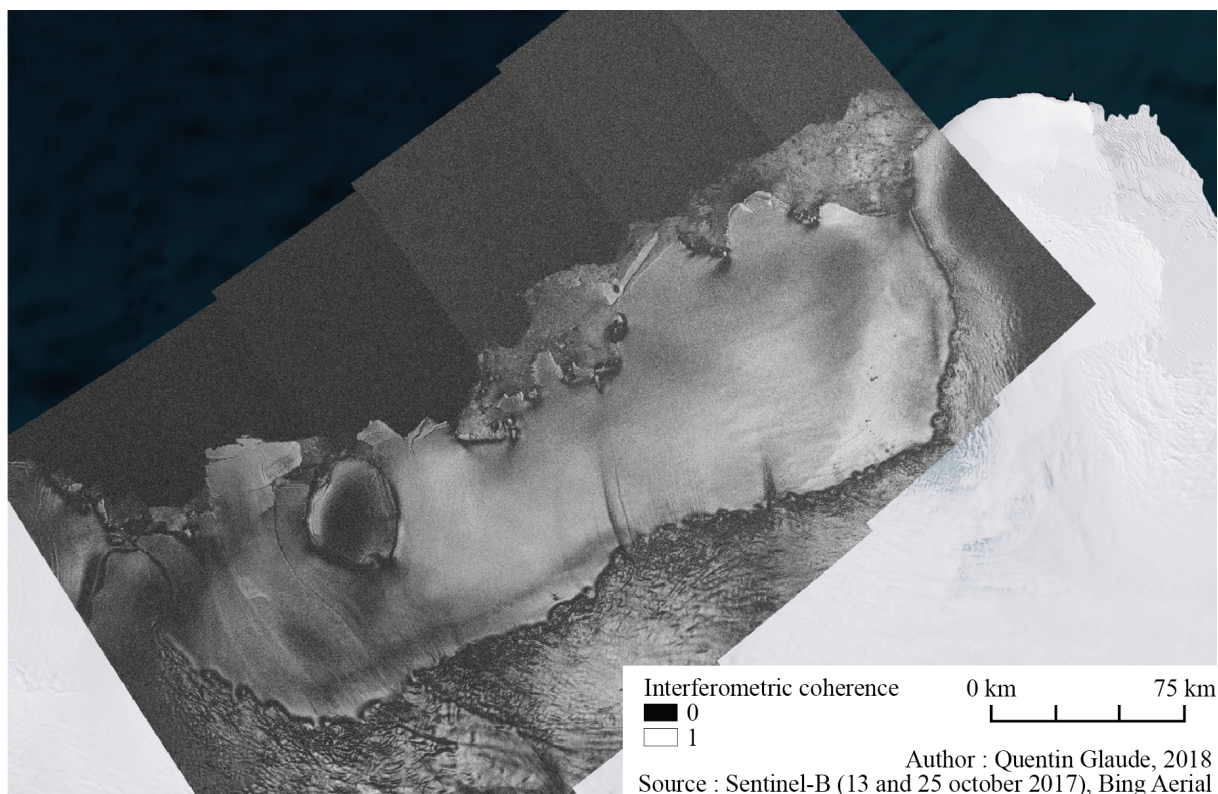
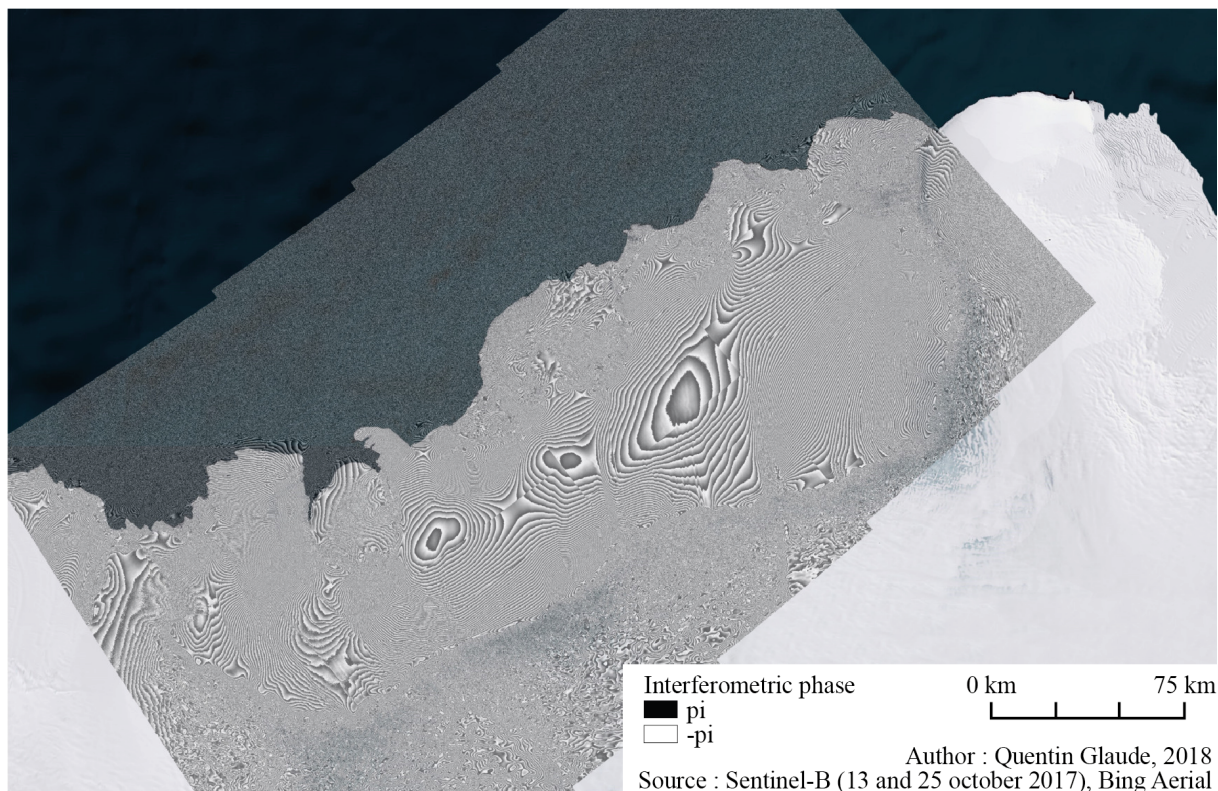


Figure 2.39: Interferogram and coherence maps of a 12-day Sentinel-1 pair in Extended Wideswath mode (track 88). In the Western part of the RBIS, surface velocity of around 300 meters per year is observed, reducing the interferometric coherence. The large round-shaped dark element is the Derwael ice rise. A low signal is recorded in that place, compromising interferometric studies.

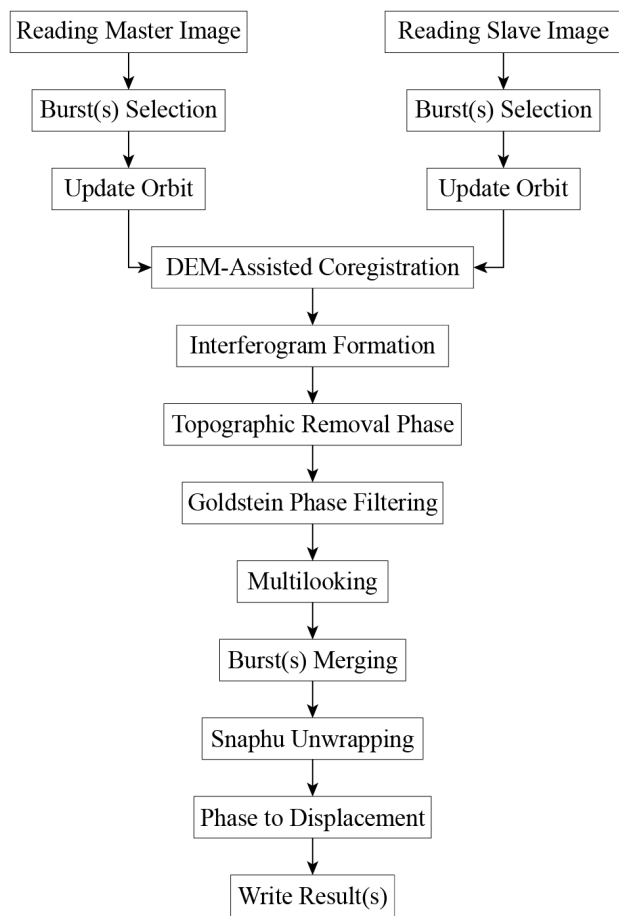


Figure 2.40: Sentinel-1 DInSAR mass processing flowchart.

Temporal Decorrelation Analysis and New Acquisition Scheme over the Roi Baudouin Ice Shelf

In Antarctica, temporal decorrelation is the main threat to DInSAR studies. Areas of interest are moving fast, inducing high fringe rates, and surface changes are occurring rapidly, due to meteorological processes (precipitations, snow deposits, or melt events), or due to snow-to-firn densification processes. Meteorological influence links the ability to use SAR with seasonal effects. We observe better interferometric measurements during austral winters. Due to the rapid temporal decorrelation, it is difficult to link SAR pairs with a large temporal baseline (Fig. 2.41), limiting the use of SBAS or PSI methods.

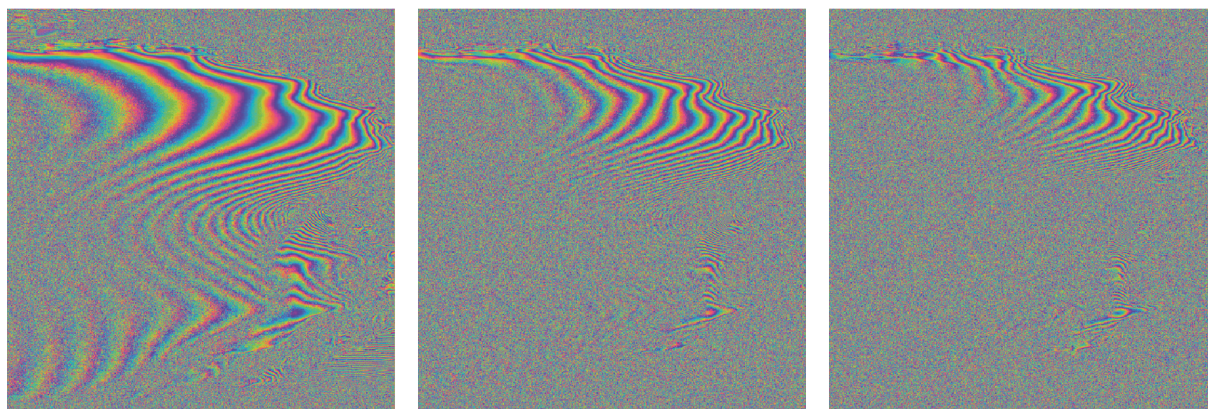


Figure 2.41: Examples of coherence loss due to an increase of the temporal baseline (from left to right: 12, 24, and 36-day interferograms).

In this context, we need temporal baselines as short as possible because of coherence loss. Referencing the Sentinel-1 High-Level Operation Plan, we submitted a request to ESA in 2018 to locally decrease the repeat-pass from 12 to 6 days, using both Sentinel-1 A and B. After a feasibility study performed by ESA Copernicus planners, the Roi Baudouin Ice Shelf study area has been acquired at a 6-day repeat pass basis since the 27th of Aug 2018. These recent 6-day interferograms enable us to sample the displacement at a double rate. It means that the fringe rates are expected to be lower with higher coherence. Also, artifacts related to the temporal baseline are reduced too. The benefit of using a temporal baseline of 6 days instead of 12 is enormous (Fig. 2.42, top). This is particularly the case for grounding zone where high fringe rates related to tides are present (Fig. 2.42, bottom). Overall, the coherence distribution is drastically better (Fig. 2.43).

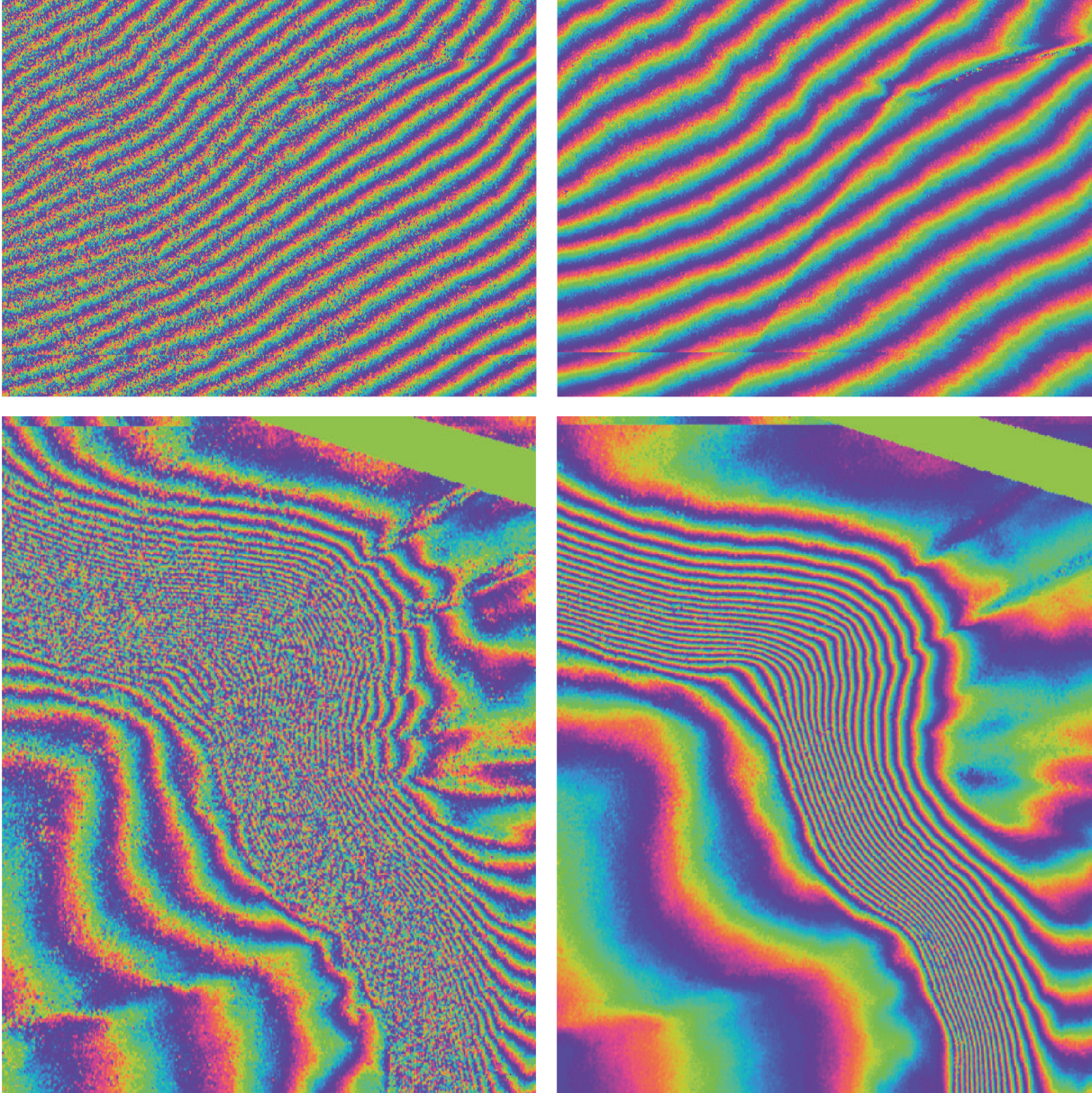


Figure 2.42: Difference in fringe rates between a 12-day interferogram (left) and a 6-day interferogram (right).

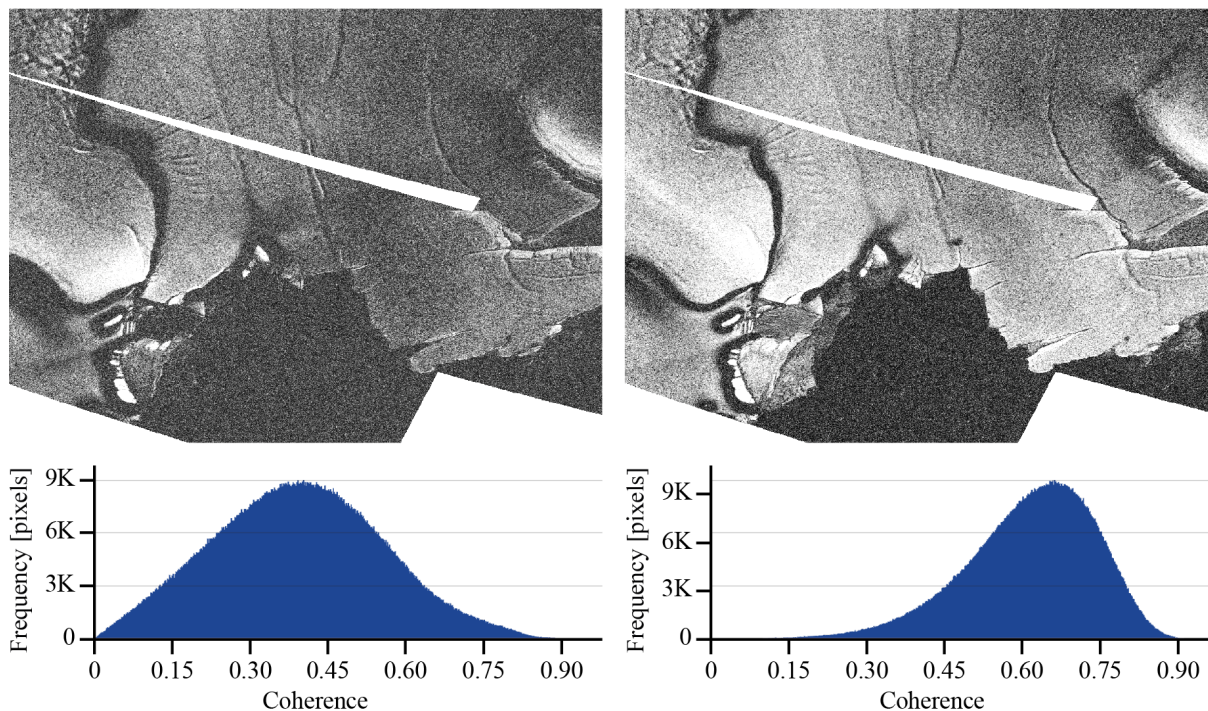


Figure 2.43: Difference in coherence between a 12-day interferogram (left, mean coherence = 0.39) and a 6-day interferogram (right, mean coherence = 0.61).

2.2.2.2 The Importance of Tracking Coherence in Ice Shelves Studies


On top of the presented issues in interferometric studies over ice shelves, the high displacements observed in Antarctica induce local geometric misregistrations. These local misregistrations strongly decrease the coherence of the interferometric signal, and are the major limitations of DInSAR in ice-shelves studies. As an example, the continent-wide interferometric mapping of the AIS by Mouginot, Rignot, and Scheuchl (2019) is purposely omitting a large portion of Antarctic ice shelves for this reason.

We already presented coherence tracking in section 2.2.1.3, where we focused on the estimation of bidimensional displacements from maximization of the coherence criteria. The estimated displacements can also be used in order to correct interferograms from local misregistrations, and drastically increase the coherence.

In an article to be submitted in *Remote Sensing* (ISSN: 2072-4292, Impact Factor: 4.848), we present the fundamentals of coherence tracking, with figures and important results. In addition, we present a statistical analysis of coherence gain through the coherence tracking technique, and why tracking coherence is fundamental in ice-shelves studies. The adaptation of coherence tracking to the TOPSAR acquisition mode is also presented. Where we thought SAR interferometry was not feasible, coherence tracking can, to a certain point, recover displacements-induced coherence loss.

Article

The Importance of Tracking Coherence for Interferometric Studies over Ice Shelves - Case study over the Roi Baudouin Ice Shelf, East Antarctica

Quentin Glaude ^{1,2,†,*}, Dominique Derauw  ^{2,3,†}, Christian Barbier ², Frank Pattyn ¹, and Anne Orban ²

¹ Laboratoire de Glaciologie, Université Libre de Bruxelles, Bruxelles, Belgium

² Centre Spatial de Liège, Université de Liège, Angleur, Belgium

³ Laboratorio de Estudio y Seguimiento de Volcanes Activos (LESVA), IIPG - Universidad Nacional de Rio Negro – CONICET, General Roca, Argentina

* Correspondence: quentin.glaude@uliege.be

† These authors contributed equally to this work.

Version January 31, 2022 submitted to Remote Sens.

Abstract: Synthetic Aperture Radar (SAR) allows the measurement of surface displacements based on two SAR images taken at different times. In particular, interferometry makes it possible to measure very precise movements in the line-of-sight direction of the sensor, on the basis of differential phase measurements. However, large displacements induce important decorrelations, compromising the applicability of SAR Interferometry. This problem is generally overcome using incoherent or coherent speckle tracking techniques, although the results are one order-of-magnitude less precise. In Antarctica, the problem of displacement-induced decorrelations is common, especially over glaciers and ice shelves, where displacements between two dates can exceed the image resolution. In consequence, a vast majority of ice-shelves studies rely on speckle tracking techniques to estimate ice-flow fields. The use of the more precise SAR Interferometry technique over ice shelves requires correcting these displacements. This is performed by locally tracking the 2D-displacements of the moving scatterers, using coherence maximization criterion. As a result, locally tracking coherence makes SAR Interferometry viable where surface elements move rapidly, but also to obtain an estimate of the bidimensional displacements. Nevertheless, the specific use of the Sentinel-1 acquisition mode, TOPSAR, introduces an azimuthal phase bias to be removed. In this study, we present the benefits of tracking coherence over ice shelves. The results are presented over the Roi Baudouin Ice Shelf, Dronning Maud Land, East Antarctica. Overall, coherence tracking allows a drastic improvement of interferometric coherence over fast-moving areas, from 0.22 to 0.52 in fast-moving areas.

Keywords: Coherence Tracking; Interferometry; Sentinel-1; Ice Shelves, TOPSAR

1. Introduction

The Antarctic Ice Sheet (AIS) lost 1365 Gt of ice between 1992 and 2011. Together with the Greenland Ice Sheet, this represents a total of 1.1 cm of Sea-Level Rise (SLR) [1]. The ice losses in the Antarctic have increased by a factor of 5 in 25 years [2] and there is evidence of long-term Antarctic decline [3]. Future projections of SLR from Antarctica are rather uncertain, and ranges from -0.75 to +1.6 meters depending on Representative Concentration Pathway (RCP) scenarios [4]. In particular, in scenario RCP8.5, it is not excluded that Antarctica alone contributes to one-meter SLR in 2100 [5].

Ice shelves are the floating extensions of the AIS, at the interface between the ocean, the atmosphere, and the grounded ice sheet [6,7]. Ice shelves gain mass from the continental ice streams and snow accumulations, and lose their ice mass by calving, and basal and surface melting [8]. In

30 some cases, ice shelves can gain mass from basal refreezing. Ice shelves are crucial gatekeepers of the
31 AIS because they restrain ice flow as they are often laterally constrained by embayments or locally
32 grounded on rigid obstacles in the bathymetry [9,10]. Thinning of Antarctic ice shelves and the
33 corresponding decrease in the restraint experienced by inland ice flow [11,12] are recognized as major
34 drivers of current Antarctic ice loss [3]. Ice-shelf thinning causes an instantaneous acceleration and a
35 retreat of the grounding line, i.e. the limit between the grounded ice sheet and the floating ice-shelf
36 [13], an increase in grounded ice loss hence a sea-level rise [14].

37 Point-based velocity measurements are unrepresentative of the reality of the AIS and are
38 time-consuming to produce. In that sense, remote sensing appeared as a revolution for geophysical
39 research [15]. Satellite remote sensing is an essential tool in monitoring ice-shelf health by deriving ice
40 flow fields, strain rates, and tracking grounding line positions over time, among others. In that domain,
41 Synthetic Aperture Radar (SAR) remote sensing became the first-choice solution for the computation
42 of ice velocity, thanks to its day-and-night and cloud-free capabilities.

43 Based on SAR images, several techniques are available to infer local displacements between
44 different acquisition dates, generally distinguished between offset- and phased-based methods.
45 Offset-based techniques are based on image matching algorithms. The resulting coarse determination
46 of range and azimuth offsets employs incoherent or coherent complex correlation between small tiles
47 of two coregistered images. Phase-based techniques are based on the idea that if a range displacement
48 occurred between two dates, a phase shift will be visible in an interferogram. Range displacements
49 from phase-based measurements belong to the branch of Differential SAR Interferometry (DInSAR).
50 DInSAR is able to determine displacements along to the line of sight of the sensor with an accuracy
51 of a fraction of the used radar wavelength [16], and has already been demonstrated for the study
52 of ice motion and grounding line location in Antarctica, with the Rutford ice stream as an example
53 [17]. In order to obtain two- or three-dimensional displacement components, different observation
54 orbits and incidence angles must be combined to solve for the three-dimensional problem [18,19]. This
55 required disparity of orbits and viewing geometries is far from being granted everywhere on Earth. In
56 particular, on many Antarctic areas, only a limited number of orbits are available.

57 DInSAR has the advantage of being more precise, but the rapid changes over the AIS induce an
58 important temporal decorrelation due to the relatively fast displacements of the ice streams, or due to
59 meteorological events such as snow precipitations or melting events [20,21]. This problem is common
60 in Antarctica, where the magnitude of the measured displacements introduces a decorrelation such that
61 the combination of the wavefronts emitted at two different dates does not provide a coherent signal.
62 This temporal decorrelation is particularly pronounced in the coastal areas of Antarctica, where the ice
63 is moving faster than on the inner part, meaning that the scatterers have undergone a displacement
64 sometimes greater than the spatial resolution of the sensor. In consequence, offset tracking is generally
65 adopted for practical reasons, and the majority of SAR-based ice motion techniques are using offset
66 tracking techniques [22]. In addition, while DInSAR, if applicable, allows getting a high precision
67 estimate of the range velocity component, offset tracking allows us to get a first estimate of the azimuth
68 component of surface velocity vector too.

69 Offset- and phased-based techniques allowed the determination of the continental-wide mapping
70 of the mean Antarctic velocity field [23] as well as establishing grounding-line products [24], which
71 form the base for all major ice-sheet model predictions [25]. [24] provides 15 years of grounding
72 line mapping using double differential SAR interferometry using ERS, RADARSAT, and ALOS data
73 from 1994 to 2009. Both products are also essential in determining the current state of the ice sheet
74 by determining its basin-wise mass balance through the input-output method, in combination with
75 atmospheric modeling [3].

76 Similarly, in 2012, [20] computed a global surface velocity mapping of Antarctica using SAR
77 data, using ASAR, ERS-1 and -2, ALOS, and both RADARSAT satellites. In 2017, [26] updated the
78 annual velocity maps of Antarctica by including optical (Landsat-8) on top of SAR data (Sentinel-1 and
79 RADARSAT-2). While SAR images produce better results, the amount of optical data greatly helps

80 in the determination of surface displacements. RADARSAT is found particularly useful thanks to its
81 left-looking acquisition geometry, allowing observations closer to the South Pole.

82 In 2019, [27] went a step further by drastically improving the accuracy of Antarctic Velocity fields
83 by providing a continent-wide estimate of the annual velocity from DInSAR. Nevertheless, the velocity
84 determination is limited in ice shelves areas or along important ice streams, where the high temporal
85 decorrelation does not allow the interferometric measurements. When this local coherence loss is
86 principally due to the displacement itself, one can adapt coherent speckle tracking in order to track
87 spatial events optimizing local coherence [28]. However, applying coherence tracking to Sentinel-1
88 TOPSAR acquisition requires some adaptations due to the phase ramp introduced by this varying
89 Doppler centroid acquisition mode. In non-stationary scenarios, phase ramps do not coincide anymore
90 in areas of relative displacement leading to some local phase ramp superimposed to the InSAR fringe
91 pattern. Therefore, for proper coherence tracking process, both the master and the slave images must
92 be cleaned up from their respective phase ramp after the coregistration process.

93 The open-data policy of the Copernicus program enables us to have free access to Sentinel-1
94 data every 6-12 days. This with the high resolution of Sentinel-1 products brings a paradigm shift
95 in interferometry: the opportunity to monitor and address rapid and local changes. The number of
96 wide swath acquisitions of Antarctica and Greenland is important, with a high revisit rate. It allows
97 the computation of frequent and precise velocity fields [29]. In addition, Sentinel-1 has a long-term
98 commitment, and the new Sentinel-1 C and D to be launched in the next years.

99 In this article, we present the statistical gain of coherence tracking for Differential SAR
100 Interferometry over fast-moving areas, such as Antarctic ice shelves. We then express how to adapt the
101 technique to the TOPSAR acquisition mode of Sentinel-1. The results focus on displacements over the
102 Roi Baudouin Ice Shelf, Dronning Maud Land (East Antarctica). These results are then be compared
103 qualitatively and quantitatively with traditional interferometric approaches.

104 2. Method

105 2.1. Coherence Maximization

106 Coherence is a measure of the ability of two waves or wavefronts to stay in phase spatially and/or
107 temporally. Therefore, it indicates the ability to get an interferometric fringe pattern stable in space
108 and/or in time.

109 In SAR, the internal oscillator of the system is keeping a highly stable time base granting a
110 coherence time much larger than the requested time for one acquisition. This allows performing
111 aperture synthesis, keeping time coherence between chirps, and allowing to reconstruct a synthetic
112 holographic wave-front to be focused at scene level [30]. Once focused, the intrinsic scene rugosity
113 at wavelength size will lead to the coherent addition of the contribution of many independent areas
114 within the resolution cell. This basic interferometric superposition is the origin of the speckle observed
115 in SAR imagery, like in laser speckle patterns, radar astronomy, or acoustic imagery [31].

116 Therefore, considering the interference of two focused images taken exactly in the same
117 geometrical conditions and the absence of any scene change would lead to a perfectly coherent
118 wavefront with the same speckle reconstruction process. Consequently, speckle is a deterministic
119 process. In such ideal conditions, the waves coming from a given scatterer considered as a source point
120 stay perfectly in phase in one and the other acquisition.

121 If we now consider the two acquisitions made from slightly different orbits, this point source can
122 be considered as two perfectly coherent point sources, like in the Lloyds mirror experiment but with
123 an additional constant phase term for the second source, leading to a stable fringe pattern in time and
124 space. The additional phase term is due to the optical path differences between the scatterer relative
125 positions in one and the other acquisition.

126 However, a scene is not made of a single scatterer, therefore, even if considering a perfectly
127 stable scene observed from two slightly different positions, the interference process will be issued

128 from pairs of scatterers whose relative optical path difference is not constant but varies due to the
 129 variable observation geometry within the scene element. Considering a perfectly uniform distribution
 130 of scatterers on a plane surface, if this relative optical path difference varies by more than half a
 131 wavelength within a resolution cell, every phase difference in the interval $[0; 2\pi]$ will be equiprobable
 132 in the interferometric process leading to a decorrelated signal from one to the other resolution cell.
 133 This situation is represented in Figure 1. From this schematic representation, one can deduce the limit
 134 angle between both acquisitions leading to this complete *geometrical* decorrelation of signals, and from
 135 there derive the so-called limit baseline [32].

136 If considering relief and rugosity, this purely geometrical decorrelation limit can be reached before
 137 reaching the limit baseline.

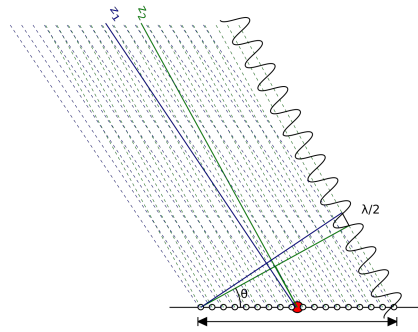


Figure 1. Schematic representation of total geometrical decorrelation

138 With a shorter baseline, one keeps an average phase, even if noisy, linked to the average optical
 139 path difference for a considered resolution cell. The noise level is linked to the degree of coherence
 140 between both signals.

141 If we now consider a non perfectly stable scene with time, in addition to the geometrical
 142 decorrelation, one has to deal with the temporal one. Every relative displacement of scatterers or
 143 back-scattering response in amplitude or phase of scatterers within the resolution cell will participate
 144 in the coherence loss.

145 The complex degree of coherence between two signals $s_1(t)$ and $s_2(t)$ is defined by [33]:

$$\gamma(s_1, s_2) = \frac{\mathbb{E}\{s_1 \cdot s_2^*\}}{\sqrt{\mathbb{E}|s_1|^2 \cdot \mathbb{E}|s_2|^2}} \quad (1)$$

146 The amplitude of the complex degree of coherence is the coherence in itself and its phase is the
 147 interferometric phase issued from the interferometric superposition of both signals. This degree of
 148 coherence is measured as an expected value in time. Therefore in SAR interferometry, we compute this
 149 expectation value locally on a moving window of a given size in range and azimuth which are nothing
 150 else than time coordinates; range being also known as the fast time coordinate and azimuth the slow
 151 time coordinate [34].

$$\hat{\gamma}(s_1(x, y), s_2(x, y)) = \frac{\left| \sum_{(x, y) \in n} s_1(x, y) \cdot s_2^*(x, y) \right|}{\sqrt{\sum_{(x, y) \in n} |s_1(x, y)|^2 \cdot \sum_{(x, y) \in n} |s_2(x, y)|^2}} \quad (2)$$

152 Where (x, y) is a given location in pixel coordinates, and n is a neighborhood around it.

153 In addition to time and geometrical coherence losses, one can also face processing losses. This
 154 expression of coherence, as also the schematic representation of Figure 1 intrinsically assumes a

155 perfect coregistration of a pair of corresponding scatterers in one and the other acquisition. Any
 156 misregistration of a SAR image pair will induce additional, but apparent, coherence losses. The reason
 157 why local coherence optimization is often used as a fine coregistration process in SAR interferometry.

158 In stripmap SAR interferometry, coregistration is generally a three-step process; the first step is
 159 based on orbitography to coarsely locate the common area of interest. The second step is generally
 160 performed identifying a grid of anchor points correlating master and slave multi-looked intensity
 161 sub-windows. Fine registration generally uses the same algorithmic but cutting sub-windows within
 162 full resolution complex images and using local coherence measurement to register candidates anchor
 163 points in one and the other image. This grid of corresponding anchor points is then used to determine
 164 the transform or the mapping to be applied to the slave image to be superimposable to the master one
 165 within a sub-pixel accuracy. In the case of Sentinel-1, the 3D 5-centimeters orbitography accuracy and
 166 digital elevation models allow getting the requested transform directly from geometrical calculation
 167 [35]. Ultra-fine accuracy up to one-thousandth of a pixel can even be reached using additionally
 168 Enhanced Spectral Diversity [36].

169 2.2. Coherence Tracking

170 Coherence tracking is coherent speckle tracking based on the idea that, locally, the scatterers on
 171 the surface of the ground can move from date to date up to decorrelating the interferometric signal, as
 172 recalled in [22]. This technique proved particularly effective in glaciology where displacements over
 173 ice shelves can easily exceed the image resolution [37].

174 If two SAR images are perfectly coregistered, the same well-defined image element corresponds
 175 to the same well-defined geographical area in these two images. Working in an Eulerian space, any
 176 surface displacement between two dates will result in a movement of the scatterers according to our
 177 reference system. In practice, excessive displacements move the scatterers from one pixel coordinate in
 178 the first image to another image coordinate in the second image, inducing an incoherent interferometric
 179 signal. This displacement-induced coherence loss is the major limitation of DInSAR in ice-shelves
 180 studies.

181 Coherence tracking aims to recover the displacements made by our scatterers. This displacement
 182 is estimated by looking within a given window for a certain pixel translation which would maximize
 183 the quality of the interferometric phase, through the coherence value:

$$(i, j) = \arg \max_{(i, j)} \{ \hat{\gamma}(s_1(x, y), s_2(x + i, y + j)) \} \quad (3)$$

184 Where i and j correspond to a translation included in a neighborhood N around a location
 185 (x, y) , while $\hat{\gamma}$ has been defined in Eq. 2. This search is performed either for each pixel of the
 186 image, or according to a particular grid, depending on the computational capacities. While providing
 187 an estimation of the bidimensional displacements from coherence maximization criteria, coherence
 188 tracking also provide an improved interferometric signal.

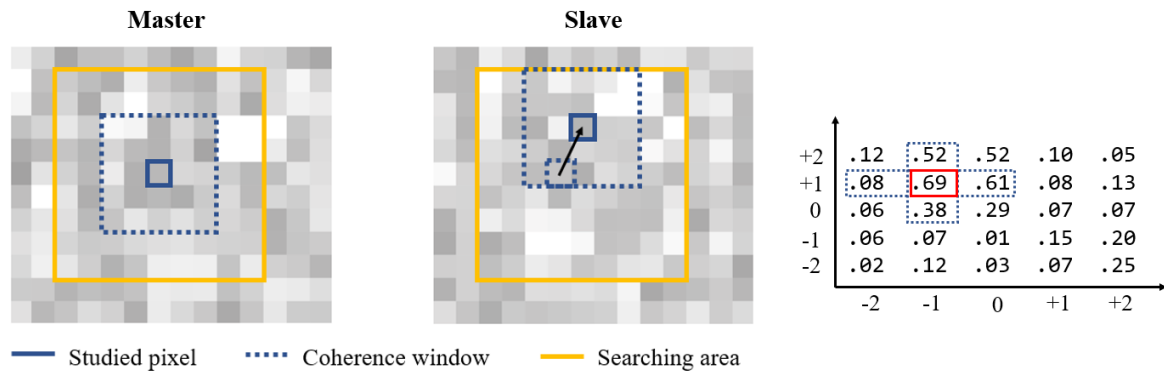


Figure 2. Representation of an offset tracking algorithm. For each location in the master image, a searching area is defined in the slave image. In this area, local coherence is computed for each potential candidate, giving a matrix of coherence values. To each element of the matrix corresponds a given offset. The maximum coherence of the matrix determine the 2D displacement.

189 At the end of the process, coherence tracking provides us with four products:

- 190
- 191
- 192
- 193
- The tracked interferogram, produced after finding the scatterers on the ground $[-\pi, +\pi]$;
 - The tracked coherence $[0,1]$.
 - The translation in the azimuthal direction, expressed either in picture elements or in meters.
 - The translation in the range direction, expressed either in picture elements or in meters.

194 Coherence tracking, therefore, has the advantage of being able to roughly determine a
 195 two-dimensional displacement via translations in azimuth/range, while recovering the interferometric
 196 signal, optimizing local coherence, for very high precision displacement measurements. This idea of
 197 coherence tracking was developed in [28] in the study of the Shirase glacier ($70^{\circ}55'S$ $38^{\circ}45'E$), where
 198 ice flow velocity of 2000 m.a^{-1} was observed.

199 Subpixel azimuth and range displacements can be estimated using supersampling techniques,
 200 such as the chirp-z transform, or by probabilistic approaches. In the latter case, the most probable
 201 position is determined from a probability distribution function, whose center is at the exact position of
 202 the scatterers' displacement, and decreases with its distance. We assumed here is that this probability
 203 density function approximates a two-dimensional Gaussian, fitted from the best 2D-shift candidate,
 204 and its close neighbors. Once the distribution has been adjusted, we determine its peak and thus the
 205 sub-pixel translation.

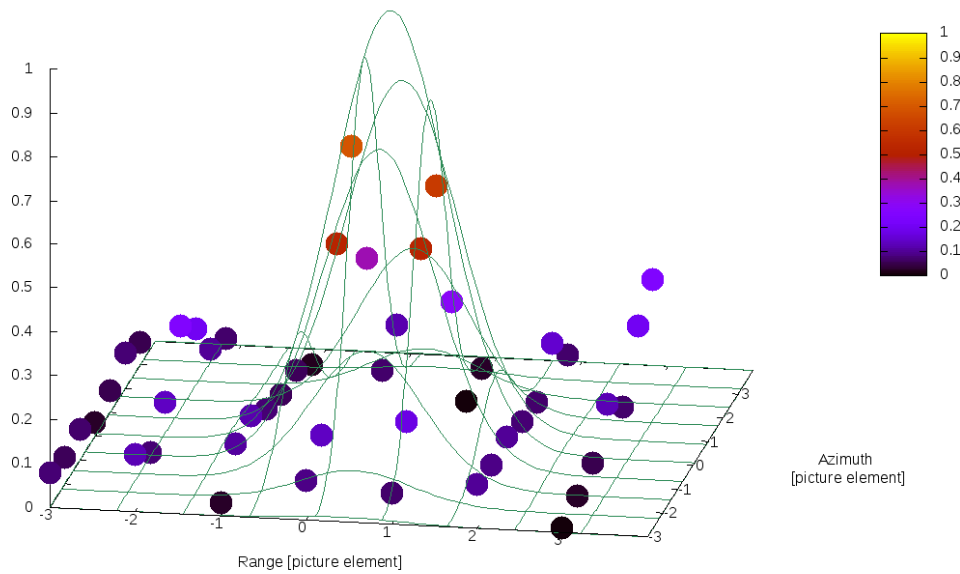


Figure 3. Sub-pixel shift estimation using 2D Gaussian 5-points fitting. In this figure, the coherence (z-axis) is computed for each shift in a search window around the (x,y) location in the slave image. The shift that maximizes the coherence value is determined. A 2D Gaussian fitting is performed around this shift, with its peak determining the best sub-pixel estimate of the range and azimuth shift. Using pixel spacing and acquisition time interval, these shifts can be translated into 2D velocity.

206 2.3. TOPSAR Case

207 2.3.1. Coregistration

208 In order to fulfill a systematic observation scheme over the Earth at high resolution and with a low
 209 revisit time, Sentinel-1 A and B use a specific acquisition mode, which brings some subtleties in terms
 210 of signal that must be taken into account. The acquisition mode, Terrain Observation by Progressive
 211 Scans (TOPSAR), induces an electronically beam steering, from back to front during the acquisition,
 212 and allows to save time and produce several parallel swaths and ultimately an improvement in spatial
 213 coverage. Depending on the rotation speed of the antenna, Sentinel-1 can produce 3 or 5 parallel
 214 swaths. These modes are called Interferometric Wide (IW) and Extra Wide swath (EW), respectively,
 215 with a spatial coverage of 250 and 400 kilometers. One of the consequences of beam steering is a
 216 reduction in azimuthal sampling and ultimately a loss of azimuthal spatial resolution.

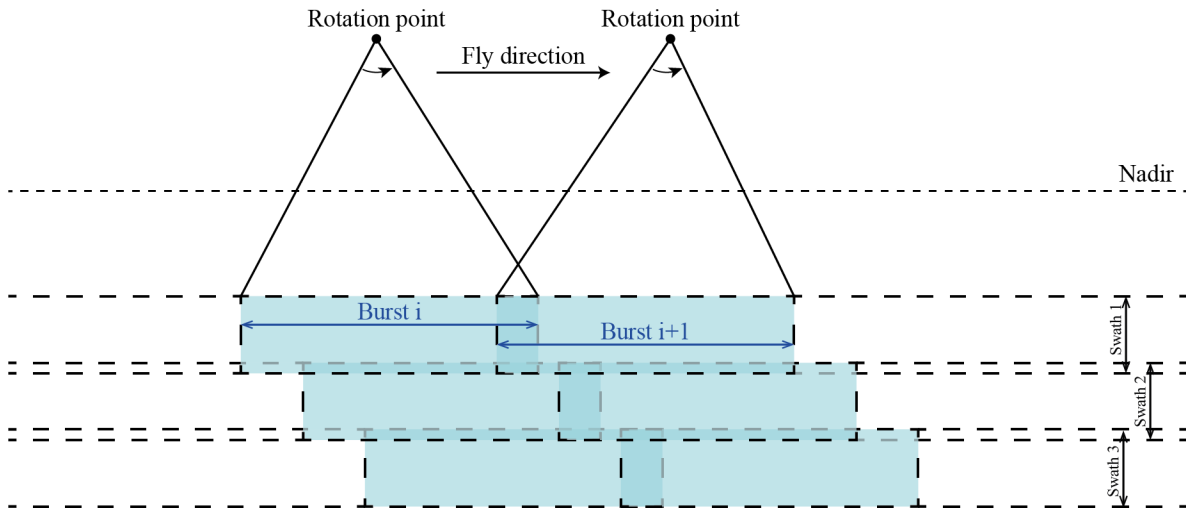


Figure 4. Acquisition geometry of a TOPSAR image. In TOPSAR mode, the satellite rapidly steers its sensors from backward to frontwards in order to switch to different parallel bands and increases its spatial coverage. In consequence, the image is composed of sub-swaths and bursts with overlapping areas. A process of debursting and merge is necessary to reconstruct the entire scene.

217 A second consequence of beam steering is the introduction of an additional azimuthal phase
 218 ramp, which is very large in magnitude and strongly under-sampled. As a result, this phase ramp
 219 must be removed from the slave image to allow a proper resampling without aliasing issues. This
 220 phase ramp is then reintroduced, taking into account the applied transform equation, in order that it
 221 cancels out with the phase ramp present in the master image during the interferometric process. Phase
 222 ramp removal procedure is described in [38]. As coherence tracking involves a reconstruction of the
 223 interferometric signal from shifted pixel positions between master and slave images, the azimuthal
 224 phase ramp induces an important bias in the tracked interferogram.

225 2.3.2. Deramping

226 The deramping is the operation by which the azimuth phase ramp specific to TOPSAR will be
 227 eliminated. By sweeping its sensor from the back to the front, the acquisition mode introduces a
 228 variation of the Centroid Doppler in azimuth (figure 4).

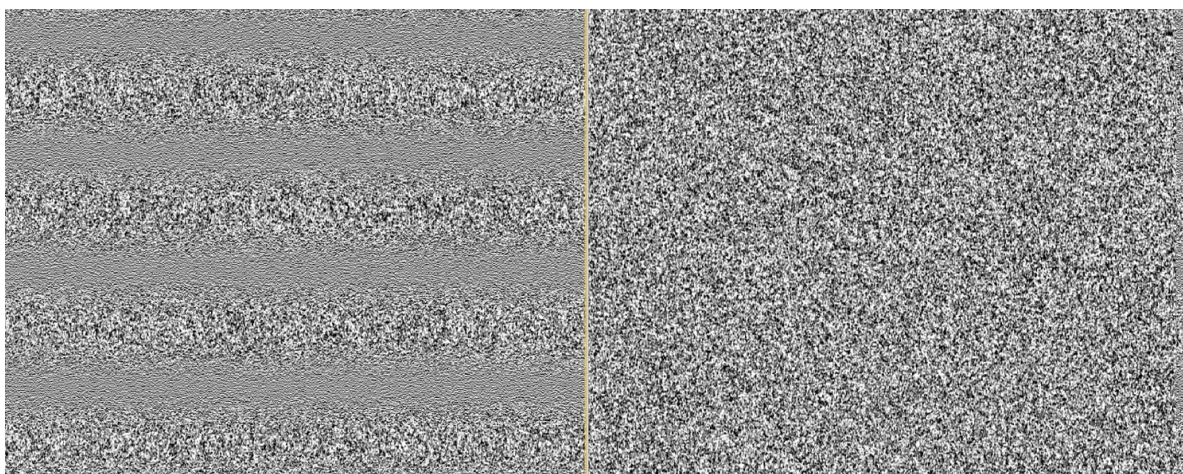


Figure 5. Terrain Observation by Progressive Scans [39] acquisition mode introduces an azimuthal phase ramp in the Single-Look-Complex images. On perfectly coregistered SAR images, this phase ramp cancels out in the interferometric process. However, when local misregistrations are corrected using coherence tracking, this phase ramp does not entirely get removed.

229 This Doppler variation is translated into a fairly large residual azimuthal phase term. This term
 230 depends on the position in azimuth and in range. Taking the terminology of [38], this phase ramp ϕ at
 231 azimuth / range location (η, τ) is given by

$$\phi(\eta, \tau) = \exp(-j \cdot \pi \cdot k_t(\tau) \cdot (\eta - \eta_{ref}(\tau))^2) \quad (4)$$

232 with k_t Doppler centroid rate in the SLC TOPS data and $\eta_{ref}(\tau)$ the azimuthal reference time for a
 233 given range τ . Following the procedure developed by [38], we can remove this phase term and obtain
 234 a deramped SLC images, ready for coherence tracking.

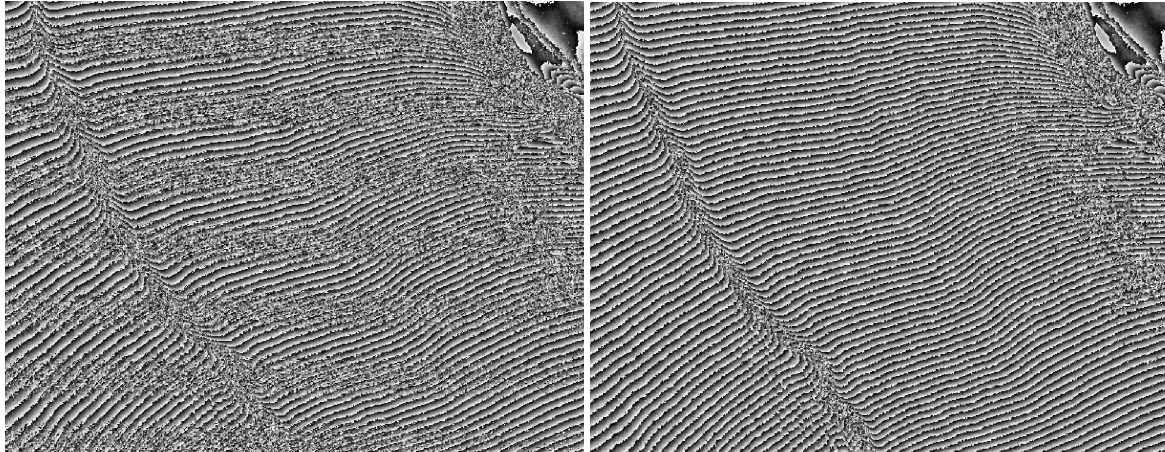


Figure 6. On perfectly coregistered SAR images, this phase ramp cancels out in the interferometric process. However, when large local misregistrations are corrected using coherence tracking, this phase ramp does not entirely get removed. Left: tracked interferogram on ramped data. Right: tracked interferogram on deramped data.

235 Once deramped and coregistered, coherence tracking presented in section 2.2 can be applied. The
 236 complete process leading to coherence tracking products is presented in figure 7.

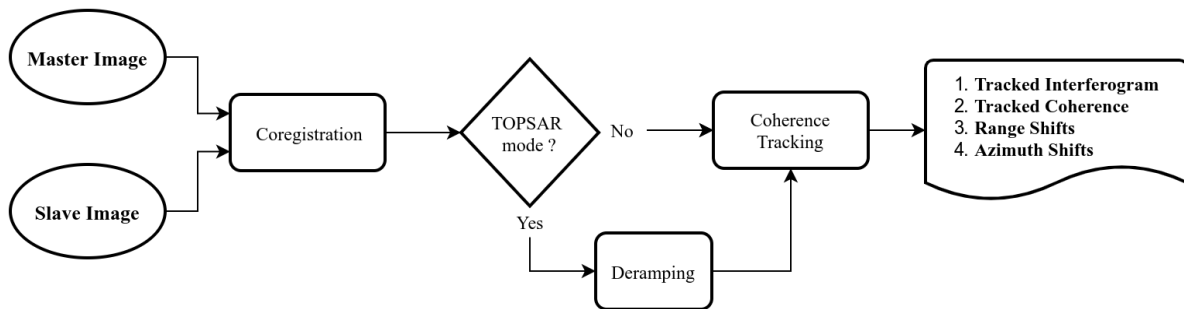


Figure 7. Coherence tracking flowchart. Based on orbital data and a DEM, two SAR images are coregistered. If TOPSAR mode is used, the azimuthal phase bias is removed. Then, coherence tracking is applied using a coherent speckle tracking method, giving four products, namely the tracked interferogram, the tracked coherence, the range shifts and the azimuthal shifts.

237 3. Data

238 3.1. Study Case - Roi Baudouin Ice Shelf

239 We focus the present study on the Roi Baudouin Ice Shelf (RBIS, -24 to -33° East), located in
 240 Dronning Maud Land (DML), East Antarctica (Figure 8). The RBIS is the second-largest ice shelf of

241 Dronning Maud Land. With around 350 kilometers length, the RBIS is covered by a single Sentinel-1
242 acquisition in Extra Wideswath mode.

243 The ice shelf is fed by the Ragnhild glacier, and surface displacements up to 300 m yr^{-1} are
244 recorded on the Western part of the ice shelf. The use of SAR data long revisit rates does not allow the
245 use of displacement measurement on the basis of phase measurements. With Sentinel-1 data 12 days
246 apart, we are here at the limit conditions for the use of DInSAR. Around the main ice stream, we keep
247 an interferometric signal, but the coherence decreases as the ice shelf gains speed.

248 The ice shelf is constrained on its sides by two promontories, and an important structural element,
249 the Derwael Ice Rise. With an elevation of a couple of hundred meters, it acts as an important regulator
250 of ice-flow amplitudes and directions. [40] studied the ice rises and ice rumples in Dronning Maud
251 Land. In the specific case of the Eastern part of the RBIS, a series of ice rumples are present, easily
252 distinguishable in velocity maps. The Derwael Ice Rise, situated on the RBIS, is one of them, and
253 strongly impacts the flow direction of the Western Ragnhild glacier [41]. Dronning Maud Land is
254 particular by its abundance of these features, partly explaining the number of ice shelves surrounding
255 the DML coast. These ice shelves are rather small in comparison to other regions in Antarctica.
256 Nevertheless, they are important regulators of the major part of the AIS. Concerning the RBIS, these
257 topographic structures are located near the calving front of the ice shelf. The high buttressing role of a
258 small but important pinning point was studied in [42].

259 Important katabatic winds over RBIS are responsible for a higher temperature than neighboring
260 ice shelves, especially in the Eastern part of the shelf. This specificity makes RBIS subject to important
261 surface melt periods in austral summer. The winds also change the surface structure, removing the
262 low-density snow deposits and exposing the surface to blue ice areas near the grounding line. This
263 observation is confirmed by looking at the SAR backscattering coefficient. [43] put evidence of the
264 interaction of warm katabatic winds in the productions of surface meltwater.

265 The RBIS is also characterized by its long stability [44]. Since measurements exist, initially via
266 land-survey measurements (during the 1960s) and subsequently by remote sensing and GNSS more
267 recently, ice flows are extremely stable. No significant acceleration or deceleration has been identified
268 overall.

269 These reasons make RBIS an interesting case study, allowing to demonstrate the feasibility of the
270 technique, where the traditional approaches are limited by the speed on the surface.

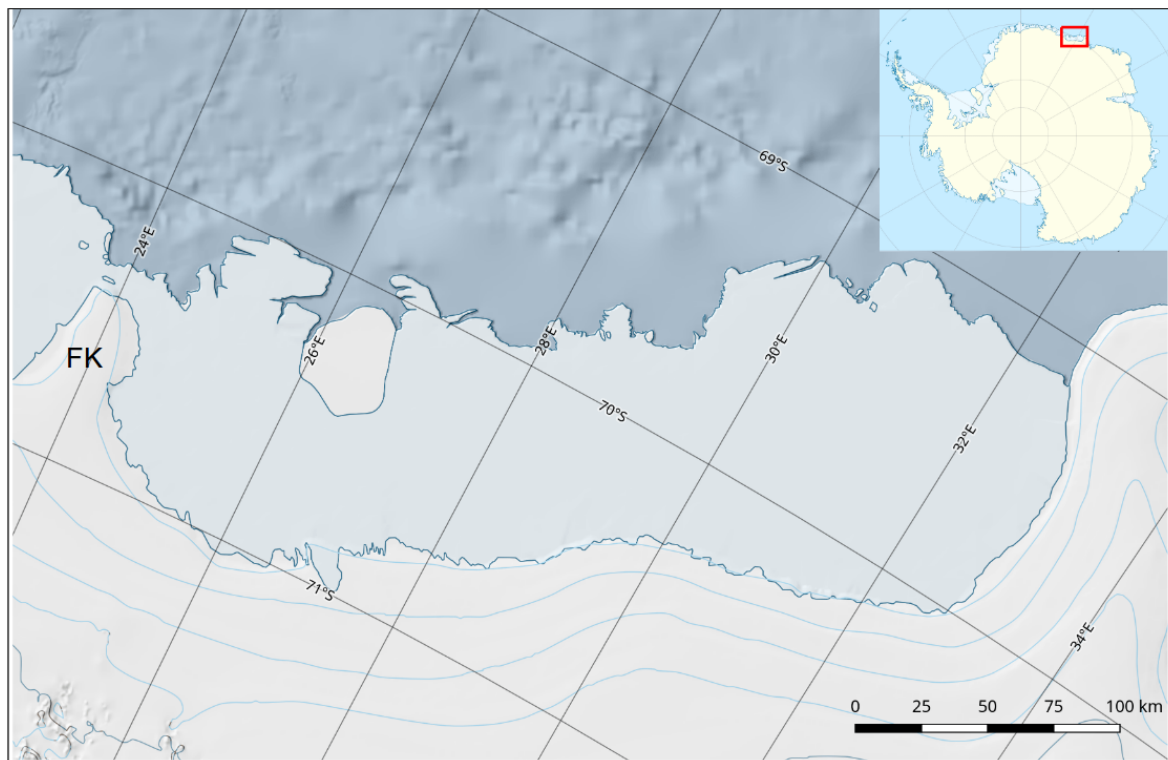


Figure 8. Location of the Roi Baudouin Ice Shelf, Dronning Maud Land, East Antarctica.

271 3.2. Data

272 The coherence tracking results of this study were derived using freely available Sentinel-1 data.
 273 Sentinel-1 is a C-band synthetic aperture radar satellite (wavelength: 5.56 cm), available free-of-charge
 274 and in open access. The main acquisition mode of Sentinel-1 is TOPSAR, having the advantage of
 275 producing images with a very large spatial coverage and therefore a reduction in revisiting time. In
 276 Interferometric Wide Swath (IW) mode, the images have a spatial coverage of 250 km, for a pixel
 277 spacing of 2.3×14.1 m (range \times azimuth). IW is the default mode for Sentinel-1. In polar zones,
 278 however, we will mainly use the Extra Wideswath (EW) mode, having a coverage of 400 km at the cost
 279 of a lower resolution 5.9×19.9 m (range \times azimuth). Unfortunately, the reduced resolution in EW
 280 mode makes it difficult to apply techniques based on offset tracking. For this reason, we need to focus
 281 on the regions acquired in IW mode.

282 Sentinel-1 is a constellation made up of 2 satellites (Sentinel-1 A and B). If used together, it is
 283 possible to reduce the revisit time from 12 to 6 days, thus drastically reducing the influence of temporal
 284 decorrelation. In Antarctica, areas with a 6-days revisit time include the Antarctic Peninsula, the
 285 coastal areas of the Amundsen Sea, and a series of specific ice-shelves such as Totten, Amery, Ronne,
 286 or Ross ice shelves. Despite an acquisition, every 6 days, the dynamics in these regions are such that it
 287 is not possible to use the phase information of the images.

288 Compared to previous satellite systems, Sentinel-1's high repeat pass cycle (6-12 days) now
 289 allows evaluating changes between velocity fields, while previously only a mean state could be
 290 determined. This has already allowed for determining sub-shelf melt rates over periods of 1-2 years
 291 using Lagrangian techniques [42,45]. This constitutes a drastic change from previous studies, largely
 292 focused on single velocity maps or only inter-annual studies. With its 300 meters per year velocity,
 293 the RBIS is a good candidate for both speckle tracking and interferometry, considering the Sentinel-1
 294 spatial resolution, wavelength, and revisit time.

295 In this study, we are working with 12-days IW images in orbit 59, largely covering the RBIS. The
 296 period considered is from June 14, 2018, to November 24, 2019, for a total of 45 images. The list of data
 297 is included in the appendices.

298 4. Results

299 4.1. Coherence Gain

300 SAR pairs are selected by minimizing the temporal decorrelation. The results are thus produced
301 in series, each pair being composed of two SAR images separated by 12 days.

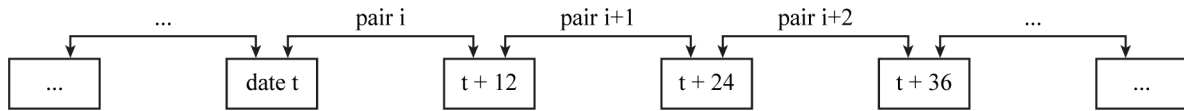


Figure 9. SAR pairs for coherence tracking are selected using successive SAR images, with a 12-days temporal baseline.

302 For each of our pairs, we produce a full-resolution interferogram according to standard
303 interferometry procedures [46,47]. In addition, we add a coherence map, which shows the quality
304 of the interferometric signal. We then compare these results with those produced by the coherence
305 tracking technique.

306 In general, the quality of the classically obtained interferometric signal decreases with the velocity
307 at the ice surface. This is strongly visible when looking at the faster parts of the ice shelf, where speeds
308 approaching a meter per day are observed.

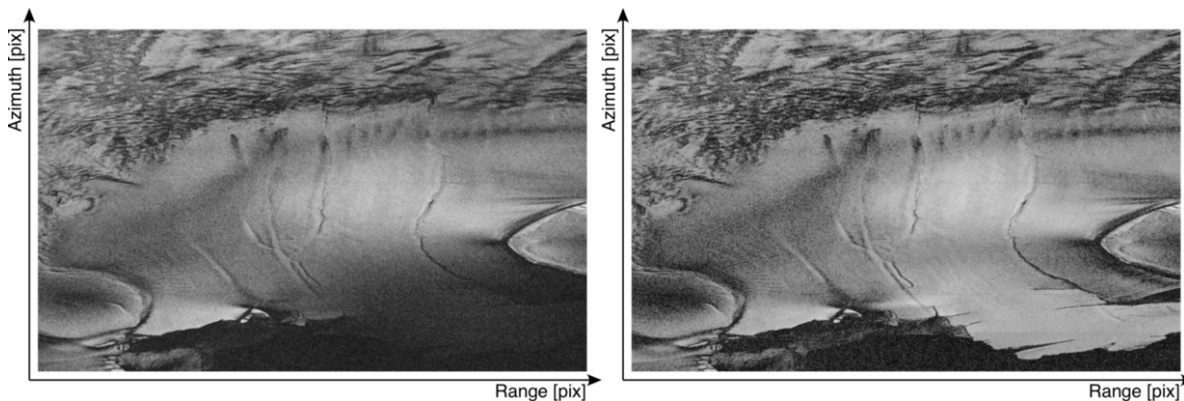


Figure 11. Full resolution, slant-range / azimuth geometry, coherence samples. Left = original coherence. Right = Coherence derived after tracking.

309 To highlight this effect, we selected a fast-moving area (300 meters per year) and a slower one
310 (< 100 meters per year) where we compare the coherence produced by the two methods. The gain
311 brought by coherence tracking is important in the fast-moving area, while the gain is low in the slower
312 zone. On average and with more than a million samples per zone and per date, we go from 0.22 of
313 coherence to 0.52 on average. Translated in terms of standard deviation, it is an improvement by a
314 factor of 2.7 using Cramér Rao bound.

315 4.2. Range and Azimuth Shifts

316 In addition to phase information giving us a precise measurement of the movements along the
317 line of sight, coherence tracking also gives an estimate of the two-dimensional movement. These
318 translations in azimuth and in range are obtained as a subproduct of the coherence maximization
319 criteria. The accuracy of these displacement estimates depends on the resolution of the input images.
320 These displacements are then converted into velocity fields. These 2D velocity fields are similar to
321 those obtained using solely coherent speckle tracking (Figure 13).

322 Similar to [22], one can follow the evolution of the speed over time and observe intra / inter-annual
323 trends or anomalies, witnesses of deeper changes (ice shelf thinning for example). Similar to [48], is

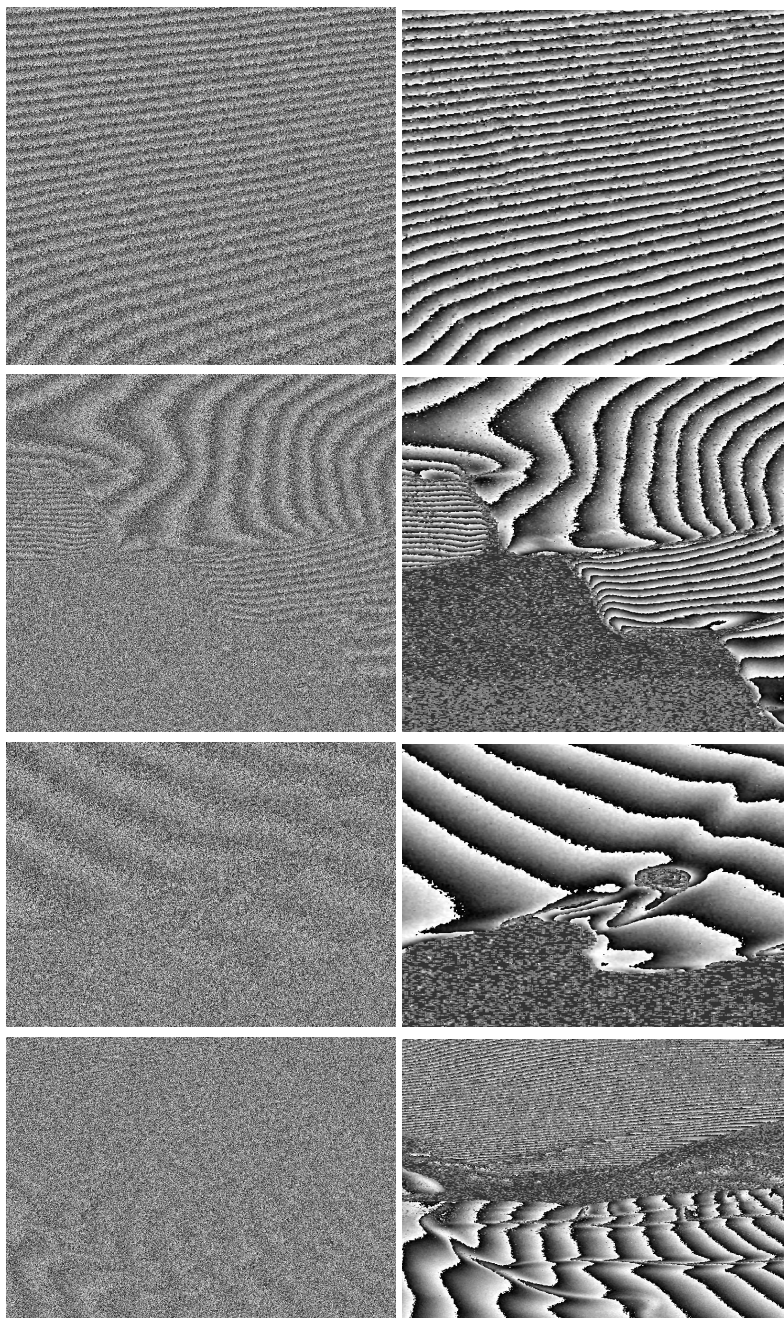


Figure 10. Full resolution, slant-range / azimuth geometry, sample interferograms before (left) and after tracking (right).

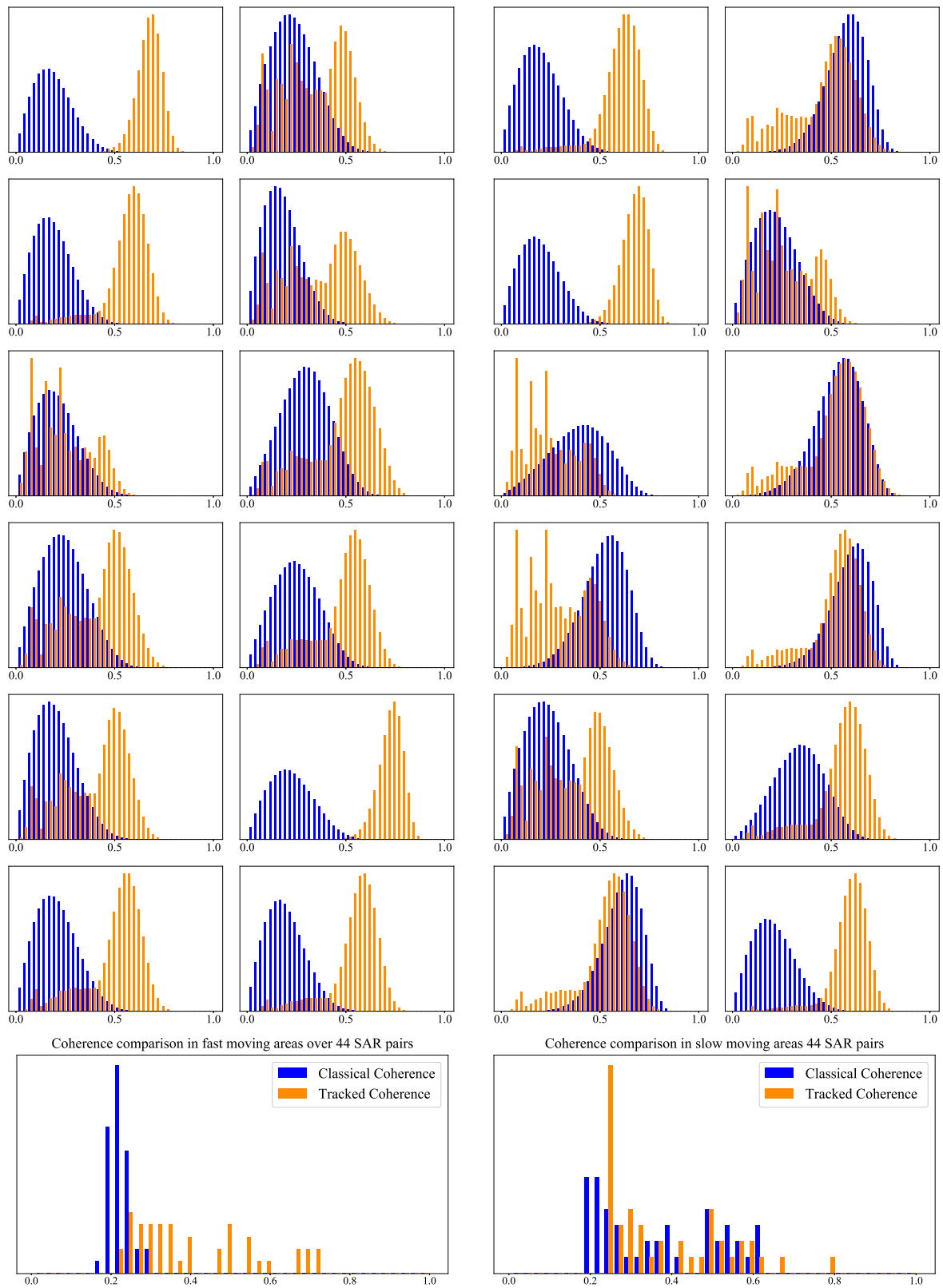


Figure 12. Coherence histograms in slow and fast moving areas the RBIS, for twelve different SAR pairs. The two left columns represent the coherence histogram in fast moving areas (over 200 $m.a^{-1}$) on over 2 millions samples. The blue histogram is the classical coherence, and the orange histogram is the coherence after tracking. Each histogram represents a different acquisitions' pair. The two right columns are related to the slow moving areas (less than 100 $m.a^{-1}$, on over 1.6 million samples). The bottom pictures represents the average coherence over the 44 pairs for the fast (left) and slow (right) moving regions.

324 also possible to study the spatial variation of displacements to study internal stresses in ice. On the
325 basis of longitudinal, transverse, and shear stresses, it is possible to study the effects of buttressing
326 of ice-shelves, crucial for understanding the ice-shelves' stability (Figure 14). While the analysis of
327 individual results shows important variations from pair to pairs (up to 50 meters/year), the time-series
328 analysis confirms the remarkable ongoing stable behavior of the RBIS.

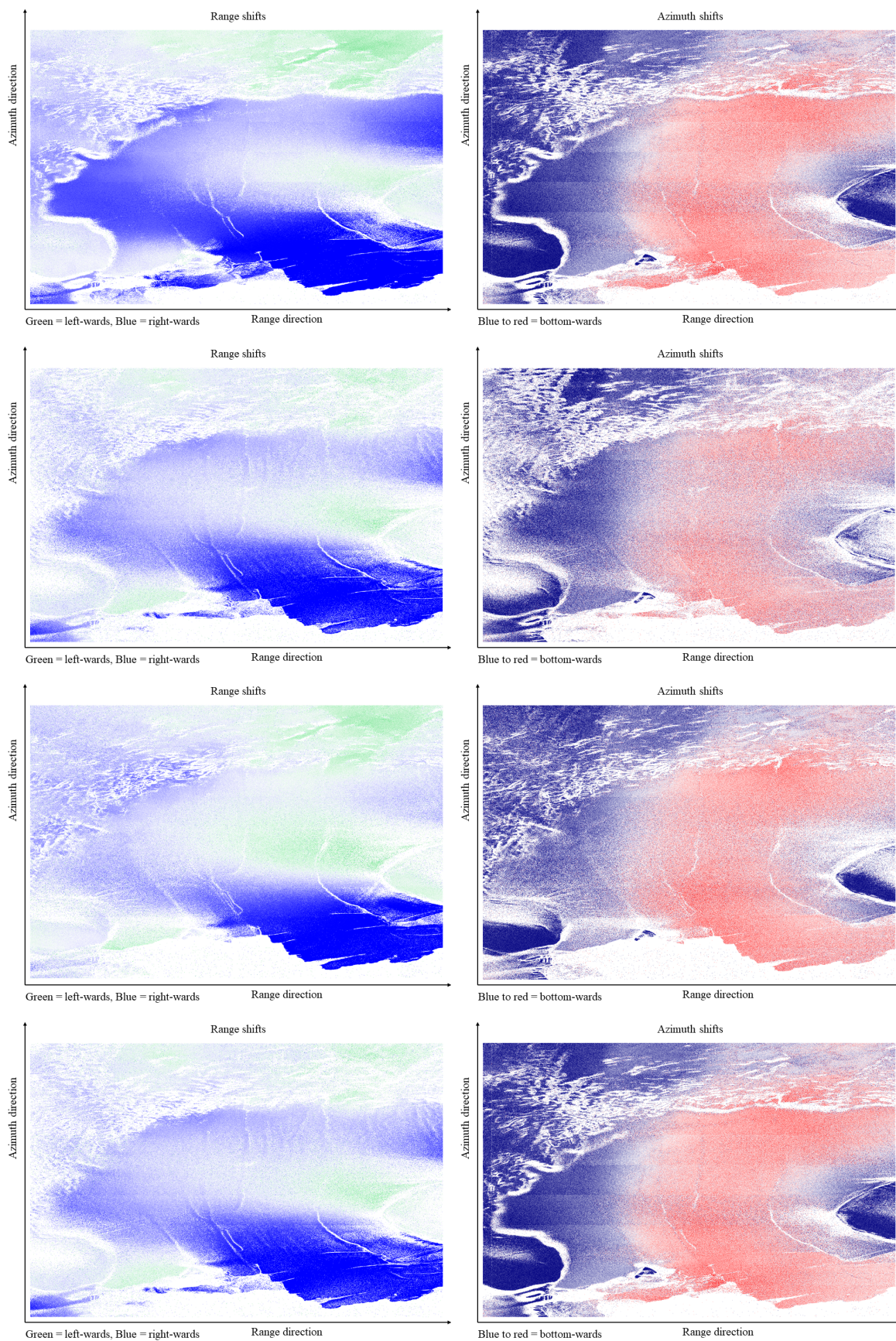


Figure 13. Examples and range and azimuth shifts.

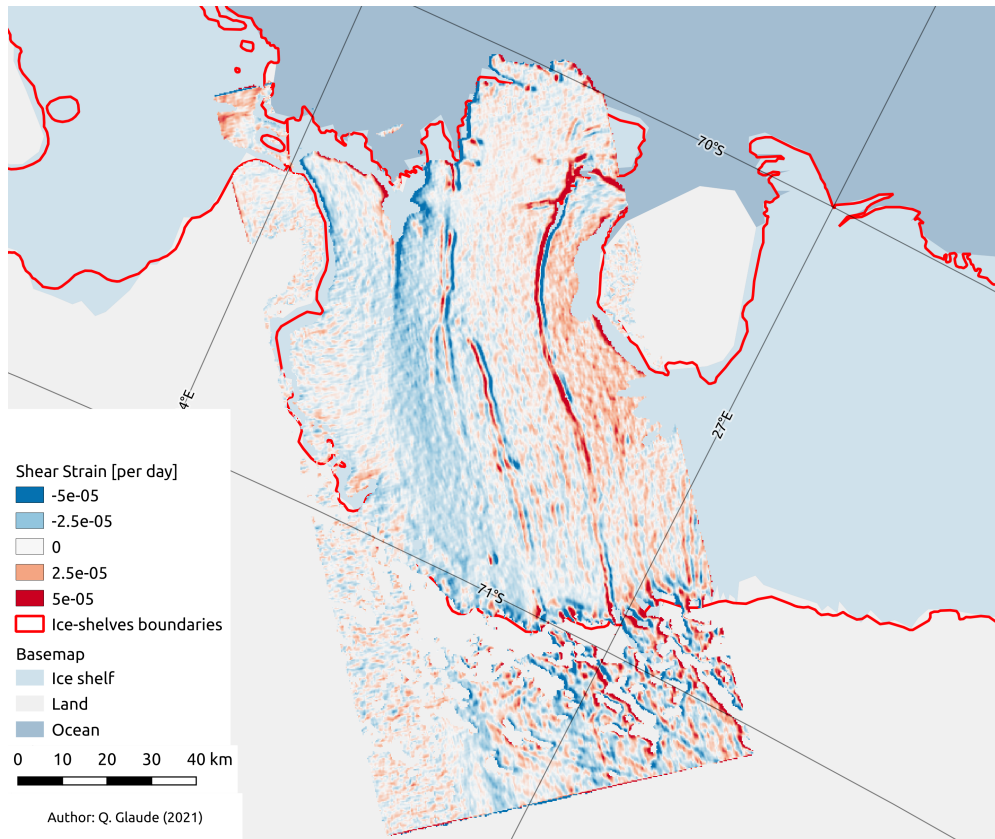


Figure 14. Shear strain computed from azimuth and range shifts.

329 4.3. Merging Products

330 The coherence tracking provides 4 products: an interferogram and its associated coherence, as well
 331 as the two components of the estimated displacement. From the last two products, we can represent
 332 the velocity map with the magnitude associated with the hue while the direction is represented with a
 333 superimposed grid of arrays. Note that it is also possible to use the interferogram instead of range
 334 shifts for a more precise determination of the range component of the speed.

335 Since the determination of 2D displacements depends on the phase, the coherence information is
 336 also a measure of the quality of the 2D displacements. Coherence is used here via the saturation channel.
 337 In this way, vivid colors represent the best results. Finally, we use the effective radar cross-section,
 338 expressed in dB for the intensity channel.

339 The ice-shelf velocity shows the different major features of the RBIS. With a velocity higher than
 340 300 meters per year, the West Ragnhild glacier terminus represents the major component of RBIS ice
 341 discharge. This important ice flow is regulated by the Derwael and FrankKenny ice rises.

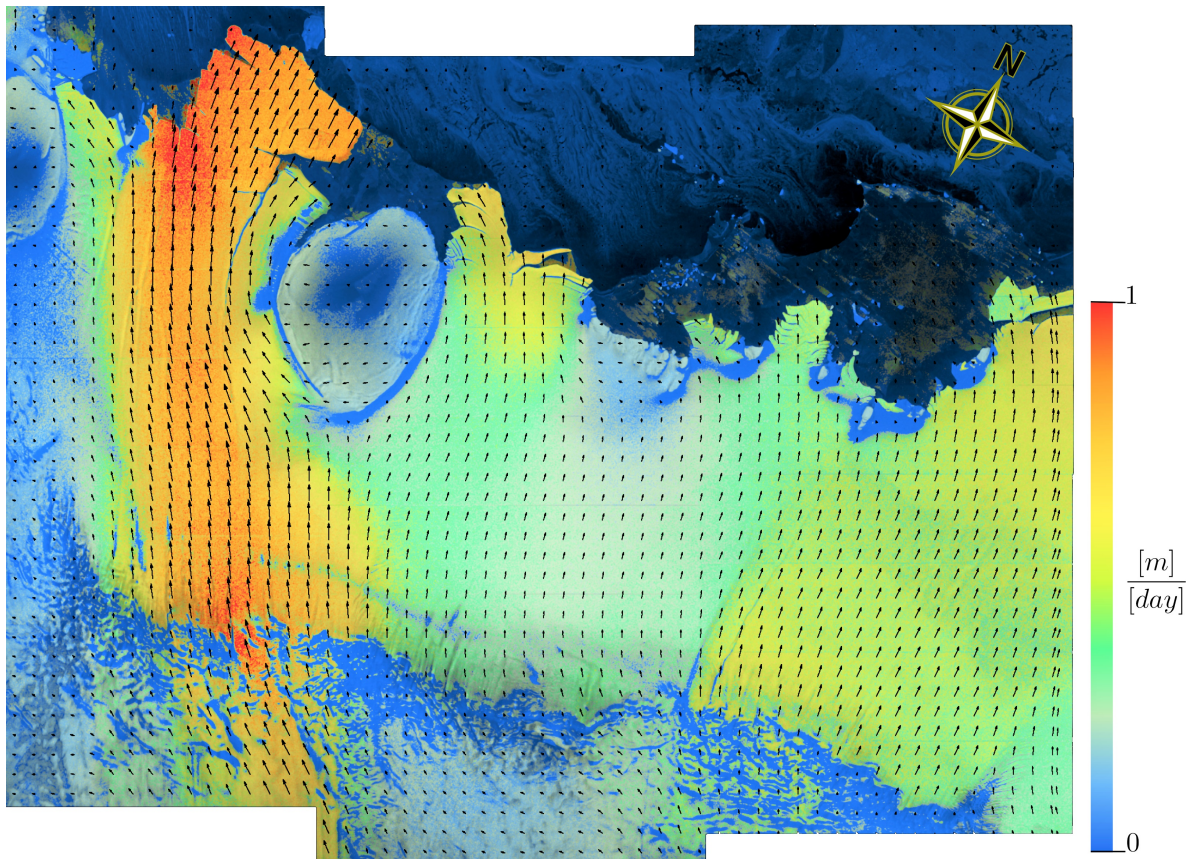


Figure 15. Full hue, saturation, lightness representation of coherence tracking results. To the hue channel is associated the absolute velocity, given by azimuth and range shifts. The range shifts can also be replaced by the tracked interferogram, unwrapped, and translated into displacements. The saturation channel is given by the tracked coherence. Doing so, high coherent areas are represented by vivid color, while low coherence areas are gray. Finally, the lightness is given by the amplitude channel. This lightness serves as a background for better interpretation.

342 5. Conclusion

343 In this article, we have presented the statistical gains of tracking coherence over fast-moving
 344 areas, in comparison with more traditional techniques. In coherence tracking, we use a local coherence
 345 maximization algorithm to determine the displacement of scatterers in a given neighborhood of
 346 the pixel. Coherence tracking allows the recovery of the interferometric signal where applicable. It
 347 allows among other things to move the border between offset-tracking and DInSAR, by correcting the
 348 interferometric phase from displacement-induced decorrelations. Where the displacements are more
 349 important, one observes a significant improvement of the coherence.

350 Sentinel-1 TOPSAR acquisition mode requires particular attention due to the azimuthal phase
 351 ramp. Indeed, the phase difference from shift image locations introduces azimuthal phase residuals
 352 in the corrected interferogram. In this sense, interferometric coherence tracking requires an *a priori*
 353 deramping of the TOPSAR input data.

354 In addition to the interferometric phase, coherence tracking provides an estimate of the 2D
 355 displacements using coherent cross-correlation techniques. Together and with phase measurements,
 356 coherence tracking provides quality information on a highly dynamic surface. This is particularly
 357 useful in glaciology and specifically over ice shelves. In our study, we used sentinel-1 images at 12-day
 358 intervals over the RBIS area. We produced displacement maps as well as an example of a derivative
 359 product, such as strain rates.

360 **Author Contributions:** Dominique Derauw developed the *cohTrack* module, aiming at performing the presenting
 361 coherence tracking technique. *cohTrack* is an independent part of complete SAR processor, the *CSL InSAR Suite*
 362 (CIS). Quentin Glaude conceptualized the study, processed the Sentinel-1 images, developed the adjustments
 363 related to the TOPSAR acquisition mode, and performed the statistical analysis. Dominique Derauw and Quentin
 364 Glaude participated equally in the figure creation and writing of the article. Christian Barbier, Frank Pattyn, and
 365 Anne Orban participated in the analysis of results, as well as their integration in their respective fields of expertise.
 366 All authors contributed in giving suggestions, reviewing, and editing the presented work.

367 **Funding:** This research is supported by the French Community of Belgium in the funding context of a FRIA grant,
 368 and carried out in the framework of the MIMO (Monitoring melt where Ice Meets Ocean) project funded by the
 369 Belgian Science Policy contract Nos. SR/00/336. The *Fondation Jaumotte-Demoulin et Fonds David et Alice Van*
 370 *Buuren* is also acknowledged for the financial support.

371 **Acknowledgments:** TanDEM-X data for DEM-assisted coregistration originate from the German Aerospace
 372 Center (ATI-GLAC0267). Sentinel-1 acquisitions are provided by the European Space Agency, in the frame of
 373 the Copernicus program. We also thanks Brockmann Consult for the Sentinels Application Platform, which is
 374 part of different steps of the present work. Finally, we acknowledge the Norwegian Polar Institute's Quantarctica
 375 package for different mapping tools.

376 **Conflicts of Interest:** The authors declare no conflict of interest.

377 Abbreviations

378 The following abbreviations are used in this manuscript:

379 TOPSAR or TOPS	Terrain Observation by Progressive Scans
SAR	Synthetic Aperture Radar
InSAR	SAR Interferometry
DInSAR	Differential SAR Interferometry
RBIS	Roi Baudouin Ice Shelf
380 ESA	European Space Agency
IW	Interferometric Wide-swath
EW	Extra Wide-swath
SLC	Single Look Complex
SNAP	SentiNel Application Platform
CIS	Centre spatial de Liège Interferometric Suite

381 **Appendix A List of Sentinel-1 Acquisitions****Table A1.** This is a table caption. Tables should be placed in the main text near to the first time they are cited.

Product Names
S1A_IW_SLC__1SSH_20180614T184525_20180614T184552_022356_026BA8_86DA
S1A_IW_SLC__1SSH_20180626T184525_20180626T184552_022531_0270CE_AEDC
S1A_IW_SLC__1SSH_20180708T184526_20180708T184553_022706_0275EB_9A9A
S1A_IW_SLC__1SSH_20180720T184527_20180720T184554_022881_027B46_B81B
S1A_IW_SLC__1SSH_20180801T184527_20180801T184554_023056_0280DO_FCD1
S1A_IW_SLC__1SSH_20180813T184528_20180813T184555_023231_02866D_85DA
S1A_IW_SLC__1SSH_20180825T184529_20180825T184556_023406_028C0C_AAC9
S1A_IW_SLC__1SSH_20180906T184530_20180906T184557_023581_0291A3_A479
S1A_IW_SLC__1SSH_20180918T184530_20180918T184557_023756_02973F_1B05
S1A_IW_SLC__1SSH_20180930T184530_20180930T184557_023931_029CEE_4553
S1A_IW_SLC__1SSH_20181012T184530_20181012T184557_024106_02A2AC_86FB
S1A_IW_SLC__1SSH_20181024T184530_20181024T184557_024281_02A858_1101
S1A_IW_SLC__1SSH_20181105T184530_20181105T184557_024456_02AE50_4AC4
S1A_IW_SLC__1SSH_20181117T184530_20181117T184557_024631_02B4BD_0087
S1A_IW_SLC__1SSH_20181129T184529_20181129T184556_024806_02BB10_3FOC
S1A_IW_SLC__1SSH_20181211T184529_20181211T184556_024981_02C10F_E52A
S1A_IW_SLC__1SSH_20181223T184529_20181223T184556_025156_02C75E_1DC1
S1A_IW_SLC__1SSH_20190104T184528_20190104T184555_025331_02CDAD_3BDB
S1A_IW_SLC__1SSH_20190116T184528_20190116T184555_025506_02D3FF_7BC3
S1A_IW_SLC__1SSH_20190128T184528_20190128T184555_025681_02DA63_6E33
S1A_IW_SLC__1SSH_20190209T184527_20190209T184554_025856_02E0AF_6350
S1A_IW_SLC__1SSH_20190221T184527_20190221T184554_026031_02E6E3_2ACD
S1A_IW_SLC__1SSH_20190305T184527_20190305T184554_026206_02ED2D_D140
S1A_IW_SLC__1SSH_20190317T184527_20190317T184554_026381_02F39D_5C23
S1A_IW_SLC__1SSH_20190329T184527_20190329T184554_026556_02FA08_A840
S1A_IW_SLC__1SSH_20190410T184527_20190410T184554_026731_03007A_FAA2
S1A_IW_SLC__1SSH_20190422T184528_20190422T184555_026906_0306C9_7AC2
S1A_IW_SLC__1SSH_20190504T184529_20190504T184555_027081_030D2B_60E2
S1A_IW_SLC__1SSH_20190516T184529_20190516T184556_027256_0312C4_3CC1
S1A_IW_SLC__1SSH_20190528T184530_20190528T184557_027431_03183A_8706
S1A_IW_SLC__1SSH_20190609T184530_20190609T184557_027606_031D9F_3B02
S1A_IW_SLC__1SSH_20190621T184531_20190621T184558_027781_0322D4_6402
S1A_IW_SLC__1SSH_20190703T184532_20190703T184559_027956_03281D_9133
S1A_IW_SLC__1SSH_20190715T184533_20190715T184600_028131_032D69_D38B
S1A_IW_SLC__1SSH_20190727T184533_20190727T184600_028306_0332C0_F35A
S1A_IW_SLC__1SSH_20190808T184534_20190808T184601_028481_033825_1COB
S1A_IW_SLC__1SSH_20190820T184535_20190820T184602_028656_033E36_3E13
S1A_IW_SLC__1SSH_20190901T184535_20190901T184602_028831_034450_2F7D
S1A_IW_SLC__1SSH_20190913T184536_20190913T184603_029006_034A62_EB67
S1A_IW_SLC__1SSH_20190925T184536_20190925T184603_029181_035057_18A3
S1A_IW_SLC__1SSH_20191007T184537_20191007T184604_029356_035664_9025
S1A_IW_SLC__1SSH_20191019T184537_20191019T184604_029531_035C6D_31FF
S1A_IW_SLC__1SSH_20191031T184537_20191031T184604_029706_036282_99C9
S1A_IW_SLC__1SSH_20191112T184537_20191112T184604_029881_0368A5_B4B5
S1A_IW_SLC__1SSH_20191124T184536_20191124T184603_030056_036EB5_C4EC

382 **Appendix B Coherence Tracking Algorithm**

383

- 384 1. Shepherd, A.; Ivins, E.R.; A, G.; Barletta, V.R.; Bentley, M.J.; Bettadpur, S.; Briggs, K.H.; Bromwich,
385 D.H.; Forsberg, R.; Galin, N.; Horwath, M.; Jacobs, S.; Joughin, I.; King, M.A.; Lenaerts, J.T.M.; Li,
386 J.; Ligtenberg, S.R.M.; Luckman, A.; Luthcke, S.B.; McMillan, M.; Meister, R.; Milne, G.; Mouginot,

Algorithm 1 Compute tracked coherence, tracked interferogram and 2D shifts

```

Master Image M,
Slave Image S,
Search Window W
Grid G, a systematic sample of M
for every location  $X \in G$  do
   $max\gamma = 0$ 
  for all  $i \in W$  do
    compute  $\gamma(M_X, S_{X+i})$ 
    if  $\gamma > max\gamma$  then
       $max\gamma = \gamma$ 
      compute  $\phi(M_X, S_{X+i})$ 
      compute 2D-Norm distr. from  $\gamma$  at  $X + i \pm 1$ 
       $2D-Shift = \max(2D - Norm)$ 
    end if
  end for
end for

trackedCoherence = resample  $\gamma$  from G to M
trackedInterferogram = resample  $\phi$  from G to M
2D-Shift = resample 2D-Shift from G to M

```

- 387 J.; Muir, A.; Nicolas, J.P.; Paden, J.; Payne, A.J.; Pritchard, H.; Rignot, E.; Rott, H.; Sørensen, L.S.;
388 Scambos, T.A.; Scheuchl, B.; Schrama, E.J.O.; Smith, B.; Sundal, A.V.; van Angelen, J.H.; van de Berg, W.J.;
389 van den Broeke, M.R.; Vaughan, D.G.; Velicogna, I.; Wahr, J.; Whitehouse, P.L.; Wingham, D.J.; Yi, D.;
390 Young, D.; Zwally, H.J. A Reconciled Estimate of Ice-Sheet Mass Balance. *Science* **2012**, *338*, 1183–1189,
391 [<https://www.science.org/doi/pdf/10.1126/science.1228102>]. doi:10.1126/science.1228102.
- 392 2. Shepherd, A.; Gilbert, L.; Muir, A.S.; Konrad, H.; McMillan, M.; Slater, T.; Briggs, K.H.; Sundal, A.V.;
393 Hogg, A.E.; Engdahl, M.E. Trends in Antarctic Ice Sheet Elevation and Mass. *Geophysical Research*
394 *Letters* **2019**, *46*, 8174–8183, [<https://agupubs.onlinelibrary.wiley.com/doi/pdf/10.1029/2019GL082182>].
395 doi:<https://doi.org/10.1029/2019GL082182>.
- 396 3. Shepherd, A.; Fricker, H.A.; Farrell, S.L. Trends and connections across the Antarctic cryosphere. *Nature*
397 **2018**, *558*, 223–232. doi:10.1038/s41586-018-0171-6.
- 398 4. Slater, T.; Shepherd, A. Antarctic ice losses tracking high. *Nature Climate Change* **2018**, *8*, 1025–1026.
399 doi:10.1038/s41558-018-0284-9.
- 400 5. Seroussi, H. Fate and future climatic role of polar ice sheets. *Nature* **2019**, *566*, 48+.
- 401 6. Pritchard, H.D.; Ligtenberg, S.R.M.; Fricker, H.A.; Vaughan, D.G.; van den Broeke, M.R.; Padman,
402 L. Antarctic ice-sheet loss driven by basal melting of ice shelves. *Nature* **2012**, *484*, 502–505.
403 doi:10.1038/nature10968.
- 404 7. Paolo, F.S.; Fricker, H.A.; Padman, L. Volume loss from Antarctic ice shelves is accelerating. *Science* **2015**,
405 *348*, 327–331, [<https://www.science.org/doi/pdf/10.1126/science.aaa0940>]. doi:10.1126/science.aaa0940.
- 406 8. Dinniman, M.S.; Asay-Davis, X.S.; Galton-Fenzi, B.K.; Holland, P.R.; Jenkin, A.; Timmermann, R. Modeling
407 Ice Shelf/Ocean Interaction in Antarctica: A Review. *Oceanography* **2016**.
- 408 9. Favier, L.; Pattyn, F. Antarctic ice rise formation, evolution, and stability. *Geophysical Research Letters* **2015**,
409 *42*, 4456–4463. doi:10.1002/2015GL064195.
- 410 10. Dupont, T.K.; Alley, R.B. Assessment of the importance of ice-shelf buttressing to ice-sheet flow. *Geophysical*
411 *Research Letters* **2005**, *32*, [<https://agupubs.onlinelibrary.wiley.com/doi/pdf/10.1029/2004GL022024>].
412 doi:<https://doi.org/10.1029/2004GL022024>.
- 413 11. Payne, A.J.; Vieli, A.; Shepherd, A.P.; Wingham, D.J.; Rignot, E. Recent dramatic thinning of largest West
414 Antarctic ice stream triggered by oceans. *Geophysical Research Letters* **2004**, *31*. doi:10.1029/2004GL021284.

- 415 12. Pritchard, H.D.; Arthern, R.J.; Vaughan, D.G.; Edwards, L.A. Extensive dynamic thinning on the margins
416 of the Greenland and Antarctic ice sheets. *Nature* **2009**, *461*, 971–975. doi:10.1038/nature08471.
- 417 13. Goldberg, D.; Holland, D.M.; Schoof, C. Grounding line movement and ice shelf buttressing in marine ice
418 sheets. *Journal of Geophysical Research: Earth Surface* **2009**, *114*. doi:10.1029/2008JF001227.
- 419 14. Gudmundsson, G.H.; Paolo, F.S.; Adusumilli, S.; Fricker, H.A. Instantaneous Antarctic
420 ice sheet mass loss driven by thinning ice shelves. *Geophysical Research Letters* **2019**,
421 *46*, 13903–13909, [<https://agupubs.onlinelibrary.wiley.com/doi/pdf/10.1029/2019GL085027>].
422 doi:https://doi.org/10.1029/2019GL085027.
- 423 15. Bindschadler, R. Monitoring ice sheet behavior from space. *Reviews of Geophysics*
424 **1998**, *36*, 79–104, [<https://agupubs.onlinelibrary.wiley.com/doi/pdf/10.1029/97RG02669>].
425 doi:https://doi.org/10.1029/97RG02669.
- 426 16. Massonnet, D.; Rossi, M.; Carmona, C.; Adragna, F.; Peltzer, G.; Feigl, K.; Rabatte, T. The
427 displacement field of the Landers earthquake mapped by radar interferometry. *Nature* **1993**, *364*, 138–142.
428 doi:10.1038/364138a0.
- 429 17. Goldstein, R.M.; Engelhardt, H.; Kamb, B.; Frolich, R.M. Satellite Radar Interferometry for
430 Monitoring Ice Sheet Motion: Application to an Antarctic Ice Stream. *Science* **1993**, *262*, 1525–1530,
431 [<https://www.science.org/doi/pdf/10.1126/science.262.5139.1525>]. doi:10.1126/science.262.5139.1525.
- 432 18. Wright, T.J.; Parsons, B.E.; Lu, Z. Toward mapping surface deformation
433 in three dimensions using InSAR. *Geophysical Research Letters* **2004**,
434 *31*, [<https://agupubs.onlinelibrary.wiley.com/doi/pdf/10.1029/2003GL018827>].
435 doi:https://doi.org/10.1029/2003GL018827.
- 436 19. Pepe, A.; Calò, F. A Review of Interferometric Synthetic Aperture RADAR (InSAR) Multi-Track Approaches
437 for the Retrieval of Earth's Surface Displacements. *Applied Sciences* **2017**, *7*. doi:10.3390/app7121264.
- 438 20. Mouginot, J.; Scheuchl, B.; Rignot, E. Mapping of Ice Motion in Antarctica Using Synthetic-Aperture Radar
439 Data. *Remote Sensing* **2012**, *4*, 2753–2767. doi:10.3390/rs4092753.
- 440 21. Joughin, I.; Smith, B.E.; Abdalati, W. Glaciological advances made with interferometric synthetic aperture
441 radar. *Journal of Glaciology* **2010**, *56*, 1026–1042. doi:10.3189/002214311796406158.
- 442 22. Dirscherl, M.; Dietz, A.J.; Dech, S.; Kuenzer, C. Remote sensing of ice motion in Antarctica – A review.
443 *Remote Sensing of Environment* **2020**, *237*, 111595. doi:https://doi.org/10.1016/j.rse.2019.111595.
- 444 23. Rignot, E.; Mouginot, J.; Scheuchl, B. Ice Flow of the Antarctic Ice Sheet. *Science* **2011**, *333*, 1427–1430,
445 [<https://www.science.org/doi/pdf/10.1126/science.1208336>]. doi:10.1126/science.1208336.
- 446 24. Rignot, E.; Mouginot, J.; Scheuchl, B. Antarctic grounding line mapping
447 from differential satellite radar interferometry. *Geophysical Research Letters*
448 **2011**, *38*, [<https://agupubs.onlinelibrary.wiley.com/doi/pdf/10.1029/2011GL047109>].
449 doi:https://doi.org/10.1029/2011GL047109.
- 450 25. Favier, L.; Durand, G.; Cornford, S.L.; Gudmundsson, G.H.; Gagliardini, O.; Gillet-Chaulet, F.; Zwinger, T.;
451 Payne, A.J.; Le Brocq, A.M. Retreat of Pine Island Glacier controlled by marine ice-sheet instability. *Nature*
452 *Climate Change* **2014**, *4*, 117–121. doi:10.1038/nclimate2094.
- 453 26. Mouginot, J.; Rignot, E.; Scheuchl, B.; Millan, R. Comprehensive Annual Ice Sheet Velocity Mapping Using
454 Landsat-8, Sentinel-1, and RADARSAT-2 Data. *Remote Sensing* **2017**, *9*. doi:10.3390/rs9040364.
- 455 27. Mouginot, J.; Rignot, E.; Scheuchl, B. Continent-Wide, Interferometric SAR
456 Phase, Mapping of Antarctic Ice Velocity. *Geophysical Research Letters* **2019**,
457 *46*, 9710–9718, [<https://agupubs.onlinelibrary.wiley.com/doi/pdf/10.1029/2019GL083826>].
458 doi:https://doi.org/10.1029/2019GL083826.
- 459 28. Derauw, D. DInSAR and Coherence Tracking Applied to Glaciology : The Example of Shirase. 1999.
- 460 29. Nagler, T.; Rott, H.; Hetzenecker, M.; Wuite, J.; Potin, P. The Sentinel-1 Mission: New Opportunities for Ice
461 Sheet Observations. *Remote Sensing* **2015**, *7*, 9371–9389. doi:10.3390/rs70709371.
- 462 30. Fitch, J.P. *Synthetic Aperture Radar*; Springer-Verlag: Berlin, Heidelberg, 1988.
- 463 31. Dainty, J.C. *Laser Speckle and Related Phenomena*; Springer-Verlag: Berlin, Heidelberg, 1975.
464 doi:10.1007/978-3-662-43205-1.
- 465 32. Zebker, H.; Villasenor, J. Decorrelation in interferometric radar echoes. *IEEE Transactions on Geoscience and*
466 *Remote Sensing* **1992**, *30*, 950–959. doi:10.1109/36.175330.

- 467 33. Born, M.; Wolf, E. *Principles of Optics: Electromagnetic Theory of Propagation, Interference and Diffraction of*
468 *Light (7th Edition)*, 7th ed.; Cambridge University Press, 1999.
- 469 34. Bamler, R.; Schättler, B., SAR Data Acquisition and Image Formation; 1993; pp. 53–102.
- 470 35. Peter, H.; Jäggi, A.; Fernández, J.; Escobar, D.; Ayuga, F.; Arnold, D.; Wermuth, M.; Hackel, S.; Otten, M.;
471 Simons, W.; Visser, P.; Hugentobler, U.; Féménias, P. Sentinel-1A – First precise orbit determination results.
472 *Advances in Space Research* **2017**, *60*, 879–892. doi:https://doi.org/10.1016/j.asr.2017.05.034.
- 473 36. Prats-Iraola, P.; Scheiber, R.; Marotti, L.; Wollstadt, S.; Reigber, A. TOPS Interferometry With TerraSAR-X.
474 *IEEE Transactions on Geoscience and Remote Sensing* **2012**, *50*, 3179–3188. doi:10.1109/TGRS.2011.2178247.
- 475 37. Pattyn, F.; Derauw, D. Ice-dynamic conditions of Shirase Glacier, Antarctica, inferred from ERS SAR
476 interferometry. *Journal of Glaciology* **2002**, *48*, 559–565. doi:10.3189/172756502781831115.
- 477 38. Miranda, N.; Hajduch, G. Definition of the TOPS SLC deramping function for products generated by the
478 S-1 IPF. Technical report, 2017.
- 479 39. De Zan, F.; Monti Guarnieri, A. TOPSAR: Terrain Observation by Progressive Scans. *IEEE Transactions on*
480 *Geoscience and Remote Sensing* **2006**, *44*, 2352–2360. doi:10.1109/TGRS.2006.873853.
- 481 40. Goel, V.; Matsuoka, K.; Berger, C.D.; Lee, I.; Dall, J.; Forsberg, R. Characteristics of ice rises and ice
482 rumpled in Dronning Maud Land and Enderby Land, Antarctica. *Journal of Glaciology* **2020**, *66*, 1064–1078.
483 doi:10.1017/jog.2020.77.
- 484 41. Drews, R.; Matsuoka, K.; Martín, C.; Callens, D.; Bergeot, N.; Pattyn, F. Evolution of Derwael Ice
485 Rise in Dronning Maud Land, Antarctica, over the last millennia. *Journal of Geophysical Research: Earth*
486 *Surface* **2015**, *120*, 564–579, [https://agupubs.onlinelibrary.wiley.com/doi/pdf/10.1002/2014JF003246].
487 doi:https://doi.org/10.1002/2014JF003246.
- 488 42. Berger, S.; Drews, R.; Helm, V.; Sun, S.; Pattyn, F. Detecting high spatial variability of ice
489 shelf basal mass balance, Roi Baudouin Ice Shelf, Antarctica. *The Cryosphere* **2017**, *11*, 2675–2690.
490 doi:10.5194/tc-11-2675-2017.
- 491 43. Lenaerts, J.T.M.; Lhermitte, S.; Drews, R.; Ligtenberg, S.R.M.; Berger, S.; Helm, V.; Smeets, C.J.P.P.; Broeke,
492 M.d.; van de Berg, W.J.; van Meijgaard, E.; Eijkelboom, M.; Eisen, O.; Pattyn, F. Meltwater produced
493 by wind–albedo interaction stored in an East Antarctic ice shelf. *Nature Climate Change* **2017**, *7*, 58–62.
494 doi:10.1038/nclimate3180.
- 495 44. Berger, S.; Favier, L.; Drews, R.; Derwael, J.J.; Pattyn, F. The control of an uncharted pinning point on the
496 flow of an Antarctic ice shelf. *Journal of Glaciology* **2016**, *62*, 37–45. doi:10.1017/jog.2016.7.
- 497 45. Marsh, O.J.; Fricker, H.A.; Siegfried, M.R.; Christianson, K.; Nicholls, K.W.; Corr, H.F.J.; Catania, G. High
498 basal melting forming a channel at the grounding line of Ross Ice Shelf, Antarctica. *Geophysical Research*
499 *Letters* **2016**, *43*, 250–255. doi:10.1002/2015GL066612.
- 500 46. Yagüe-Martínez, N.; Prats-Iraola, P.; Rodríguez González, F.; Brcic, R.; Shau, R.; Geudtner, D.; Eineder, M.;
501 Bamler, R. Interferometric Processing of Sentinel-1 TOPS Data. *IEEE Transactions on Geoscience and Remote*
502 *Sensing* **2016**, *54*, 2220–2234. doi:10.1109/TGRS.2015.2497902.
- 503 47. Yague-Martinez, N.; De Zan, F.; Prats-Iraola, P. Coregistration of Interferometric Stacks of Sentinel-1 TOPS
504 Data. *IEEE Geoscience and Remote Sensing Letters* **2017**, *14*, 1002–1006. doi:10.1109/LGRS.2017.2691398.
- 505 48. Alley, K.E.; Scambos, T.A.; Anderson, R.S.; Rajaram, H.; Pope, A.; Haran, T.M. Continent-wide estimates
506 of Antarctic strain rates from Landsat 8-derived velocity grids. *Journal of Glaciology* **2018**, *64*, 321–332.
507 doi:10.1017/jog.2018.23.

508 **Sample Availability:** Sentinel-1 data are available open and free-of-charge from the Copernicus Open Access
509 Hub or other mirroring repositories, such as the Alaska Satellite Facility’s Data Portal (VERTX). The coherence
510 tracking module is available as the form of self-installation *.run* file, upon request through the correspondence
511 information (tested on debian-based distributions).

512 © 2022 by the authors. Submitted to *Remote Sens.* for possible open access publication
513 under the terms and conditions of the Creative Commons Attribution (CC BY) license
514 (<http://creativecommons.org/licenses/by/4.0/>).

2.2.2.3 The Influence of Tides and Inverse Barometer Effect on Measurements

One of the characteristics of DInSAR is to be very sensitive to displacements. As our ice shelves are afloat, they react to sea-level variations. Considering that tides have an amplitude generally comprised between -1 and +1 meter, and 2.8 centimeters in the line-of-sight direction induce a 2π phase shift in a differential interferogram, we understand that tides have strong signatures in DInSAR.

The Earth and Space Research - ESR and the Oregon State University - OSU provide a Matlab API, the Tide Model Driver - TMD package, to make tidal predictions (among others). The TMD package consists of low-level scripts. In our case, we use the CATS2008 Circum-Antarctic Inverse Model.

In addition, differences in atmospheric pressure between two dates are responsible for what is called Inverse Barometer Effect - IBE, which is an ocean isostatic response to atmospheric pressure changes. The response is about 1 cm HPa^{-1} (Padman et al., 2002).

The Laboratory of Climatology of ULiège is continuously developing a regional climate model called MAR which can determine the atmospheric pressure variable at coarse resolution ($5 \times 5 \text{ km}$) in netCDF4 format (Fig. 2.44, left and center images). The vertical displacement bias is due to the atmospheric pressure change between the two dates. Fig. 2.44 (right) shows the surface atmospheric pressure difference for two dates over the RBIS.

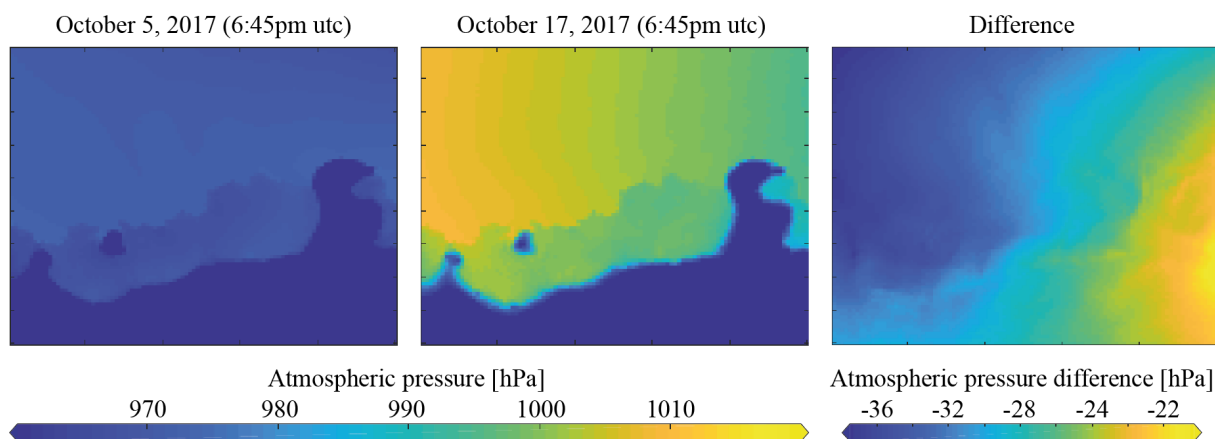


Figure 2.44: Surface atmospheric pressure (hPa) from MAR for October 5 and 17, 2017, and their difference (right).

From a differential interferogram only remains the phase component related to a displacement. This displacement can be translated into its two components, namely horizontal and vertical. Starting from the grounding line to the part of the ice shelf in hydrostatic equilibrium, we have a progressive increase of the vertical variation, leading to a high spatial frequency phase pattern.

We can subtract two consecutive DInSARs to cancel out an *a priori* stable horizontal component and observe the vertical changes. Such a product is called a Double Differential Interferogram - DDInSAR (see figure 2.45). A DDInSAR is a specific interferogram whose fringes are related to vertical displacements.

By properly scaling the DDInSAR, we can correct the DDInSAR and remove the vertical bias.

The proposed algorithm was presented during the EGU General Assembly 2019 (Vienna, Austria) and the IEEE International Geoscience and Remote Sensing Symposium 2019 event (Yokohama, Japan). The reviewed proceeding of the conference is available here-after, and can be cited as:

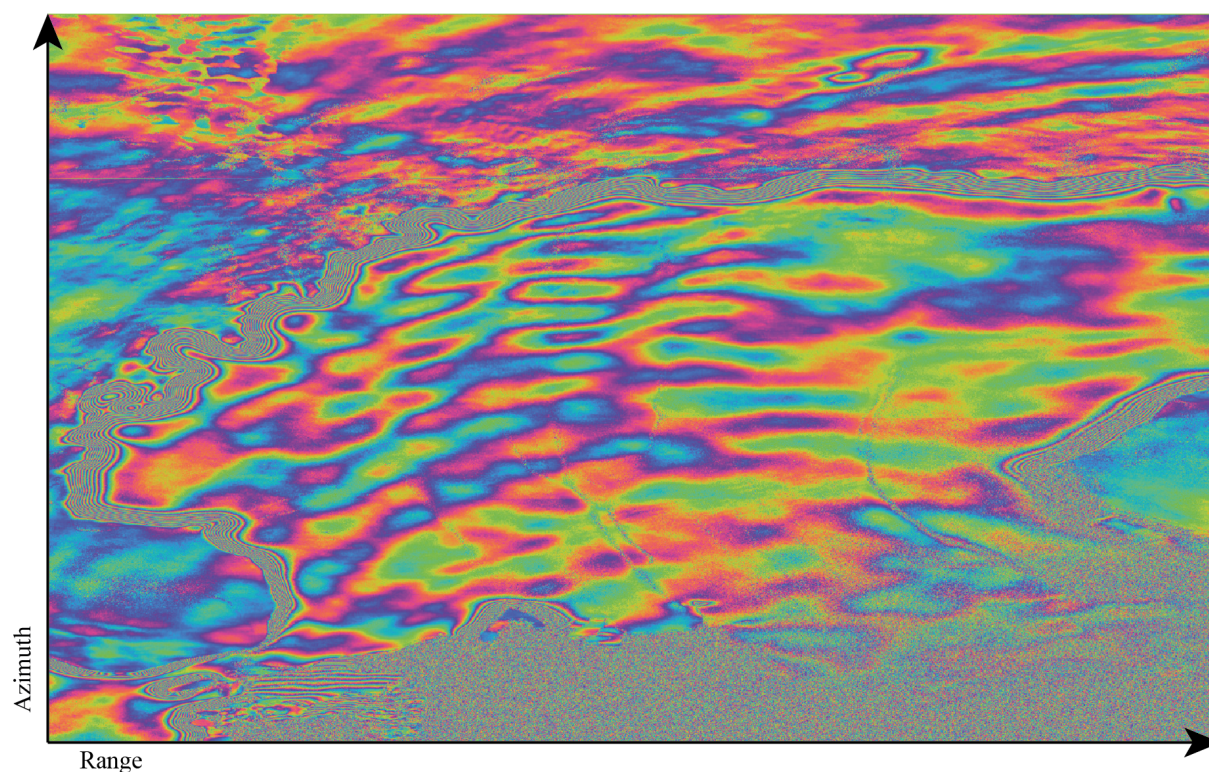


Figure 2.45: Double Difference Interferogram, revealing the grounded and floating ice, separating by the hinge zone, represented by a high fringe rate.

Glaude, Q., Berger, S., Amory, C., Derauw, D., Pattyn, F., Barbier, C., & Orban, A. (2019). Empirical Correction of Tides and Inverse Barometer Effect Phase Components from Double DInSAR and Regional Models. *IGARSS 2019 - 2019 IEEE International Geoscience and Remote Sensing Symposium*, Yokohama, Japan, 2019, pp. 2034-2037, doi: 10.1109/IGARSS.2019.8899171.

A deeper revision of the technique led to the production of an article in *IEEE Journal of Selected Topics in Applied Earth Observations and Remote Sensing* (Impact Factor: 3.784). In there, we further describe our tides/IBE correction method, with more results and figures. We introduce additional Sentinel-1 acquisition modes and the concept of corrections network. Finally, a mathematical description of the variance propagation was developed. The article is accessible here-after, and can be cited as:

Glaude, Q., Amory, C., Berger, S., Derauw, D., Pattyn, F., Barbier, C., & Orban, A. (2020). Empirical Removal of Tides and Inverse Barometer Effect on DInSAR From Double DInSAR and a Regional Climate Model. *IEEE Journal of Selected Topics in Applied Earth Observations and Remote Sensing*, vol. 13, pp. 4085-4094, 2020, doi: 10.1109/JSTARS.2020.3008497.

This article is available in open access on the official IEEE-JSTARS repository.

EMPIRICAL CORRECTION OF TIDES AND INVERSE BAROMETER EFFECT PHASE COMPONENTS FROM DOUBLE DINSAR AND REGIONAL MODELS

Q. Glaude (1,2), S. Berger (3), C. Amory (4), F. Pattyn (1), C. Barbier (2) and A. Orban (2)

(1) Laboratoire de Glaciologie, Université Libre de Bruxelles, Bruxelles, Belgium

(2) Centre Spatial de Liège, Université de Liège, Angleur, Belgium

(3) Alfred Wegener Institute for Polar and Marine Research, Bremerhaven, Germany

(4) Laboratoire de Climatologie et de Topoclimatologie, Université de Liège, Liège, Belgium

ABSTRACT

Surface displacements are of particular interest for characterizing the dynamics of Antarctic ice shelves. Differential Synthetic Aperture Radar Interferometry (DInSAR) is a common technique from which high-resolution velocity maps can be inferred at high accuracy. However, though vertical displacement may be useful in some contexts, the main component of interest is the horizontal velocity when analyzing ice fluxes. Since SAR sensors are side-looking, it is the vector sum of both the vertical and horizontal components along the line of sight (LOS) that can be measured, creating some ambiguity in separating the two elements. Impacted by ocean tides and inverse barometer effect (IBE), ice shelves are subject to a vertical bias to be removed. Here, we present an empirical technique using Sentinel-1 radar satellite and regional models to estimate and remove the corresponding bias and show preliminary results on the Roi Baudouin Ice Shelf (RBIS) in Dronning Maud Land (Antarctica).

Index Terms— DInSAR, DDInSAR, Ice Shelf, Antarctica, Tides, Inverse Barometer Effect, Sentinel-1

1. INTRODUCTION

In the context of studying the dynamics of the ice sheet, DInSAR has proven useful to produce centimeter-precision displacement maps of large remote places such as Antarctica.

The principle of DInSAR is to subtract the phase of two coherent radar waves to produce a displacement map. The resulting differential phase (visualized with an interferogram) is made up by 5 different terms, namely (i) the orbital phase, (ii) the topographic phase, (iii) the displacement phase, in the LOS direction, (iv) the atmospheric phase screen and (v) an additional noise (equation 1).

With differential interferometry, the goal is to measure the phase component related to displacements. Knowing the orbits of the satellites and the topography of the region, the two first terms can be estimated and removed. For topography, we used the global Dronning Maud Land DEM created by the Alfred-Wegener Institute, based on TanDEM-X data. If the

atmospheric phase component can be neglected or corrected, the differential phase obtained after removing the geometric component is:

$$\begin{aligned}\phi_{DInSAR} &= \phi_{t_2} - \phi_{t_1} \\ &= \underbrace{\phi_{orb} + \phi_{topo}}_{\text{geometric}} + \phi_{displ_{LOS}} + \underbrace{\phi_{atm} + \phi_{noise}}_{\text{negligible}} \\ &\approx \phi_{displ_H} + \phi_{displ_V}\end{aligned}\tag{1}$$

The displacement phase in the LOS can be decomposed into horizontal and vertical components. The horizontal displacements are caused by a horizontal motion of ice, which can be assumed stable from one acquisition to the other if close in time. On the other hand, the vertical displacements of ice shelves are mainly due to short-term variations of the local sea level, which are influenced by tides and variable atmospheric pressure – known as Inverse Barometer Effect [1].

On the grounded part of the ice-sheet, the vertical response to the tides and pressure variations is negligible. On the floating part which is in hydrostatic equilibrium, the vertical displacement strictly follows the oceanic readjustment. In the *grounding zone* – the transition between grounded and floating areas – the progressive response to oceanic readjustment is translated into a high fringe rate in the differential interferogram.

Considering a 12 day revisit time (Sentinel-1) and an incidence angle of about 33 degrees, if erroneously interpreting the line of sight measurement as only due to a horizontal displacement, a vertical bias of one meter will lead to a 25 meters per year error in the horizontal velocity estimate. In low velocity areas, this bias is of the order of measured speed, leading to erroneous interpretation of the ice dynamics.

In this context the problem of ice-shelf bending and its associated vertical bias has already been studied in several ways, using ice-flexure modelling [2, 3, 4, 5, 6] or more empirical techniques [7, 8, 9, 10]. In this work, we are presenting

an easily implementable approach that produces satisfying results using tides and regional climate models on Sentinel-1 data.

2. DATA

In this work, we use four Sentinel-1 SAR acquisitions in Single-Look-Complex format (SLC) in Interferometric Wide-Swath mode (IW) with a 12-day revisit time (Table 1).

Table 1. S1 SLC TOPS acquisitions

SAR Acquisition Date	Time (utc)	Relative Orbit
11/09/2017	18h45	59
23/09/2017	18h45	59
05/10/2017	18h45	59
17/10/2017	18h45	59

The computation of tides is performed using the CATS2008 model [11] while surface pressure data come from the regional climate model MAR, whose ability to reproduce climate specificities of coastal East Antarctica has already been demonstrated (e.g. [12]). In addition, surface atmospheric pressure from MAR has been evaluated against independent measurement from an automatic weather station (AWS) set up 300 m from Princess Elizabeth Station ($71^{\circ}57'S$, $23^{\circ}20'E$) which is part of the IMAU Antarctic AWS Project [13]. Figure 1 illustrates the good agreement between daily observed and modelled values of surface pressure. Unbiased root mean square error (RMSE) is 0.7689 hPa. The CATS model in this particular region is in good agreement with GNSS receivers [14].

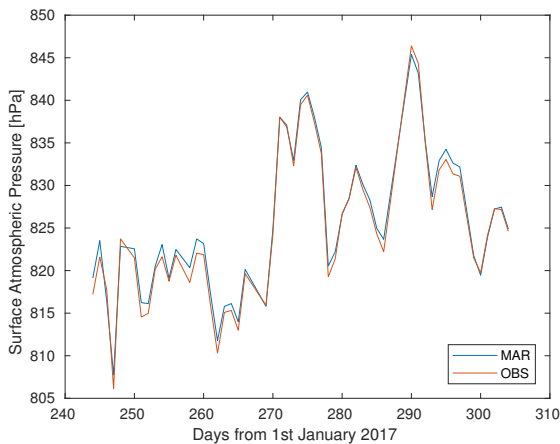


Fig. 1. Comparison between observed (red curve) and modelled (blue curve) daily averages of surface atmospheric pressure.

3. METHODOLOGY

With the revisit rate of Sentinel-1, we can assume that between successive SAR pairs, the horizontal velocity stays constant between consecutive differential interferograms [9]. However, the vertical displacement component is highly variable due to atmospheric pressure and tides change on short timescales. By subtracting two consecutive interferograms, it is thus possible to create a double differential interferogram (DDInSAR) that only relies on vertical bias (equation 2).

$$\begin{aligned}\phi_{DDInSAR} &= \phi_{DInSAR_2} - \phi_{DInSAR_1} \\ &\approx \phi_{displ_{H_2}} + \phi_{displ_{V_2}} - (\phi_{displ_{H_1}} + \phi_{displ_{V_1}}) \\ &\approx \phi_{displ_{V_2}} - \phi_{displ_{V_1}}\end{aligned}\quad (2)$$

The $\phi_{displ_{V_1}}$ is associated with a vertical displacement A_1 and the $\phi_{displ_{V_2}}$ with a vertical displacement A_2 . This vertical displacement at a given location is given by equation 3 with its components displayed in Figure 2.

$$A_i(x, y) = \Delta tides_i(x, y) - \Delta pressure_i(x, y) \quad (3)$$

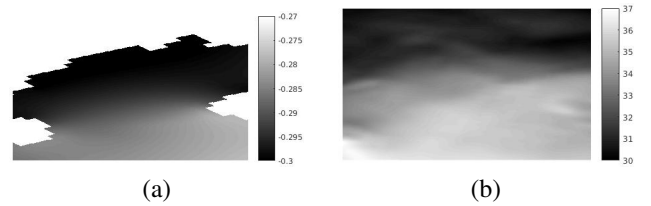


Fig. 2. (a) modelled tides difference [cm] obtained from CATS2008 and (b) modelled surface pressure difference [hPa] obtained from MAR simulations between the October 17 2017 and October 05 2017.

In consequence, the $\phi_{DDInSAR}$ (equation 2) is associated with a vertical displacement given by $A_2 - A_1$ (Figure 3). From this fringe pattern, it is possible to distinguish the grounded area (not affected by tides) from the floating area (in hydrostatic equilibrium), with a transition corresponding to the grounding zone.

After unwrapping the double differential interferometric phase, we can correct each differential interferogram by removing the vertical phase by properly rescaling the DDInSAR component :

$$\Phi_{displ_{H_1}} = \Phi_{DInSAR_1} - \frac{A_1}{A_2 - A_1} \cdot \Phi_{DDInSAR} \quad (4)$$

Where Φ represents the unwrapped phase. Figure 4 represents a simplified flowchart of the Tides/IBE correction.

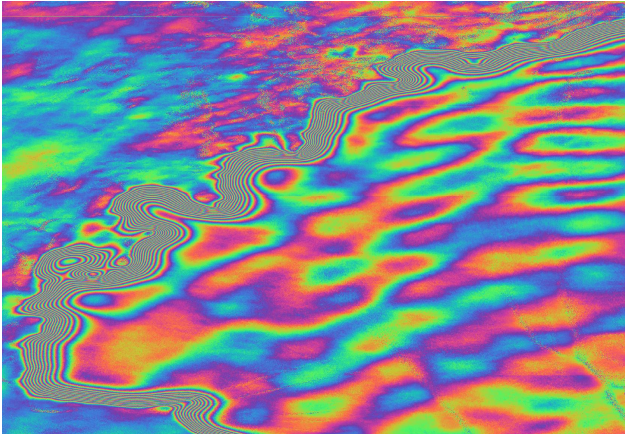


Fig. 3. Double Differential Interferogram.

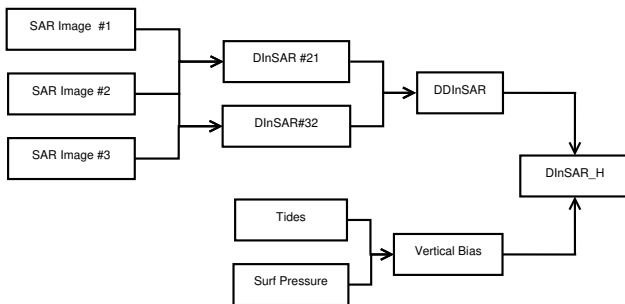


Fig. 4. Flowchart of Tides/IBE correction.

4. RESULTS AND CONCLUSION

Our preliminary results show that the correction brings a totally different interpretation of the fringe pattern (Figure 5).

In Figure 5.a, if interpreting the fringe pattern as only due to horizontal displacement, one would observe an unrealistic sudden horizontal acceleration from left to right. Hence the very high fringe rate in Figure 5.a is an artifact resulting from vertical displacement. The technique used here enables to estimate the corresponding bias (Figure 5.b) and remove it (Figure 5.c).

By making a profile (Figure 6) from left to right of Figure 5, the ice flow is more coherent with physical interpretation of a horizontal displacement, though the little overshoot suggests a small over-correction.

One issue with the technique is that by subtracting two interferograms, the noise component of the interferogram is amplified. The effect can be highly pronounced in the case of an important scale factor $\frac{A_1}{A_2 - A_1}$ in equation 4, when A_1 is, by chance, close to A_2 . Similarly, a high scale factor also amplifies badly modelled tides and IBE.

In the future, we will extend the analysis to Extended Wide-swath mode (EW), more commonly used in polar regions.

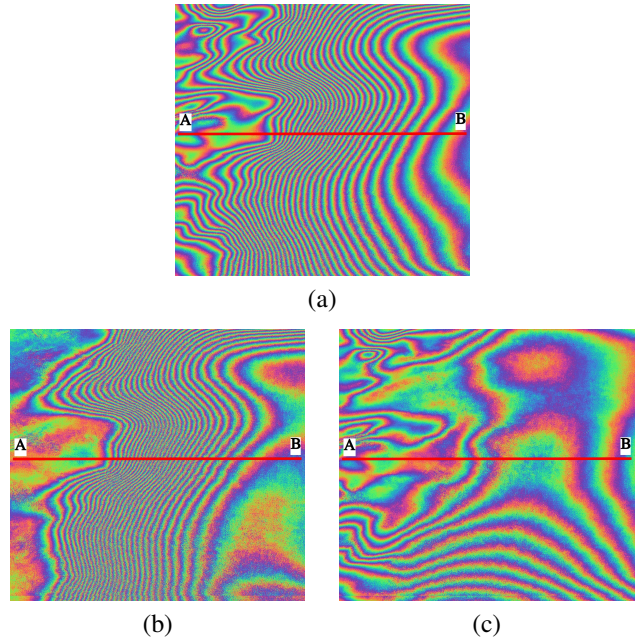


Fig. 5. Correction of a DInSAR. (a) Non-corrected DInSAR, (b) Rescaled rewrapped DDInSAR, (c) Corrected DInSAR.

With the minimum amount of required SAR pairs (three), we can correct the vertical bias related to tides and IBE. However, if we have more data available, we can constrain the problem assuming constant horizontal displacement over a longer time period. Using five consecutive SAR images, we can produce strong connections of vertical bias corrections, adding several degrees of freedom in our equations. Moreover, it can be used to select the DInSAR pairs that minimize the scale factor in equation 4.

5. ACKNOWLEDGMENTS

Carleen Reijmer is acknowledged for providing the data from AWS16. The installation and maintenance of AWS16 was financed by the Belgian Science Policy Office under grant number EN/01/4B supervised by Nicole van Lipzig and Irina Gorodetskaya (KU Leuven). In addition, this research is supported by the French community of Belgium in the funding context of a FRIA grant, and carried out in the framework of the MIMO (Monitoring melt where Ice Meets Ocean) project funded by the Belgian Science Policy contract Nos. SR/00/336.

6. REFERENCES

- [1] Laurie Padman, Matt King, Derek Goring, Hugh Corr, and Richard Coleman, “Ice-shelf elevation changes due

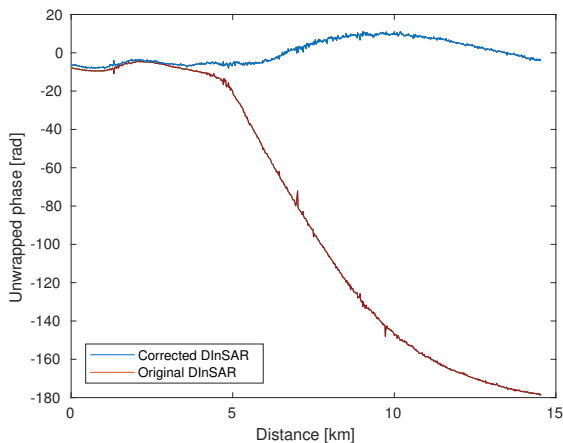


Fig. 6. Comparison between the LOS unwrapped phases along a 14km profile, visible on Figure 5.

to atmospheric pressure variations,” *Journal of Glaciology*, vol. 49, no. 167, pp. 521–526, 2004.

- [2] Matt A. King, Tavi Murray, and Andy M. Smith, “Non-linear responses of Rutford Ice Stream, Antarctica, to semi-diurnal and diurnal tidal forcing,” *Journal of Glaciology*, vol. 56, no. 195, pp. 167–176, 2010.
- [3] Sebastian H.R. Rosier, Oliver J. Marsh, Wolfgang Rack, G. Hilmar Gudmundsson, Christian T. Wild, and Michelle Ryan, “On the interpretation of ice-shelf flexure measurements,” *Journal of Glaciology*, vol. 63, no. 241, pp. 783–791, 2017.
- [4] Wolfgang Rack, Matt A. King, Oliver J. Marsh, Christian T. Wild, and Dana Floricioiu, “Analysis of ice shelf flexure and its InSAR representation in the grounding zone of the southern McMurdo Ice Shelf,” *Cryosphere*, vol. 11, no. 6, pp. 2481–2490, 2017.
- [5] Christian T. Wild, Oliver J. Marsh, and Wolfgang Rack, “Viscosity and elasticity: A model intercomparison of ice-shelf bending in an Antarctic grounding zone,” *Journal of Glaciology*, vol. 63, no. 240, pp. 573–580, 2017.
- [6] Christian T. Wild, Oliver J. Marsh, and Wolfgang Rack, “Unraveling InSAR Observed Antarctic Ice-Shelf Flexure Using 2-D Elastic and Viscoelastic Modeling,” *Frontiers in Earth Science*, vol. 6, no. April, pp. 1–11, 2018.
- [7] Malcolm Mcmillan, Andrew Shepherd, Noel Gourmelon, Jeong Won Park, Peter Nienow, Eero Rinne, and Amber Leeson, “Mapping ice-shelf flow with interferometric synthetic aperture radar stacking,” *Journal of Glaciology*, vol. 58, no. 208, pp. 265–277, 2012.
- [8] Hyangsun Han and Hoonyol Lee, “Tide deflection of campbell glacier tongue, antarctica, analyzed by double-differential SAR interferometry and finite element method,” *Remote Sensing of Environment*, vol. 141, pp. 201–213, 2014.
- [9] Hyangsun Han and Hoonyol Lee, “Tide-corrected flow velocity and mass balance of Campbell Glacier Tongue, East Antarctica, derived from interferometric SAR,” *Remote Sensing of Environment*, vol. 160, pp. 180–192, 2015.
- [10] O. J. Marsh, W. Rack, D. Floricioiu, N. R. Golledge, and W. Lawson, “Tidally induced velocity variations of the beardmore glacier, Antarctica, and their representation in satellite measurements of ice velocity,” *Cryosphere*, vol. 7, no. 5, pp. 1375–1384, 2013.
- [11] Laurie Padman, Helen A. Fricker, Richard Coleman, Susan Howard, and Lana Erofeeva, “A new tide model for the Antarctic ice shelves and seas,” *Annals of Glaciology*, vol. 34, pp. 247–254, 2002.
- [12] C. Amory, A. Trouvilliez, H. Gallée, V. Favier, F. Naaim-Bouvet, C. Genthon, C. Agosta, L. Piard, and H. Bellot, “Comparison between observed and simulated aeolian snow mass fluxes in Adélie Land, East Antarctica,” *Cryosphere*, vol. 9, no. 4, pp. 1373–1383, 2015.
- [13] Institute for Marine and Atmospheric Research (IMAU), “Ice and Climate: Automatic Weather Stations on glaciers,” <https://www.projects.science.uu.nl/iceclimate/aws/antarctica.php>.
- [14] R. Drews, “Evolution of ice-shelf channels in Antarctic ice shelves,” *Cryosphere*, vol. 9, no. 3, pp. 1169–1181, 2015.

Empirical Removal of Tides and Inverse Barometer Effect on DInSAR From Double DInSAR and a Regional Climate Model

Quentin Glaude^{1b}, Graduate Student Member, IEEE, Charles Amory^{1b}, Sophie Berger, Dominique Derauw, Frank Pattyn^{1b}, Christian Barbier, and Anne Orban

Abstract—Ice shelves—the floating extensions of the Antarctic ice sheet—regulate the Antarctic contribution to sea-level rise by restraining the grounded ice flowing from upstream. Therefore, ice-shelf change (e.g., ice-shelf thinning) results in accelerated ice discharge into the ocean, which has a direct effect on sea level. Studying ice-shelf velocity allows the monitoring of the ice shelves' stability and evolution. Differential synthetic aperture radar interferometry (DInSAR) is a common technique from which highly accurate velocity maps can be inferred at high resolution. Because ice shelves are afloat, small sea-level changes—i.e., ocean tides and varying atmospheric pressure (aka inverse barometer effect) lead to vertical displacements. If not accounted for in the interferometric process, these effects will induce a strong bias in the horizontal velocity estimation. In this article, we present an empirical DInSAR correction technique from geophysical models and double DInSAR, with a study on its variance propagation. The method is developed to be used at large coverage on short timescales, essential for the near-continuous monitoring of rapidly changing areas on polar ice sheets. We used Sentinel-1 SAR acquisitions in interferometric wide and extra-wide swath modes. The vertical interferometric bias is estimated using a regional climate model (MAR) and a tide model (CATS2008). The study area is located on the Roi Baudouin Ice Shelf in Dronning Maud Land, East Antarctica. Results show a major decrease ($67 \text{ m}\cdot\text{a}^{-1}$) in the vertical-induced displacement bias.

Index Terms—Antarctica, differential synthetic aperture radar (SAR) interferometry (DInSAR), double DInSAR (DDInSAR), ice shelf, inverse barometer effect (IBE), tides.

I. INTRODUCTION

THINNING of Antarctic ice shelves (the floating extensions of ice sheets [1], [2]) and the corresponding decrease in the restraint experienced by inland ice flow [3], [4] are recognized as major drivers of current Antarctic ice loss [5]. Ice shelves play a crucial role in regulating the Antarctic ice discharge into the ocean because they restrain ice flow as they are often laterally constrained by embayments or locally regrounded on rigid obstacles in the bathymetry [6]. Ice-shelf thinning causes an instantaneous acceleration and a retreat of the grounding line, i.e., the limit between the grounded ice sheet and the floating ice shelf [7]. These consequences lead to an increase in ice discharge into the ocean, hence a contribution to sea level rise.

Radar remote sensing, and interferometry, in particular, is an essential tool to monitor ice-shelf behavior by deriving ice flow fields and tracking grounding line positions over time, among others. This has led to the continental-wide mapping of the surface velocities in Antarctica [8], which is the basis for all major ice-sheet model predictions [9]. Ice velocity is also essential for determining the current state of the ice sheet to determine its basinwise mass balance through the input–output method, in combination with atmospheric modeling [5].

Using pairs of synthetic aperture radar (SAR) images, it is possible to derive surface velocity of the Antarctic ice shelves. Depending on the speed of the ice flow, the SAR sensor and the revisit time of the satellite, one can use techniques based on local correlation maximization, namely speckle tracking [10]–[12] or based on phase shifts measurement using differential SAR Interferometry (DInSAR)[13]. The latter is one order of magnitude more precise, but often less widely applicable. Over ice shelves, the location of individual scatterers can rapidly move from one acquisition to another, leading to important coherence losses if their relative displacement between two dates is greater than a fraction of the wavelength. Adding snow accumulation and compaction, these temporal decorrelation sources are the main limiting factors in SAR interferometry when studying ice sheet [14], [15]. Nevertheless, the subcentimeter accuracy of

Manuscript received February 24, 2020; revised May 3, 2020 and June 30, 2020; accepted July 7, 2020. Date of publication July 10, 2020; date of current version July 24, 2020. This work was supported by the French Community of Belgium in the funding context of an FRIA grant and carried out in the framework of the MIMO (Monitoring melt where Ice Meets Ocean) Project funded by the Belgian Science Policy contract SR/00/336. (Corresponding author: Quentin Glaude.)

Quentin Glaude is with the Laboratoire de Glaciologie, Université libre de Bruxelles, 1050 Brussels, Belgium, and also with the Centre Spatial de Liège, Université de Liège, 4031 Angleur, Belgium (e-mail: qglaude@ulb.ac.be).

Charles Amory is with the Laboratoire de Climatologie, Université de Liège, 4031 Liège, Belgium (e-mail: charles.amory@uliege.be).

Sophie Berger is with the Alfred-Wegener-Institut Helmholtz-Zentrum für Polar-und Meeresforschung, 27570 Bremerhaven, Germany (e-mail: sophie.berger@awi.de).

Dominique Derauw is with the Centre Spatial de Liège, Université de Liège, 4031 Angleur, Belgium, and also with the Instituto de Investigación en Paleobiología y Geología, Universidad Nacional De Rio Negro, 27570 General Roca, Argentina (e-mail: dderauw@uliege.be).

Frank Pattyn is with the Laboratoire de Glaciologie, Université libre de Bruxelles, 8332 Brussels, Belgium (e-mail: fpattyn@ulb.ac.be).

Christian Barbier and Anne Orban are with the Centre Spatial de Liège, Université de Liège, 4031 Angleur, Belgium (e-mail: cbarbier@ulg.ac.be; aorban@ulg.ac.be).

Digital Object Identifier 10.1109/JSTARS.2020.3008497

differential SAR interferometry makes it a first-choice technique for ice motion estimation [16], provided that the method is applicable. For example, Mouginot *et al.* [17] achieved $20 \text{ cm}\cdot\text{a}^{-1}$ velocity accuracy in the interior part of the Antarctic ice sheet, using multiple SAR satellites from ERS to ALOS PALSAR 2.

Unfortunately, for ice shelves, an additional problem appears. When entering the ocean, the ice sheet slowly begins to float and is subject to sea-level fluctuations. These fluctuations will impact the displacement measurement in differential SAR interferometry and, consequently, the horizontal velocity. These vertical displacements are due, on the one hand, to the effects of tides and, on the other hand, to variations in the atmospheric pressure between two dates, causing a hydrostatic readjustment, known as inverse barometer effect (IBE) [18]. Moreover, when studying an area over a short time interval, errors in the velocity estimation are even more accentuated. Working with Sentinel-1 SAR acquisitions at a 6-day revisit time, the vertical bias can be as important as the horizontal velocity that has to be measured.

Compared to previous satellite systems, Sentinel-1's high repeat pass cycle (6–12 days) now allows the evaluation of changes on short time scales, whereas previously, only a mean state could be determined. This has already allowed the determination of subshef melt rates over periods of 1–2 years using Lagrangian techniques [19]–[21]. However, determining the basal mass balance of the ice shelves requires precise velocity divergence fields, which still contain large errors to be accounted for. This paradigm shift in earth observation enables us to study subtle changes in ice dynamics. Nevertheless, these changes are within the error interval produced by tides and IBE, among others, thus require the development of correction methods.

Tides and IBE biases are well-known problems in DInSAR applied in glaciology. Some authors have confronted the physics of the problem, trying to model the ice-shelf bending, according to ice rheology [22]–[26]. While being very efficient, these ice flexure models are also complicated to adapt in every real case study. For instance, the topography of the study area (pinning points, bathymetry, embayment, etc.) brings a complexity rarely taken into account in these models. Other researchers have also developed empirical methods [27]–[30] to correct for tide-related vertical motions, for example by temporally aggregating ERS-1/2 results over longer time series [27], or by computing the deflection ratio to correct tides/IBE biases on Cosmo-SkyMed results [28], [29].

In this article, we describe a fast implementable empirical technique that is capable of removing the main contribution of vertical displacements using double difference SAR interferograms and geophysical models. Using some hypotheses, it also avoids the use of more complex ice physics solutions. The method is presented in Section II. In Section III, we present the study case, the Sentinel-1 SAR images, and the geophysical models used in the study. Section IV exposes the results obtained over the Roi Baudouin Ice Shelf (RBIS), located in Dronning Maud Land, East Antarctica. Section V provides concluding remarks. Finally, uncertainty propagation of the method is formalized in Appendix.

II. METHODOLOGY

A. Differential SAR Interferometry

Interferometry is the superposition of two coherent wavefronts, resulting in a fringe pattern that depends on the local optical path differences. In SAR interferometry (InSAR), this fringe pattern is produced by multiplying the first SAR image by the complex conjugate of the second SAR image leading directly to the interferometric phase. This InSAR phase being the subtraction of the phase of each of the two SAR images, it is directly proportional to the local optical path difference [13].

In terms of phase, this optical path difference is made up by five different terms, namely the orbital phase ϕ_{orb} , the topographic phase ϕ_{topo} , the displacement phase $\phi_{\text{displ}_{\text{LOS}}}$, in the line-of-sight (LOS) direction, the atmospheric phase screen ϕ_{atm} , and an additional noise ϕ_{noise} , given by

$$\begin{aligned}\phi_{\text{InSAR}} &= \phi_{t_2} - \phi_{t_1} \\ &= \phi_{\text{orb}} + \phi_{\text{topo}} + \phi_{\text{displ}_{\text{LOS}}} + \phi_{\text{atm}} + \phi_{\text{noise}}.\end{aligned}\quad (1)$$

Differential SAR Interferometry allows the measure of the phase component related to displacements. Knowing the orbits of the satellites and the topography of the region, the first two terms can be estimated and removed from (1). Precise orbits are generated by the Copernicus Precise Orbit Determination Service. For topography, we use the Dronning Maud Land TanDEM-X DEM created by the Alfred-Wegener Institute [31]. If the atmospheric and noise phase components can be neglected or corrected [32], the differential phase obtained after removing the geometric component is retrieved, leading to direct estimation of the LOS displacement component. The relation between the differential interferometric phase and the LOS displacement is given by

$$\phi_{\text{displ}_{\text{LOS}}} = \frac{4\pi}{\lambda} \cdot \text{displ}_{\text{LOS}} \quad (2)$$

where λ is the radar wavelength (0.0556 m in the case of Sentinel-1) and $\text{displ}_{\text{LOS}}$ is the estimated displacement in meters. Considering the time lapse between SAR acquisitions in the DInSAR processing, we finally obtain the velocity.

Since SAR sensors are side looking, they measure the vector sum of both the vertical and horizontal displacements (displ_{H} and displ_{V}), projected along the LOS according to the incidence angle θ , given by

$$\text{displ}_{\text{LOS}} = \text{displ}_{\text{H}} \cdot \sin \theta + \text{displ}_{\text{V}} \cdot \cos \theta. \quad (3)$$

The last component of the 3-D deformation vector, the along-track displacement, cannot be reliably estimated from a single SAR interferogram.

Separating both the vertical and the horizontal components can only be performed using different viewing geometries or using *a priori* knowledge of the observed displacements (e.g., assuming the determined ice flow only follows the surface slope). From (3), we understand that interpreting the LOS measurement as it comes from a purely horizontal displacement while a vertical one is also present will induce a bias.

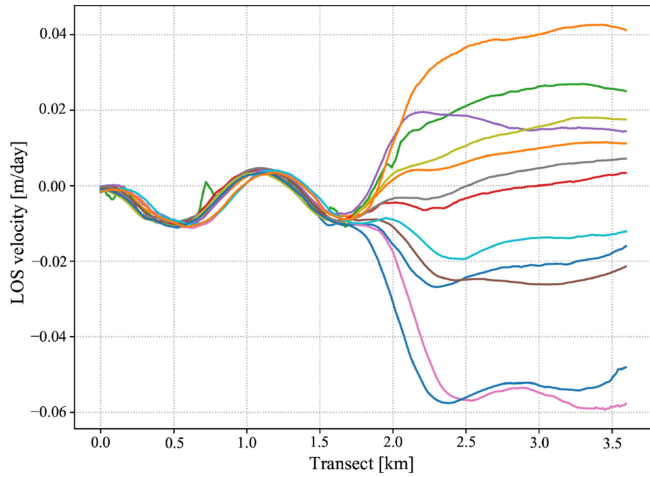


Fig. 1. Sentinel-1 DInSAR-based LOS velocity changes through a transect crossing the grounding zone ($70^{\circ} 45'S$, $24^{\circ} 40'E$), over the period December 2018 to August 2019. Each curve represents a velocity profile determined from 6-day displacements. The velocity change has been set to zero at the start of the transect. Without correction, a vertical displacement brings an additional phase pattern over the ice shelf, which changes significantly for every pair of dates. This effect is negligible over the grounded ice in our region.

B. Tides and IBE

Horizontal and vertical components of the displacement are related to different geophysical processes, which cannot be measured separately without prior hypothesis. Over ice shelves, the horizontal displacements are caused by a horizontal motion of ice that can reach several hundreds of meters per year. These ice shelves move by spreading, due to the pressure balance of the ocean water against the ice front. This horizontal displacement is assumed stable from one acquisition to the other, on a sub-monthly basis [28], [29], though small tidally induced variations can be observed [33]. On the other hand, the vertical displacements of ice shelves are mainly due to short-term variations of the local sea level, which are influenced by tides and variable atmospheric pressure [18].

On the grounded part of the ice sheet, the displacement response to the tides and pressure variations is negligible. On the floating part, which is in hydrostatic equilibrium, the vertical displacement of the ice strictly follows the oceanic readjustment (tides/IBE). In the grounding zone—the transition area between grounded and floating areas—the progressive response to oceanic readjustment is translated into a high fringe rate in the differential interferogram. Converted into velocity, the vertical displacement strongly affects the measure of the surface velocity (see Fig. 1).

Considering a 6-day revisit time (Sentinel-1 in EW mode) and an incidence angle of 33° , erroneously interpreting a 1-m vertical displacement induces a bias of $\pm 95 \text{ m}\cdot\text{a}^{-1}$ in the resulting horizontal flow field. In low-velocity areas, this bias is of the same order of magnitude as the measured speed, misleading the interpretation of the ice dynamics. While increasing the temporal baseline between SAR images may reduce the relative influence of the vertical displacements, it also critically increases the temporal decorrelation and leads to an incoherent interferometric signal.

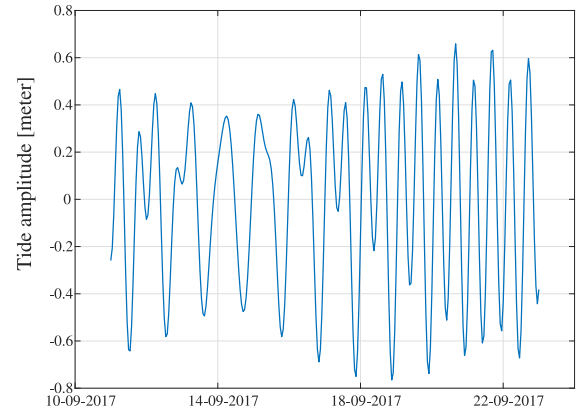


Fig. 2. Tide amplitude estimation between 12 days using CATS2008 model [35] over the RBIS ($70^{\circ} 54'S$, $26^{\circ} 24'E$). Vertical displacements are rapidly varying, even on short timescales.

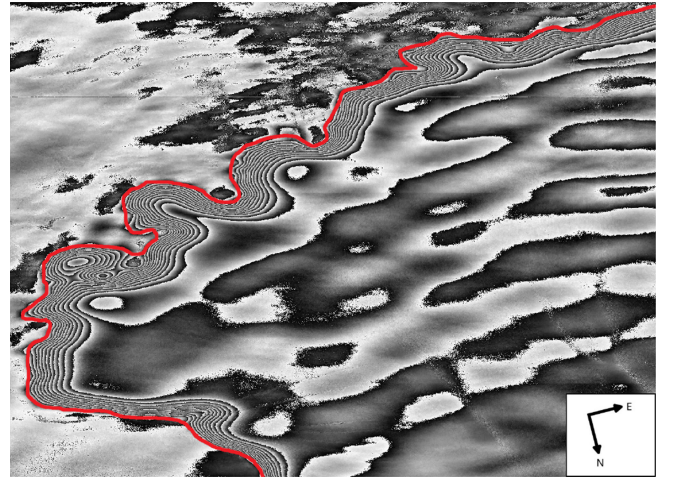


Fig. 3. Double difference Interferogram, represented in azimuth-range geometry. This particular interferogram contains mainly vertical displacement phase components. On the figure, we can delineate the floating from the grounded ice areas thanks to the high fringe pattern, representing the grounding zone. The grounding line is represented in red.

C. Empirical Removal of the Vertical Bias

Over short periods, we can assume that between successive SAR pairs, ice-shelf velocity is constant [29], and observed changes are attributed to rapid fluctuations of tides and IBE. This can be observed estimating tidal amplitudes using the CATS2008 tide model [34], [35] over the RBIS on short time period (see Fig. 2).

Subtracting two consecutive differential interferograms yields a double difference interferogram (double DInSAR or DDInSAR, Fig. 3). This DDInSAR contains the changes in the ice-shelf velocity. These changes are mainly vertical (following the sea-level adjustment to tides and IBE) but small tidally induced horizontal variations can also be observed [25]

$$\begin{aligned}
 \phi_{\text{DDInSAR}} &= \phi_{\text{DInSAR}_2} - \phi_{\text{DInSAR}_1} \\
 &\approx \phi_{\text{displ}_{H_2}} + \phi_{\text{displ}_{V_2}} - (\phi_{\text{displ}_{H_1}} + \phi_{\text{displ}_{V_1}}) \\
 &\approx \phi_{\text{displ}_{V_2}} - \phi_{\text{displ}_{V_1}}.
 \end{aligned} \tag{4}$$

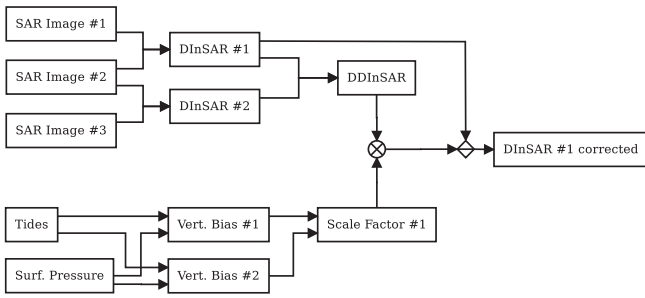


Fig. 4. Flowchart of tides/IBE correction. From three SAR acquisitions, two consecutive differential interferograms can be created. Using geophysical models, vertical biases of each DInSAR is computed (5) at any given position. Finally, a DDInSAR is created (4). This DDInSAR is rescaled to match the vertical bias of the DInSAR, then removed (6). The same reasoning is applied to correct the second differential interferogram. The unwrapping process is not represented here.

$\phi_{\text{displ}_{H_1}}$ is associated with horizontal displacements of the ice shelf between the first two SAR acquisition dates, whereas $\phi_{\text{displ}_{V_1}}$ corresponds to ice-shelf displacements related to a vertical change Δz_1 of the sea level. Similarly, $\phi_{\text{displ}_{H_2}}$ and $\phi_{\text{displ}_{V_2}}$ are related to the displacements between the two following SAR acquisitions dates. The oceanic vertical displacement Δz at a given location (x, y) and time period t is defined by

$$\Delta z_t(x, y) = \Delta \text{tides}_t(x, y) - \Delta \text{pressure}_t(x, y). \quad (5)$$

A difference of tidal amplitudes directly gives the vertical displacement: a positive Δtides is translated into a positive vertical bias, meaning an upward displacement. On the contrary, varying pressure differences $\Delta \text{pressure}$ need to be converted into metric oceanic readjustment. The theoretical IBE value is $-1 \text{ cm} \cdot \text{hPa}^{-1}$ [34], although this theoretical value can slightly change over the different ice shelves or coastal areas [18].

From (4), ϕ_{DDInSAR} (see Fig. 3) is associated with the vertical displacement $\Delta z_2 - \Delta z_1$ between the two considered interferometric pairs. From this double difference fringe pattern, it is possible to distinguish the grounded area (not affected by tides) from the floating area (in hydrostatic equilibrium), with a high-fringe transition corresponding to the grounding zone. This property was already used in [31] and [36] to define the position of the grounding line.

To remove the vertical bias of each differential interferogram, we need to subtract the corresponding vertical phase component. This vertical bias can be estimated by properly rescaling the unwrapped DDInSAR phase component

$$\begin{aligned} \phi_{\text{displ}_{H_1}} &= \phi_{\text{DInSAR}_1} - \phi_{\text{displ}_{\text{tide}/\text{IBE}_1}} \\ &= \phi_{\text{DInSAR}_1} - \frac{\Delta z_1}{\Delta z_2 - \Delta z_1} \cdot \phi_{\text{DDInSAR}} \end{aligned} \quad (6)$$

where $\frac{\Delta z_1}{\Delta z_2 - \Delta z_1}$ is the scale factor applied to the DDInSAR to correct for the bias caused by Δz_1 present in the first differential interferogram DInSAR₁. Fig. 4 represents a simplified flowchart of the tides/IBE correction. One important aspect of this technique is that the DDInSAR simulates the flexure of the ice by assuming elastic behavior, putting aside concepts of ice rheology, such as ice viscosity, flexural rigidity, Young's

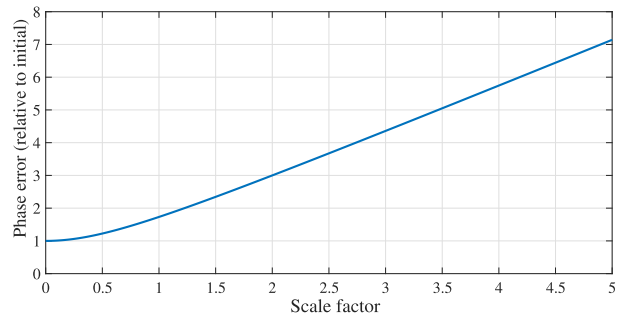


Fig. 5. Standard deviation of the corrected interferogram as a function of the DDInSAR scale factor $\frac{\Delta z_1}{\Delta z_2 - \Delta z_1}$. The more similar the vertical biases, the greater the scale factor and *in fine* the less accurate the correction. Displacement accuracy is linearly dependent on the interferometric phase error.

modulus, or Poisson's ratio. While viscoelastic modeling better represents the bending process in some circumstances, especially at low tide [25], the residuals remain small compared to the tides/IBE bias.

D. Variance Propagation

The scale factor $\frac{\Delta z_1}{\Delta z_2 - \Delta z_1}$ has an important consequence in the estimated accuracy of the corrected interferogram. Focusing only on the interferometric noise, variance propagation of the correction (6) can be expressed as

$$\sigma_{\text{corrected}}^2 = \begin{pmatrix} 1 & \frac{\Delta z_1}{\Delta z_2 - \Delta z_1} \\ 0 & \sigma_{\text{DD}} \end{pmatrix} \cdot \begin{pmatrix} \sigma_{\text{D}} & 0 \\ 0 & \sigma_{\text{DD}} \end{pmatrix} \cdot \begin{pmatrix} 1 \\ \frac{\Delta z_1}{\Delta z_2 - \Delta z_1} \end{pmatrix} \quad (7)$$

where σ_{D} and σ_{DD} are the phase standard deviations of the differential interferogram and the double difference interferogram, respectively. For a pair of interferograms with similar phase standard deviation, this expression leads to

$$\sigma_{\text{corrected}} = \sigma_{\text{D}} \cdot \sqrt{1 + 2 \cdot \left(\frac{\Delta z_1}{\Delta z_2 - \Delta z_1}\right)^2}. \quad (8)$$

This expression is represented in Fig. 5. Since the displacement accuracy is directly proportional to $\sigma_{\text{corrected}}$, it demonstrates the importance of the scale factor in the processing. In cases where interferograms involved in the correction have similar vertical biases, we are more likely to increase the scale factor and consequently the phase noise after correction. Formal quantification of uncertainty is available in the Appendix, including the influence of tidal and atmospheric pressure accuracy, with numerical examples. Depending on the image geometry, coherence, and scale factor, the precision of the corrected horizontal velocity ranges from less than a meter per year accuracy to a few meters per year. If above, we need to consider correcting or not, depending on the interferogram.

E. Network of DInSARs

With a minimum of three SAR images, we can correct the vertical bias related to tides and IBE. However, if we have more data available, we can overconstrain the problem. Each SAR image is combined to its closest acquisition in time to make a

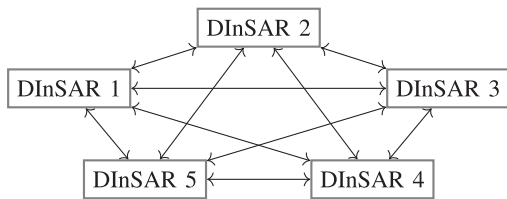


Fig. 6. Interaction graph between five interferograms. In this configuration, each differential interferogram can be corrected four times. Overconstrained problems allow the user to select the DDInSAR that minimizes the scale factor.

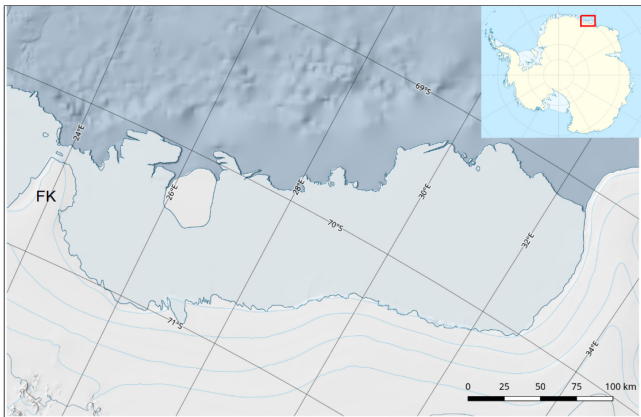


Fig. 7. RBIS, Dronning Maud land, Antarctica. FK: Fran-Kenny Ice Rise. Basemap from [40], with modifications.

differential interferogram. These DInSARs are then connected, generating several double difference interferograms. These connections open up new possibilities for correcting each interferogram, adding several degrees of freedom in our problem. In a configuration where five DInSAR are available, for instance, each differential interferogram can be corrected four times (see Fig. 6). Each of the possible correction introduces a unique scale factor. Having the possibility to select how the interferogram is corrected allows us to select the DInSAR pairs that minimize the scale factor in (6) and (8), reducing the estimated phase variance of the corrected interferogram, and so the uncertainty of the ice-flow fields.

III. DATA

A. Study Case

Our test case focuses on the RBIS, -24 to -33° East), Dronning Maud Land, East Antarctica (see Fig. 7). RBIS has presumably been stable for several millennia [37], [38]. The ice shelf is fed by the Ragnhild glaciers. On the western part of the RBIS, velocity reaches 0.82 m per day ($300 \text{ m} \cdot \text{a}^{-1}$), and have not changed significantly since the 1960s [39]. It is far from spatially homogeneous, and velocity can go below than $100 \text{ m} \cdot \text{a}^{-1}$.

B. SAR Data

In the frame of this work, we used Sentinel-1 SAR single-look-complex (SLC) acquisitions in interferometric wide (IW) swath and extra wide (EW) swath modes. For each mode, we

TABLE I
S1 IW SLC TOPS ACQUISITIONS

SAR Acquisition Date	Time (utc)	Relative Orbit	Pixel Spacing (m)
11/09/2017	18h45	59	2.3×14.1
23/09/2017	18h45	59	2.3×14.1
05/10/2017	18h45	59	2.3×14.1
17/10/2017	18h45	59	2.3×14.1

TABLE II
S1 EW SLC TOPS ACQUISITIONS

SAR Acquisition Date	Time (utc)	Relative Orbit	Pixel Spacing (m)
Period 1			
01/12/2018	18h30	88	5.9×19.9
07/12/2018	18h30	88	5.9×19.9
13/12/2018	18h30	88	5.9×19.9
19/12/2018	18h30	88	5.9×19.9
25/12/2018	18h30	88	5.9×19.9
31/12/2018	18h30	88	5.9×19.9
Period 2			
11/02/2019	18h30	88	5.9×19.9
17/02/2019	18h30	88	5.9×19.9
23/02/2019	18h30	88	5.9×19.9
01/03/2019	18h30	88	5.9×19.9
Period 3			
18/04/2019	18h30	88	5.9×19.9
24/04/2019	18h30	88	5.9×19.9
30/04/2019	18h30	88	5.9×19.9
06/05/2019	18h30	88	5.9×19.9

selected image pairs keeping a high interferometric coherence. IW and EW distinguish themselves by their spatial resolution and coverage. The resolution of IW allows SLC images with a pixel spacing of 2.3×14.1 m (range \times azimuth). The three subswaths obtained by this acquisition mode covers a width of about 250 km. In EW, the swath coverage is increased to 400 km at the cost of a coarser resolution (and increased pixel spacing, i.e., 5.9×19.9 m).

In IW mode, the revisit time over the RBIS is 12 days. We selected a set of four acquisitions for the experiment (see Table I).

For the EW mode, we employed acquisitions from December 2018 to August 2019, with a 6-day revisit time. From this time series, we computed each possible 6-day full-resolution interferogram. We discarded interferogram with coherence below 0.6 over the ice shelf. Finally, we selected the following three periods with useful interferograms (see Table II).

- 1) *December 2018*: Five successive differential interferograms on a one-month time period.
- 2) *February 2019*: Two differential interferograms from four consecutive SAR pairs.
- 3) *April 2019*: Three successive differential interferograms from four consecutive SAR pairs.

The December 2018 time period is particularly interesting because of the number of potential interconnections, as detailed in Section II-E. With five consecutive interferograms, each DInSAR has four possible corrections.

C. Tides and Regional Climate Models

The computation of tides is performed using the CATS2008 model [35]. CATS2008 is a regional high-resolution ocean tide and ocean tide loading model that uses, among others, the ten major tidal components. Besides, the model can produce tide estimates over ice-shelf areas. Linear regression analysis between

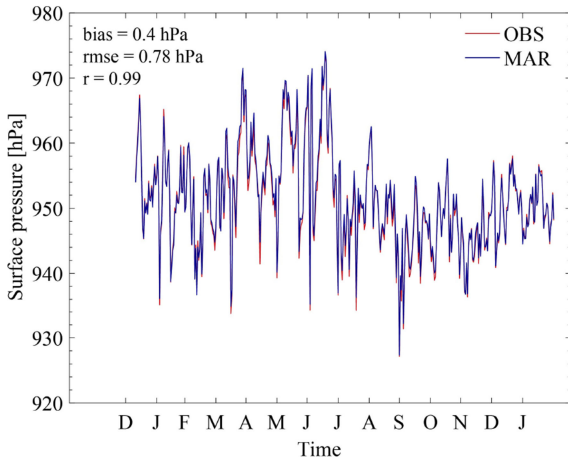


Fig. 8. Comparison of daily mean surface pressure simulated by MAR (blue) and measured on the Fran-Kenny ice rise (red) (see Fig. 7) for the period December 2017–January 2019.

InSAR-based vertical displacements and the CATS2008 model predictions, corrected from IBE, shows a coefficient of determination of 0.938 and a root-mean-square error of 0.5 cm [28]. Over the RBIS, the tidal amplitudes from CATS2008 vary within less than 2 m.

Surface pressure fields are obtained from the regional climate model MAR version 3.10, which is among the state-of-the-art regional climate models to simulate near-surface climate and surface mass balance of the Antarctic ice sheet [16]. MAR has been run at a high spatial resolution (5-km horizontal gridding) on a domain focusing on the RBIS, and forced at its lateral boundaries by atmospheric profiles (pressure, wind speed, temperature, and specific humidity) and at the ocean surface by sea-surface temperatures and sea-ice concentration from ERA5 reanalysis fields [41]. The forcing is prescribed every 6 h, and the model can evolve freely in its inner spatial domain. Simulated surface pressure compares well ($r > 0.99$) with observed surface pressure on the Fran-Kenny Ice Rise (70.3° S, 24.18° E, 266-m asl) west of the RBIS (see Fig. 7), over the period December 2017 to January 2019 (see Fig. 8).

Both tides and atmospheric pressure are slowly varying in space. That allowed some studies to compute tidal estimates at a single location, considered spatially constant over the entire studied region. While this remains true for satellites with low spatial coverage, keeping this hypothesis valid becomes more challenging over wide areas, such as Sentinel-1 250- or 400-k swath coverage, depending on the acquisition mode. Therefore, the vertical bias should be computed on an interpolated grid covering the study area. For instance, components of the vertical bias computed for the October 5th and 17th, 2017 SAR pair are represented in Fig. 9.

IV. RESULTS

Our results show that the correction brings a totally different interpretation of the fringe pattern (see Figs. 10 and 12). For the IW case (see Fig. 10), if interpreting the fringe pattern as

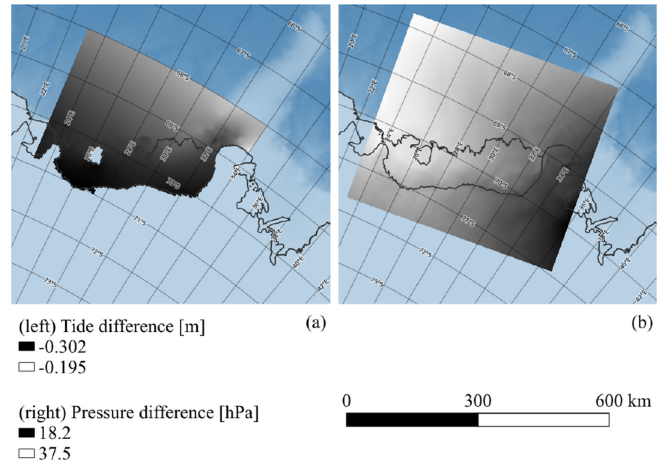


Fig. 9. (a) Modeled tides difference obtained from CATS2008 and (b) modeled surface pressure difference obtained from MAR simulations between October 17th, 2017 and October 5th, 2017. Spatial variability on large scale requires the computation of the vertical bias on grid covering the study area.

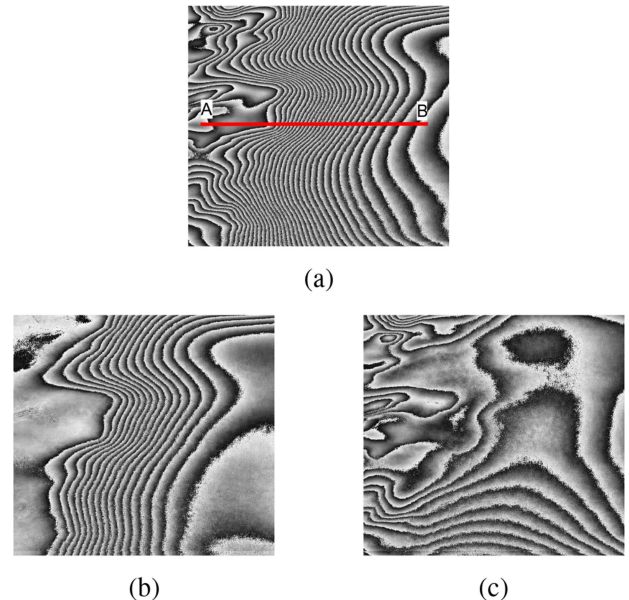


Fig. 10. Correction of a DInSAR over the grounding zone, IW case ($70^\circ 45' S$, $24^\circ 40' E$, with acquisition geometry presented in Fig. 3). (a) Noncorrected DInSAR, (b) rescaled rewrapped DDInSAR, corresponding the vertical phase bias, and (c) corrected DInSAR. Vertical biases phase component is captured through the DDInSAR, which is rescaled then removed from the interferogram. A 4-km profile is visible in Fig. 11.

only due to horizontal displacements, one would observe an unrealistic sudden horizontal acceleration along the profile in Fig. 10(a). This fringe rate is an artifact resulting from vertical displacement, as already observed in Fig. 1. The proposed technique used here allows the estimation and removal of the corresponding bias [see Fig. 10(b) and (c)].

The profile across Fig. 10(a) shows the difference between the LOS displacement with and without correction (see Fig. 11). The estimated LOS velocity without correction shows a $24 \text{ m}\cdot\text{a}^{-1}$ velocity at the edge of the transect. Interpreting it as solely due

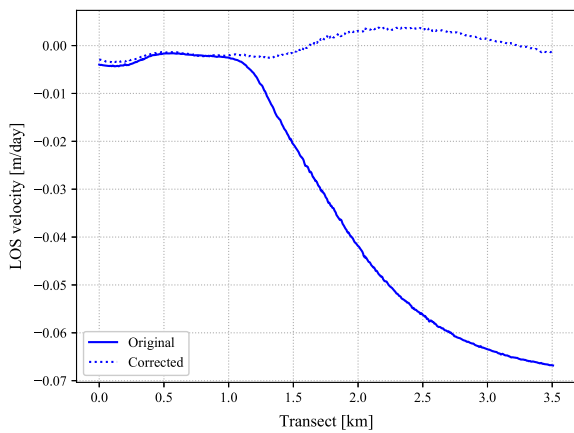
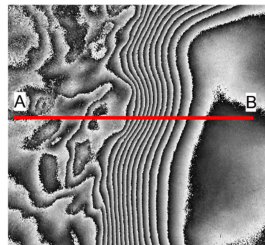
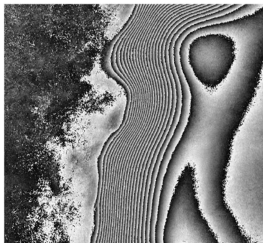


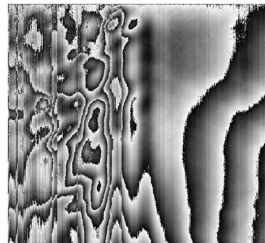
Fig. 11. Comparison between the LOS velocity through a 4-km profile, visible in Fig. 10. The correction manages to reduce the important velocity deviation that occurred in the grounding zone.



(a)



(b)



(c)

Fig. 12. Correction of a DInSAR over the grounding zone, EW case ($70^{\circ}45'S, 24^{\circ}40'E$, with acquisition geometry presented in Fig. 3). (a) Non-corrected DInSAR, (b) DDInSAR, and (c) corrected DInSAR. A 4-km profile is visible in Fig. 13.

to horizontal displacements and with an incidence angle of 21° , this value translates as $67 \text{ m}\cdot\text{a}^{-1}$. After correction, we observe a more realistic displacement of the ice flow, although we also observe a small overshoot, suggesting a slight overcorrection. Nevertheless, the fringe cleaning observed in Fig. 10 shows the validity of the proposed approach. Indirectly, it also constitutes a cross validation of the used tidal and IBE models. Similar observations are met for the EW Sentinel-1 mode (see Figs. 12 and 13). Using consecutive interferograms, we can overconstrained the problem. In Fig. 13, all the different possible solutions are between a few meters per year velocity.

As suggested by (8) and in the Appendix, the technique may amplify the noise component of the interferogram. The effect can

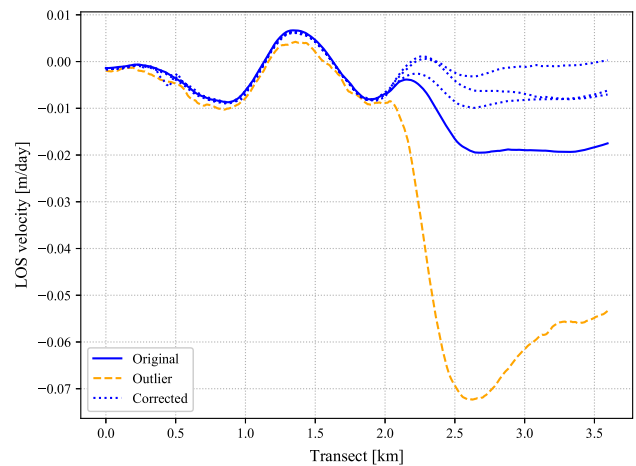


Fig. 13. LOS velocity profiles through a transect crossing the grounding zone (see Fig. 12). The solid blue line represents the LOS velocity prior correction. Over the four possible corrections (dotted curves), three results produced similar corrections (dotted blue). The orange dotted curve represents the correction in a nonideal case, with a scale factor greater than 10.

TABLE III
TIDES AND PRESSURE ESTIMATION FOR DECEMBER 2018 PERIOD
($70^{\circ}54'S, 26^{\circ}24'E$)

SAR Acquisition Date	Time (utc)	pressure [hPa]	tide [m]
01/12/2018	18h30	985.951	-0.2548
07/12/2018	18h30	971.125	0.4156
13/12/2018	18h30	970.732	0.1626
19/12/2018	18h30	983.402	0.0575
25/12/2018	18h30	982.877	0.4597
31/12/2018	18h30	973.336	0.0056

TABLE IV
NUMERICAL EXAMPLE OF DECEMBER 2018 PERIOD
CORRECTION—SENTINEL-1 EW MODE ($70^{\circ}54'S, 26^{\circ}24'E$)

DDInSAR	Δz_1 [m]	Δz_2 [m]	Scaling 1	Scaling 2
(2)-(1)	0.818	-0.249	-0.767	0.233
(3)-(2)	-0.231	-0.249	13.473	14.473
(4)-(3)	0.407	-0.231	-0.637	0.363
(5)-(4)	-0.358	0.407	-0.468	0.532
(5)-(1)	-0.358	0.818	-0.305	0.695
(3)-(1)	-0.231	0.818	-0.221	0.779
(4)-(1)	0.407	0.818	0.991	1.991
(4)-(2)	0.407	-0.249	-0.621	0.379
(5)-(2)	-0.358	-0.249	-3.269	-2.269
(5)-(3)	-0.358	-0.231	-2.826	-1.826

be highly pronounced in the case of an important scale factor $\frac{\Delta z_1}{\Delta z_2 - \Delta z_1}$ in (6), when Δz_1 is, by chance, close to Δz_2 .

This case arose with some of the EW SAR images. Focusing on December 2018 period, we compute for each SAR image the atmospheric pressure (MAR) and the tides (CATS2008). Numerical values for one given position on the RBIS are displayed in Table III, as an example. Based on these values, we can, for each successive interferogram, compute the vertical bias given by (6). As such we can form the double difference interferograms and compute the scale factors to be applied to the DDInSAR to correct each interferogram (see Table IV). In the second row, in bold, the vertical bias of the second and the third interferograms are very similar, resulting in an important scale factor (13.473).

In these cases, the correction is unlikely to produce satisfying results, as shown by the orange curve in Fig. 13.

V. CONCLUSION

Ice shelves are subject to vertical fluctuations related to tides and varying atmospheric pressure, which introduce a bias in the computation of the horizontal displacements by differential SAR interferometry. This effect propagates in the velocity estimation, whose errors are further amplified by the short revisit time of current SAR satellites, such as Sentinel-1. For instance, this bias can reach up to $0.25 \text{ m}\cdot\text{day}^{-1}$ absolute horizontal velocity anomaly with 6-day interferograms, if not corrected. In these cases, this artifact can be as important as the horizontal velocity. Recent SAR satellites have shorter revisit time, which allows the study of ice dynamics and ice shelves at near-continuous timescales. These improvements go along with technical adaptations, which in this case consists of correcting the velocity fields.

Here, we propose a simple approach to correct differential interferograms using scaled double difference interferograms to estimate the phase component due to vertical displacements; this scaling factor being computed from CATS2008 tides and a regional climate model (MAR). The method represents the ice flexure by assuming elastic behavior. It brings a rapid solution to a complex problem while still managing to remove the major contribution due to vertical biases. Working at short timescales over large areas makes the technique in line with current and future SAR satellite constellations.

Results on RBIS with Sentinel-1 in IW and EW modes demonstrate the applicability of the technique. Nevertheless, the technique can suffer from CATS2008/MAR model uncertainties, especially when these estimates are similar from different dates (see Section II-D and Appendix). If the acquisition plan allows us to use more than two SAR pairs, we can overconstrain the problem and limit this effect by selecting the differential interferograms that minimize the estimated phase standard deviation.

The method is sensor independent. In particular, it would be useful to apply it to other sensors, specifically when the revisit time is low, such as Cosmo-Skymed or Radarsat Constellation Mission for example (1 and 4 days, respectively).

APPENDIX

UNCERTAINTY PROPAGATION OF THE METHOD

In this article, a tides/IBE correction has been proposed (6)

$$\phi_{\text{displ}_{H_1}} = \phi_{\text{DInSAR}_1} - \frac{\Delta z_1}{\Delta z_2 - \Delta z_1} \cdot \phi_{\text{DDInSAR}}. \quad (\text{A.9})$$

Tides and atmospheric pressure modeling are tainted with errors, as well as the interferometric phase. These errors are gradually propagated through the method.

The variables that intervene are as follows:

- 1) the tide, estimated with a precision σ_{tide} ;
- 2) the atmospheric pressure, estimated with a precision σ_{pres} ;
- 3) the phase of the differential interferogram, estimated with a precision σ_{D} ; and

- 4) the phase of the double difference interferogram, estimated with a precision σ_{DD} .

The tides and atmospheric pressure are computed independently for each acquisition date. Then, between two dates, a difference of tides and atmospheric pressure is estimated. The resulting difference of tides Δ_{tides} is estimated with a precision $\sqrt{2} \cdot \sigma_{\text{tide}}$. Similarly, the difference of atmospheric pressures Δ_{pressure} is estimated with a precision $\sqrt{2} \cdot \sigma_{\text{pres}}$. By propagation, the vertical displacement Δz (5) is estimated with a precision $\sqrt{2} \cdot \sqrt{\sigma_{\text{tide}}^2 + \sigma_{\text{pres}}^2}$.

This leads us to the scale factor $\frac{\Delta z_1}{\Delta z_2 - \Delta z_1}$. Each Δz_i is considered independent and attached with the precision $\sqrt{2} \cdot \sqrt{\sigma_{\text{tide}}^2 + \sigma_{\text{pres}}^2}$. The variance of the scale factor σ_{scale}^2 is given by the nonlinear propagation of uncertainty

$$\sigma_{\text{scale}}^2 = J \cdot \Sigma \cdot J^T \quad (\text{A.10})$$

with

$$\Sigma = \begin{pmatrix} 2 \cdot (\sigma_{\text{tide}}^2 + \sigma_{\text{pres}}^2) & 0 \\ 0 & 2 \cdot (\sigma_{\text{tide}}^2 + \sigma_{\text{pres}}^2) \end{pmatrix} \quad (\text{A.11})$$

and

$$J = \begin{pmatrix} \frac{\partial \text{scale}}{\partial \Delta z_1} & \frac{\partial \text{scale}}{\partial \Delta z_2} \end{pmatrix} \\ = \begin{pmatrix} \frac{\Delta z_2}{(\Delta z_2 - \Delta z_1)^2} & -\frac{\Delta z_1}{(\Delta z_2 - \Delta z_1)^2} \end{pmatrix} \quad (\text{A.12})$$

which leads to

$$\sigma_{\text{scale}} = \frac{\Delta z_1 + \Delta z_2}{(\Delta z_2 - \Delta z_1)^2} \cdot \sqrt{2} \cdot \sqrt{\sigma_{\text{tide}}^2 + \sigma_{\text{pres}}^2}. \quad (\text{A.13})$$

Finally, the full variance propagation of the correction proposed in (6) can be expressed as [similar reasoning as for (A.13)]

$$\sigma_{\text{corrected}}^2 = J \cdot \Sigma \cdot J^T \quad (\text{A.14})$$

with

$$\Sigma = \begin{pmatrix} \sigma_{\text{D}}^2 & 0 & 0 \\ 0 & \sigma_{\text{DD}}^2 & 0 \\ 0 & 0 & \sigma_{\text{scale}}^2 \end{pmatrix} \quad (\text{A.15})$$

and

$$J = \left(1 \quad \frac{\Delta z_1}{\Delta z_2 - \Delta z_1} \quad -\phi_{\text{DD}} \right) \quad (\text{A.16})$$

For a pair of interferograms with similar phase standard deviation, we can estimate the precision of the double difference to be $\sqrt{2} \cdot \sigma_{\text{D}}$. The resulting standard deviation of the corrected phase is given by

$$\sigma_{\text{corrected}} = \sqrt{\sigma_{\text{D}}^2 \cdot \left(1 + 2 \cdot \left(\frac{\Delta z_1}{\Delta z_2 - \Delta z_1} \right)^2 \right) + \phi_{\text{DD}}^2 \cdot \sigma_{\text{scale}}^2} \quad (\text{A.17})$$

With σ_{scale}^2 expressed in (A.13), σ_{D} can be estimated thanks to the Cramér Rao bound

$$\sigma_{\text{D}} = \frac{1}{\sqrt{2N}} \cdot \sqrt{\frac{1 - \gamma^2}{\gamma^2}} \quad (\text{A.18})$$

with N the number of looks and γ the interferometric coherence.

Equation (A.17) is the precision associated to the unwrapped corrected interferometric phase. This mathematical expression can be interpreted as follows: first part of the right-hand side expression translates how the scale factor increases the interferometric phase accuracy, whereas the second part expresses how the precision of the scale factor will affect the amount of unwrapped double difference interferometric phase that is removed.

To convert the corrected phase into horizontal velocity error estimates, the factor $\frac{\lambda}{B_t \cdot 4\pi \cdot \sin \theta}$ has to be applied, λ being the wavelength, θ the incidence angle, and B_t the temporal baseline between acquisitions.

As a practical example, with a coherence of 0.8, 12 looks, an incidence angle of 33° , Δz_1 of 0.50 m, Δz_2 of -0.25 m, a tide accuracy of 1 cm, and an atmospheric pressure accuracy of 0.7 hPa, the resulting absolute phase error is 1.104 rad, i.e., $0.55 \text{ m}\cdot\text{a}^{-1}$ accuracy. If the accuracy of the tides becomes 5 cm, the velocity precision is $2.23 \text{ m}\cdot\text{a}^{-1}$, to put in comparison to the $-46.8 \text{ m}\cdot\text{a}^{-1}$ brought by the tides and IBE bias in the first interferogram.

In a less ideal configuration with Δz_2 of 0.40 m, the estimated velocity error of the correction becomes around $7.01 \text{ m}\cdot\text{a}^{-1}$.

In Section IV, an extreme case where Δz_1 and Δz_2 are equal to -0.231 and -0.249 m, respectively, is presented. The scale and the uncertainty around this scale factor become too important to use the technique, with an annual velocity precision that can exceed the hundred of meters per year if the tides are poorly estimated.

ACKNOWLEDGMENT

The authors would like to thank J. Lenaerts for providing the weather station data on the Fran-Kenny Ice Rise. They would also like to thank the Norwegian Polar Institute for the Quantarctica package. TanDEM-X data originate from the German Aerospace Center (ATI-GLAC0267).

REFERENCES

- [1] H. D. Pritchard, S. R. M. Ligtenberg, H. A. Fricker, D. G. Vaughan, M. R. V. D. Broeke, and L. Padman, "Antarctic ice-sheet loss driven by basal melting of ice shelves," *Nature*, vol. 484, no. 7395, pp. 502–505, 2012. [Online]. Available: <http://dx.doi.org/10.1038/nature10968>
- [2] F. S. Paolo, H. A. Fricker, and L. Padman, "Volume loss from Antarctic ice shelves is accelerating," *Science*, vol. 348, no. 6232, pp. 327–331, 2015. [Online]. Available: <https://science.sciencemag.org/content/348/6232/327>
- [3] A. J. Payne, A. Vieli, A. P. Shepherd, D. J. Wingham, and E. Rignot, "Recent dramatic thinning of largest West-Antarctic ice stream triggered by oceans," *Geophys. Res. Lett.*, vol. 31, 2004, Paper L23401. [Online]. Available: <http://dro.dur.ac.uk/1231/>
- [4] H. D. Pritchard, R. J. Arthern, D. G. Vaughan, and L. A. Edwards, "Greenland and Antarctic ice sheets," *Nature*, vol. 461, no. 7266, pp. 971–975, 2009. [Online]. Available: <http://dx.doi.org/10.1038/nature08471>
- [5] A. Shepherd *et al.*, "Mass balance of the Antarctic ice sheet from 1992 to 2017," *Nature*, vol. 558, no. 7709, pp. 219–222, 2018.
- [6] L. Favier and F. Pattyn, "Antarctic ice rise formation, evolution, and stability," *Geophys. Res. Lett.*, vol. 42, no. 11, pp. 4456–4463, 2015. [Online]. Available: <https://agupubs.onlinelibrary.wiley.com/doi/abs/10.1002/2015GL064195>
- [7] D. Goldberg, D. M. Holland, and C. Schoof, "Grounding line movement and ice shelf buttressing in marine ice sheets," *J. Geophys. Res., Earthq. Surf.*, vol. 114, no. F4, 2009, Art. no. F04026. [Online]. Available: <https://agupubs.onlinelibrary.wiley.com/doi/abs/10.1029/2008JF001227>
- [8] E. Rignot, J. Mouginot, and B. Scheuchl, "Ice flow of the Antarctic ice sheet," *Science*, vol. 333, no. 6048, pp. 1427–1430, 2011. [Online]. Available: <https://science.sciencemag.org/content/333/6048/1427>
- [9] L. Favier *et al.*, "Retreat of Pine Island Glacier controlled by marine ice-sheet instability," *Nature Climate Change*, vol. 5, no. 2, pp. 1–5, 2014. [Online]. Available: <http://dx.doi.org/10.1038/nclimate2094>
- [10] L. D. Euillades *et al.*, "Detection of glaciers displacement time-series using SAR," *Remote Sens. Environ.*, vol. 184, pp. 188–198, 2016. [Online]. Available: <http://dx.doi.org/10.1016/j.rse.2016.07.003>
- [11] F. Pattyn and D. Derauw, "Ice-dynamic conditions of Shirase Glacier, Antarctica, inferred from ERS SAR interferometry," *J. Glaciology*, vol. 48, no. 163, pp. 559–565, 2002.
- [12] F. Casu, A. Manconi, A. Pepe, and R. Lanari, "Deformation time-series generation in areas characterized by large displacement dynamics: The SAR amplitude pixel-offset SBAS technique," *IEEE Trans. Geosci. Remote Sens.*, vol. 49, no. 7, pp. 2752–2763, Jul. 2011.
- [13] D. Massonet *et al.*, "The displacement field of the Landers earthquake mapped by radar interferometry," *Nature*, vol. 364, no. 6433, pp. 138–142, 1993.
- [14] J. Mouginot, B. Scheuch, and E. Rignot, "Mapping of ice motion in Antarctica using synthetic-aperture radar data," *Remote Sens.*, vol. 4, no. 9, pp. 2753–2767, 2012.
- [15] I. Joughin, B. E. Smith, and W. Abdalati, "Glaciological advances made with interferometric synthetic aperture radar," *J. Glaciology*, vol. 56, no. 200, pp. 1026–1042, Dec. 2010.
- [16] R. Mottram *et al.*, "What is the surface mass balance of Antarctica? An intercomparison of regional climate model estimates," *Cryosphere Discuss.*, vol. 2020, pp. 1–42, 2020. [Online]. Available: <https://www.the-cryosphere-discuss.net/tc-2019--333/>
- [17] J. Mouginot, E. Rignot, and B. Scheuchl, "Continent-wide, interferometric SAR phase, mapping of Antarctic ice velocity," *Geophys. Res. Lett.*, vol. 46, no. 16, pp. 9710–9718, 2019. [Online]. Available: <https://agupubs.onlinelibrary.wiley.com/doi/abs/10.1029/2019GL083826>
- [18] L. Padman, M. King, D. Goring, H. Corr, and R. Coleman, "Ice-shelf elevation changes due to atmospheric pressure variations," *J. Glaciology*, vol. 49, no. 167, pp. 521–526, 2004.
- [19] P. Dutrieux *et al.*, "Pine island glacier ice shelf melt distributed at kilometre scales," *Cryosphere*, vol. 7, no. 5, pp. 1543–1555, 2013. [Online]. Available: <https://www.the-cryosphere.net/7/1543/2013/>
- [20] G. Moholdt, L. Padman, and H. A. Fricker, "Basal mass budget of ross and Filchner-Ronne ice shelves, Antarctica, derived from Lagrangian analysis of ICESat altimetry," *J. Geophys. Res., Earthq. Surf.*, vol. 119, no. 11, pp. 2361–2380, 2014. [Online]. Available: <https://agupubs.onlinelibrary.wiley.com/doi/abs/10.1002/2014JF003171>
- [21] S. Berger, R. Drews, V. Helm, S. Sun, and F. Pattyn, "Detecting high spatial variability of ice shelf basal mass balance, Roi Baudouin ice shelf, Antarctica," *Cryosphere*, vol. 11, no. 6, pp. 2675–2690, 2017. [Online]. Available: <https://www.the-cryosphere.net/11/2675/2017/>
- [22] M. A. King, T. Murray, and A. M. Smith, "Non-linear responses of Rutford ice stream, Antarctica, to semi-diurnal and diurnal tidal forcing," *J. Glaciology*, vol. 56, no. 195, pp. 167–176, 2010.
- [23] S. H. Rosier, O. J. Marsh, W. Rack, G. H. Gudmundsson, C. T. Wild, and M. Ryan, "On the interpretation of ice-shelf flexure measurements," *J. Glaciology*, vol. 63, no. 241, pp. 783–791, 2017.
- [24] W. Rack, M. A. King, O. J. Marsh, C. T. Wild, and D. Floricioiu, "Analysis of ice shelf flexure and its InSAR representation in the grounding zone of the southern McMurdo Ice Shelf," *Cryosphere*, vol. 11, no. 6, pp. 2481–2490, 2017.
- [25] C. T. Wild, O. J. Marsh, and W. Rack, "Viscosity and elasticity: A model intercomparison of ice-shelf bending in an Antarctic grounding zone," *J. Glaciology*, vol. 63, no. 240, pp. 573–580, 2017.
- [26] C. T. Wild, O. J. Marsh, and W. Rack, "Unraveling InSAR observed Antarctic ice-shelf flexure using 2-D elastic and viscoelastic modeling," *Frontiers Earth Sci.*, vol. 6, 2018, Art. no. 28. [Online]. Available: <https://www.frontiersin.org/article/10.3389/feart.2018.00028>
- [27] M. Mcmillan *et al.*, "Mapping ice-shelf flow with interferometric synthetic aperture radar stacking," *J. Glaciology*, vol. 58, no. 208, pp. 265–277, 2012.
- [28] H. Han and H. Lee, "Tide deflection of Campbell Glacier Tongue, Antarctica, analyzed by double-differential SAR interferometry and finite element method," *Remote Sens. Environ.*, vol. 141, pp. 201–213, 2014. [Online]. Available: <http://dx.doi.org/10.1016/j.rse.2013.11.002>

- [29] H. Han and H. Lee, "Tide-corrected flow velocity and mass balance of Campbell Glacier Tongue, East Antarctica, derived from interferometric SAR," *Remote Sens. Environ.*, vol. 160, pp. 180–192, 2015. [Online]. Available: <http://dx.doi.org/10.1016/j.rse.2015.01.014>
- [30] O. J. Marsh, W. Rack, D. Floricioiu, N. R. Golledge, and W. Lawson, "Tidally induced velocity variations of the beardmore glacier, Antarctica, and their representation in satellite measurements of ice velocity," *Cryosphere*, vol. 7, no. 5, pp. 1375–1384, 2013.
- [31] M. Ruckamp, N. Neckel, S. Berger, A. Humbert, and V. Helm, "Calving induced speedup of Petermann Glacier," *J. Geophys. Res., Earthq. Surf.*, vol. 124, no. 1, pp. 216–228, 2019. [Online]. Available: <https://agupubs.onlinelibrary.wiley.com/doi/abs/10.1029/2018JF004775>
- [32] G. Gomba, A. Parizzi, F. De Zan, M. Eineder, and R. Bamler, "Toward operational compensation of ionospheric effects in SAR interferograms: The split-spectrum method," *IEEE Trans. Geosci. Remote Sens.*, vol. 54, no. 3, pp. 1446–1461, Mar. 2016.
- [33] G. H. Gudmundsson, "Tides and the flow of Rutford ice stream, West Antarctica," *J. Geophys. Res., Earthq. Surf.*, vol. 112, no. F4, 2007, Art. no. F04007. [Online]. Available: <https://agupubs.onlinelibrary.wiley.com/doi/abs/10.1029/2006JF000731>
- [34] L. Padman, H. A. Fricker, R. Coleman, S. Howard, and L. Erofeeva, "A new tide model for the Antarctic ice shelves and seas," *Ann. Glaciology*, vol. 34, pp. 247–254, 2002.
- [35] L. Padman, S. Y. Erofeeva, and H. A. Fricker, "Improving Antarctic tide models by assimilation of ICESat laser altimetry over ice shelves," *Geophys. Res. Lett.*, vol. 35, no. 22, 2008, Art. no. L22504. [Online]. Available: <https://agupubs.onlinelibrary.wiley.com/doi/abs/10.1029/2008GL035592>
- [36] E. Rignot, J. Mouginot, and B. Scheuchl, "Antarctic grounding line mapping from differential satellite radar interferometry," *Geophys. Res. Lett.*, vol. 38, no. 10, 2011, Art. no. L10504. [Online]. Available: <https://agupubs.onlinelibrary.wiley.com/doi/abs/10.1029/2011GL047109>
- [37] R. Drews, "Evolution of ice-shelf channels in Antarctic ice shelves," *Cryosphere*, vol. 9, no. 3, pp. 1169–1181, 2015.
- [38] D. Callens, R. Drews, E. Witrant, M. Philippe, and F. Pattyn, "Temporally stable surface mass balance asymmetry across an ice rise derived from radar internal reflection horizons through inverse modeling," *J. Glaciology*, vol. 62, no. 233, pp. 525–534, 2016.
- [39] S. Berger, L. Favier, R. Drews, J.-J. Derwael, and F. Pattyn, "The control of an uncharted pinning point on the flow of an Antarctic ice shelf," *J. Glaciology*, vol. 62, no. 231, p. 37–45, 2016.
- [40] K. Matsuoka, A. Skoglund, and G. Roth, "Quantarctica," 2018. [Online]. Available: <https://doi.org/10.21334/npolar.2018.8516e961>
- [41] H. Hersbach and D. Dee, "Era5 reanalysis is in production," *ECMWF Newsl.*, vol. 147, no. 7, pp. 5–6, 2016.



Quentin Glaude (Graduate Student Member, IEEE) received the master's degree in geomatics in 2017. He is currently working toward the Ph.D. degree in cograduation with the Universite Libre de Bruxelles (ULB) Brussels, Belgium, and the Universite de Liege (ULiege), Liège, Belgium. His Ph.D. thesis aims at improving the short-term monitoring of ice shelves using TOPSAR mode.

He is a Remote Sensing Specialist, especially in SAR remote sensing and TOPSAR interferometry. His research is supported by the French Community of Belgium in the funding context of a FRIA grant.



Charles Amory received the master's degree in environmental and earth sciences and the Ph.D. degree in Antarctic climate from the University Grenoble Alpes, Saint-Martin-d'Hères, France, in 2012 and 2016, respectively.

Since then has been a Postdoctoral Researcher with the FNRS, University of Liège, Liège, Belgium. His research interests include the climate system over the Antarctic and the Greenland ice sheets. He is mainly involved in the development and use of the regional climate model MAR designed to simulate climate specificities of polar regions and collection and analysis of meteorological data in polar environments, with a particular emphasis on drifting snow processes.



Sophie Berger received the Ph.D. degree in stability of Antarctic ice shelves from the Universite Libre de Bruxelles, Brussels, Belgium, in 2017.

She is currently a Postdoc with the Alfred Wegener Institut, Bremerhaven, Germany. She is working on various remote sensing data and techniques to investigate the dynamics and stability of the ice shelves in Dronning Maud Land (East Antarctica). She tweets as @SoBrgr.



Dominique Derauw received the M.Sc. degree in physics and the Ph.D. degree in sciences from the University of Liège, Liège, Belgium, in 1989 and 1999, respectively.

He is currently an Assistant Professor with the University of Rio Negro, General Roca, Argentina, a research fellow with the Ecole de Commerce et de Gestion, Luxembourg City, Luxembourg, and a Project Manager with the Signal Processing Lab, Centre Spatial de Liège, Liège, Belgium. His researches concentrate on SAR remote sensing and interferometric SAR applications and developments.



Frank Pattyn received the Ph.D. degree in sciences from the Vrije Universiteit Brussel, Brussels, Belgium, in 1998.

He is currently a Full Professor with the Université libre de Bruxelles, Brussels, Belgium. His research concentrates on Antarctic ice dynamics and ice sheet modeling. He is a President of the Belgian National Committee for Antarctic Research and the Associate Chief Editor of *Journal of Glaciology*.



Christian Barbier received the master's degree in physics mathematical physics and the Ph.D. degree in physics (unimolecular decay of electronically excited ions) from the University of Liège, Liège, Belgium, in 1980 and 1983, respectively.

He pursued a theoretical physicist career in the field of *ab initio* quantum mechanical calculation of linear and nonlinear optical properties of organic molecules and polymers. He entered Centre Spatial de Liège, in 1988 and began to be active in the field of SAR soon thereafter. Through ESA and Belgian government contract, he set up SAR image reconstruction and interferometry. He headed the Signal Processing Laboratory from 1989 to 2017. He also has teaching activities with the University of Liège with courses on theoretical cosmology, remote sensing, and space mission designs.



Anne Orban received the M.S. degree in physics in ionizing radiation and radioprotection from the Université Catholique de Louvain, Ottignies-Louvain-la-Neuve, Belgium, in 1987.

Since 1988, she has been with the Centre Spatial de Liège, Liège, Belgium, first in the Space Environment group, then in the Signal Processing Laboratory since 2017. Her main research interests are oriented toward remote sensing and earth observation, including SAR processing and InSAR, PolSAR, and PolInSAR applications.

2.2.2.4 An Observed Stable Grounding Line Around the Roi Baudouin Ice Shelf

We noticed in previous sections that tides and inverse barometer effect have a strong influence on the velocity measurements from DInSAR or even offset tracking techniques. Although we developed methods to correct these biases, we can also use these noticeable effects to determine the grounding line location, i.e. the limit between the grounded ice and the floating ice shelf.

By using the technique of the double differential interferometry - DDInSAR, we have information about vertical changes in the ice-shelf elevation and so a distinction between the grounded ice and the ice shelf. Using this information, precise delineation of the grounding line can be operated.

We analyzed Sentinel-1 image double pairs, 6 days apart, with a common date between the two pairs. We limit the period from 2018 to 2020. The complete process of grounding line delineation is presented in Fig. 2.46.

From the DDInSAR, we can manually determine the grounding line (Fig. 2.47). From our results, the grounding line is varying within a one-kilometer range. In some cases, the continuity of the grounding line mapping is compromised by a low interferometric signal. These cases occurred in the presence of blue ice, near the grounding line, especially of the Eastern part of the RBIS. Overall, no grounding line retreat is observed, and we conclude that the grounding line positions are rather stable through time, especially in comparison with grounding line locations in 1996, 2000, and 2007, using ERS, RADARSAT, and ALOS (Rignot et al., 2011a).

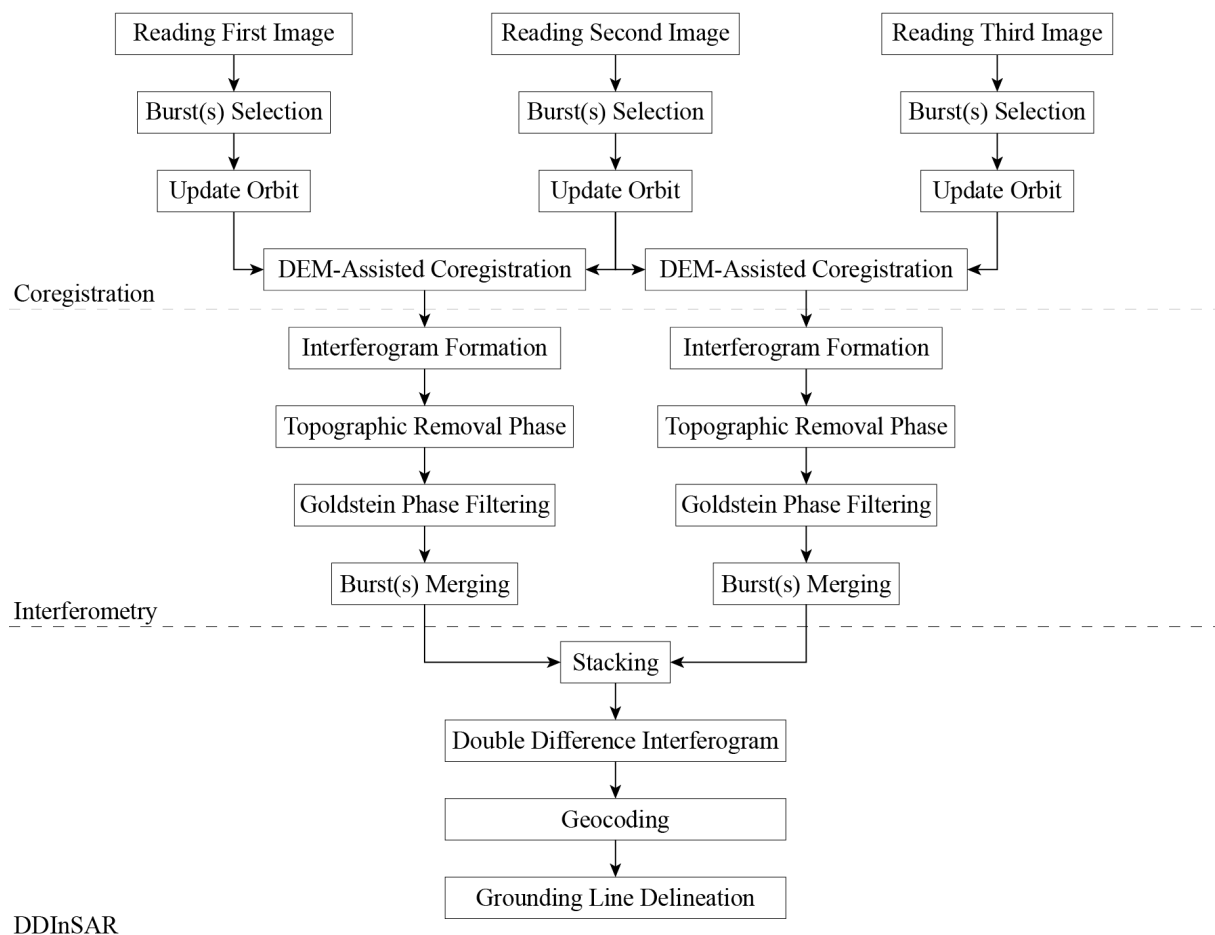


Figure 2.46: Processing Scheme of Double Difference Interferometry for grounding line extraction.

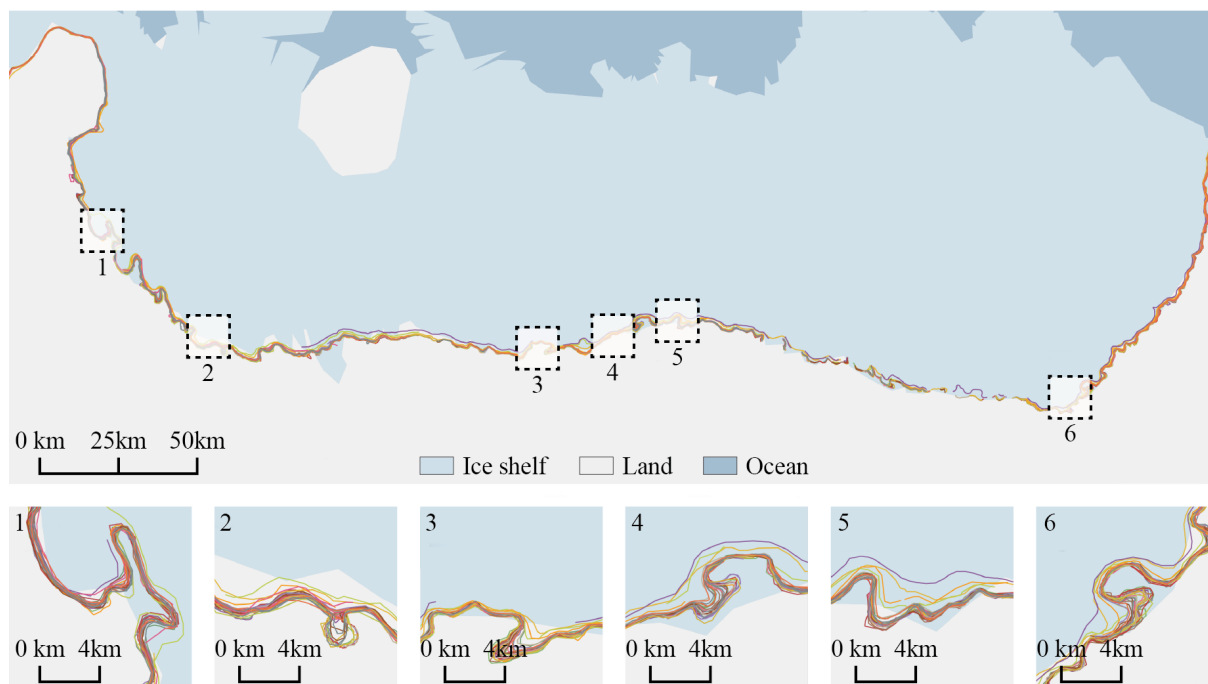


Figure 2.47: Grounding line migration over the RBIS (2018 to 2020).

2.2.2.5 Detection of Landfast Sea Ice Along the Calving Front from Dual Polarimetric SAR Interferometry

In Antarctica, ice-shelves boundaries are surrounded by sea ice. This sea ice, with ice *mélange*, participates in a portion of the buttressing properties of the ice shelf (Robel, 2017). Sea ice has different polarimetric responses in SAR remote sensing. We demonstrate the potential of using both HH and HV polarimetry of Extended Wide-swath Sentinel-1 products in order to detect landfast sea ice areas.

Using a pair of EW SAR images, we can compute an interferogram. The HH and HV interferograms are quite similar in most regions. Nevertheless, in coastal regions, the presence of stable sea ice is visible in the co-polarized interferometric coherence, but the cross-polarized interferogram has a very weak return signal. It is possible to use this property to perform semantic segmentation of landfast sea ice around ice shelves, which is rather generally performed using optical or thermal infrared sensors (Fraser et al., 2020). Fig. 2.48 shows the coherence in HH and HV polarizations. This is this coherence difference that will be used to detect sea ice.

The idea of the semantic segmentation proposed here is to take advantage of that difference to delineate thin ice areas. A priori, the difference between HH and HV is high where sea ice is. The simple difference is somehow noisy (Fig. 2.49 and 2.50, top left). We performed a cascade of 3 average filters (5x5) to filter and enhance the difference between the two *a priori* classes (Fig. 2.49 and 2.50, top right).

Sampling sea ice values, we set a threshold beyond which the pixel is considered as belonging to sea ice. By mathematical morphology, we can reduce erratic pixels. In our case, we used a closing operator of size 7x7 (Fig. 2.49 and 2.50, middle left). Then, a cascade of 2 median filters of a large window size is employed (11x11) (Fig. 2.49 and 2.50, middle right). Superimposed results are visible in Fig. 2.49 and 2.50, bottom.

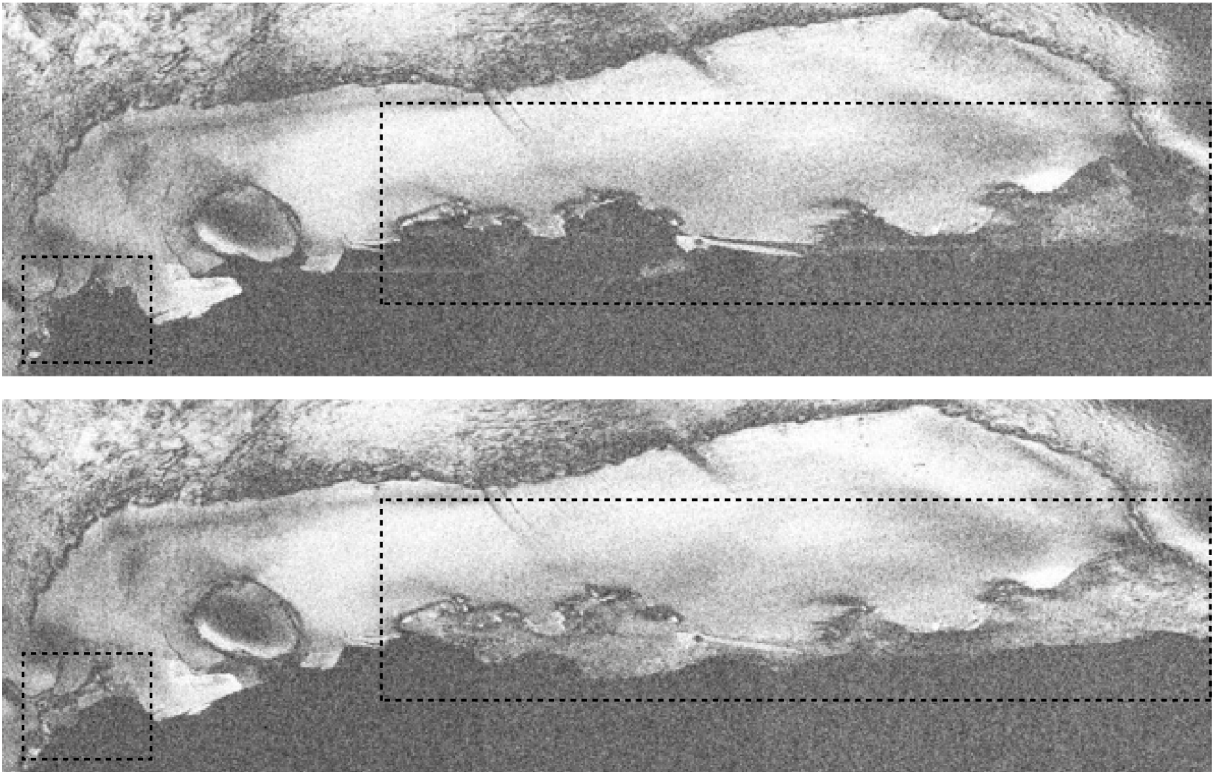


Figure 2.48: Comparison between HV and HH coherence. Top = HV ; Bottom = HH. Dark areas in the bottom of the images represent the ocean. However, near the ice-shelf, HH polarization enables the recognition of stable sea ice.

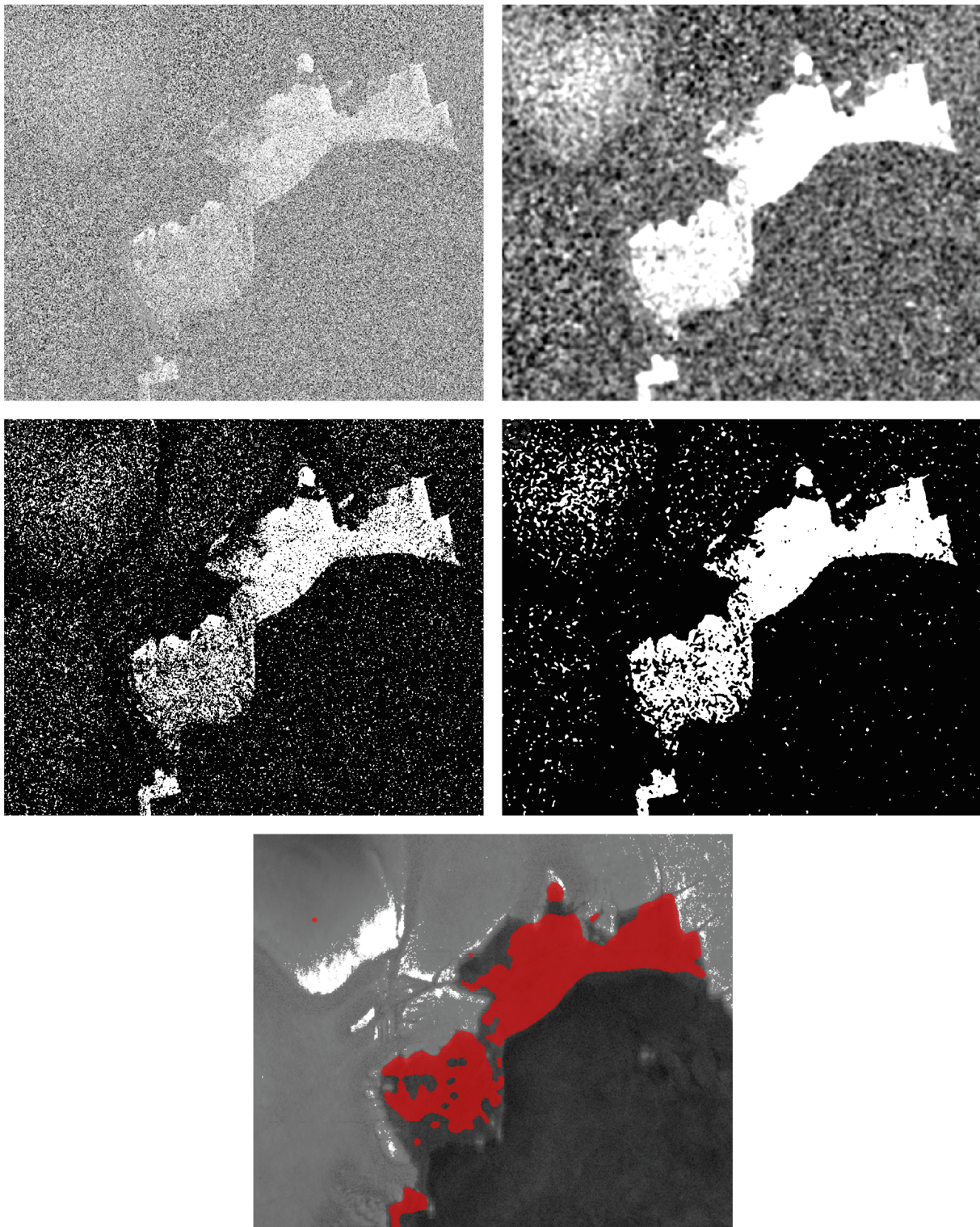


Figure 2.49: Process of the stable sea ice detection algorithm. The area cover the left square of Fig. 2.48. Top-left = difference between HH and HV coherence. Top-right = average filter output (5x5). Center-left = classification by thresholding. Center-right = classification enhancement by mathematical morphology. Bottom = classification overlay (red) on HV coherence image.

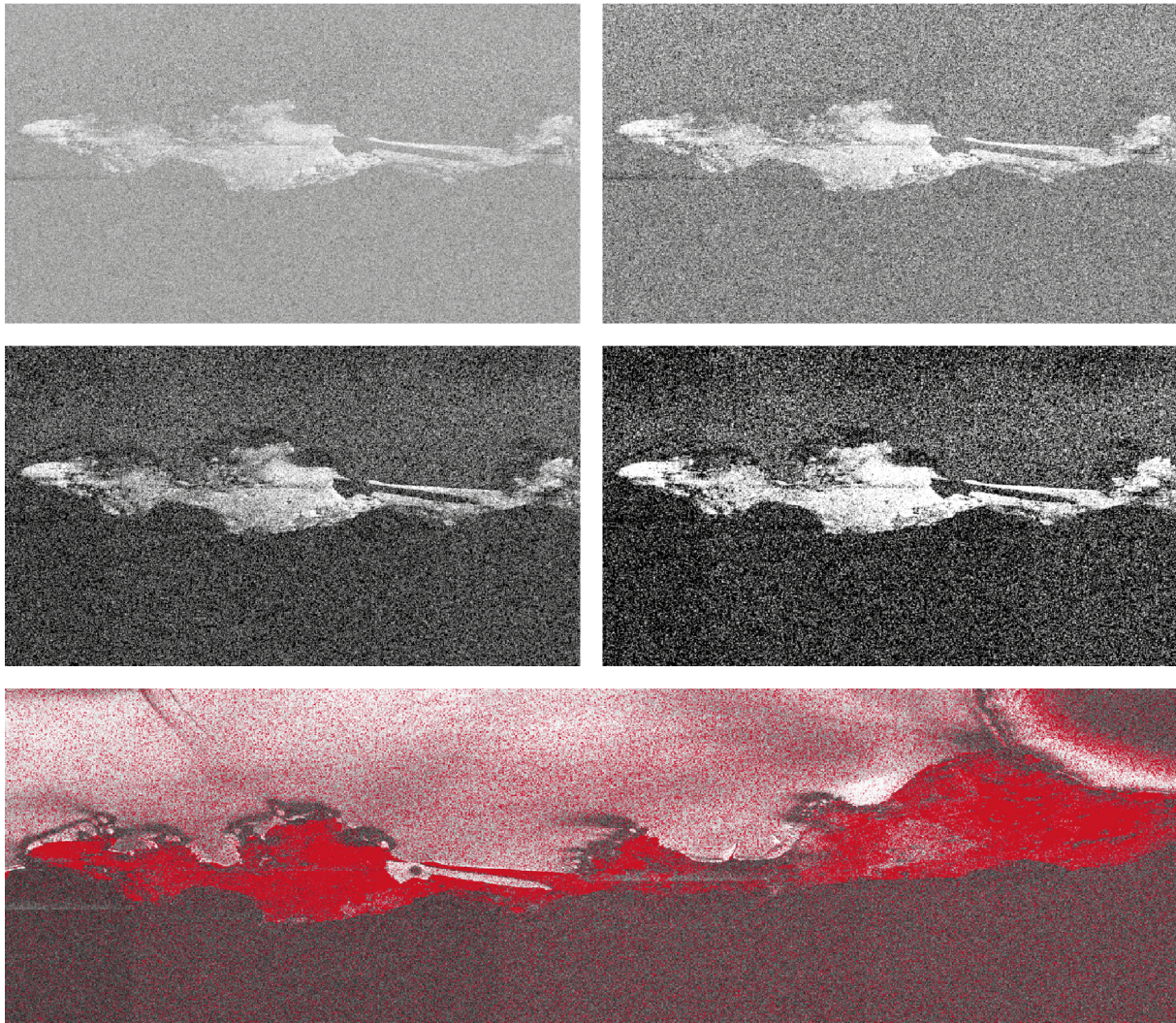


Figure 2.50: Process of the stable sea ice detection algorithm. The area cover the right rectangle of Fig. 2.48. Top-left = difference between HH and HV coherence. Top-right = average filter output (5x5). Center-left = classification by thresholding. Center-right = classification enhancement by mathematical morphology. Bottom = classification overlay (red) on HV coherence image.

2.2.2.6 Along-Track Displacement Estimations Using Multiple Aperture Interferometry and Burst Overlapping Interferometry

If DInSAR became a very common tool for measuring displacement fields, its major limitation is that it is only sensitive to displacements in one dimension: the line-of-sight direction. This can be overcome using different viewing geometries, but this cannot be guaranteed everywhere on Earth.

Techniques for estimating displacements in the along-track direction should be exploited to better estimate bi- or three-dimensional deformations. Among these, Multiple Aperture Interferometry - MAI has been proposed by Bechor and Zebker (2006). The goal of MAI is to extract azimuthal displacements from a single pair of SAR images. Compared to pixel offset tracking, which also allows a determination of bidimensional displacements, MAI is about twice more precise. Burst Overlapping Interferometry - BOI uses a similar approach, exploiting TOPSAR particularities. MAI cannot achieve the accuracy of Burst Overlapping Interferometry, but the latter is constrained to the burst overlapping regions in TOPSAR acquisitions.

2.2.2.6.1 Multiple Aperture Interferometry Adaptation to TOPSAR Mode

While Synthetic Aperture Radar simulates a large antenna by combining the different echoes that illuminate a specific ground target (see section 2.1), Multiple Aperture Interferometry goes a step further by separating the echoes received when the satellite was behind the ground target from the echoes received when the satellite was after the target, using sub-aperture processing. The MAI technique has been proposed to measure along-track displacements from InSAR data (Bechor & Zebker, 2006; Jung et al., 2009, 2013, 2014). The technique makes forward- and backward-looking SLC images from SAR raw images by modifying the focusing for simulating two images integrated with a reduced antenna angular beam width: one around a squint angle obtained by increasing the original one by an angle β (the forward-looking one) and one around the squint angle obtained by decreasing the original squint angle by the same angle β (the backward-looking one). The creation of the two forward- and backward-looking SLC images is obtained by modification of the focusing through shifting the Doppler centroids and reducing the Doppler bandwidths.

Applying InSAR on the forward- and backward-looking SLC images of master and slave data produces forward- and backward-looking interferograms. The MAI interferogram is a differential interferogram, created by the complex-conjugate multiplication of these two interferograms: the MAI phase is the difference between these forward- and the backward-looking phases. While MAI was originally performed on raw data by modifying the focusing operation, it is also possible to create the subaperture *a posteriori* from SLC images using azimuthal subaperture techniques. The MAI phase is proportional to an azimuth displacement given by the linear relation:

$$\phi_{MAI} = \frac{2\pi \cdot \Delta x}{L} \quad (2.10)$$

L being the length of the antenna and Δx the displacement in resolution unit. Using signal properties, the MAI phase can also be linked to the spectral separation Δf and the azimuthal sampling frequency AF :

$$\phi_{MAI} = \frac{2\pi \cdot \Delta f \cdot \Delta x}{AF} \quad (2.11)$$

The variance of the MAI phase is given by the propagation of the Cramer Rao bound:

$$\sigma_{\phi_{MAI}} = \frac{1}{\sqrt{N}} \cdot \sqrt{\frac{1-\gamma^2}{\gamma^2}} \quad (2.12)$$

N being the number of looks and γ the coherence. Variance propagation gives the uncertainty of the displacement:

$$\sigma_x = \frac{AF}{2\pi \cdot \Delta f} \cdot \sigma_{\phi_{MAI}} \quad (2.13)$$

We choose to split the Doppler band into two separated subbands (without overlap) with widths as large as possible. The division in two subbands ensures that the two produced images simulate two different views: the image corresponding to the left sub-band is the backward-looking SLC image and the other one the forward-looking SLC image (Jung et al., 2009). The widths of the subbands are as large as possible to maximize the azimuth resolution, since this latter increases with the azimuth bandwidth. A minimum overlap ensures a large spectral separation and this property implies a higher sensitivity to azimuth displacements (H. J. Jiang et al., 2017).

In order to provide transitions between the sub-bands as soft as possible, we split the original Doppler spectrum by multiplying it with two filters of the same width (fraction of the original full bandwidth) centered on two distinct Doppler frequencies selected symmetrically around the central Doppler centroid - DC frequency, slightly different from zero, as shown in the results. The spectral separation is then computed as the distance between the filter centers.

The selection of the parameters designing the two filters is based on the spectral properties of the azimuth signal of TOPSAR SLC data. Figure 2.51 (left) shows the azimuth time-frequency diagram of a single burst. f_t represents the Doppler frequency and t the azimuth time.

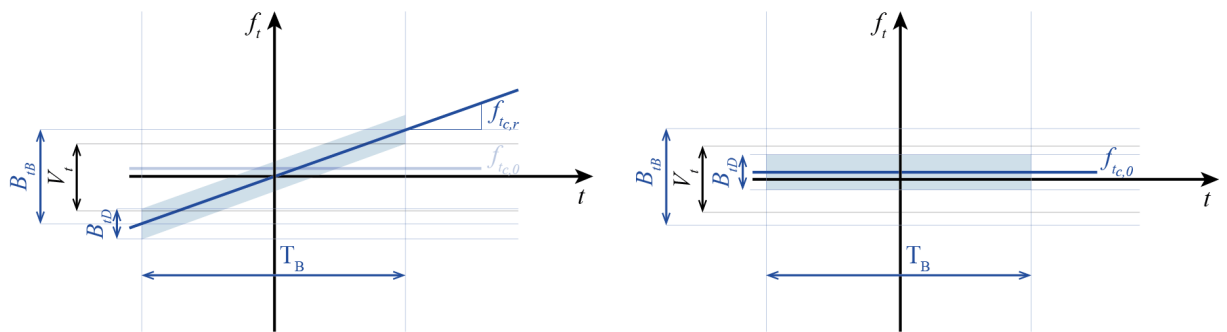


Figure 2.51: Azimuth time-frequency diagram of a single burst acquired in TOPS before and after deramping.

The slope of the DC frequencies (f'_{tc}) along the azimuth direction produces azimuth aliasing: although the beam bandwidth (B_{tD}) is smaller than the azimuth sampling frequency (ν_t), the effective azimuth bandwidth spanned during a burst (B_{tB}) is larger than B_{tD} , so that the sampling criterion for ν_t (i.e., $B'_{tB} > \nu_t$) is not fulfilled.

To circumvent the azimuth aliasing problem, we apply Doppler band splitting into data obtained after deramping, a process consisting in removing the slope of the DC frequencies. Figure 2.51 (right) shows what becomes the azimuth time-frequency diagram of a single burst after deramping.

The full bandwidth of the spectrum of SLC data obtained after deramping is the beam bandwidth and can be computed as

$$B_{tD} = \alpha \cdot |FM_t| \cdot T_D \quad (2.14)$$

where FM_t is the Doppler rate of the raw data, T_D is the dwell-time and α is the mode factor, which depends on the slant range coordinate of the Doppler centroid r_0 , the effective velocity of the satellite v_e and the beam steering rate k_ψ .

Figure 2.52 represents the splitting of the Doppler band. The two filters are shown in blue and green. The green one (F_b) provides the backward-looking SLC image, the left one F_f the forward-looking SLC image. Their bandwidth is indicated by B_s and their respective center with a subscript b or f . The spectral separation Δf is the distance between the centers in the frequency space.

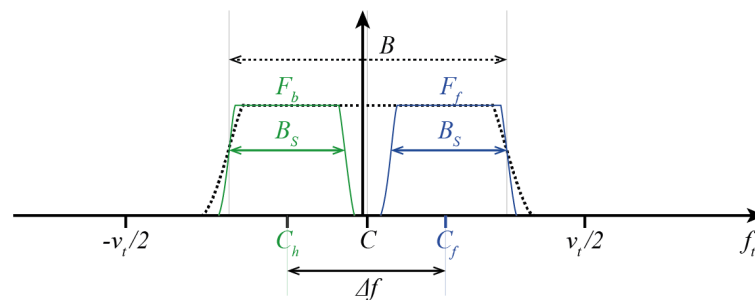


Figure 2.52: Doppler band filtering. Backward and forward filters are displayed in green and blue.

To strongly decrease the side lobes of the azimuth signal, an apodization filter F_a is applied at the end of focalization in both azimuth and range directions. Before applying Doppler band splitting, we must recover the initial azimuth spectrum by applying the inverse of F_a . We call this operation the de-apodization and the filter applied to that aim the de-apodization filter (indicated by F_{de}).

Performing Doppler band splitting after de-apodization leads to side lobes recovery in the azimuth signal. Therefore, we apply apodization on each subband after splitting to perform a correct apodization of the azimuth signal in the forward- and the backward-looking images. The apodization is performed by multiplication by apodization filters centered on the center of each subband. These filters are indicated by $F_{a,f}$ and $F_{a,b}$ for the forward- and the backward-looking images, respectively.

Figure 2.53 shows the block diagram of the pre-processing for MAI. The input of the pre-processing (in light grey) are the data: a binary file in ENVI format with the burst image (obtained after the acquisition, coregistration with deramping) and a metadata file (an XML file containing the metadata of the sub-swath including the burst) and specific parameters (δ and ϵ). The outputs of the pre-processing (in dark grey) are the parameters related to the region of interest, the parameters required for setting the filters F_b and F_f (the vectors B and C with the widths and the centers of the full band (one value per slant range coordinate), the apodization coefficient a and the Doppler frequency sampling step Δf_t) and the two images provided by Doppler band splitting: the corresponding burst of the forward- and the backward-looking SLC images.

The types of windows vary depending on whether the spectra are apodized or not. In the first case, the window is a Hamming window with apodization parameter a , otherwise, it is a rounded rectangle window with transition parameter δ .

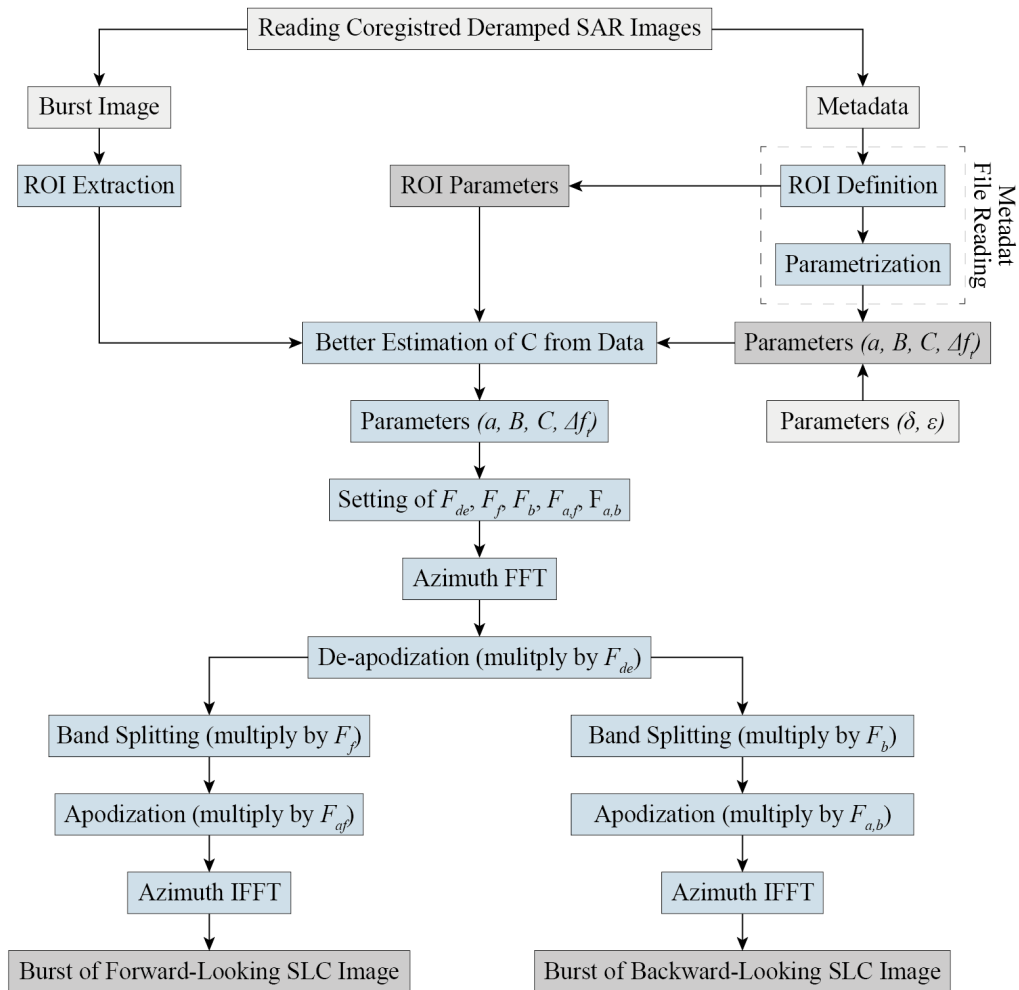


Figure 2.53: Block-diagram of Doppler band splitting for MAI.

The most simple way to perform band splitting is based on the use of rectangle windows. Besides its simplicity, such kind of window has the advantage to maximize the widths of the subbands, and thus the azimuth resolution of the subband images. Nevertheless, such a window does not satisfy the Shannon theorem and the band splitting will produce important side lobes in the azimuth signal. To reduce these lobes, we round the edges of such windows by replacing the transition between 1 and 0 with smoother steps as cosine functions.

More precisely, we define the rounded rectangle windows as function of frequency coordinate f_t by:

$$\begin{cases} 1 & \text{if } |f_t - c| \leq \frac{W}{2} - \frac{\delta}{2} \\ \frac{1}{2} \sin\left(\frac{2\pi}{\delta}\left(f_t + \frac{W - \delta/2}{2} - C\right)\right) + \frac{1}{2} & \text{if } -\frac{W}{2} < f_t - c < -\frac{W}{2} + \frac{\delta}{2} \\ -\frac{1}{2} \sin\left(\frac{2\pi}{\delta}\left(f_t + \frac{W - \delta/2}{2} - C\right)\right) + \frac{1}{2} & \text{if } \frac{W}{2} - \frac{\delta}{2} < f_t - c < \frac{W}{2} \\ 0 & \text{otherwise} \end{cases}$$

where W and c are the width and the center of the filter (in Hz), respectively, and δ is the transition parameter. In the implementation, the filter is discretized by sampling the frequency coordinate f_t with the Doppler frequency sampling step given by:

$$\Delta f_t = \frac{\nu_t}{S_{B,a}} \quad (2.15)$$

where $S_{B,a}$ is the number of azimuth pixels of the burst.

Related to de-apodization and apodization filters, the most common kinds of apodization filters are the cosine windows defined as a function of frequency coordinate f_t by:

$$\begin{cases} a + (1 - a) \cdot \cos\left(\frac{2\pi}{W}(f_t - c)\right) & \text{if } |f_t - c| < \frac{W}{2} \\ 0 & \text{otherwise} \end{cases}$$

where W is the filter width (in Hz), a is the apodization coefficient (between 0 and 1) and c is the filter centre (in Hz). If $a = 0.54$, the apodization filter is a Hamming filter. By language abuse, such window is called a Hamming window for any value of parameter a . For the de-apodization filter F_{de} , the width W and the center c of the window are the full bandwidth B and the center C of the initial azimuth spectrum.

The MAI technique was tested on Sentinel-1 SLC images in EW mode, on relative orbit 88, over the Roi Baudouin Ice Shelf (East Antarctica). The acquisition dates are the 20 and 26th of October 2018. The initial azimuth spectrum is visible at Fig. 2.54, top left. This signal is de-apodized in order to enhance the edges (Fig. 2.54), top right. This preprocessed signal is split according to the corresponding filters (Fig. 2.54, bottom left). The result is re-apodized to create the SAR images (Fig. 2.54, bottom right).

If we designate i and q the real and imaginary parts of the image, respectively, the inputs of the process are two SAR images can be written as:

$$\begin{aligned} SAR_1 &= i_1 + j \cdot q_1 \\ SAR_2 &= i_2 + j \cdot q_2 \end{aligned} \quad (2.16)$$

The azimuthal subbanding presented previously decomposes the complex signal into two non-overlapping signals, designated as *back* and *for* the backward and forward-looking, respectively.

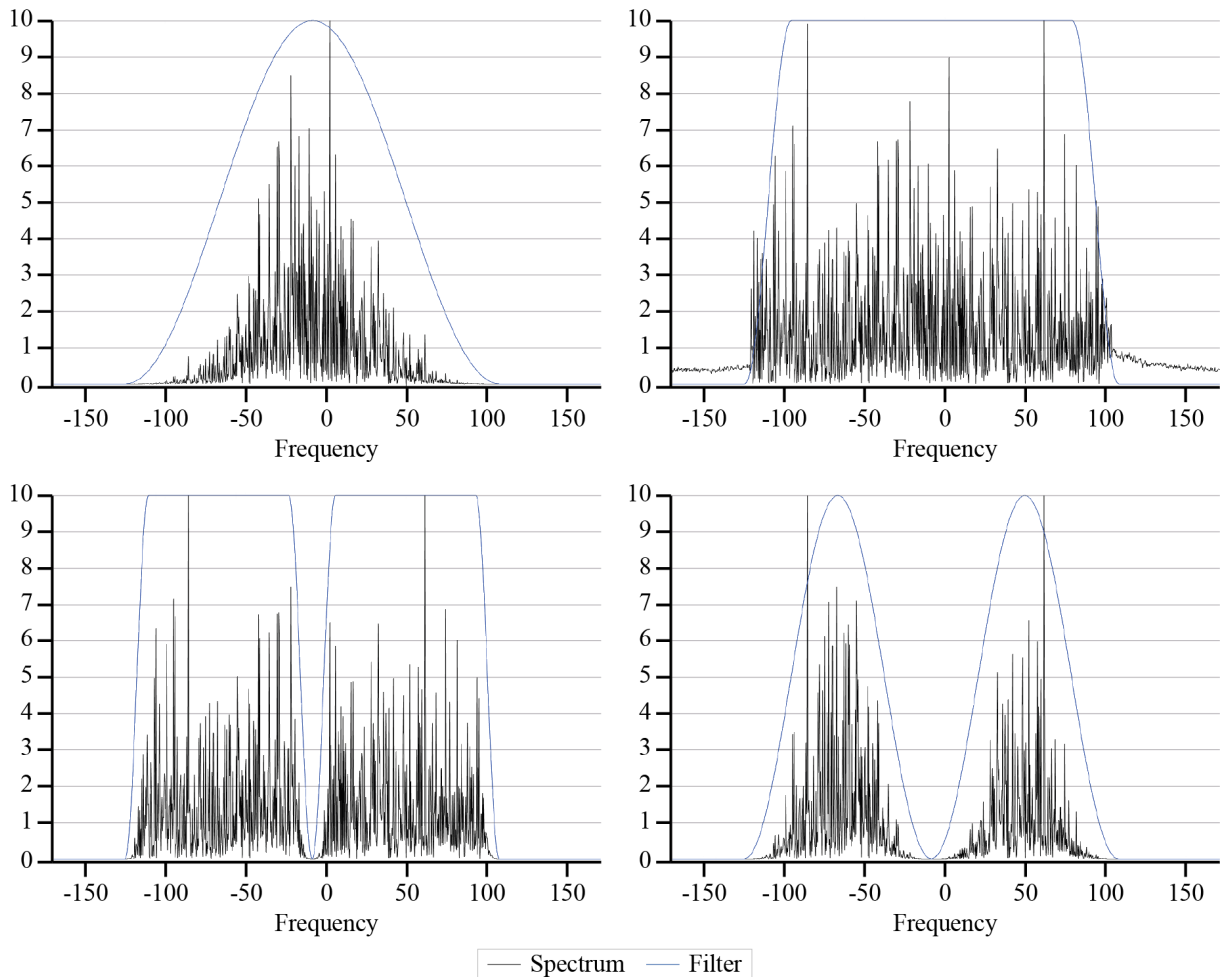


Figure 2.54: (top left) Initial spectrum of azimuth line at mid-range. (top right) Spectrum of azimuth line at mid-range after de-apodization. (bottom left) Spectrum of azimuth line at mid-range after band splitting (rounded rectangle filter in blue). (bottom right) Spectrum of azimuth line at mid-range (after apodization). In bottom figures, both forward and backward spectra are represented, but corresponds to two different signals.

It is possible to create an interferogram by combining the backward-looking signals. The same reasoning can be done for forward-looking signals. These interferograms are also complex signals, and thus can be decomposed into their real and imaginary parts, which make the computation more convenient :

$$\left. \begin{aligned} i_{intf,back} &= i_{1,back} \cdot i_{2,back} + q_{1,back} \cdot q_{2,back} \\ q_{intf,back} &= i_{2,back} \cdot q_{1,back} - i_{1,back} \cdot q_{2,back} \end{aligned} \right\} \text{Backward Looking Interferogram} \quad (2.17)$$

$$\left. \begin{aligned} i_{intf,for} &= i_{1,for} \cdot i_{2,for} + q_{1,for} \cdot q_{2,for} \\ q_{intf,for} &= i_{2,for} \cdot q_{1,for} - i_{1,for} \cdot q_{2,for} \end{aligned} \right\} \text{Forward Looking Interferogram} \quad (2.18)$$

Then, the MAI signal can be computed:

$$\begin{aligned} i_{MAI} &= i_{intf,back} \cdot i_{intf,for} + q_{intf,back} \cdot q_{intf,for} \\ q_{MAI} &= i_{intf,for} \cdot q_{intf,back} - i_{intf,back} \cdot q_{intf,for} \end{aligned} \quad (2.19)$$

$$\longrightarrow \phi_{MAI} = \arctan \frac{q_{MAI}}{i_{MAI}}$$

Forward- and backward-looking interferograms look similar, but their subtraction lets appear the azimuthal displacement (Fig. 2.55). This MAI phase can finally be translated into a azimuthal displacement (Fig. 2.56). Results show a good correspondence with pixel offset tracking results, but the low SNR strongly influences the expected accuracy, especially in fast-moving areas.

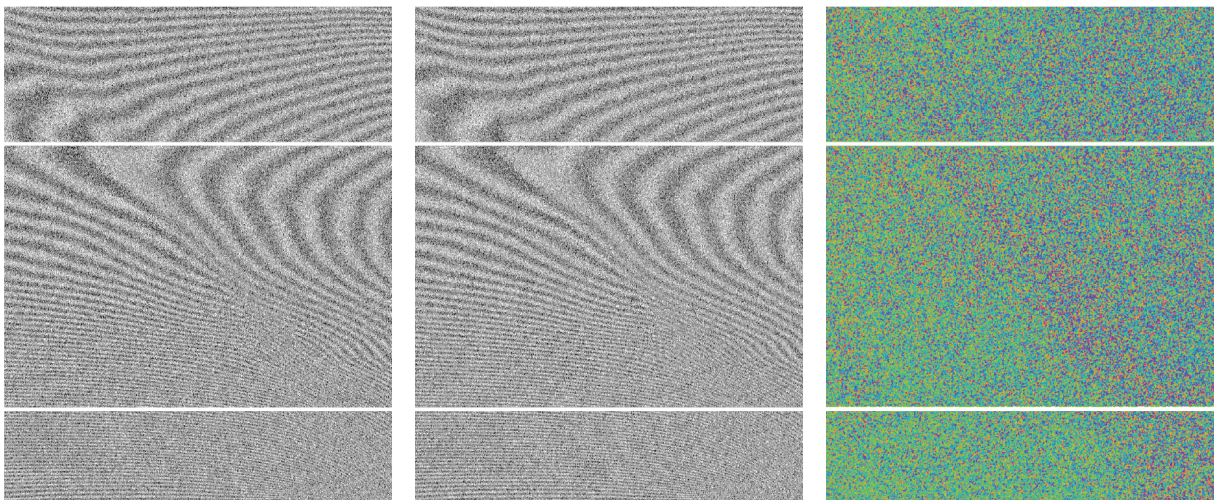


Figure 2.55: Forward, Backward, and Multiple Aperture Interferograms (zoomed-in).

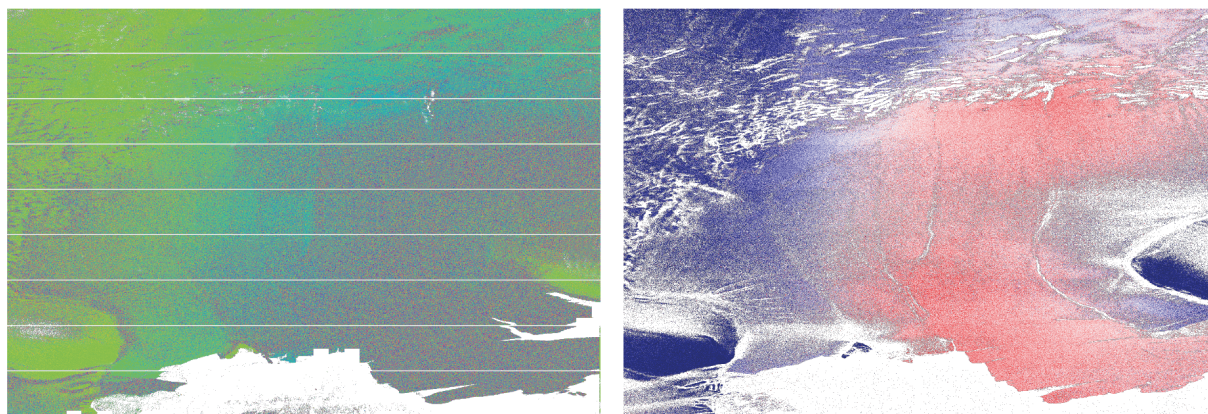


Figure 2.56: Comparison between Multiple Aperture Interferogram and Azimuth shifts estimated from coherence tracking.

The method is original for two reasons. First, it takes into account the Sentinel-1 TOPSAR specific signal characteristics. Secondly, the method is approaching MAI from SLC images instead of refocusing RAW data. We presented the MAI developments during the IEEE International Symposium on Geoscience and Remote Sensing (IGARSS) 2021 event. We condensed the essential information of the current section in a reviewed proceeding, available here-after, and can be cited as

Kirkove, M., **Glaude, Q.**, Derauw, D., Pattyn, F., Barbier, C., & Orban, A. (2021). Sentinel-1 Azimuth Subbanding for Multiple Aperture Interferometry - test case over the Roi Baudouin Ice Shelf, East Antarctica. *IGARSS 2021 - 2021 IEEE International Geoscience and Remote Sensing Symposium*, Brussels, Belgium.

SENTINEL-1 AZIMUTH SUBBANDING FOR MULTIPLE APERTURE INTERFEROMETRY - TEST CASE OVER THE ROI BAUDOIN ICE SHELF, EAST ANTARCTICA

M. Kirkove (1), Q. Glaude (1,2), D. Derauw (1,3), C. Barbier (1), F. Pattyn (2), and A. Orban (1)

(1) Liège Space Center, Université de Liège, Angleur, Belgium

(2) Laboratory of Glaciology, Université Libre de Bruxelles, Bruxelles, Belgium

(3) Instituto de Investigación en Paleobiología y Geología, Universidad Nacional De Rio Negro, General Roca, Argentina

ABSTRACT

As an extension of Synthetic Aperture Radar Interferometry, Multiple Aperture Radar (MAI) is a spectral diversity technique that allows the determination of azimuth displacements from phase shift measurements. This is made possible through the creation of backward- and forward-looking Single-Look-Complex (SLC) data. Then, the phase difference between the backward and forward-looking interferogram is translated into a displacement. Using SLC data, MAI requires a proper azimuth splitband operator. Different techniques exist to split the azimuth band, but they are often too briefly described in the MAI literature. In this conference paper, we analyze the signal properties of the Sentinel-1 TOPS acquisition mode and define an azimuth subbanding protocol. In particular, we look at the role of de-apodization and apodization in the band filtering operation. We focus our analysis on Sentinel-1 data in Interferometric Wideswath mode over the Roi Baudouin Ice Shelf, East Antarctica.

Index Terms— Multiple Aperture Interferometry, Splitband, Sentinel-1, Ice Shelf

1. INTRODUCTION

Differential SAR interferometry (InSAR) become a very common tool for measuring displacement maps [1]. The major limitation of InSAR is that it is only sensitive to displacements in one dimension: the light-of-sight direction. This can be overcome using different viewing geometries [2], but this cannot be guaranteed everywhere on Earth, in particular in polar regions.

Multiple Aperture Interferometry (MAI) has been proposed by Bechor and Zebker in 2006 [3], extracting azimuth displacements from a single pair of SAR images. Compared to pixel offset tracking, MAI is estimated to be twice more precise.

This conference paper carefully details the azimuth subbanding approach, required for Multiple Aperture Interferometry. We focus here on the Sentinel-1 data acquired in Interferometric Wide Swath (IW) and Extra Wide (EW) modes

using the Terrain Observation by Progressive Scans (TOPS), but the method is not bounded by the acquisition mode. In section 2, we describe the rationale of the MAI and the implementation of the azimuth subbanding technique. Then, we present spectral results in section 3 and conclude in section 4.

2. METHODS

2.1. Displacements Measurements by MAI

The MAI technique has been proposed to measure along-track displacements [3, 4, 5, 6, 7]. The idea of MAI is to separate the radar echoes emitted by the satellite received when it was behind the target from the echoes received when the satellite was in front of the target, using sub-aperture processing. The technique makes forward- and backward- looking SLC images from SAR raw images by modifying the focusing for simulating two images integrated with a reduced antenna angular beamwidth. The creation of the two forward- and backward-looking SLC images is obtained by modification of the focusing through shifting the Doppler centroids (DCs) and reducing the azimuth bandwidths. Applying InSAR on the forward- and backward-looking SLC images of master and slave data of an InSAR pair produces forward- and backward-looking interferograms. The MAI interferogram is a differential interferogram, created by complex-conjugate multiplication of these two interferograms; the MAI phase is the difference between these forward- and the backward-looking phases.

The MAI phase is proportional to the azimuth displacement. The linear relation is given by :

$$\phi_{MAI} = \frac{2\pi \cdot \Delta x}{L}, \quad (1)$$

L being the length of the antenna and Δx the displacement in resolution unit. Using signal properties, the MAI phase can also be linked to the spectral separation Δf and azimuth sampling frequency ν

$$\phi_{MAI} = \frac{2\pi \cdot \Delta f \cdot \Delta x}{\nu} \quad (2)$$

In many cases, authors are developing MAI from RAW data, by combining the correct echoes to produce the two SAR images. It is also possible to create the subaperture *a posteriori* from SLC images [8]. The forward- and the backward-SLC images can be seen as the products of splitting the initial Doppler spectrum of an SLC image in two subbands of reduced bandwidth having distinct frequency centers.

In this conference paper, we choose to split the Doppler band into two separated subbands with their bandwidth as large as possible. The division in two subbands ensures that the two produced images simulate two different views: the image corresponding to the left subband is the backward-looking SLC image and the other one the forward-looking SLC image [4]. The widths of the subbands are as large as possible to maximize the azimuth resolution, since this latter increases with the azimuth bandwidth. A minimum overlap ensures a large spectral separation and this property implies a high sensitivity to azimuth displacements [8].

2.2. Azimuth subbanding

To provide transitions between the subbands as soft as possible, we split the original azimuth spectrum by multiplying it with two rounded rectangle filters of the same width (fraction of the original full bandwidth) centered on two distinct azimuth frequencies selected symmetrically around the central Doppler centroid (DC) frequency. This operation is called azimuth band splitting. The left filter (F_b) provides the backward-looking SLC image, the right one (F_f) the forward-looking SLC image. The spectral separation is then computed as the distance between the filter centers (C_b and C_f).

To strongly decrease the side lobes of the azimuth signal, an apodization filter F_a is applied at the end of focalization in both azimuth and range directions. Before azimuth band splitting, we must recover the initial azimuth spectrum. To this aim, we apply the inverse of F_a . We call this operation the de-apodization and the filter the de-apodization filter (noted F_{de}).

Executing azimuth band splitting after de-apodization leads to side lobes recovery in the azimuth signal. We perform apodization on each subband after splitting to achieve a correct apodization of the azimuth signal in the forward- and the backward-looking images. We employ apodization filters centered on the center of each subband. These filters are indicated by $F_{a,f}$ and $F_{a,b}$ for the forward- and the backward-looking images, respectively.

The design of the filters F_b and F_f is based on the spectral properties of the azimuth signal of TOPSAR SLC data. Figure 1.a shows the azimuth time-frequency diagram of a single burst. The slope s of the DC frequencies along the azimuth

direction produces azimuth aliasing: although the beam bandwidth (B_D) is smaller than the azimuth sampling frequency (ν), the effective azimuth bandwidth spanned during a burst (B_B) is larger than B_D , so that the sampling criterion for ν (i.e., $B_B > \nu$) is not fulfilled.

To circumvent the azimuth aliasing problem, we apply azimuth band splitting on data obtained after deramping, a process consisting in removing the slope of the DC frequencies. This operation is equivalent to the frequency scaling technique applied in the CSL TOPSAR processor [9]. Figure 1.b shows what becomes the azimuth time-frequency diagram of a single burst after deramping.

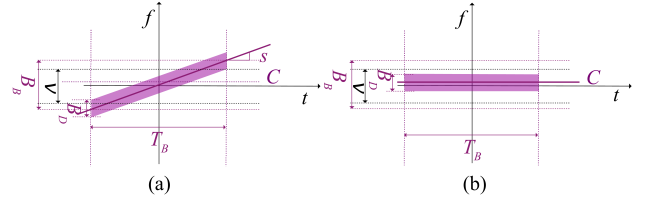


Fig. 1. Azimuth time-frequency diagram of a single burst (a) acquired in TOPS, (b) after deramping. f represents the Doppler frequency, t the azimuth time, T_B the burst time, ν the azimuth sampling frequency, B_D the azimuth bandwidth of a beam, B_B the full Doppler bandwidth, C the center of DC frequencies of the burst and s the DC rate.

The characteristics of the azimuth spectrum (C and B_B) depend on the slant range coordinates. Figure 2.a represents the Doppler spectrum of an azimuth line of a single burst after deramping. In this figure, the notation B_B is replaced by B . The application of azimuth band splitting to this spectrum is illustrated in Figure 2.b where the two filters F_b and F_f are displayed in light and dark blue. Their bandwidth is indicated by B_s .

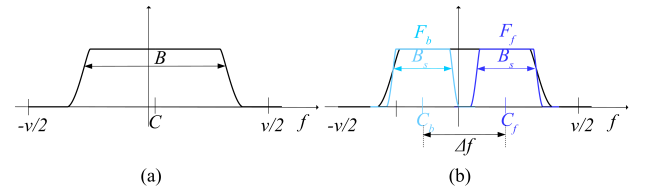


Fig. 2. (a) Doppler spectrum of an azimuth line of a single burst of SLC data after deramping, (b) azimuth band splitting (the two filters are displayed in dark and light blue).

The spectral separation Δf is the distance between the centres in the frequency space:

$$\Delta f = 2C_f - 2C \quad (3)$$

Figure 3 shows the block-diagram of azimuth subbanding applied to a single burst. For Sentinel-1 format, the main

input data are a SLC image (resulting of deramping applied after acquisition) and a metadata file (an XML file containing the metadata of the sub-swath including the burst). The outputs are the burst of the forward- and the backward-looking SLC images. Initialization consists in (1) extracting the burst data from the input data, (2) estimating the range-dependent parameters C from the data and (3) setting the filters F_{de} , F_f , F_b , $F_{a,f}$, $F_{a,b}$. After initialization, the core of azimuth subbanding (azimuth band splitting) is executed. First, the processes of (1) azimuth fast Fourier transform (FFT), (2) de-apodization (multiplication by F_{de}), and (3) azimuth band splitting (multiplication by F_b and F_f) are carried out to provide two products (corresponding to the forward- and the backward-looking SLC images). Then, the processes of (4) apodization (multiplication by $F_{a,b}$ or $F_{a,f}$) and (5) azimuth inverse fast Fourier transform (IFFT) are applied to each product for finally providing the burst of the forward- and the backward-looking SLC images.

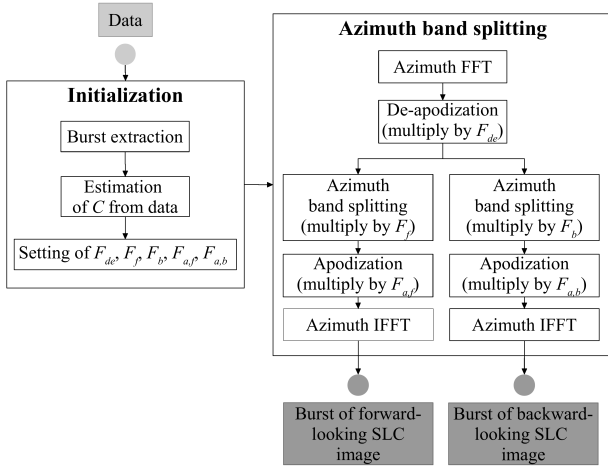


Fig. 3. Block-diagram of azimuth subbanding applied to a single burst. Inputs are shown in light grey, outputs in dark grey.

3. DATA AND RESULTS

In this work, we consider Sentinel-1 SLC images in EW mode, on relative orbit 88, over the Roi Baudouin Ice Shelf (East Antarctica). Acquisition dates are the 20 and 26th of October 2018.

Figure 4 summarizes the spectral results of the subbanding approach. First, the Sentinel-1 data are deramped and the azimuth spectrum is computed (Figure 4.a). From there, the bandwidth and center of the azimuth spectrum of SLC data are derived. At mid-range, these are evaluated at 233 and -8.12343 Hz, respectively. These parameters are required for the definition of the bandpass filters (Figure 4.c, in red).

Then, the de-apodization filter is applied to enhance the signal by reducing side lobes (Figure 4.b). Figure 4.c shows the bandpass filtered signals, with their respective filter. The left and right filters correspond to the backward- and forward-looking Single-Look-Complex data. In Figure 4.d, the results after the apodization are displayed. In the end, the signal is split into two subbanded signals, focused around different Doppler frequencies.

4. CONCLUSION

In this conference paper, we carefully described one approach to split the azimuth band for Multiple Aperture Interferometry (MAI). Particular attention was drawn to the Sentinel-1 TOPSAR acquisition mode. First, the azimuth spectrum of deramped Sentinel-1 acquisition was analyzed, allowing to extract the different parameters of the bandpass filter. We employed a de-apodization filter to decrease the sidelobes of the signal. Then, the signal is split using two rounded rectangle filters. Finally, an apodization filter is applied to recover the original signal properties. The approach was applied on Sentinel-1 acquisitions in Interferometric Wideswath mode, on the Roi Baudouin Ice Shelf, Antarctica. The results show the ability of the technique in providing azimuth band splitting of the data. In future work, the exploitation of these results from Multiple Aperture Interferometry will be discussed.

5. ACKNOWLEDGMENTS

This research is supported by the French community of Belgium in the funding context of a FRIA grant, and carried out in the framework of the MIMO (Monitoring melt where Ice Meets Ocean) and SMAIAD (Sentinel-1 Multiple Aperture Interferometry for Azimuth Displacement Retrieval) projects funded by the Belgian Science Policy contracts Nos. SR/00/336 and Nos. SR/12/207.

6. REFERENCES

- [1] Didier Massonnet, Marc Rossi, César Carmona, Frédéric Adragna, Gilles Peltzer, Kurt Feigl, and Thierry Rabaute, “The displacement field of the Landers earthquake mapped by radar interferometry,” *Nature*, vol. 364, no. 6433, pp. 138–142, 1993.
- [2] Tim J. Wright, Barry E. Parsons, and Zhong Lu, “Toward mapping surface deformation in three dimensions using insar,” *Geophysical Research Letters*, vol. 31, no. 1, 2004.
- [3] Noa B.D. Bechor and Howard A. Zebker, “Measuring two-dimensional movements using a single InSAR pair,” *Geophysical Research Letters*, vol. 33, no. 16, pp. 1–5, 2006.

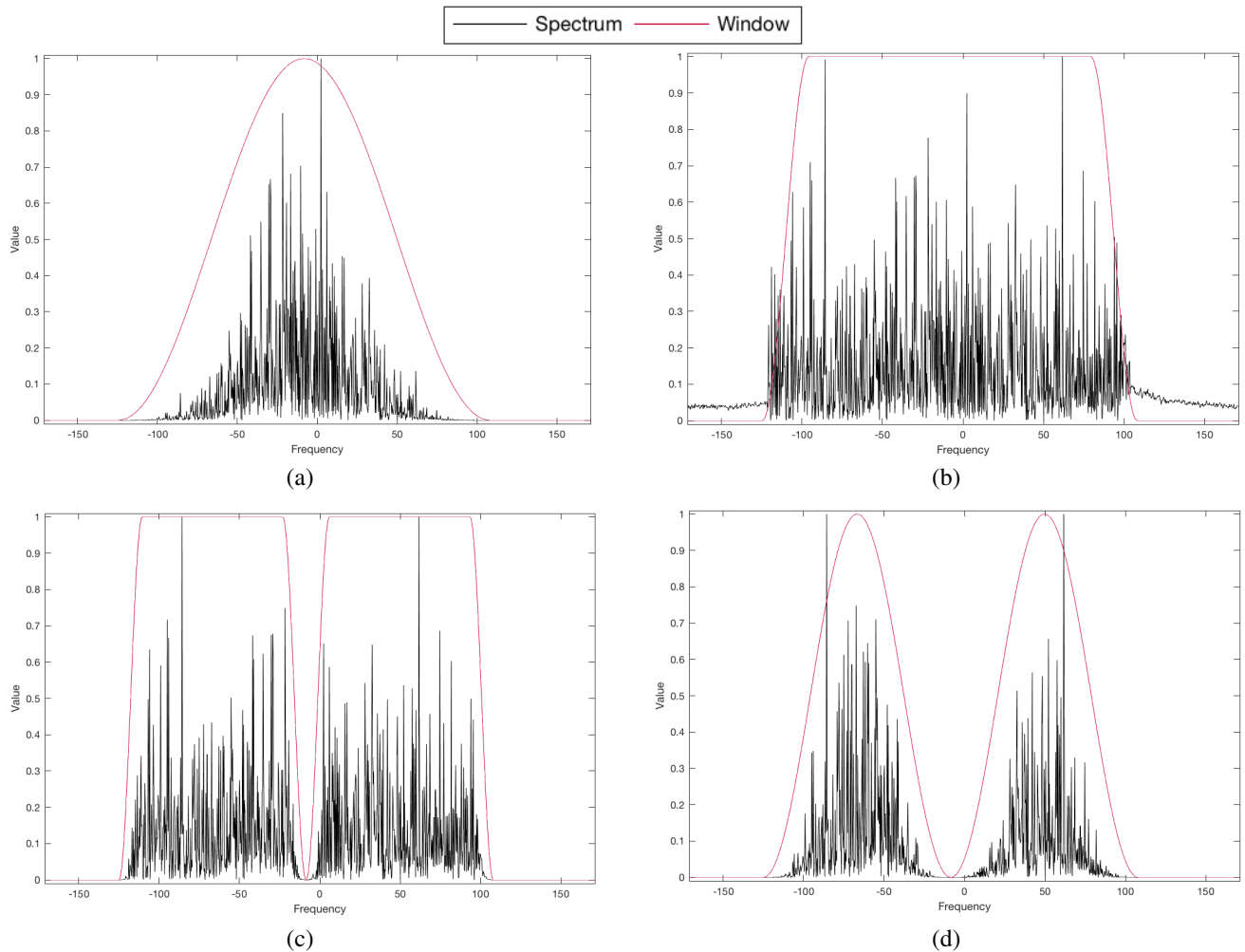


Fig. 4. Spectrum of azimuth line at mid-range ((a) initial, (b) after de-apodization, (c) after band splitting, (d) after apodization). In (c) and (d), both split signals are displayed; the left and right corresponding to the backward- and forward-looking parts of the signal, respectively.

- [4] Hyung Sup Jung, Joong Sun Won, and Sang Wan Kim, "An improvement of the performance of multiple-aperture SAR interferometry (MAI)," *IEEE Transactions on Geoscience and Remote Sensing*, vol. 47, no. 8, pp. 2859–2869, 2009.
- [5] H. Jung, Z. Lu, and L. Zhang, "Feasibility of along-track displacement measurement from sentinel-1 interferometric wide-swath mode," *IEEE Transactions on Geoscience and Remote Sensing*, vol. 51, no. 1, pp. 573–578, 2013.
- [6] Hyung Sup Jung, Won Jin Lee, and Lei Zhang, "Theoretical accuracy of along-track displacement measurements from multiple-aperture interferometry (MAI)," *Sensors (Switzerland)*, vol. 14, no. 9, pp. 17703–17724, 2014.
- [7] Pietro Mastro, Carmine Serio, Guido Masiello, and Antonio Pepe, "The multiple aperture sar interferometry (mai) technique for the detection of large ground displacement dynamics: An overview," *Remote Sensing*, vol. 12, no. 7, 2020.
- [8] H J Jiang, Y Y Pei, and J Li, "Sentinel-1 TOPS interferometry for along-track displacement measurement," *IOP Conference Series: Earth and Environmental Science*, vol. 57, pp. 012019, feb 2017.
- [9] M. Kirkove, A. Orban, D. Derauw, and C. Barbier, "A topsar processor based on the omega-k algorithm: Evaluation with sentinel-1 data," in *Proceedings of EUSAR 2016: 11th European Conference on Synthetic Aperture Radar*, 2016, pp. 1–5.

2.2.2.6.2 Azimuthal Displacement Retrieval from Burst Overlapping Interferometry on Sentinel-1 Acquisitions

In TOPSAR mode, the sensor, instead of looking perpendicular to the satellite track direction, steers its sensor from backward to frontward to reduce the needed acquisition time. In this particular acquisition mode, an observed scene is composed of bursts. To stitch all these bursts together, overlapping regions are planned (Fig. 2.57). In these superposition areas, ground scatterers are observed twice; firstly with the sensor backward aiming frontward, and once on the next burst, with the sensor frontward aiming backward. We can make an interferogram on each burst.

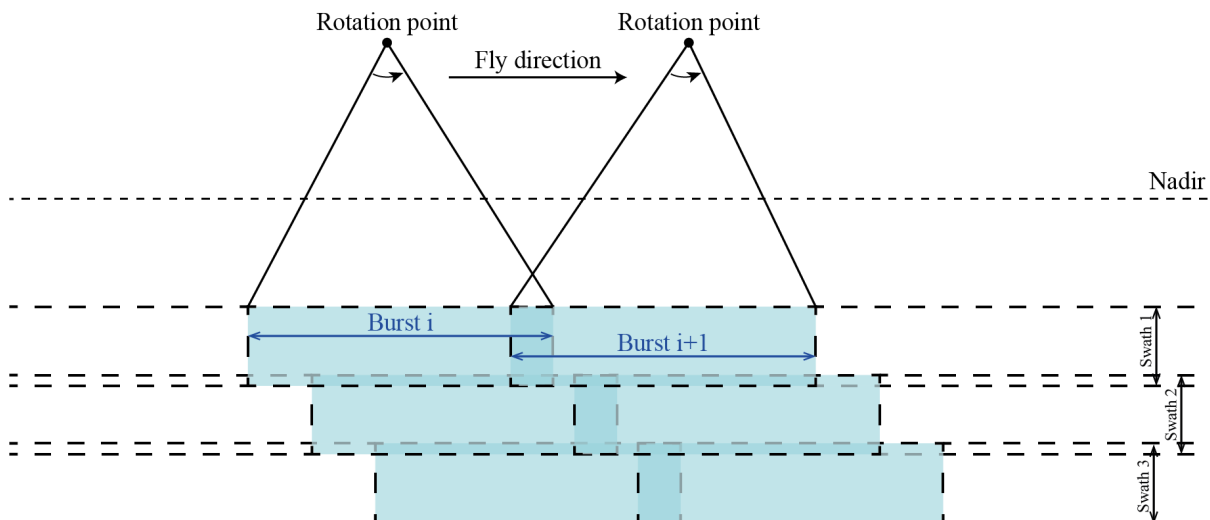


Figure 2.57: Acquisition geometry of a TOPSAR image. The image is composed of sub-swaths and bursts with overlapping areas.

If an along-track displacement occurred in these overlapping areas, an additional phase component appear in the differential interferogram. This phase component will be equal in absolute but opposite in sign in the two successive interferograms. Burst Overlapping Interferometry - BOI consists in subtracting two successive interferograms in the overlapping areas in order to cancel all phase terms except the azimuthal one (Fig. 2.58).

The resulting phase can be noisy. Goldstein phase filtering is a very popular phase filter algorithm. Easy to implement, few parameters and overall impressive results, it is thus on this algorithm that we will try to build our BOI-adapted phase filtering. The filtering works in the frequency domain. Taking a subset i of the interferogram and taking its Fourier transform I , the transfer function is built upon

$$H(u, v) = |I(u, v)|^\alpha \quad (2.20)$$

Where alpha is the only parameter chosen by the user and is comprised between 0 and 1. A zero value means no filtering while 1 is quite a strong filter. In practice, 0.2 to 1 are common values. The convolution is performed in the frequency domain such as

$$I_{filtered} = H(u, v) \cdot I(u, v) \quad (2.21)$$

We then obtain the interferogram by computing its inverse Fourier transform.

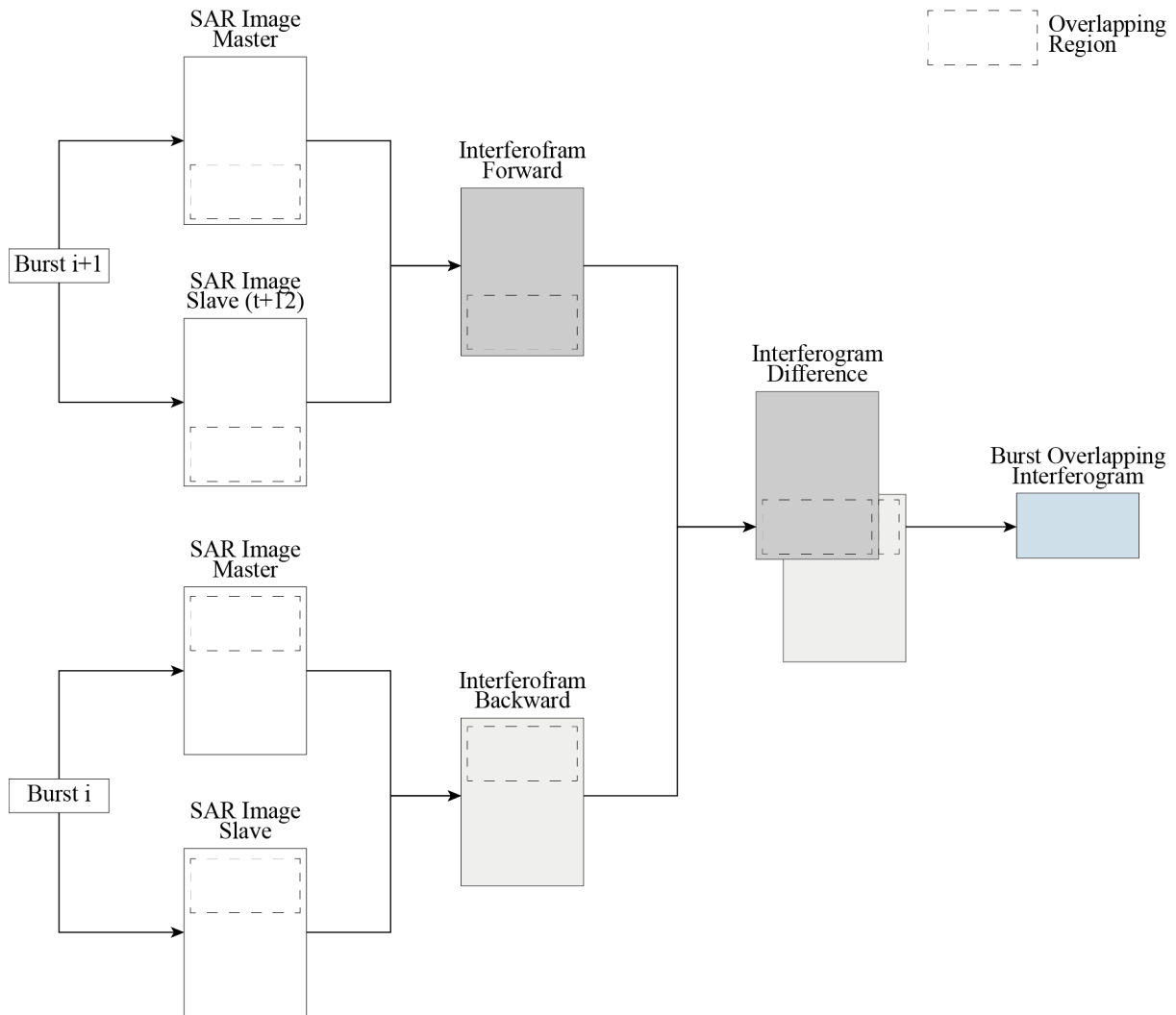


Figure 2.58: Block diagram of Burst Overlapping Interferometry - BOI.

Nevertheless, in TOPSAR, the elongated characteristic of the burst overlapping (100×8000 pixels) areas makes the Goldstein algorithm unusable.

The proposed modification proceeds as a sliding window inside which an iterative low-alpha Goldstein phase filtering is employed. The filter produces the filtered BOI phase column by column when moving. We are using $\alpha = 0.3$ and three iterations.

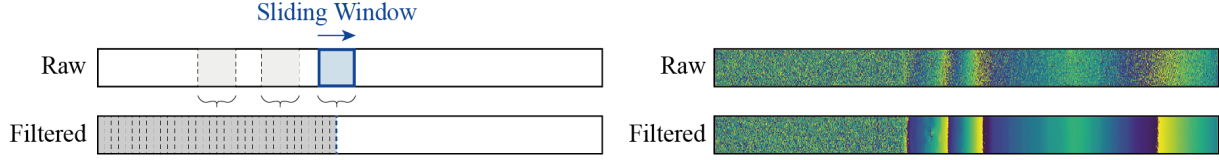


Figure 2.59: On the left side, we present the concept of the BOI-adapted Goldstein phase filtering. The filter is applied iteratively through a moving window that generates the output phase column-by-column. On the right side, we can see the result of the filter applied to the BOI phase.

Burst overlapping interferometry is a technique related to *spectral diversity* techniques. The burst overlapping interferometric phase can be related to an azimuthal displacement by the relation :

$$\phi_{BOI} = \frac{2\pi \cdot \Delta f \cdot x}{AF} \quad (2.22)$$

Where AF is the azimuthal frequency and Δf if the spectral separation. By inverting the equation, we obtain an azimuthal displacement (in pixel unit). This is the same relation as the one presented in MAI:

$$x_{az} = \frac{AF}{2\pi \cdot \Delta f} \cdot \phi_{BOI} \quad (2.23)$$

Nevertheless, we need to know the azimuthal frequency and spectral separation Δf . From Yague-Martinez & al., the Doppler frequency in TOPSAR SLC images is computed as follow :

$$f_{DC} = k_t \cdot t_{az} \quad (2.24)$$

With k_t being the Doppler centroid rate in zero-Doppler geometry (focused). The spectral separation Δf is finally obtained by taking the azimuth time difference Δt_{az} :

$$\Delta f_{DC} = k_t \cdot \Delta t_{az} \quad (2.25)$$

The Doppler centroid rate k_t is a function of the Doppler rate k_a and the Doppler centroid rate in raw data k_{rot} .

The Doppler centroid rate is given by :

$$k_t = \frac{k_{rot} - k_a}{k_{rot} \cdot k_a} \quad (2.26)$$

And k_{rot} is a function of the satellite velocity v_s , the wavelength λ and the steering rate of the sensor ω_r :

$$k_{rot} = -\frac{2 \cdot v_s}{\lambda} \cdot \omega_r \quad (2.27)$$

The azimuth time separation from the two bursts on the burst overlapping area is computed as the number of lines per burst divided by the azimuth frequency.

$$\Delta t_{az} = \frac{\#lines}{AF} = -\frac{2 \cdot v_s}{c} \cdot f_c \cdot \omega_r \quad (2.28)$$

The number of lines per burst is 1500 for Interferometric Wide-swath mode (IW) and 1170 for Extended Wideswath mode (EW). The azimuthal frequency is 486.49 Hz for IW data and 342.56 Hz for EW data.

With $v_s = 7566.93$ m/s, $f_c = 5405000459$ Hz, $\omega_r = 0.0349$ rad/sec, and $c = 299792458$ m/s, we find $k_{rot} = 9522.48$ Hz/sec.

The Doppler rate k_a is range variant in TOPSAR acquisition. It is computed from a polynom given in the metadata.

$$k_a(i) = c_0 + c_1 \cdot (\tau(i) - \tau_0) + c_2 \cdot (\tau(i) - \tau_0)^2 \quad (2.29)$$

Where i denotes the range dimension (in pixel) and $\tau(i)$ is its related slant-range acquisition time.

With $(c_0, c_1, c_2) = (-2457.5353, 479177, -73975318)$, and $\tau_0 = 0.00505182323$ sec we find k_a as a range varying variable going from -2455.28 Hz/sec to -2318.39 Hz/sec (near range to far range).

The Doppler centroid rate in the focused SLC TOPSAR data is given by the formula

$$k_t = \frac{k_a \cdot k_{rot}}{k_a - k_{rot}} \quad (2.30)$$

Since k_a is range varying and k_{rot} is almost constant, the Doppler centroid rate is also range varying, and here goes from 1953 Hz/sec to 1861 Hz/sec (near range to far range).

With $\Delta t_{az} = 3.04$ sec and using $\Delta f_{DC} = k_t \cdot \Delta t_{az}$, the Δf_{DC} ranges from 5938 Hz (near range) to 5657 Hz (far range).

The BOI phase is only known modulo 2π , meaning that large displacements will wrap the phase. A displacement that leads to a 2π BOI phase will be called here *azimuthal displacement ambiguity*.

Using Extended Wide-swath Sentinel-1 images and using the median spectral separation Δf of 5798 Hz (mid-range), we find an azimuthal displacement ambiguity of 0.059 pixels, that is to say 1.17576 m (pixel spacing = 19.9281m). Since August 2018, both Sentinel-1 A and B are acquiring images in EW mode, leading to a revisit time of 6 days, meaning that two separated pixels moving with a difference in azimuthal velocity of 0.19596 meters per day (71.5m / year) will be observed with a 2π phase difference. Fig. 2.60 shows the results on burst overlapping areas near the calving front, where coherent burst overlapping interferograms can be extracted. Zooming out, the coherence is also high on the ice shelf. Focusing on the filtered BOI phase of the burst #3 (Fig. 2.61), we can see how well the estimated accuracy fits with azimuthal

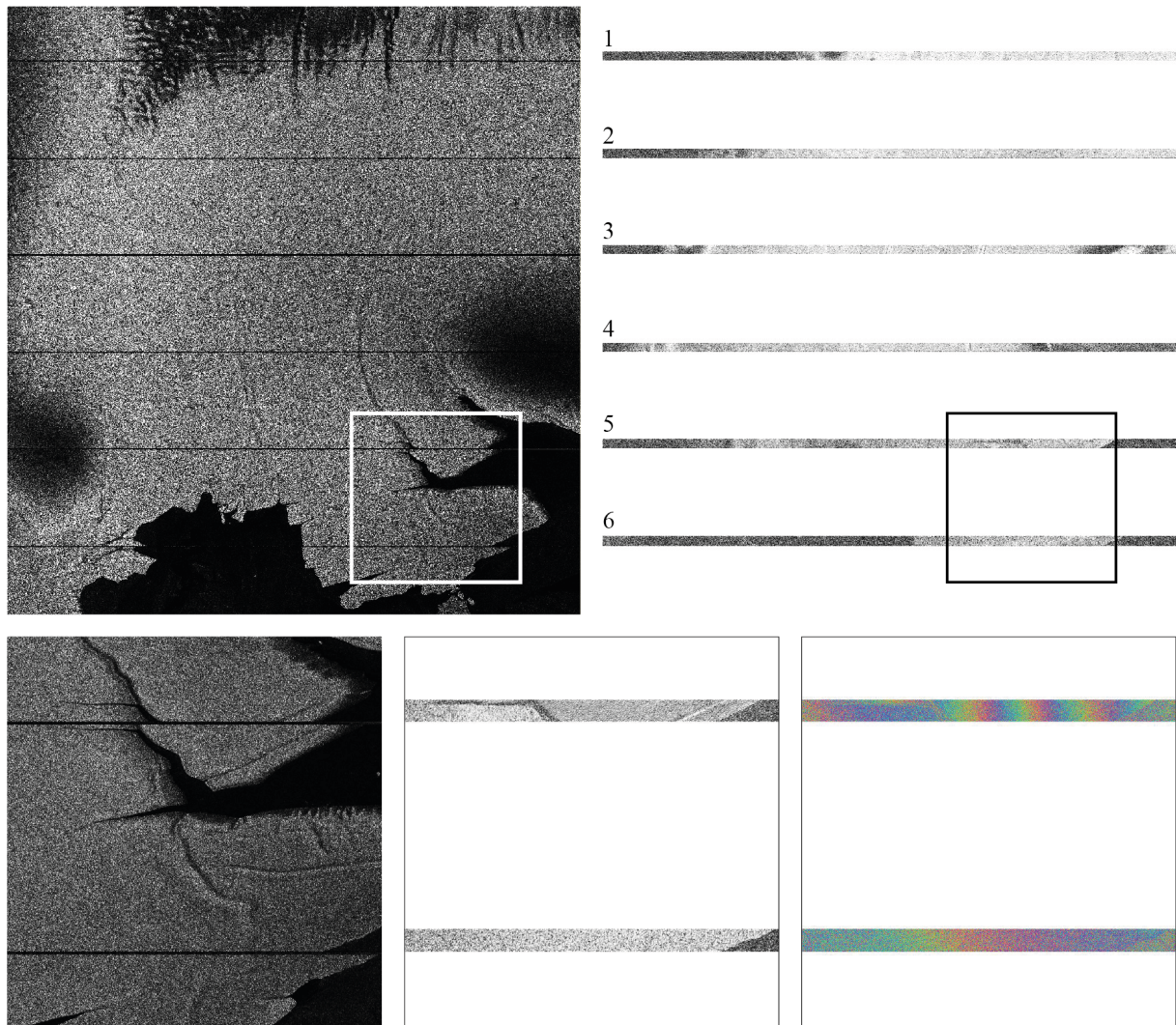


Figure 2.60: (Top) Intensity of the master image (left) and BOI coherence before filtering (right). (Bottom) Intensity, BOI coherence and BOI phase



Figure 2.61: BOI phase of the third burst of Fig. 2.60.

displacements from offset tracking. If we unwrap the BOI phase and multiply by 71.5 m/year, we find the ≈ 300 meters per year velocity in the center towards the edges of the ice stream.

The accuracy of BOI-retrieved azimuthal displacement can be used from the development of the Cramér-Rao bound

$$\sigma_x = \frac{AF}{2\pi \cdot \Delta f} \cdot \frac{1}{\sqrt{N}} \cdot \sqrt{\frac{1 - \gamma^2}{\gamma^2}} \quad (2.31)$$

Where γ is the estimated coherence and N is the number of looks. Using an azimuth frequency of 342.46 Hz (EW) and a median value of Δf_{ovl} of 5798 Hz/sec, we can simulate the accuracy. This accuracy can be expressed in terms of phase value (table 2.5).

	0.5	0.6	0.7	0.8	0.9
1	99.37	76.50	58.53	43.03	27.78
3	57.37	44.16	33.79	24.84	16.04
12	28.68	22.08	16.89	12.42	8.021
48	14.34	11.04	8.448	6.211	4.010

Table 2.5: Estimation of the phase standard deviation (in degree) according to the coherence (columns) and the number of looks (rows).

The BOI phase is rather low varying in space, meaning that a number of looks of 48 are perfectly reachable without over-passing the Nyquist criterion. Also, after filtering, the coherence can be quite high. To give an idea, coherence before filtering in our 1-look burst-overlap interferogram lies around 0.8 on the core of the shelf.

Note that the 4° error present in the table is the witness of a displacement of 1.2 cm between 2 acquisitions (i.e. 6 days). Said in other words, the estimated accuracy of azimuthal displacement from BOI can reach a displacement rate of 2mm/day (73cm/year). This is more than 10 times better than offset tracking results.

BOI can be enhanced in two ways. First, we can refocus raw data to increase the size of the overlapping regions. Indeed, the European Space Agency delivers truncated Single-Look-Complex images. We can expect up to a 20 % increase, with a decrease in signal quality. Secondly, BOI can be adapted to the overlapping areas between the different subswaths. If the spectral separation is smaller (and so the sensitivity to azimuthal displacements), it can greatly increase the overlapping regions.

Our results from burst overlapping and our proposed filtering method were presented during the European Conference on Synthetic Aperture 2021 scientific congress. We condensed the essential information of the current section in a reviewed proceeding, available here-after, and can be cited as

Glaude, Q., Derauw, D., Barbier, C., & Pattyn, F. (2021). Fast Azimuthal Displacement Retrieval from TOPSAR Burst Overlapping Interferometry: Application in Dronning Maud Land (Antarctica). *EUSAR 2021 - 2021 European Conference on Synthetic Aperture Radar*, Leipzig, Germany.

Fast Azimuthal Displacement Retrieval from TOPSAR Burst Overlapping Interferometry: Application in Dronning Maud Land (Antarctica)

Quentin Glaude^{a,b}, Dominique Derauw^{b,c}, Christian Barbier^b, and Frank Pattyn^a

^aLaboratoire de Glaciologie, Université Libre de Bruxelles, Bruxelles, Belgium

^bCentre Spatial de Liège, Université de Liège, Angleur, Belgium

^cInstituto de Investigación en Paleobiología y Geología, Universidad Nacional De Rio Negro, General Roca, Argentina

Abstract

Differential SAR Interferometry allows deriving velocity maps only along the line of sight. Bi-dimensional displacement estimation may be overcome using TOPSAR mode acquisition. TOPSAR acquisition mode implies burst-by-burst acquisition with beam steering from backward to forward during burst acquisition. Consecutive bursts have a superposition area to allow proper stitching. In these superposition areas, each point is observed twice with different azimuthal viewing angles (i.e. backward and forward). Burst Overlapping Interferometry (BOI) exploits these superposition areas to extract azimuthal displacements. We present here results of the BOI technique applied on Antarctic ice shelves, i.e. fast-moving area, and propose a filtering algorithm.

1 Introduction

Synthetic Aperture Radar (SAR) gained increasing interest in the remote sensing community, due to day-and-night, and almost atmospheric-free characteristics of the Radar wavelength. This is particularly the case using differential SAR interferometry (DInSAR) to monitor ground displacements [1]. Sentinel-1, the SAR component of Copernicus, uses the TOPSAR acquisition mode [2] in order to reduce the revisit time and increase its coverage.

One major issue with DInSAR is the displacements being observed only in the line-of-sight of the sensor. In addition, it suffers from some limitations related to spaceborne SAR acquisition geometry. SAR Earth observation satellites use polar heliosynchronous orbits. Consequently, since sensors are acquiring data perpendicular to their orbits, differential interferometry allows getting principally the East-West displacement component of horizontal displacements, while displacements in the along-track direction stay unresolved. TOPSAR acquisition mode offers unique peculiarities to infer azimuthal displacements. In this mode, the sensor steers its beam from backward to forward, forming a burst, instead of looking perpendicular to the satellite track direction. This steering reduces the aperture synthesis acquisition time and allows to aim the beam at different parallel sub-swaths (and thus increases its coverage up to 400 kilometers). Finally, bursts are stitched together using overlapping bands as shown in Figure 1 and formed an observing scene.

In these overlapping areas, displacements occurring in the azimuth direction induce additional interferometric phase terms. By exploiting these overlapping areas, Burst Overlapping Interferometry (BOI) can retrieve the azimuthal

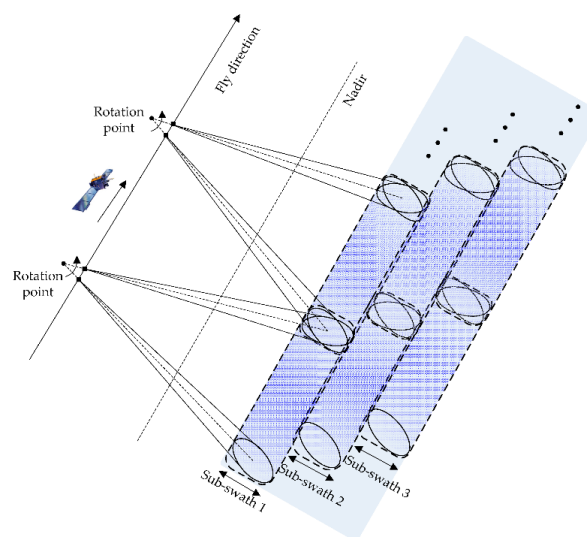


Figure 1 Acquisition geometry of a TOPSAR image. The image is composed of sub-swaths and bursts with overlapping areas. Illustration from [3].

component of the displacement.

This technique has been recently used by several authors to produce at high accuracy along-track displacements [4, 5], and by using several passes, reconstruct three-dimensional displacement maps [6, 7, 8].

In this article, we present results obtained by applying the technique in a fast-moving context in Antarctica. Additionally, we propose a modified Goldstein filtering algorithm adapted to suit BOI geometric specificities.

2 Method

2.1 Burst Overlapping Interferometry

In TOPSAR superposition areas, ground scatterers are observed twice; firstly with the sensor behind the scattering element aiming forward, and once on the next burst, with the sensor in front of the scatterer, aiming backward. Since interferograms can be generated on a burst-by-burst basis, a backward and a forward interferogram can be generated on bursts superposition areas.

For classical DInSAR purposes, azimuthal displacements are biasing the interferometric signal by adding phase information. This phase component is equal in absolute value but opposite in sign in the backward and forward interferograms. Burst Overlapping Interferometry (BOI) consists of performing differential interferometry between backward and forward interferograms in the overlapping areas in order to cancel out all phase terms except the one induced by the azimuth component of local displacements (Figure 2).

The burst overlapping interferometric phase ϕ_{BOI} is linearly proportional to an azimuthal displacement x (in pixel unit) by the relation :

$$\phi_{BOI} = \frac{2\pi \cdot \Delta f \cdot x}{AF} \quad (1)$$

where AF is the azimuthal frequency and Δf if the spectral separation. By inverting the equation, we obtain an azimuthal displacement :

$$x_{az} = \frac{AF}{2\pi \cdot \Delta f} \cdot \phi_{BOI} \quad (2)$$

This is the same relation as the one presented in extended spectral diversity techniques in order to remove small azimuth shifts in stationary areas.

2.2 Accuracy Estimation

The variance propagation results from the variance of individual interferograms [9], leading to the estimated displacement accuracy :

$$\sigma_x = \frac{AF}{2\pi \cdot \Delta f} \cdot \frac{1}{\sqrt{N}} \cdot \sqrt{\frac{1-\gamma^2}{\gamma^2}} \quad (3)$$

where γ is the estimated coherence and N is the number of looks.

Using azimuth frequency of 342.46 Hz (Extended interferometric Wide-swath mode) and a median value of the Doppler frequency difference Δf of 5798 Hz/sec, we can simulate the accuracy in terms of standard deviation. This accuracy can be expressed in terms of pixel or phase value. Even for the case of fast displacement, the BOI phase is rather low varying in space. It allows us to increase the number of looks and reach the lower part of Table 1. Also, after filtering, the coherence can be quite high (see next section).

Table 1 Estimation of the phase standard deviation (in degree) according to the coherence (columns) and the number of looks (rows).

	0.5	0.6	0.7	0.8	0.9
1	99.4	76.5	58.5	43.0	27.8
3	57.4	44.2	33.8	24.8	16.0
12	28.7	22.1	16.9	12.4	8.0
48	14.3	11.0	8.4	6.2	4.0

Note that the 4-degrees error present in the table (coherence of 0.9 and 48 looks) corresponds to a displacement of 1.2 cm between 2 acquisitions (i.e. 6 days). Said in other words, the estimated accuracy of azimuthal displacement from BOI can reach a displacement rate of 2mm/day (73cm/year). This is more than 10 times better than offset tracking results with Sentinel-1 [10].

2.3 BOI-Adapted Goldstein Phase Filtering

Phase computed using the BOI technique is quite noisy. Since the BOI phase is a difference between two phases, the noise component is increased by a $\sqrt{2}$ factor. Moreover, the scatterer is observed from slightly different view angles, resulting in geometric decorrelation.

Goldstein phase filtering is a very popular phase filter algorithm [11]. The method is easy to implement, has few parameters and significantly filters results while preserving sharp spatial changes. These constitute the reasons why we built our BOI-adapted phase filtering based on the Goldstein phase filtering.

The elongated characteristic of the burst overlapping areas (around 100×8000 pixels in EW mode) makes the Goldstein algorithm quite obsolete. We adapted the filter as a sliding window inside which an iterative low Goldstein phase filtering is employed. The filter produces the filtered BOI phase column by column when moving (Figure 4). No weighted average is implemented since the column by column sliding ensures a continuous estimation of the BOI phase.

3 Results

BOI has been applied on the Roi Baudouin Ice Shelf, in Queen Maud Land, Antarctica (Figure 5).

The application of BOI in Antarctica is tricky because of the fast-moving nature of the ice at the surface. This is particularly the case in the boundaries of Antarctica, at the surface of ice shelves.

The azimuthal displacement in BOI is expressed as a phase value. Here, we call azimuthal displacement ambiguity the azimuthal displacement leading to a 2-pi shift. Using equation (2), a 2-pi shift corresponds to a 0.059 pixel azimuthal displacement, this is to say a 1.176 meters displacement (pixel spacing of 19.9281 meters). When using SAR pairs with a 6-days revisit time, any displacement greater than 71.5 meters per year will wrap the BOI phase. On the Roi Baudouin Ice Shelf, displacements on the main ice stream

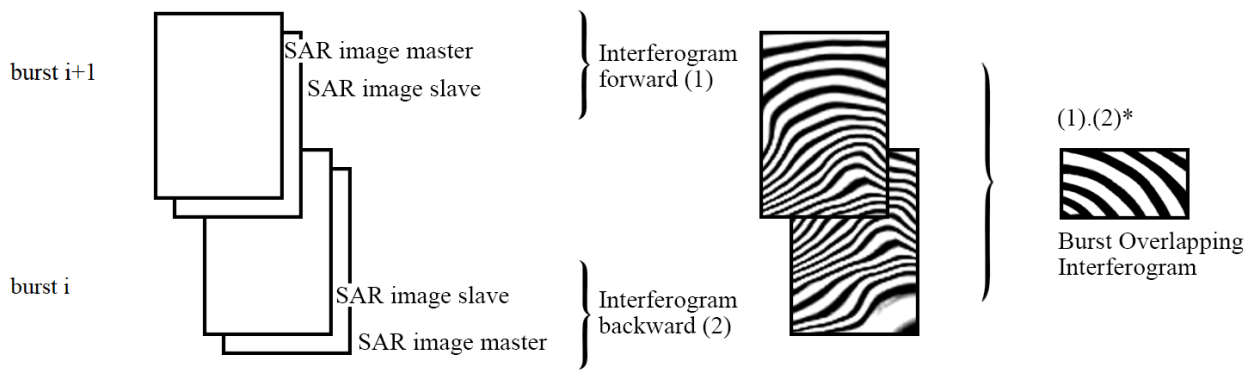


Figure 2 Burst Overlapping Interferometry (BOI).

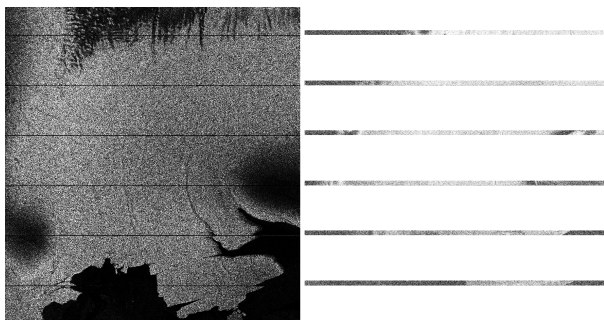


Figure 3 The intensity of the master image (left) and BOI coherence (right). Coherence in our 1-look burst-overlap interferogram lies around 0.8 on the core of the shelf

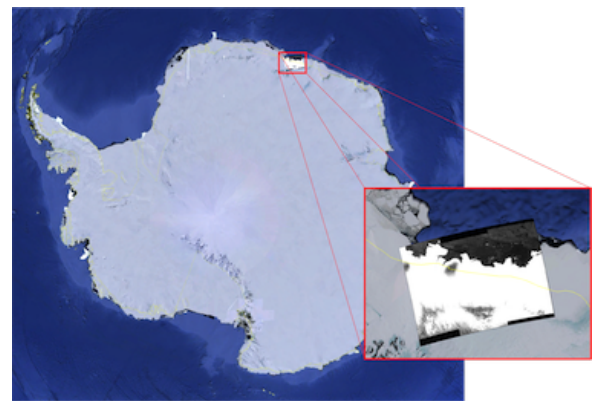


Figure 5 Roi Baudouin Ice Shelf, Queen Maud land, Antarctica.

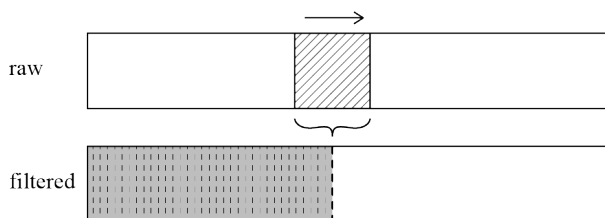


Figure 4 Concept of the BOI-adapted Goldstein phase filtering. The Goldstein filter is applied iteratively as a moving window that generates the output phase column-by-column.

go further than 300 meters per year. Using references and unwrapping the signal allows obtaining the absolute azimuthal velocity. An example of the filter and the wrapped BOI signal is displayed in Figure 6.

4 Conclusion

DInSAR allows to derive at high accuracy displacements maps in the line-of-sight direction. With the specificities of Sentinel-1 and its particular acquisition TOPSAR mode, we can also use BOI in order to extract the azimuthal component of surface displacements.

In the present study, we applied the BOI technique in Antarctica. Considering the fast-moving nature of the observed surface, we showed that the BOI signal can be wrapped. Proper unwrapping is needed before conversion into azimuthal displacements. In addition, we proposed a Goldstein-adapted BOI phase filtering to filter the BOI phase.

Our results suggest that BOI and our developed filter are working properly. We can retrieve azimuthal displacement in fast-moving areas with a single SAR with centimeter accuracy.

5 Acknowledgment

This research is supported by the French Community of Belgium in the funding context of a FRIA grant, and carried out in the framework of the MIMO (Monitoring melt where Ice Meets Ocean) project funded by the Belgian Science Policy contract Nos. SR/00/336.

6 Literature

- [1] Massonnet, D.: Rossi, M.: Carmona, C.: Adragna, F.: Peltzer, G.: Feigl, K.: Rabaute, T.: The displacement

Figure 6 Example of the application of our BOI-Adapted Goldstein phase filtering. Top: raw BOI Phase. Bottom: filtered phase. In the illustration, we focus on the BOI phase of the third burst overlapping area in figure 3.

- field of the Landers earthquake mapped by radar interferometry. *Nature*, 364(6433), 1993, pp. 138–142
- [2] De Zan, F.: Guarnieri, A. M.: TOPSAR: Terrain observation by progressive scans. *IEEE Transactions on Geoscience and Remote Sensing*, 44(9), 2006, pp. 2352–2360
- [3] Yang, W.: Chen, J.: Zeng, H.C.: Wang, P.B.: Liu, W.: A Wide-Swath Spaceborne TOPS SAR Image Formation Algorithm Based on Chirp Scaling and Chirp-Z Transform. *Sensors* 2016, 16, 2095
- [4] Jiang, H. J.: Pei, Y. Y.: Li, J.: Sentinel-1 TOPS interferometry for along-track displacement measurement, *IOP Conf. Ser.: Earth Environ. Sci.* 57 012019, 2017
- [5] Mancon, S.: Monti Guarnieri, A.: Giudici, D.: Tebaldini, S.: On the Phase Calibration by Multisquint Analysis in TOPSAR and Stripmap Interferometry, in *IEEE Transactions on Geoscience and Remote Sensing*, vol. 55, no. 1, pp. 134-147, Jan. 2017.
- [6] Jiang, H.: Feng, G.: Wang, T.: Bürgmann, R.: Toward full exploitation of coherent and incoherent information in Sentinel-1 TOPS data for retrieving surface displacement: Application to the 2016 Kumamoto (Japan) earthquake, *Geophys. Res. Lett.*, 44, 2017, pp. 1758–1767
- [7] Grandin, R.: Klein, E.: Métois, M.: Vigny, C.: Three-dimensional displacement field of the 2015 Mw8.3 Illapel earthquake (Chile) from across- and along-track Sentinel-1 TOPS interferometry, *Geophys. Res. Lett.*, 43, 2016, pp. 2552–2561
- [8] Prats-Iraola, P.: Member, S.: Lopez-dekker, P.: Member, S.: De Zan, F.: Yagüe-Martínez, N.: Rodríguez-cassola, M.: Performance of 3-D Surface Deformation Estimation for Simultaneous Squinted SAR Acquisitions, 56(4), 2018, pp. 2147–2158.
- [9] Just, D.: Bamler, R.: Phase statistics of interferograms with applications to synthetic aperture radar, *Appl. Opt.* 33, 4361-4368, 1994
- [10] Mouginot, J.: Rignot, E.: Scheuchl, B.: & Millan, R.: Comprehensive annual ice sheet velocity mapping using Landsat-8, Sentinel-1, and RADARSAT-2 data. *Remote Sensing*, 9(4), 2017, pp. 1–20
- [11] Goldstein, R.: Werner, C.: Radar interferogram filtering for geophysical applications. *Geophysical Research Letters*, 25, 1998, pp. 4035-4038

2.3 Damages, Crevasses, and Calving Front Monitoring: the Causes and the Consequences of some Ice Shelves' Destabilization

When losing mass, ice shelves lose their gatekeeper property, with potential local destabilization of the AIS. Losing mass from calving is a sophisticated process that is rarely coupled with observations in ice sheet models. Calving and damages are visible in SAR remote sensing products.

Recent studies show how damaged structures are participating in the destabilization of ice shelves (Lhermitte et al., 2020). Looking at crevasses evolution (Figure 2.62), we can make causal relations with how ice shelves in the Amundsen sea sector are subject to unprecedented and unmodelled behaviors.

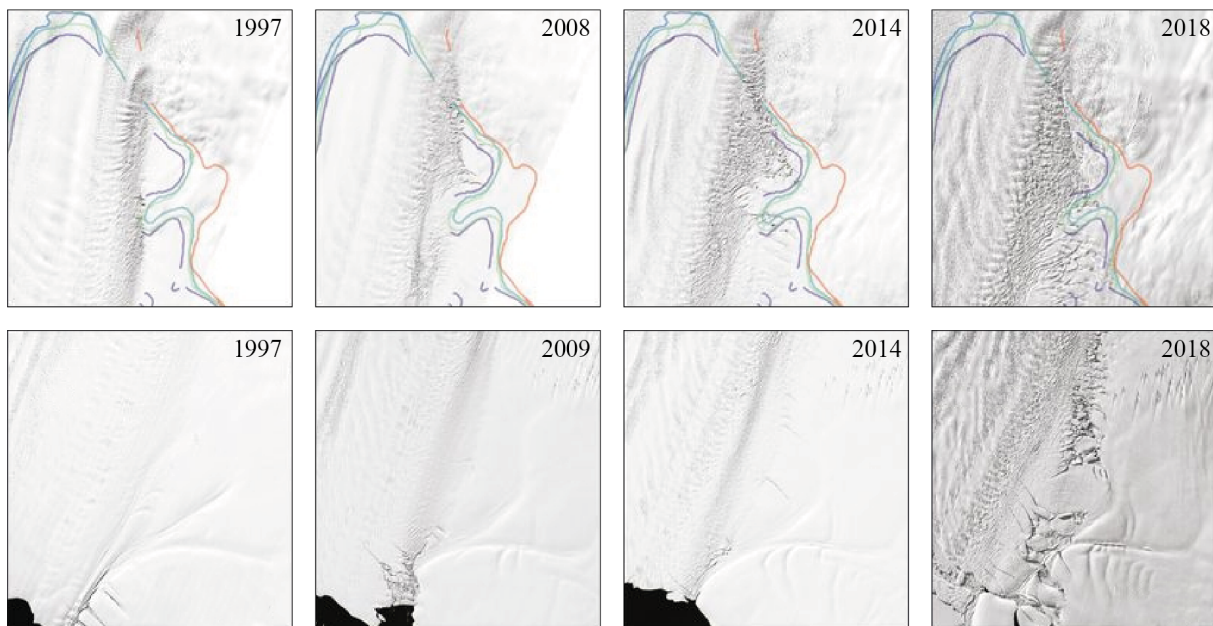


Figure 2.62: Over time, the number of cracks increased drastically where the shear stress is relatively important. This crack propagation participates in the destabilization of an ice shelf, calving events, and retreat of the ice front towards the continent. In parallel, we can observe a retreat of the hinge line of several kilometers in some cases. The first two lines cover 2 different parts of the Pine Island Glacier. Illustration reworked from Lhermitte et al. (2020), with authorizations.

We developed a method dedicated to automatic crack propagation and calving front monitoring using Synthetic Aperture Radar and computer vision techniques. We analyzed the Pine Island Glacier over the period 2017-2020. This represents 197 Sentinel-1 Acquisitions, with 6 days between each image. We used Ground-Range-Detected - GRD images in Interferometric Wideswath mode, on relative orbit 65. Preprocessing steps include calibration and log-transform to decibels, speckle filtering, geoprojection in the Polar Stereographic Reference Coordinates System with a 20 meters pixel spacing. The processing chart is visible in Fig. 2.63.

Crevasses can be regarded as contrasted linear elements in SAR images. In computer vision, an edge in an image can be defined as an abrupt spatial change in values. In one dimension, we can analyze the first and second derivatives to retrieve the edge location (Fig. 2.64).

In SAR, images are tainted with a high-frequency noise called the speckle. One solution is to smooth the signal first by the application of a low pass filter. We can use a gaussian-shaped kernel and compute its convolution with the signal. Then we compute the derivative of the result and locate the local maximum. Using the convolution theorem $\frac{\partial(f*h)}{\partial x} = \frac{\partial h}{\partial x} * f$, we can compute

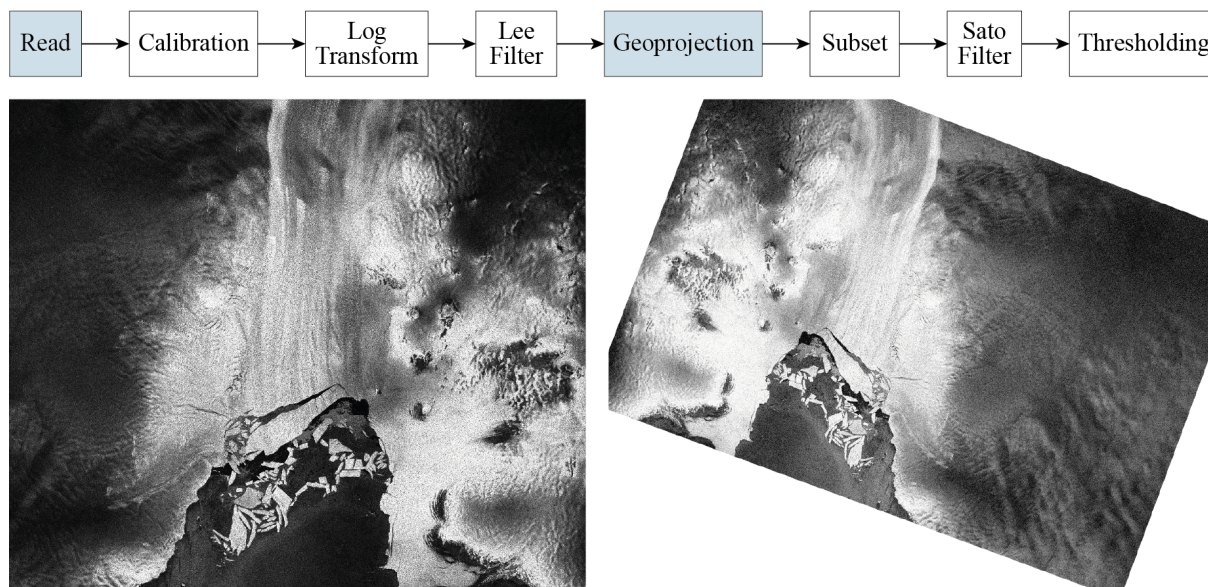


Figure 2.63: Processing scheme of the crevasses and calving front monitoring. The bottom images illustrate the input and output images of the preprocessing step (colored in chart).

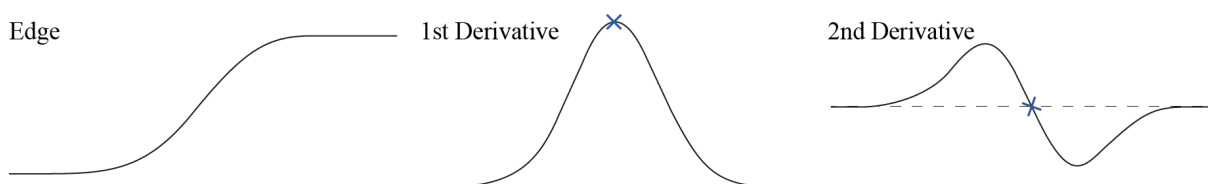


Figure 2.64: Edge detection by first and second derivatives analysis, using the location of the peak or the zero-crossing (resp.).

the expression of the derivative of the gaussian, which is well known, and then convolute it with the signal f , sparing one operation in the detection process (Fig. 2.65).

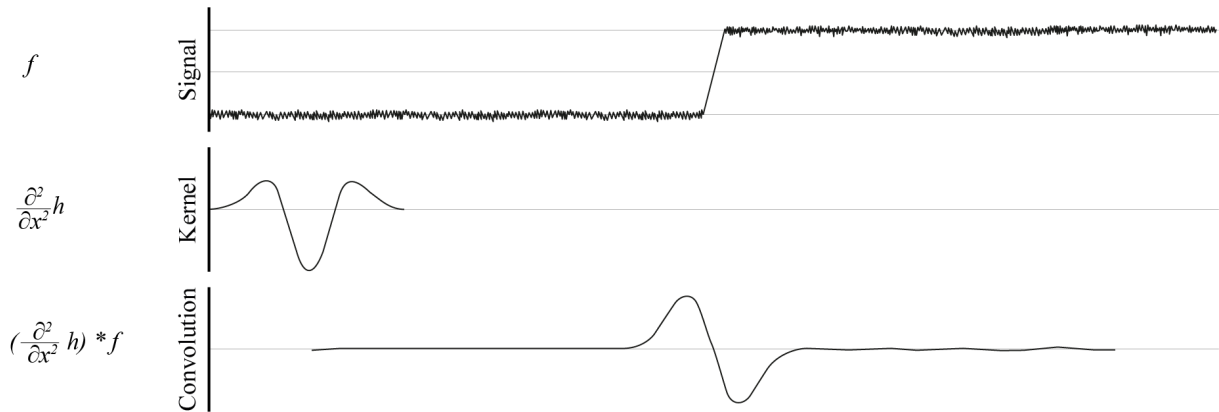


Figure 2.65: Edge detection of the filtered signal by gaussian-2nd-derivative, using one property of the convolution product.

Since $\frac{\partial^2(h)}{\partial x^2}$ is negative in its center, it is common to use the inverted Laplacian of Gaussian instead.

An image being a multidimensional signal, derivations are to be accounted for each dimension. Using a second-order derivative approach, all these information are contained in the Hessian matrix. The Hessian matrix is the matrix of second-order partial derivatives. It is a symmetric matrix expressed as

$$H(f) = \begin{bmatrix} \frac{\partial^2 f}{\partial x_1^2} & \frac{\partial^2 f}{\partial x_1 \partial x_2} & \cdots & \frac{\partial^2 f}{\partial x_1 \partial x_n} \\ \frac{\partial^2 f}{\partial x_2 \partial x_1} & \frac{\partial^2 f}{\partial x_2^2} & \cdots & \frac{\partial^2 f}{\partial x_2 \partial x_n} \\ \vdots & \vdots & \ddots & \vdots \\ \frac{\partial^2 f}{\partial x_n \partial x_1} & \frac{\partial^2 f}{\partial x_n \partial x_2} & \cdots & \frac{\partial^2 f}{\partial x_n^2} \end{bmatrix} \quad (2.32)$$

Again, the signal f is tainted with errors. Gaussian filtering is thus applied, estimating

$$\frac{\partial^2 f}{\partial x_i \partial x_j} \approx \frac{\partial^2 (f * h)}{\partial x_i \partial x_j} = \frac{\partial^2 h}{\partial x_i \partial x_j} * f \quad (2.33)$$

In a Hessian matrix, all eigenvalues are real (property of symmetric matrices). By extracting these eigenvalues and eigenvectors, we can predict the behavior of a function at a given location.

In its research, Sato et al. (1998) defined conditions on the eigenvalues that indicate the presence of an edge. He defined a similarity index to an edge. Sato filter has been used in 3D medical imaging, with impressive results. We managed to prove the efficiency of the method in SAR remote sensing in this report. Fig. 2.66 (left) represents the subsetted calibrated geoprojected SAR image over the Pine Island Glacier. The acquisition has been subset to the main area of interest. From Fig. 2.66 (center), the Sato filter manages to remarkably extract the lines within our image. We can easily see the calving front of the ice shelf, the numerous icebergs, and the different fractures in the shear area. By thresholding, we can extract the edges from the Sato filter (Fig. 2.66, right). The quality of the lines extraction is impressive.

Analyzing the Pine Island Glacier at different dates (Fig. 2.67), we observe that the calving front retreated by overall 20 kilometers in three years.

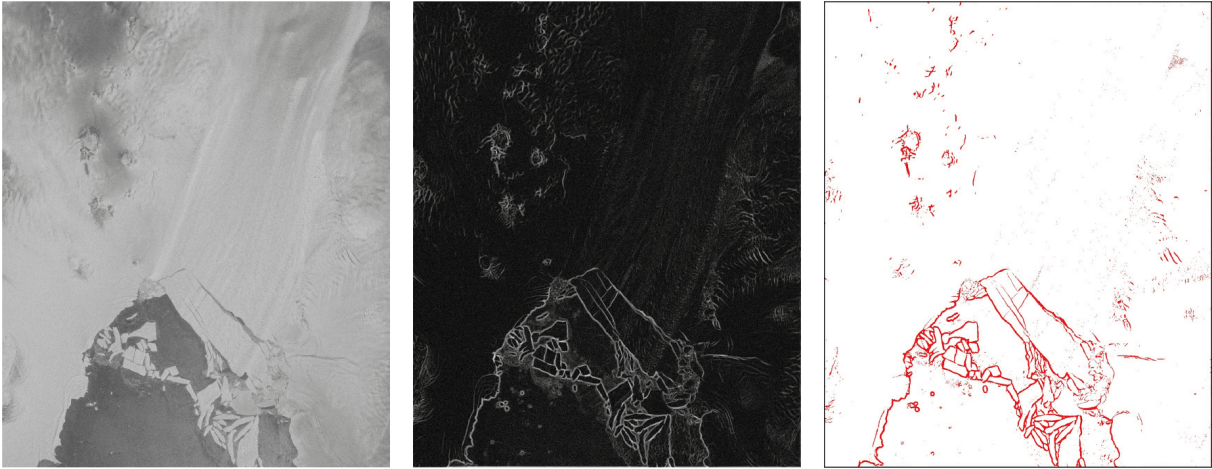


Figure 2.66: (left) subset of the calibrated Radar Cross Section of the SAR image. Center: result of the Sato filtered SAR image. (right) edges extraction by thresholding. Acquisition date: 31st of October 2018.

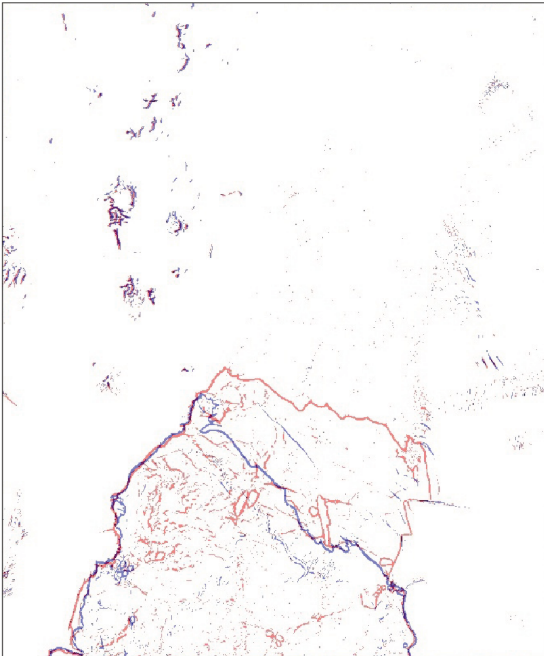


Figure 2.67: Comparison between June 2017 (blue) and June 2020 (red).

With almost 200 acquisitions, it is possible to use the results as frames of a short animation. In Fig. 2.68, PIG cracks are displayed, with important calving events.

A similar approach was performed on the Brunt Ice Shelf, East Antarctica, where a recent calving event took place in late February 2021 (Fig. 2.69).

Zooming on the Southern chasm #1, we might observe in the next couple of months a similar important calving event (Fig. 2.70). We studied the crack propagation speed and the crack opening of the ice shelf. The fracture is propagating at an average speed of 8.5 meters per day. This velocity is far from homogeneous, with a peak in 2019 at 18 meters per day, and a recent decrease at 2.5 meters per day. The opening speed follows a similar path, with an opening rate between 66 and 79 cm per day between 2018 and 2020, and a relative stabilization in 2021 (27 cm per day). The chasm #1 is currently close to the opposite coast (5 kilometers). In consequence, the Southern part of the Brunt ice shelf is likely to collapse in the next few months, encouraging its monitoring.

In this section, we built the hypothesis that state-of-the-art ridge detection techniques from the medical imaging field can be transposed to the cryosphere field. Looking at the local Hessian matrix in SAR acquisitions, we analyzed the eigenvectors that indicate the presence of ridges. Over ice shelves, these edges correspond to the calving front of the ice shelf or crevasses. Using time series, we can monitor the evolution of crevasse propagation and calving events. Results over Pine Island Glacier and the Brunt Ice Shelf shows a precise delineation of calving events, as well as the damaged areas.

The calving front and crevasses monitoring technique was presented during the EGU General Assembly 2021 and during the IEEE International Symposium on Geoscience and Remote Sensing (IGARSS) 2021 event. We condensed essential information from the current section into a reviewed proceeding, available here-after, and can be cited as

Glaude, Q., Lizin, S., Pattyn, F., Barbier, C., & Orban, A. (2021). Crack Propagation and Calving Front Monitoring Using Sato Filter. *IGARSS 2021 - 2021 IEEE International Geoscience and Remote Sensing Symposium*, Brussels, Belgium.

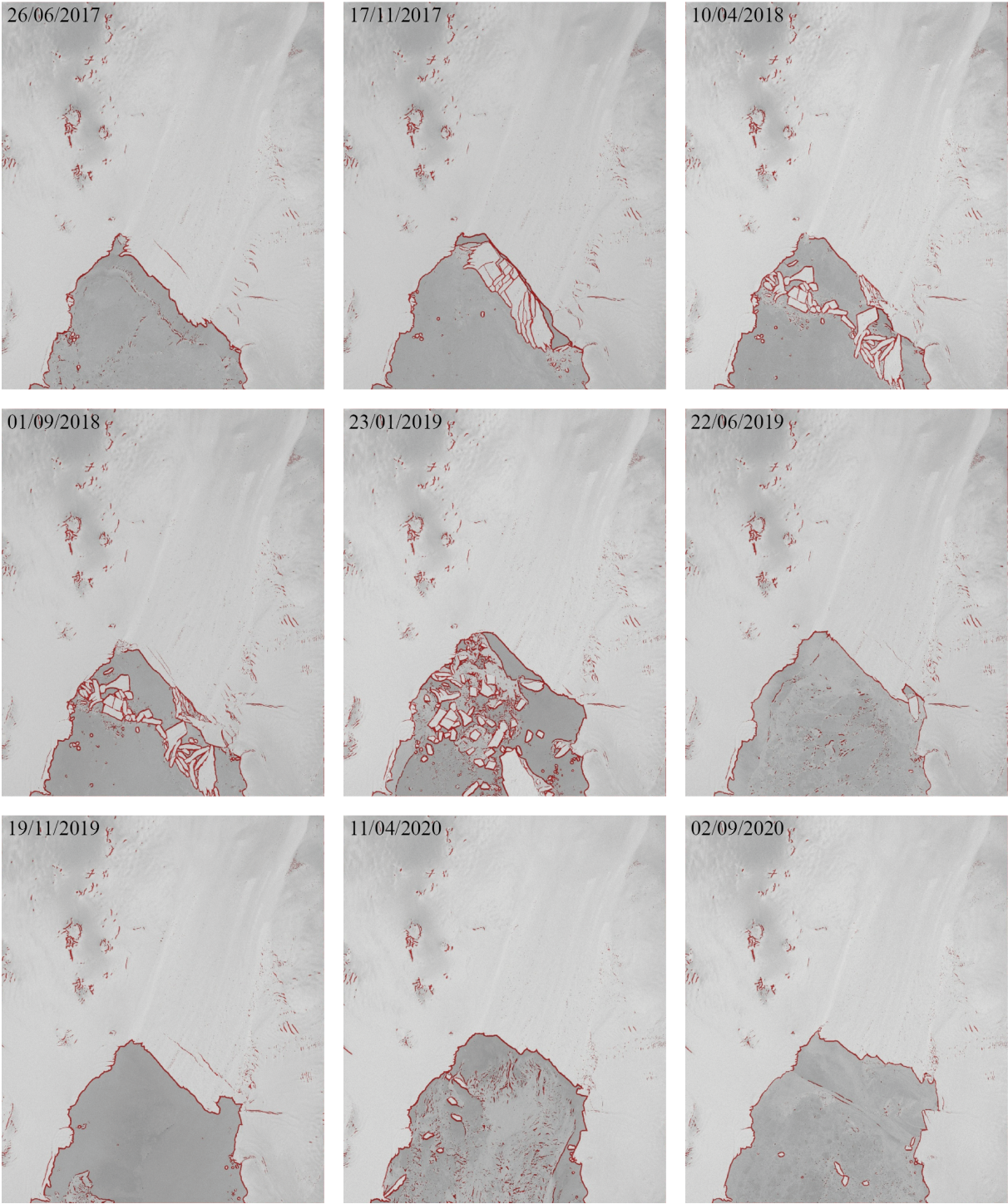


Figure 2.68: Time series of crack propagation and calving front products over Pine Island Glacier.

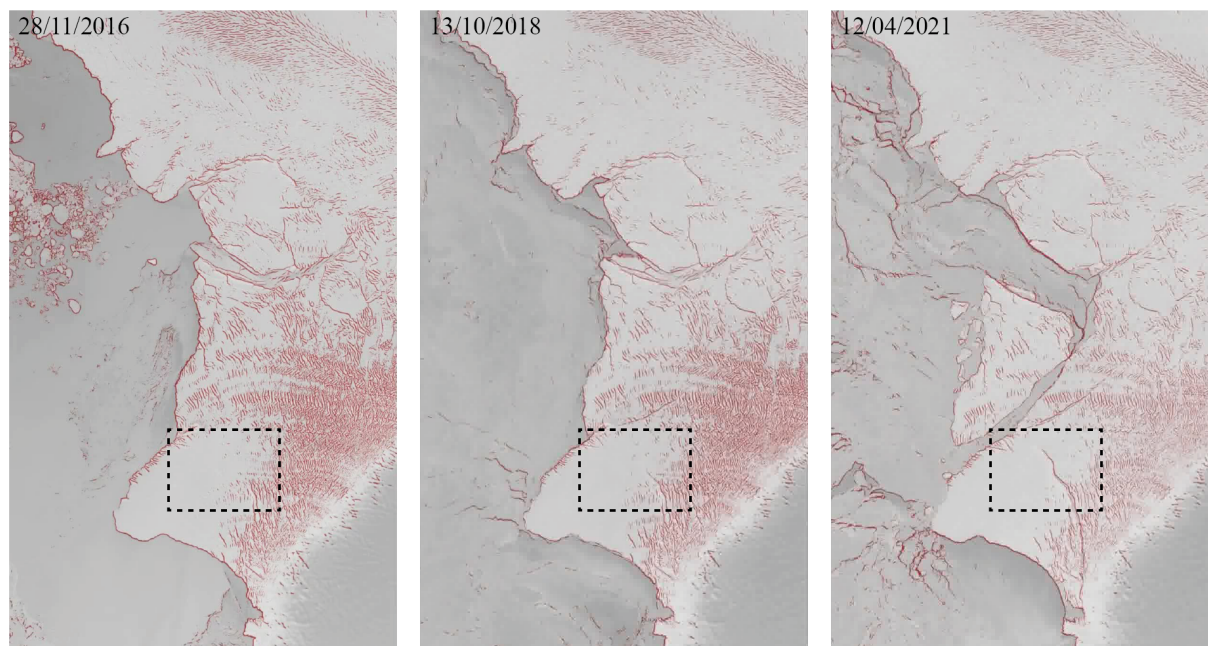


Figure 2.69: Selection of crack propagation and calving front products over Brunt Ice Shelf. We displayed the important calving event of February 2021

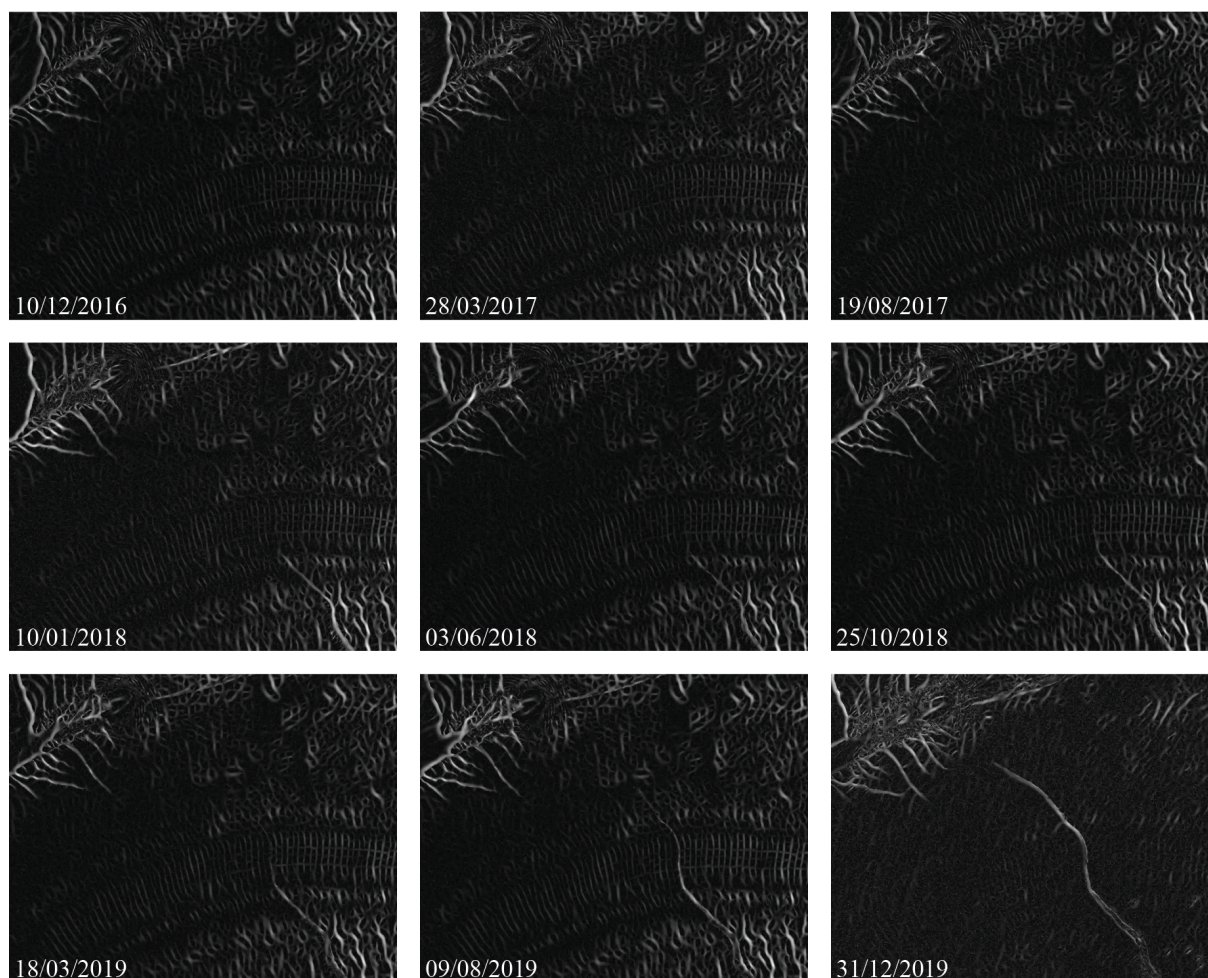


Figure 2.70: South chasm propagation observed using the Sato conditional probability criterion. The region corresponds to the bounding box visible in Fig. 2.69.

CRACK PROPAGATION AND CALVING FRONT MONITORING USING SATO FILTER

Q. Glaude (1,2), S. Lizin (3), F. Pattyn (1), C. Barbier (2) and A. Orban (2)

(1) Laboratory of Glaciology, Université Libre de Bruxelles, Bruxelles, Belgium

(2) Liège Space Center, Université de Liège, Angleur, Belgium

(3) Space Sciences, Technologies and Astrophysics Research, Université de Liège, Angleur, Belgium

ABSTRACT

Ice shelves, the floating extensions of the Antarctic Ice Sheet, are important regulators of the ice discharge and need to be monitored. Among others, calving processes and fractures control their ability to restrain the upward ice flow. While models integrate calving laws, their comparison with observations is still sparse and is mainly performed through visual inspection. In the present work, we hypothesized that the combination of high revisit rate SAR remote sensing products with medical imaging techniques can automatically detect cracks and monitor the calving front location. We focused our study on the Pine Island Glacier, in the Amundsen Sea Sector, with Sentinel-1 data over the period 2017 to 2020. Results show that the Sato filtering technique managed to precisely delineate the calving front, the icebergs, and the fractures on the ice shelf.

Index Terms— Sentinel-1, Ice Shelf, Cracks, Calving, Sato

1. INTRODUCTION

The Antarctic Ice Sheet (AIS) is a large mass of ice laying on a rocky continent, called the Antarctic. This mass undergoes gravity-driven displacements towards the AIS boundaries. When the ice flow meets the ocean, the ice begins to float and becomes an ice shelf. These ice shelves are all but passive, and actively regulate the Antarctic contribution to sea-level rise by restraining the grounded ice flowing from upstream [1]. Ice shelves produce a buttressing effect, through constraints by embayments and sub-shelf pinning points (Figure 1) [2]. When an ice shelf thins or loses mass, its ability to restrain the grounded ice flow instantaneously reduces [3]. Losing mass and thinning can occur by basal melting, surface melting, ice flow acceleration, and calving. In equilibrium, an ice shelf gains as much ice as it loses. However, this stability is compromised for an increasing number of areas around Antarctica [4, 5]. The main driving factors are the increase in basal melting and calving. Basal melting is well integrated into models through thermodynamics study. Calving is a more sophisticated process, and hardly integrated, though it is an important factor and signal for collapsing. In

that sense, remote sensing and SAR in particular are useful tools to observe the ice shelves' behavior.

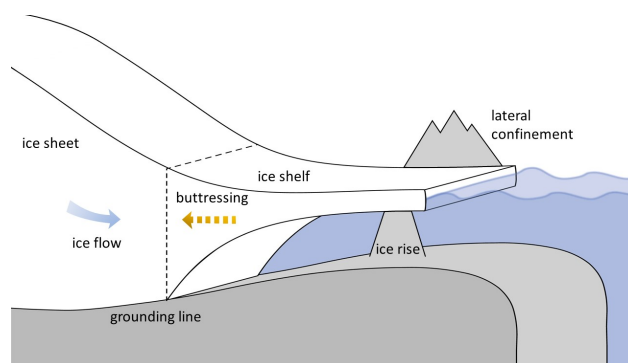


Fig. 1. Constraint by local embayment and pinning points, ice shelves actively participate in the ice flow restrain by buttressing [6].

Recent studies show how damaged structures are participating in the destabilization of ice shelves [7]. Figure 2 shows crevasses evolution over PIG. In [7], a synthetic model accounting for the ice shelves damages show the potential consequences on velocity and thickness. Nevertheless, the relation between damage and ice shelf destabilization is still performed mostly by visual inspection, rather than by quantitative measurements. Similarly, the integration of crack propagation is not coupled with observations.

The paper is structured as followed. In section 2, we summarized the concepts of edge detection in computer vision and gradually detailed the Sato filter's conceptual implementation. In section 3, we applied the technique on the Pine Island Glacier (PIG) over the period 2017-2020 and showed preliminary results of automatic crack propagation and calving front monitoring using Sentinel-1 Synthetic Aperture Radar satellite and medical imaging techniques.

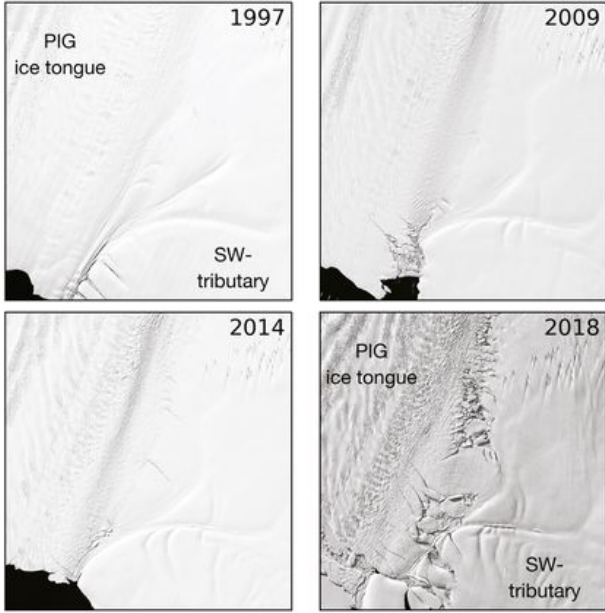


Fig. 2. Over time, the number of cracks increased drastically where the shear stress is relatively important. This crack propagation participates in the destabilization of the ice shelf, calving event, and retreat of the ice front towards the continent. Illustration reworked from [7].

2. RIDGE DETECTION USING THE SATO FILTER

2.1. Detecting Edges in Signals

An edge in an image can be seen as an abrupt spatial change in values [8]. In one dimension, it is easily understood that looking at first and second derivatives can help in retrieving the location of this edge. Using a continuous sharp hill function as a synthetic ridge (Figure 3.a), one can compute the first derivative and locate the maximum for determining the edge location (Figure 3.b). Similarly, we can compute the second derivative and detect the edge by looking at the zero-crossing location (Figure 3.c). This is equivalent to analyzing the first- and second-order terms of the Taylor approximation of the signal.

In a more realistic scenario, we can expect the signal to be tainted with a high-frequency noise. One solution is to preliminary smooth the signal first by the application of a low pass filter. We can use a gaussian-shape kernel and compute its convolution with the signal. Then we compute the derivative of the result and locate the local maximum.

2.2. The Hessian Matrix and Sato Filter

For multidimensional signals, derivations are to be accounted for each dimension. Using a second-order derivative approach, the required information are contained in the Hessian

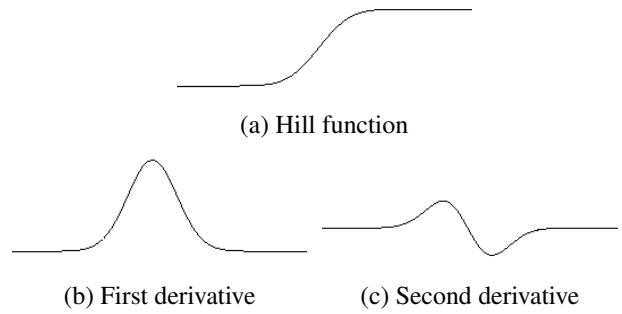


Fig. 3. Edge detection by first and second derivatives analysis.

matrix. The Hessian matrix is the matrix of second-order partial derivatives. It is a symmetric matrix expressed as:

$$H(f) = \begin{bmatrix} \frac{\partial^2 f}{\partial x_1^2} & \frac{\partial^2 f}{\partial x_1 \partial x_2} & \cdots & \frac{\partial^2 f}{\partial x_1 \partial x_n} \\ \frac{\partial^2 f}{\partial x_2 \partial x_1} & \frac{\partial^2 f}{\partial x_2^2} & \cdots & \frac{\partial^2 f}{\partial x_2 \partial x_n} \\ \vdots & \vdots & \ddots & \vdots \\ \frac{\partial^2 f}{\partial x_n \partial x_1} & \frac{\partial^2 f}{\partial x_n \partial x_2} & \cdots & \frac{\partial^2 f}{\partial x_n^2} \end{bmatrix} \quad (1)$$

In the case of images, the variables are limited to the rows and columns axis, and the computation of derivatives is estimated using the Sobel filter [9]. Again, the f signal is tainted with errors. Gaussian filtering is thus applied. By the property of the convolution, we compute the derivatives to the gaussian-shape filter:

$$\frac{\partial^2 (f * h)}{\partial x_i \partial x_j} = \frac{\partial^2 h}{\partial x_i \partial x_j} * f \quad (2)$$

In a Hessian matrix, all eigenvalues are real (property of symmetric matrices). By extracting these eigenvalues and eigenvectors of the Hessian Matrix, we can predict the behavior of a function at a given location.

In its research, [10] defined conditions on the eigenvalues that indicate the presence of an edge. The idea is to create a similarity index to a linear function. The method is sensitive to the spatial scale at which we evaluate the signal. A multiscale approach is used in the Sato filter.

3. RESULTS

Sato filter has been used in 3D medical imaging, with impressive results. This research domain is not restricted, and we managed to prove the efficiency of the method in SAR remote sensing.

In this conference paper, we focused the study on the Pine Island Glacier, over the period 2017 to 2020. We used

Sentinel-1 Ground-Range-Detected (GRD) images in Interferometric Wideswath mode, on relative orbit 65. This represents 197 acquisitions, with 6 days between each image.

The detection of cracks over SAR images requires a pre-processing step before treatment. First of all, images need to be calibrated, i.e. translating the value of the sensor to a physical meaning. Considering our application and potential multiple orbits, we decided to employ the sigma naught [11]. Secondly, the image is transformed to increase contrast. This is performed using a log transformation of the image, who drastically reduces the skewness of the image histogram. Then, noise reduction methods are applied to the image to reduce the speckle effect. In the project, we used the refined Lee Sigma filter [12], which allows a strong reduction of high spatial frequency related to speckle but still keeping the important structures in the image. Finally, a geometrical transformation is applied to project the images in a coherent reference coordinates system. In this project, we used the Antarctic Polar Stereographic projection (EPSG:3031), with a pixel spacing of 20 meters.

Figure 4 represents the calibrated geoprojected SAR image over the Pine Island Glacier with direct comparison to the detected cracks. In our results, Sato managed to remarkably extract the lines within our image. We can easily see the calving front of the ice shelf, the numerous icebergs, and the different fractures in the shear area. Time series analysis allows to monitor the creation and propagation of existing crevasses. Putting side to side the preprocessed SAR image and the extracted lines, we have spatial information of some of the processes that control the ice shelf dynamics.

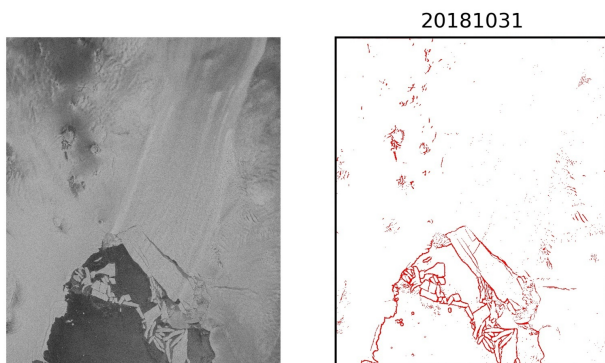


Fig. 4. The left image represents the subset of the calibrated Radar Cross Section of the SAR image. The right image shows the ridges extraction, corresponding to crevasses and calving front. These detections were performed by thresholding the Sato filtered SAR image.

With almost 200 acquisitions, it is possible to use the results as frames of a short animation. The full animation is visible at shorturl.at/uTZ16. In Figures 5 and 6, PIG cracks are displayed at different dates, with important calving



Fig. 5. Comparison between June 2017 (blue) and June 2020 (red). We observe that the calving front retreated by overall 20 kilometers, i.e. 20 meters per day on average (the retreat is far from continuous but rather results from sudden large calving events).

events.

4. CONCLUSION

In this conference paper, we proposed an approach to extract the fractures and calving front location of an ice shelf. We decided to work on the PIG, which suffers from strong dynamics, large calving events, and overall retreat of the ice shelf. We worked with almost 200 Sentinel-1 SAR acquisitions, from 2016 to 2020, with 6 days between images.

The first step of the method required a robust preprocess pipeline, including calibration of images, log-transform to enhance contrast, speckle filtering, and geoprojection in Antarctic Polar Stereographic.

Then, the principle of edge detection was described, with particular emphasis on the Sato filtering technique. Finally, the method is applied on subsetted SAR preprocessed images, giving as output the location of cracks and calving front.

The results show that the method can put contrast on important events. The monitoring of fractures is now assisted by the technique and the door to quantitative results is open. The method is not restricted to the PIG, and we can expect to apply the method to any region.

5. ACKNOWLEDGMENTS

This research is supported by the French community of Belgium in the funding context of a FRIA grant, and carried out in the framework of the MIMO (Monitoring melt where Ice Meets Ocean) project funded by the Belgian Science Policy contract Nos. SR/00/336.

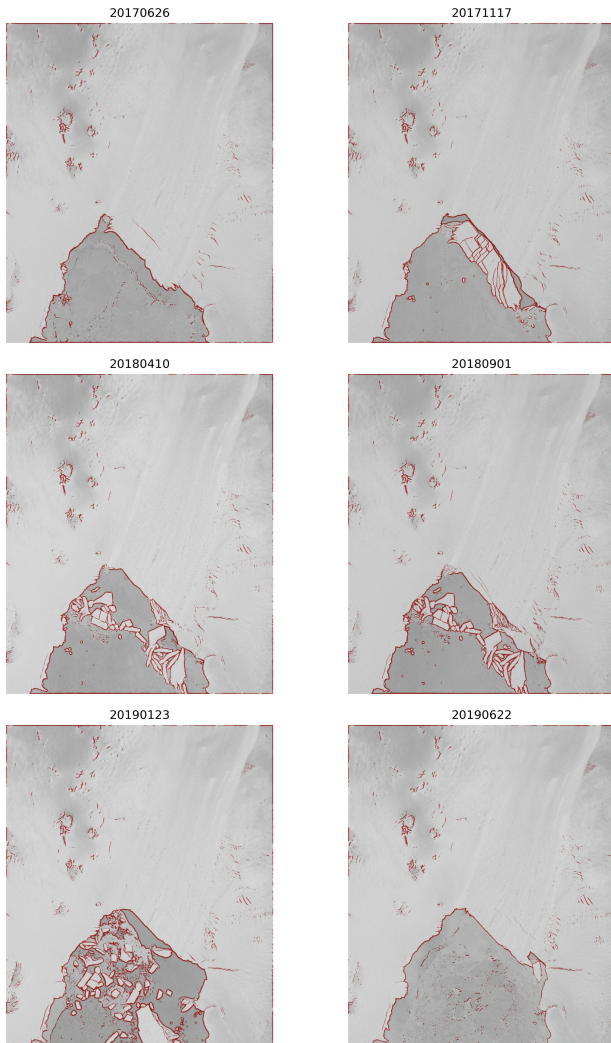


Fig. 6. Selection of crack propagation and calving front detections from the 2017-2020 time series.

6. REFERENCES

- [1] D. Goldberg, D. M. Holland, and C. Schoof, "Grounding line movement and ice shelf buttressing in marine ice sheets," *Journal of Geophysical Research: Earth Surface*, vol. 114, no. F4, 2009.
- [2] Lionel Favier and Frank Pattyn, "Antarctic ice rise formation, evolution, and stability," *Geophysical Research Letters*, vol. 42, no. 11, pp. 4456–4463, 2015.
- [3] Hamish D Pritchard, Robert J Arthern, David G Vaughan, and Laura A Edwards, "Greenland and Antarctic ice sheets," *Nature*, vol. 461, no. 7266, pp. 971–975, 2009.
- [4] J. Feldmann and A. Levermann, "Collapse of the west antarctic ice sheet after local destabilization of the amundsen basin," *Proceedings of the National Academy of Sciences of the United States of America*, vol. 112, no. 46, pp. 14191–14196, 2015, cited By 63.
- [5] S. Sun, F. Pattyn, E.G. Simon, T. Albrecht, S. Cornford, R. Calov, C. Dumas, F. Gillet-Chaulet, H. Goelzer, N.R. Golledge, R. Greve, M.J. Hoffman, A. Humbert, E. Kazmierczak, T. Kleiner, G.R. Leguy, W.H. Lipscomb, D. Martin, M. Morlighem, S. Nowicki, D. Pollard, S. Price, A. Quiquet, H. Seroussi, T. Schlemm, J. Sutter, R.S.W. Van De Wal, R. Winkelmann, and T. Zhang, "Antarctic ice sheet response to sudden and sustained ice-shelf collapse (abumip)," *Journal of Glaciology*, vol. 66, no. 260, pp. 891–904, 2020, cited By 3.
- [6] R. Reese, G. H. Gudmundsson, A. Levermann, and R. Winkelmann, "The far reach of ice-shelf thinning in Antarctica," *Nature Climate Change*, 2017.
- [7] Stef Lhermitte, Sainan Sun, Christopher Shuman, Bert Wouters, Frank Pattyn, Jan Wuite, Etienne Berthier, and Thomas Nagler, "Damage accelerates ice shelf instability and mass loss in amundsen sea embayment," *Proceedings of the National Academy of Sciences*, vol. 117, no. 40, pp. 24735–24741, 2020.
- [8] R.N. Czerwinski, D.L. Jones, and W.D. O'Brien Jr., "Detection of lines and boundaries in speckle images - application to medical ultrasound," *IEEE Transactions on Medical Imaging*, vol. 18, no. 2, pp. 126–136, 1999, cited By 121.
- [9] Nick Kanopoulos, Nagesh Vasanthavada, and Robert L Baker, "Design of an image edge detection filter using the sobel operator," *IEEE Journal of solid-state circuits*, vol. 23, no. 2, pp. 358–367, 1988.
- [10] Yoshinobu Sato, Shin Nakajima, Nobuyuki Shiraga, Hideki Atsumi, Shigeyuki Yoshida, Thomas Koller, Guido Gerig, and Ron Kikinis, "Three-dimensional multi-scale line filter for segmentation and visualization of curvilinear structures in medical images," *Medical Image Analysis*, vol. 2, no. 2, pp. 143 – 168, 1998.
- [11] D. Small, N. Miranda, and E. Meier, "A revised radiometric normalisation standard for sar," in *2009 IEEE International Geoscience and Remote Sensing Symposium*, July 2009, vol. 4, pp. IV-566–IV-569.
- [12] A. S. Yommy, R. Liu, and A. S. Wu, "Sar image despeckling using refined lee filter," in *2015 7th International Conference on Intelligent Human-Machine Systems and Cybernetics*, 2015, vol. 2, pp. 260–265.

2.4 Surface Melt Estimation from SAR Remote Sensing – Comparisons with a Regional Climate Model

Observations are a critical aspect of the assessment of geophysical models. The ability of a model to replicate observations is crucial as a benchmark. It also allows us to refine our comprehension of Earth systems, such as in cryospheric sciences.

We are using the regional climate model MAR to compute the surface melt on a domain focusing on the Roi Baudouin Ice Shelf, Dronning Maud Land, East Antarctica. MAR can derive the number of melt days in a year and compare it to previous long time series to emphasize anomalies (Fig. 2.71). From the figure, we can see that the Antarctic Peninsula is already melting 20% of the time. With melt comes thinning and hydrofracturing of ice shelves which can lead to disintegration (Scambos et al., 2003).

In parallel, we employ SAR remote sensing to obtain comparison data. Radar backscattering anomalies between different dates are witnesses of a substantial increase of soil moisture (Fig. 2.72). Using Sentinel-1 in Interferometric Wide-swath and Extra Wide-swath modes, and multiple satellite paths, near-daily acquisitions can be obtained. By comparing the two independent methods, we better constraint model's outputs while also better interpreting SAR acquisitions. While comparing climate models to SAR remote sensing has already been performed using passive microwaves, the use of high-resolution SAR data is recent.

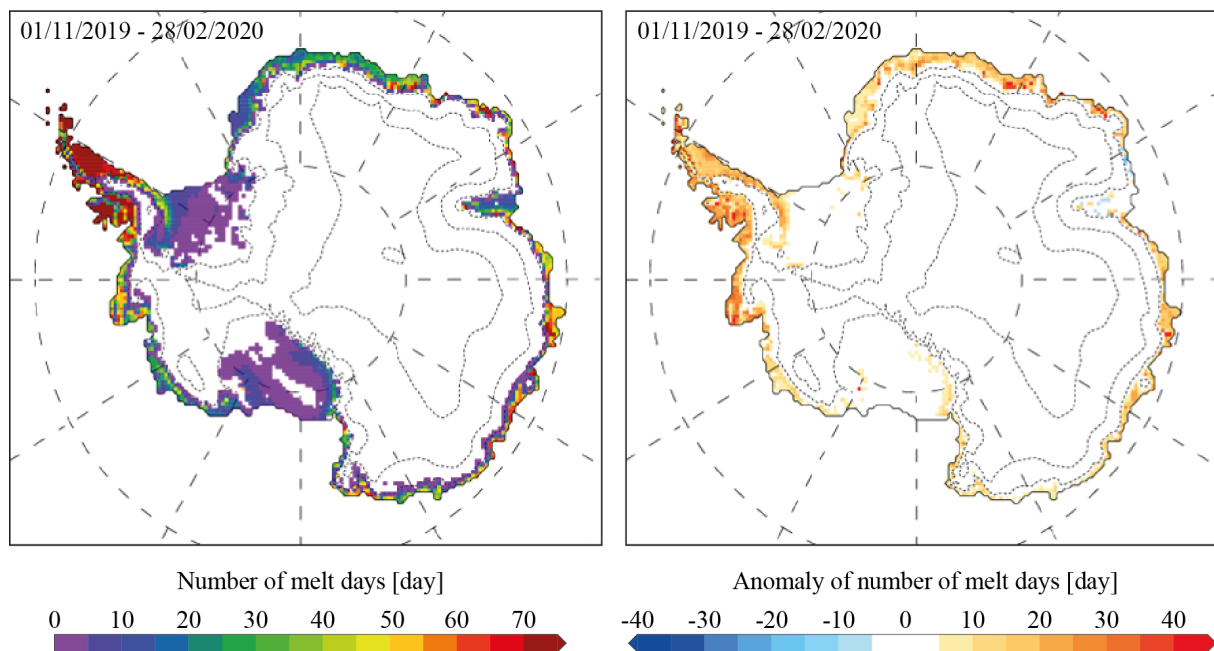


Figure 2.71: (left) Number of melt days (i.e. when the daily meltwater production is greater than 1 mmWE/day) from the 01 Nov 2019 to 28 Feb 2020. (right) Number of melt days with respect to the 1981-2010 average from 01 Nov 2019 to 28 Feb 2020. Figure obtained by Xavier Fettweis, using MARv3.10.

In Fig. 2.73, we compare the variation of the SAR backscattering coefficient over the RBIS and a selection of variables estimated from MAR. These variables include: melt, rainfall, liquid water content, albedo, surface temperature, and air temperature. There is a trivial correlation between SAR and MAR variables.

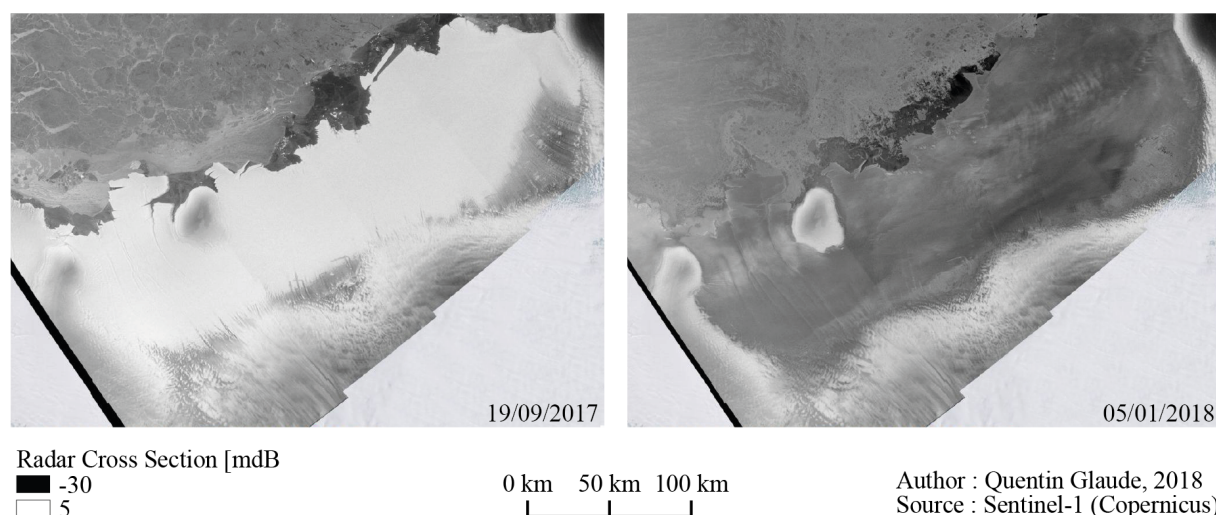


Figure 2.72: Calibrated Radar Cross Section of Synthetic Aperture Radar Sentinel-1 Acquisitions. Left figure represents a dry condition with the calving front of the ice shelf easily distinguishable from the ocean. Right figure represents an intense melting event, where we observe a strong decrease in the radar cross section.

The results were presented during the EGU General Assembly 2020. In the following article co-written with Thomas Dethinne, we went a step further by comparing the two products. In particular, we tried to answer the three following questions:

- **Statistical analysis** : What is the difference between the number of melt days predicted by MAR and observed by SAR? How the parametrization of the SAR process influence the melt detection?
- **Geospatial analysis** : Where are located the differences between MAR and SAR? How is the spatial distribution of these residuals? Can they be linked to geophysical elements (blue ice, topography)?
- **Time series analysis** : When are the differences between MAR and SAR occurring? Does the penetration capabilities of SAR detect early melt signs?

The accepted article will be published in BSGLG, vol 77, January 2022. It is available here-after and can cited as

Dethinne, T., **Glaude, Q.**, Amory, C., Kittel, C., & Fettweis, X. (2022). Comparison Between Surface Melt Estimation from Sentinel-1 Synthetic Aperture Radar and a Regional Climate Model: Case Study Over the Roi Baudouin Ice Shelf, East Antarctica. *Bulletin de la Société Géographique de Liège*, vol. 76.

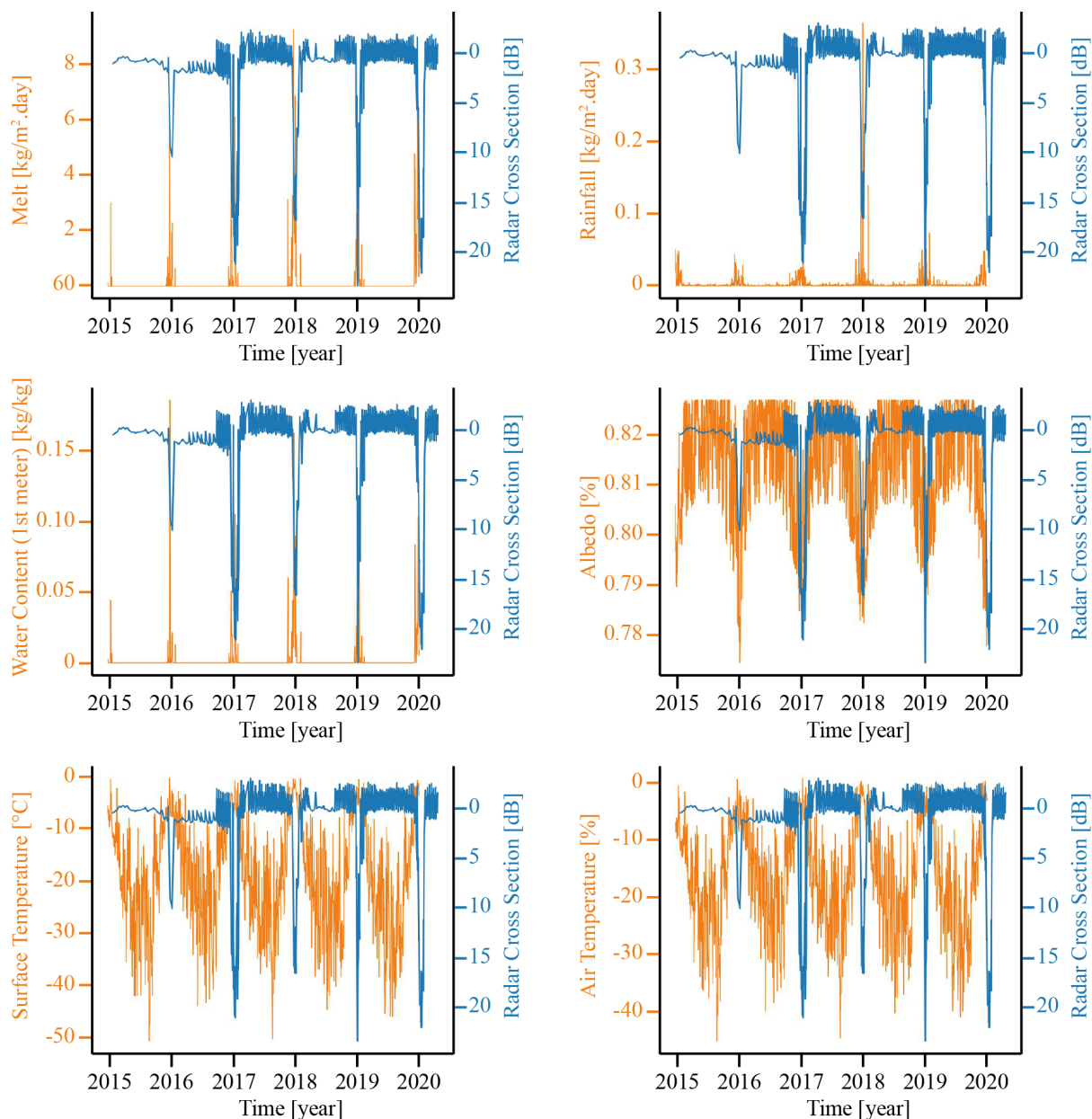


Figure 2.73: Radar backscattering, in blue, in comparison with MAR variables, in orange. (a) Melt, expressed in kilogram per m² and per day. (b) Rainfall, expressed in kilogram per m² and per day. (c) First-meter liquid water content, expressed as the ratio between the mass of liquid by the total mass. (d) Albedo in the visible spectrum [%]. (e) Surface temperature, expressed in degrees Celsius. (f) Air temperature, expressed in degrees Celsius.

COMPARISON BETWEEN SURFACE MELT ESTIMATION FROM SENTINEL-1 SYNTHETIC APERTURE RADAR AND A REGIONAL CLIMATE MODEL

CASE STUDY OVER THE ROI BAUDOUIIN ICE SHELF, EAST ANTARCTICA

Thomas DETHINNE, Quentin GLAUDE, Charles AMORY,
Christoph KITTEL, Xavier FETTWEIS

Abstract

Antarctica is the largest potential contributor to sea-level rise and needs to be monitored. It is also one of the first victims of global warming. However, it is often difficult to obtain high-resolution data on this vast and distant continent. Thanks to the Copernicus space program providing free and open access to high-quality data, this paper aims to show the complementarity between Sentinel-1 images and *Modèle Atmosphérique régional* (MAR) data over Antarctica. This study is conducted over Roi Baudouin Ice Shelf. The complementarity between the two datasets is established by a quantitative, temporal, and spatial comparison of the amplitude information of the radar signal and several variables modelled by MAR. Comparisons show strong spatial correlations between MAR variables representing melt and the backscatter coefficient recorded by the satellite. While temporal and quantitative analyses also give impressive results, further investigations are required to explain contrasting behaviors in other different areas of the ice shelf.

Keywords

SAR, MAR, ice shelf, melt, Antarctica, RBIS, Sentinel-1

Résumé

L'Antarctique est le plus grand contributeur potentiel à l'élévation du niveau de la mer et doit être surveillé. C'est aussi l'une des premières victimes du réchauffement climatique. Or, il est souvent difficile d'obtenir des données à haute résolution sur ce vaste et lointain continent qu'est l'Antarctique. Grâce au programme Copernicus qui donne un accès libre et gratuit à des images satellite de hautes qualités, le but de ce travail est de montrer la complémentarité entre les images radar Sentinel-1 et les données du Modèle Atmosphérique Régional (MAR) au niveau de l'Antarctique. Cette étude est menée au niveau de la plateforme de glace du Roi Baudouin. La complémentarité entre les données est établie par comparaisons quantitative, temporelle et spatiale entre l'information d'amplitude du signal radar et des variables MAR. Les résultats obtenus sont prometteurs. Les comparaisons montrent de fortes corrélations spatiales entre les variables MAR représentant la fonte et la rétrodiffusion enregistrée par le satellite. Si les analyses temporelles et quantitatives donnent également de bons résultats, des investigations plus profondes sont nécessaires pour expliquer les comportements différents sur d'autres régions de la plateforme de glace.

Mots-clés

SAR, MAR, plateforme de glace, fonte, Antarctique, RBIS, Sentinel-1

INTRODUCTION

The Antarctic Ice Sheet (AIS) is the main reservoir of continental water, with a potential of 57 meters sea-level rise, if totally melted. Set on a rocky continent, the AIS undergoes gravity-driven displacements, spreading itself toward the ocean, where the ice sheet dove into the water and starts to float, becoming an ice shelf. Surrounding 70 % of Antarctica, these ice shelves are all but passive, in the sense that ice shelves are constrained by topographic elements, either by being locally constrained in embayments or by subwater topographic anchor points (Favier & Pattyn, 2015). These

elements cause a buttressing effect, playing a role in the stabilization of the entire AIS (Goldberg *et al.*, 2009). The thinning of these ice shelves is caused by various factors including basal and surface melting, with important consequences on AIS long-term stability (Payne *et al.*, 2004; Pritchard *et al.*, 2012). The decrease of ice-shelf thickness induces an acceleration of the ice discharge and a retreat of the grounding line (Pritchard *et al.*, 2009). This destabilization is further amplified in the region of retrograde slopes, where Marine Ice Sheet Instability (MISI) plays a determining role (Pattyn, 2018). The resulting continental ice discharge into the

ocean finally produces a sea-level rise. Due to global warming, snow and ice melt are increasing in polar regions (Wingham *et al.*, 2006; Scambos *et al.*, 2013; IMBIE team *et al.*, 2018). In the last 40 years, we observed a six fold increase in ice discharge in Antarctica (IMBIE team, 2018; Gilbert & Kittel, 2021). Even more problematic, this phenomenon is ongoing and could increase with global warming (Paolo *et al.*, 2015). Finally, the presence of melt destabilizes the ice shelf by hydrofracturing mechanism. The water percolates into crevasses and further widen after refreezing events, encouraging glacier retreat and ice cliff failure (Pollard *et al.*, 2015).

Collecting in situ data where the ice is melting is a challenging task due to the remoteness and the size of the continent. Numerous ways of remotely observing those places have been developed (Baghdad, 2000; Nagler & Rott, 2000; Nagler *et al.*, 2015). At the University of Liege, the SPHERES laboratory is working with the predictive model MAR (*Modèle Atmosphérique Régional*) to represent the physics that governs the atmosphere and ice sheet. However, while MAR can model the melt, uncertainties remain for several reasons. Firstly, the consequences of small input errors can propagate into larger output errors. Secondly, results are provided with a kilometric resolution, which is larger than the spatial resolution satellites can achieve nowadays. With the ongoing development of spatial activity and the launch of more and more Earth observation satellites, remote sensing became one common technique to monitor polar regions at high resolution (Fettweis *et al.*, 2006, 2011; Nagler *et al.*, 2015, 2016; Lievens *et al.*, 2019; Shah *et al.*, 2019; Nagler & Rott, 2000). The rise of active remote sensing satellites began with ERS, and more recently with the Copernicus Earth observation program from the European Union, making it possible to have near-daily radar images at a resolution of around 10 meters in open access with the Sentinel-1 constellation. Because the active radar satellite output is sensitive to water content, it can be used to detect melt in images (Moreira *et al.*, 2013). Having a high-resolution technique to monitor the climate in remote places makes it possible to improve geophysical models and to better understand the mechanisms of the AIS.

As explained beforehand, remote sensing of the cryosphere is already a vast subject in scientific literature. Melt estimation from SAR images counts a couple of studies with slight variations between the different methods. When studying the melting of a thin layer of snow, the melt can be identified by an increase of the backscatter as mud has a higher backscattering coefficient than snow (Koskinen *et al.*, 1997). When studying melt on sea ice or ice shelves, a decrease of the backscattering coefficient σ_0 is observed as the presence of water in the snowpack will increase specular reflection. This leads to a rapid change from a value oscillating around 0 dB in dry snow to -20 dB for a wet snowpack. For studying melt on ice shelves in Antarctica, different approaches based on σ_0 variations are employed. In general, a threshold between -3 dB and -2 dB is used for an image normalized to its winter average (Johnson *et al.*, 2020) or for a ratio of different sources (polarization or a reference image) (Nagler & Rott, 2000; Nagler *et al.*, 2016). Recently, Liang *et al.* (2021), proposed a threshold of -2.66 dB for images after “co-orbit normalization”, i.e. normalization of images with an image from the same path but from a non-melting period.

Comparing remote sensing and MAR data has already been attempted with a passive satellite (Fettweis *et al.*, 2006, 2011), showing the complementarity between the two datasets. The complementarity of data leads to the assimilation of MODIS data in MAR to decrease inherent uncertainties linked to the use of a numerical model (Navari *et al.*, 2016, 2018).

The objective of this work is to demonstrate the complementarity of Synthetic Aperture Radar satellites – SAR – and a regional climate model – MAR – for the estimate of melting. In order to analyze the similarities and differences of the two datasets, a comparative approach is undertaken. First, data is compared temporally to see if the melt is observed and modeled at the same time. Then, when the melt season is identified, the quantity of melt is estimated through the surface of the region of interest covered by melting ice and snow. Finally, a spatial comparison is conducted to demonstrate

the spatial variabilities of the differences between the data.

The study is conducted over the Roi Baudouin Ice Shelf (RBIS, -24° to -33° East), and its surroundings, in the Dronning Maud Land, East of Antarctica (Figure 1). RBIS is a 30 000 km² ice shelf situated near the Belgian Princess Elisabeth station. It is characterized by its long-term stability, but also by its wide melt season extend (Drews, 2015; Berger *et al.*, 2016; Callens *et al.*, 2016).

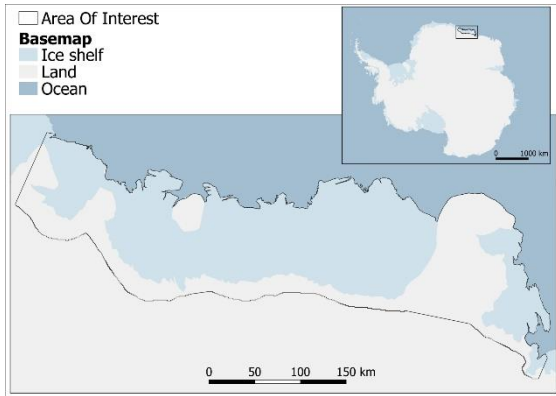


Figure 1. RBIS: the area of interest in East Antarctica. Parts of Prince Harald and Borchgrevink ice shelves are also included in the area as well as the Derwael ice rise and the Riiser-Larsenhalvøya ice ridge (basemap: Quantarctica – Matsuoka *et al.*, 2021, modified).

II. DATA PRESENTATION

A. MAR Data

MAR modelling results are gathered in a set of NetCDF files. NetCDF is a common self-document data format used in geosciences for data exchange. It can be seen as a multidimensional datacube. Two of the dimensions are the X and Y coordinates while the third one is time. In our case, each file contains one of the six chosen variables to study. Those variables have similar image size, pixel size, and time resolution (Table 1). The variables are: (i) ME: the melt variable. As SAR has strong interactions with liquid water, this variable would be best correlated with SAR under standardized conditions. As shown in figure 2, ME varies during year, reaching peak value of 10 kg / m² / day. (ii) RO1: the snow density. Divided into the same layers as WA1 (cf. vi), it is not used to be compared directly to SAR data. Together with WA1, it is

used to create a variable that represents the relative quantity of water in the snowpack. Typical values of RO1 reach 400–450 kg / m³ on the ice shelf and 600 kg / m³ at the south of the zone. (iii) RU: this variable represents the surface runoff caused by both melt and rainwater. SAR backscatter can change with both, but only the meltwater fraction is studied here. (iv) SMB: the surface mass balance is linked with ablation phenomena and thus may be correlated with the radar cross-section. SMB is calculated as the thickness change of the snowpack. It can be approximated by the sum of all the processes that cause accumulation or ablation. On ice shelves in Antarctica SMB tend to stay quite low and constant with a few kg / km² / day. (v) SU: sublimation is the change from solid-state to gas without passing through the liquid phase. If it is the liquid water that is detected with SAR, for the sublimation process to occur, snow needs heat as it is an endothermic reaction. If there is heat, melting may occur and cause the SAR cross-section to vary. (vi) WA1: WA1 is the liquid water content of snow layers. The file is divided into ten bounds / layers of snow representing the first meter of depth. WA1 can be compared with SAR thanks to the ability of radar frequency to penetrate the soil. During strong melting periods, in the first meter of depth, liquid water content of the snowpack can reach a few percent of the snow mass. A summary of all variables is displayed in table 1.

For the variables ME and WA1, melt or significant presence of water are considered when the value of the variable is higher than 0.1. This value is then used to create the melting mask used for the quantitative comparison conducted in part III. B.

Variable	Unit	Image size (km)	Pixel size (km)	Time Interval
ME	kg / m ² / day	750×720	5 × 5	1 / day
RO1	kg / m ³	750 × 720	5 × 5	1 / day
RU	kg / m ² / day	750 × 720	5 × 5	1 / day
SMB	kg / m ² / day	750 × 720	5 × 5	1 / day
SU	kg / m ² / day	750 × 720	5 × 5	1 / day

WA1 kg / kg 750 × 720 5 × 5 1 / day

Table 1. MAR variables used for this study. ME: melt, RO1: snow density, RU: runoff, SMB: surface mass balance, SU: sublimation, WA1: liquid water content.

B. SAR Data

In this study, we used SAR images from the Sentinel-1 mission. It refers to a constellation of two active radar satellites. Sentinel-1 is the first mission of the European Space Agency (ESA) for the Copernicus initiative. Copernicus brings a paradigm shift in the use of remote sensing data. The program aims to provide free, open-access, and high-quality data. The two satellites constituting the constellation (S1A and S1B) work in the C band (5.45 GHz), allowing night and day imagery. With a revisiting time of 12 days, and a near-polar Sun-synchronous orbit, the S1A and S1B allow a revisit time of 6 days. The first satellite – S1A – has been launched in April 2014 for a 7-year mission. In this study, we use data acquired at single and dual polarizations, in interferometric wide (IW) and extra-wide (EW) swaths. For this paper, only the comparison with HH (signal send with a horizontal polarization and received in the same way) polarization is used as the conclusion for the cross polarization HV (signal send horizontally but received vertically) is the same. Over our region of interest, the local period of the descendant node is around 6 PM. The data is retrieved from the Alaska Satellite Facility (ASF, 2021). To preserve the 6 days revisit time of S1A and S1B, the analysis starts in 2016. 1 417 images were used to conduct the analysis. Multiple orbits are used to ensure consistent spatial coverage with MAR data. MAR output temporal resolution can be defined according to the user's needs, but SAR has physical limitations. Even if all the possible data is used, data gaps occur and cause holes in the comparison. Nevertheless, the spatial resolution and pixel size are much finer than MAR. Ground-Range-Detected (GRD) products at high and medium resolution are used for this analysis. These images have a pixel spacing of 10 by 10m and 40 by 40m, respectively.

Pol.	Coeff. (dB)	Acquis.	Pixel size (m)	Time Interval
------	-------------	---------	----------------	---------------

HH	σ_0	IW & EW	10 × 10 & 40 × 40	1 / 6 days
HV	σ_0	IW & EW	10 × 10 & 40 × 40	1 / 6 days

Table 2. SAR Data used for this work. Four distinct types of data that are used together, depending on the polarization and acquisition mode.

As explained in the introduction part, the threshold applied for the binary classification used for the quantitative comparison (cf. III. B) is discussed in the literature. The choice is to follow the -2.6 dB threshold proposed by Liang *et al.* (2021). The co-orbit normalization is not performed as the ice on the iceshelf shows a mean σ_0 oscillating around 0 dB.

III. COMPARISON

A direct consequence of the different pixel sizes, coverages and data formats between SAR and MAR is the inability to perform a direct comparison without converting the data. For this project, the choice is to downgrade SAR pixel spacing to the 5 km MAR pixel spacing and mosaicking SAR images. A resampling was then included in the SAR processing chain to get images with a 5 by 5 km spatial spacing. The resampling is made with SNAP software (Brockmann *et al.*, 2020), using the default parameters of the Range Doppler Terrain Correction function with the TanDEM-X elevation model data originating from the German aerospace center as used in the frame of the MIMO project (for details see Glaude *et al.*, 2020). The mosaic is created from a Python script. The value of each pixel composing the mosaic for a given date is calculated using linear interpolation (or extrapolation) between the values of two overlaying images. The two chosen images are the couple with the smallest time gap between their acquisition and the given date for the mosaic.

A mosaic is created every six days to match the six days revisit time of the satellites. The first date of the study is not chosen randomly. It is set in 2016 to benefit from Sentinel A and B and between the acquisition of paths 59 and 88, covering most of the studied zone. The mosaicking of the SAR images is advantageous for different reasons. First the

mosaic from multiple SAR images allows us to create maps covering the entire studied region. Such maps offer a synoptic representation of data and underlying phenomena, and they are the basis of spatial analysis. Secondly the use of different paths and orbits can induce variations of σ_0 and interpolating a value from multiple images mitigates the variation. Finally, it allows a perfect co-registration of the two datasets by creating a grid over MAR images. This co-registration is ensured by the interpolation of the different layers on the same grid. The upper left corner of MAR and SAR products are coherent, as well as the pixel spacing. The coordinate reference system uses is the Antarctic Polar Stereographic projection (EPSG: 3031).

However, mosaicking can also lead to artifacts. The major problem is the occurrence of extreme extrapolated values in the case when no data is available in the six days before or after the desired date. A filter is used to reduce the number of extreme values. Furthermore, by interpolating between two images recorded near 6 PM, the intra-daily variations in σ_0 are omitted. Dates when the mosaic had an inadequate quality are removed.

The comparison is made between the satellite data and all the MAR variables previously presented. In the paper, we focus on the results with ME, the variable representing melt, because it is the most consistent with the observation of the satellite.

A. Temporal

SAR and MAR datasets are first directly compared together. The evolution of the quantity of melt and of σ_0 averaged on the ice shelf is displayed in figure 2. A synchronism appears clearly between the decrease of σ_0 and the increase in the quantity of melt modelled by MAR. The opposite variation is straightforward since the increase in water concentration in the snowpack leads to a mirror effect in the SAR signal, resulting in a decrease of σ_0 . However, if the decrease and increase seem to be negatively correlated, it is not the case of the intensity reached by the peaks. The maximum and minimum are not happening for the same melt season and, no

matter the quantity of melt modelled by MAR during melt seasons, the same σ_0 is observed at $-15 / -20$ dB. Furthermore, a small temporal shift of one or two weeks between the increase and the decrease is observed. There are two hypotheses to explain that shift. First, MAR tends to model melt too early. Second, a certain quantity of liquid water in the snowpack is required for a change to occur in σ_0 . Further investigations are needed to test the two hypotheses.

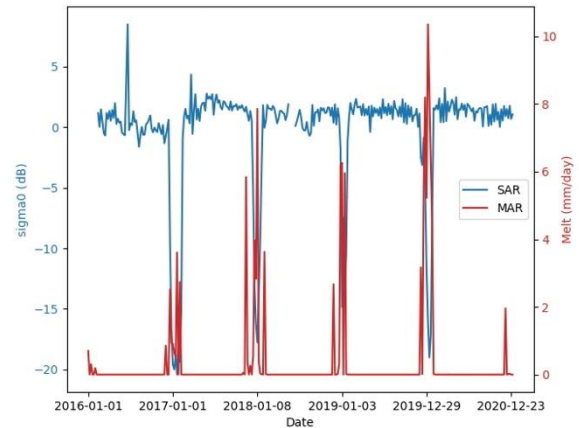


Figure 2. Comparison between SAR σ_0 and MAR melt for the studied period of 2016-2021. The opposite variation of the couple of data is explained by the decrease of σ_0 caused by the presence of water. Even if the peaks occur at the same time, the increase of ME starts before the decrease of σ_0 .

Another temporal comparison is conducted through the construction of two maps: a first regarding the correlation between σ_0 and ME and, a second based on a probability (Equation 1). The correlation map (Figure 3A) uses the value of σ_0 observed by the satellite and the output values of ME given by MAR throughout the whole period studied. With those values, the Pearson's r is calculated for each pixel, considering every value obtained for the pixel. Roughly 300 values of ME and the same amount of σ_0 are used at each pixel for the calculation. The visual interpretation of the result shows strong negative correlation values (~ -0.75) on the ice shelf and lower negative correlation over the slopes and the surrounding ice shelves (~ -0.1). Overall, a gradient appears on the image, with strong correlations near the limit between the ice shelf and the ocean and decreasing toward inland.

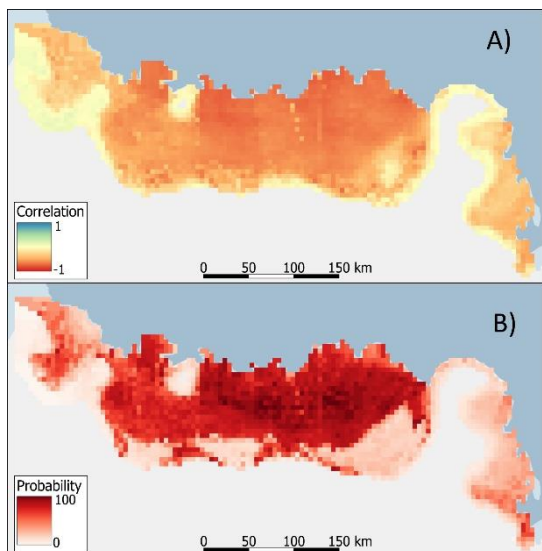


Figure 3. A) Correlation map between SAR σ_0 backscattering coefficient and MAR ME. B) Conditional probability representing the probability of MAR to detect melt, considering SAR observes melt. For both maps, the ice shelves present higher values than over the problematic zones described in part III. B.

The probability map (Figure 3B) represents the conditional probability of MAR modelling melt given SAR observes it. Following equation 1, this probability is calculated as the ratio between the probability of SAR and MAR both modelling melt and the probability of SAR observing melt. A high probability ($\sim 90\%$) appears on the ice shelf while a low ($\sim 10\%$) probability concerns the blue ice areas, the slopes, and the Prince Harald ice shelf. The low value is due to the SAR over observation of melt in the above-mentioned zones, caused by a threshold choice too high for the zone. On the other hand, the high probability results from the fact that ME is modelled a week or two before and after the observation by SAR.

$$P(X|Y) = \frac{P(X \cap Y)}{P(Y)} \quad (1)$$

In equation (1): X states for MAR modelling melt and Y for SAR observing it.

B. Quantitative

The quantitative analysis is based on the surface melt comparison determined by SAR and by MAR. The comparison is performed on the percentage of the area covered by melt,

pixel by pixel, after a binary classification (melt – no melt) of the two variables has been achieved. The melt volume is thus not included in the analysis. Quantifying the melt volume with SAR would deserve more consideration. In figure 4, the time shift is also visible. Melt modelled in the ME variable covers the studied zone before SAR observed a decrease in σ_0 and thus before SAR observed an evolution of the surface melt area. The melt modelled area first appears larger than the observed one, before converging to a similar value covering the majority or even the entire studied zone. However, figure 4 also shows the effect of the threshold choice. During the study, a constant melt cover is detected of about 10 to 20%. There is no period where SAR detects no melt over the studied zone. The cause is to be found in the lack of normalization of the SAR images and the use of a constant threshold instead of a spatially varying one. This resulting melt is mainly located on the slopes – the Prince Harald ice shelf – and the bottom of the slopes, where blue ice is located. When removing these areas from the analysis, the effect is mitigated, and the covered area matches better (Figure 5).

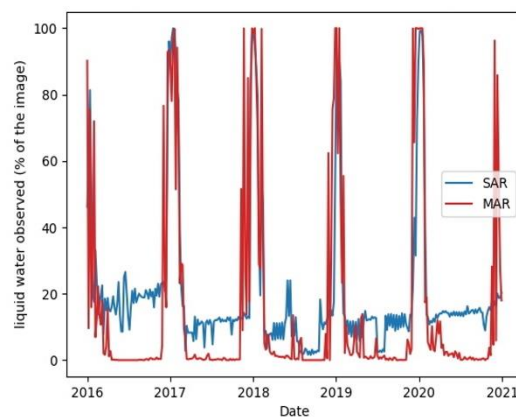


Figure 4. Comparison between SAR and MAR observed liquid water
The comparison is established with the percentage of the area covered by melt. The values for the peaks are equivalent except for the 2021 melt season and the summer period. The difference for 2021 is due to the temporal shift, still visible in the graph. The summer difference is caused by the threshold choice.

Another major difference is the start of the modelled 2021 melt season which covers up to 90% of the image while it is not observed by

SAR. This difference can also be noted in 2016 when the studied zone is restrained.

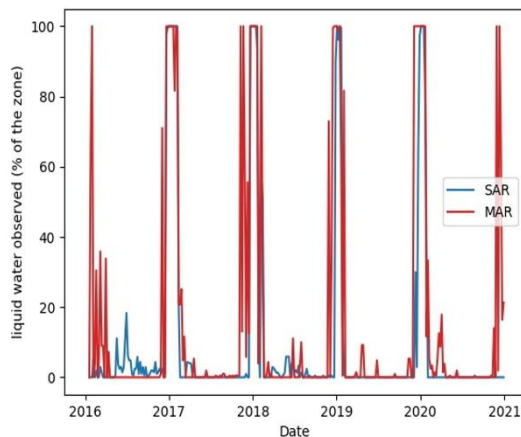


Figure 5. Comparison between SAR and MAR observed liquid water
Graph is identical to figure 4 but the problematic areas have been removed. The differences have decreased but the 2016 melt season has disappeared from SAR.

C. Spatial

The spatial comparison is carried out by means of correlation and probability maps between the outputs of SAR and MAR, then by analyzing them using the Moran's I index (Goodchild, 1986). Spatial autocorrelation is the variation of an event with itself in space. An index value of 1 (or -1) reflects a strong positive (or negative) spatial autocorrelation, meaning high values tend to have neighbors with high (or low) values. Neighborhood of a pixels is constructed with a queen-contiguity (8-connext) at the second order (neighbors of neighbors). The spatial analysis is carried out with the space section of the *GeoDa* software (Anselin *et al.*, 2006).

The Moran's I value (Figure 7A) is significant (0.786) (9999 random permutations test) for the probability map (Figure 3A). The visual interpretation of the map performed for the temporal analysis is corroborated by the local index analysis (LISA) completed (Figure 6). Values on the slopes are considered as significantly "high-high" (high values surrounded by high values), while the ice shelf is considered as "low-low" (low values surrounded by low values). Topography is then one of the main factors influencing the data

variations concerning the correlation as the r coefficient is mainly constant on flat surfaces and tend to vary in areas with strong topographical relief.

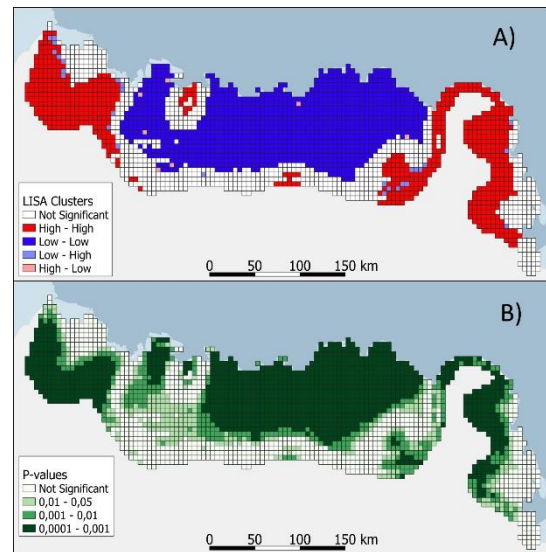


Figure 6. A) Clusters of neighbors, classified according to their LISA index. B) p-value for the LISA indexes, with 9999 permutations. Both maps are constructed for the correlation map.

For the probability map, Moran's I (Figure 7B) is also (pseudo-)significant (0.775). However, in this case, the nature of the ice also seems to be significant to explain the differences between the two variables. Nevertheless, it is important to remember that the threshold choice has an impact on the probability as it uses the binary classification of ME and σ_0 .

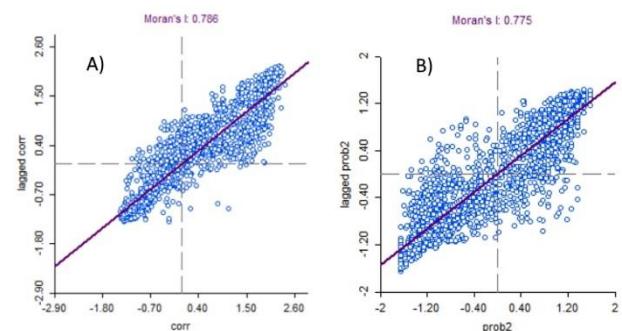


Figure 7. Moran's I scatterplot for the maps presented at figure 3. The blue dots represent the pixels. The X axis is the standardised value of the pixel and Y the mean standardised value of the neighbourhoods. A) Pearson's r : Moran's I = 0.786. B) Conditional probability: Moran's I = 0.775.

The spatial analysis performed consisted in the analysis of simple indicators. More can be

done to archive a complete analysis of the spatial variation of the phenomenon. Geographically weighted regression is a means to complete the analysis. It allows to express the values of a variable as a function of the other, while being able to consider their temporal variability.

CONCLUSION AND DISCUSSION

In this study, we analyzed the comparison of melt prediction from two independent methods. On the one hand, we are requalifying the backscattering coefficient of SAR remote sensing into a melt / not melt binary classification. On the other hand, we are studying the presence of estimated melt using MAR climate model.

The results show the complementarity nature of the two datasets. It must be kept in mind that the studied area is firstly modelled by MAR before SAR records it. The temporal shift between ME and σ_0 can mainly be caused by the need for a certain quantity of water in the snowpack before observing a variation of σ_0 . This trend of modelling melt before and after SAR melting observations is also visible in the temporal variation of the melt surface. This consideration aside, the peaks of the melt coverages for the two datasets are consistent with each other (but for the 2021 melt season as it did not start for SAR). The SAR observation of melt during winter is due to the choice of -2.6 dB for the melt threshold. That is too high for some zone that presents lower values in non-melting periods. These zones are highlighted by the spatial analyses carried out with the correlation index and the probability map. Problematic zones have lower probabilities and lower correlation coefficients. However, the results show strong and statistically significant Moran's I on the ice shelf, blue ice, and the slopes.

Nevertheless, results could be greatly enhanced by the normalization of SAR images as proposed in Liang *et al.* (2021) or the use of a spatially variable threshold.

It would be also possible to conduct the experiment on a larger zone and at a better spatial resolution to benefit from the high resolution of the Sentinel-1 SAR imaging capabilities.

Finally, MAR and SAR showed similarities for most of the studied zone, and the dissimilarities were observed where the terrain is different, whether because of the nature of the ice or the topography. Further analysis of their differences would benefit the ice sheet modelling field.

REFERENCES

- Anselin, L., Syabri, I., & Kho, Y. (2006). GeoDa: An introduction to spatial data analysis. *Geographical Analysis*, 38(1), 5–22. <https://doi.org/10.1111/j.0016-7363.2005.00671.x>.
- ASF (2021). *ASF Data Search*. Alaska Satellite facility (ASF). Retrieved 26 May 2021, from <https://search.asf.alaska.edu/#/>
- Baghdad, N. (2000). Potential and limitations of RADARSAT SAR data for wet snow monitoring. *IEEE Transactions on Geoscience and Remote Sensing*, 38 (1 I), 316–320. <https://doi.org/10.1109/36.823925>.
- Berger, S., Favier, L., Drews, R., Derwael, J.J. & Pattyn, F. (2016). The control of an uncharted pinning point on the flow of an Antarctic ice shelf. *Journal of Glaciology*, 62 (231), 37–45. <https://doi.org/10.1017/jog.2016.7>.
- Brockmann Consult, Skywatch, Sensor & C-S (2020). *SNAP - ESA Sentinel Application Platform v8.0.3* [Computer Software]. Retrieved from <http://step.esa.int/>.
- Callens, D., Drews, R., Witrant, E., Philippe, M. & Pattyn, F. (2016). Temporally stable surface mass balance asymmetry across an Ice rise derived from radar internal reflection horizons through inverse modeling. *Journal of Glaciology*, 62 (233), 525–534. <https://doi.org/10.1017/jog.2016.41>.
- Drews, R. (2015). Evolution of ice-shelf channels in Antarctic ice shelves. *Cryosphere*, 9 (3), 1169–1181. <https://doi.org/10.5194/tc-9-1169-2015>.
- Favier, L. & Pattyn, F. (2015). Antarctic ice rise formation, evolution, and stability. *Geophysical Research Letters*, 42 (11), 4456–4463. <https://doi.org/10.1002/2015GL064195>.
- Fettweis, X., Gallée, H., Lefebvre, F. & van Ypersele, J.P. (2006). The 1988–2003 Greenland ice sheet melt extent using passive microwave satellite data and a regional climate model. *Climate Dynamics*, 27 (5), 531–541. <https://doi.org/10.1007/s00382-006-0150-8>.

- Fettweis, X., Tedesco, M., Van Den Broeke, M. & Ettema, J. (2011). Melting trends over the Greenland ice sheet (1958-2009) from spaceborne microwave data and regional climate models. *Cryosphere*, 5 (2), 359–375. <https://doi.org/10.5194/tc-5-359-2011>.
- Gilbert, E. & Kittel, C. (2021). Surface Melt and Runoff on Antarctic Ice Shelves at 1.5°C, 2°C, and 4°C of Future Warming. *Geophysical Research Letters*, 48 (8), 1–9. <https://doi.org/10.1029/2020GL091733>.
- Glaude, Q., Amory, C., Berger, S., Derauw, D., Pattyn, F., Barbier, C., & Urban, A. (2020). Empirical Removal of Tides and Inverse Barometer Effect on DInSAR from Double DInSAR and a Regional Climate Model. *IEEE Journal of Selected Topics in Applied Earth Observations and Remote Sensing*, 13, 4085–4094. <https://doi.org/10.1109/JSTARS.2020.3008497>.
- Goldberg, D., Holland, D.M. & Schoof, C. (2009). Grounding line movement and ice shelf buttressing in marine ice sheets. *Journal of Geophysical Research: Earth Surface*, 114 (4), 1–23. <https://doi.org/10.1029/2008JF001227>.
- Goodchild, M.F. (1986). *Spatial Autocorrelation. Concepts and Techniques in Modern Geography (CATMOG)*, 47. Norwich : Geobooks, 57 p.
- IMBIE team (2018). Mass balance of the Antarctic Ice Sheet from 1992 to 2017. *Nature*, 558, 219–222. <https://doi.org/https://doi.org/10.1038/s41586-018-0179-y>.
- Johnson, A., Fahnestock, M. & Hock, R. (2020). Evaluation of passive microwave melt detection methods on Antarctic Peninsula ice shelves using time series of Sentinel-1 SAR. *Remote Sensing of Environment*, 250 (2020), 9p. <https://doi.org/10.1016/j.rse.2020.112044>.
- Koskinen, J.T., Pulliainen, J.T. & Hallikainen, M.T. (1997). The use of ERS-1 SAR data in snow melt monitoring. *IEEE Transactions on Geoscience and Remote Sensing*, 35 (3), 601–610. <https://doi.org/10.1109/36.581975>.
- Liang, D., Guo, H., Zhang, L., Cheng, Y., Zhu, Q. & Liu, X. (2021). Time-series snowmelt detection over the Antarctic using Sentinel-1 SAR images on Google Earth Engine. *Remote Sensing of Environment*, 256, 112318. <https://doi.org/10.1016/j.rse.2021.112318>.
- Lievens, H., Demuzere, M., Marshall, H.P., Reichle, R.H., Brucker, L., Brangers, I., de Rosnay, P., Dumont, M., Giroto, M., Immerzeel, W.W., Jonas, T., Kim, E.J., Koch, I., Marty, C., Saloranta, T., Schöber, J. & De Lannoy, G.J.M. (2019). Snow depth variability in the Northern Hemisphere mountains observed from space. *Nature Communications*, 10 (1), 1–12. <https://doi.org/10.1038/s41467-019-12566-y>.
- Matsuoka, K., Skoglund, A., Roth, G., de Pomereu, J., Griffiths, H., Headland, R., Herried, B., Katsumata, K., Le Brocq, A., Licht, K., Morgan, F., Neff, P.D., Ritz, C., Scheinert, M., Tamura, T., Van de Putte, A., van den Broeke, M., von Deschanden, A., Deschamps-Berger, C. & Melvær, Y. (2021). Quantarctica, an integrated mapping environment for Antarctica, the Southern Ocean, and sub-Antarctic islands. *Environmental Modelling and Software*, 140. <https://doi.org/10.1016/j.envsoft.2021.105015>.
- Moreira, A., Prats-iraola, P., Younis, M., Krieger, G., Hajnsek, I. & Papathanassiou, K.P. (2013). SAR-Tutorial-March-2013. *IEEE Geoscience and Remote Sensing Magazine*, 1 (1), 6–43. <https://doi.org/10.1109/MGRS.2013.2248301>.
- Nagler, T. & Rott, H. (2000). Retrieval of wet snow by means of multitemporal SAR data. *IEEE Transactions on Geoscience and Remote Sensing*, 38 (2 I), 754–765. <https://doi.org/10.1109/36.842004>.
- Nagler, T., Rott, H., Hetzenecker, M., Wuite, J. & Potin, P. (2015). The Sentinel-1 mission: New opportunities for ice sheet observations. *Remote Sensing*, 7 (7), 9371–9389. <https://doi.org/10.3390/rs70709371>.
- Nagler, T., Rott, H., Ripper, E., Bippus, G. & Hetzenecker, M. (2016). Advancements for snowmelt monitoring by means of Sentinel-1 SAR. *Remote Sensing*, 8 (4), 1–17. <https://doi.org/10.3390/rs8040348>.
- Navari, M., Margulis, S.A., Bateni, S.M., Tedesco, M., Alexander, P. & Fettweis, X. (2016). Feasibility of improving a priori regional climate model estimates of Greenland ice sheet surface mass loss through assimilation of measured ice surface temperatures. *Cryosphere*, 10 (1), 103–120. <https://doi.org/10.5194/tc-10-103-2016>.
- Navari, M., Margulis, S.A., Tedesco, M., Fettweis, X. & Alexander, P. M. (2018). Improving Greenland Surface Mass Balance Estimates Through the Assimilation of MODIS Albedo: A Case Study Along the K-Transect. *Geophysical Research Letters*, 45 (13), 6549–6556. <https://doi.org/10.1029/2018GL078448>.
- Paolo, F.S., Fricker, H.A. & Padman, L. (2015). Volume loss from Antarctic ice shelves is accelerating. *Science*, 348 (6232), 327–331. <https://doi.org/10.1126/science.aaa0940>.
- Pattyn, F. (2018). The paradigm shift in Antarctic ice sheet modelling. *Nature Communications*, 9

(1), 10–12. <https://doi.org/10.1038/s41467-018-05003-z>.

- Payne, A.J., Vieli, A., Shepherd, A.P., Wingham, D.J. & Rignot, E. (2004). Recent dramatic thinning of largest West Antarctic ice stream triggered by oceans. *Geophysical Research Letters*, 31 (23), 1–4. <https://doi.org/10.1029/2004GL021284>.
- Pollard, D., DeConto, R.M. & Alley, R.B. (2015). Potential Antarctic Ice Sheet retreat driven by hydrofracturing and ice cliff failure. *Earth and Planetary Science Letters*, 412, 112–121. <https://doi.org/10.1016/j.epsl.2014.12.035>.
- Pritchard, H.D., Arthern, R.J., Vaughan, D.G. & Edwards, L.A. (2009). Extensive dynamic thinning on the margins of the Greenland and Antarctic ice sheets. *Nature*, 461 (7266), 971–975. <https://doi.org/10.1038/nature08471>.
- Pritchard, H.D., Ligtenberg, S.R.M., Fricker, H.A., Vaughan, D.G., Van Den Broeke, M.R. & Padman, L. (2012). Antarctic ice-sheet loss driven by basal melting of ice shelves. *Nature*, 484 (7395), 502–505. <https://doi.org/10.1038/nature10968>.
- Scambos, T., Hulbe, C. & Fahnestock, M. (2013). Climate-Induced Ice Shelf Disintegration in the Antarctic Peninsula. *Antarctic Peninsula Climate Variability*, 79, 79–92. <https://doi.org/10.1029/ar079p0079>.
- Shah, E., Jayaprasad, P. & James, M.E. (2019). Image Fusion of SAR and Optical Images for Identifying Antarctic Ice Features. *Journal of the Indian Society of Remote Sensing*, 47 (12), 2113–2127. <https://doi.org/10.1007/s12524-019-01040-3>.
- Wingham, D.J., Shepherd, A., Muir, A. & Marshall, G. J. (2006). Mass balance of the Antarctic ice sheet. *Philosophical Transactions of the Royal Society A: Mathematical, Physical and Engineering Sciences*, 364 (1844), 1627–1635. <https://doi.org/10.1098/rsta.2006.1792>.

University of Liège, Belgium
thomas.dethinne@doct.uliege.be

Quentin GLAUDE
Laboratory of Glaciology
Brussels University, Belgium
& Liège Space Center
University of Liège, Belgium
Quentin.Glaude@ulb.be

Charles AMORY
Institute of environmental geophysics
University of Grenoble, France
charles.amory@univ-grenoble-alpes.fr

Christoph KITTEL
Laboratory of Climatology
Department of Geography
University of Liège, Belgium
ckittel@uliege.be

Xavier FETTWEIS
Laboratory of Climatology
Department of Geography
University of Liège, Belgium
xavier.fettweis@uliege.be

Corresponding author:
thomas.dethinne@doct.uliege.be

Authors affiliation:

Thomas DETHINNE
Laboratory of Climatology
Department of Geography
& Liège Space Center

Discussions and Conclusion: Towards a Narrower Picture of Antarctica

During the thesis, we developed an ensemble of techniques to derive information about the ice shelves dynamics, with the end goal of better understanding the short time-scale dynamics of the Antarctic Ice Sheet and its ice shelves. To fulfill this objective, we analyzed state-of-the-art techniques by taking advantage of the high spatial and temporal resolutions offered by the Sentinel-1 Synthetic Aperture Radar spaceborne sensor. Indeed, Sentinel-1's particular acquisition mode, Terrain Observation by Progressive Scans - TOPSAR, opens up new opportunities thanks to its short revisit time (6 days) and large spatial coverage (up to 400 kilometers).

The main variable studied in the thesis was the ice flow velocity and its spatial/temporal variations. In this regard, we analyzed offset tracking and SAR interferometry approaches. The importance of hyper-parametrization and oversampling factors were preliminarily established. This analysis reveals the middle ground between the computational cost of the operation, the spatial density of the velocity estimates, and the high-frequency noise induced by the speckle. Put together, offset tracking limitations are overcome by an increase in spatial resolution. This limitation is particularly observed for Sentinel-1, where the low azimuthal resolution prevents a precise estimation of the North-South component of the velocity fields. This preliminary study allowed us to create the 2016 Dronning Maud Land velocity map, from an ensemble of 255 Sentinel-1 acquisitions, distributed on 14 orbits. The results show the major ice streams of DML, and the important variability of ice shelves in the region.

Then, we applied a finer ice velocity analysis over the particular case of the Roi Baudouin Ice Shelf - RBIS. Over more than 4 years, 28 SAR pairs were selected to produce velocity maps at high resolution. The results show the strong influence of the constraints applied to the Ragnhild glacier over the RBIS. The Frankenny and Derwael ice rises on the West and East (resp.) of the main ice stream are constraining the ice shelf. Similarly, the large number of small ice rises in the Eastern part of RBIS are acting as strong anchors in the ice flow field. Focusing on temporal variations, we observe 5 to 15 % velocity variations between different SAR pairs, a part of it can be attributed to tides or inverse barometer effects. Finally, we are observing no significant trend in any regions of the RBIS. This is coherent with the long-term past and projected stability of the region. Nevertheless, a part of this explanation comes from the important variations of velocities from pairs to pairs, preventing us to draw trend lines with sufficient accuracy. Nevertheless, and following the recent RBIS calving event, we recommend continuing monitoring the region and observing any potential changes.

A 2016-aggregated velocity field over the RBIS was extracted from the previous dataset, and compared to available datasets from 1996 to 2017. From single velocity maps, we retrieved the

velocity variability we discussed in the last paragraph warning against the extrapolation of ice motion inferred from a limited number of acquisitions. Using yearly aggregated Rignot datasets, divergence points are observed in the Eastern part of the RBIS, where we computed slighter higher velocity fields. This observation is reversed near the Derwael ice rise in near range.

In a second section, we analyzed the production of phased-based displacements over the RBIS using the Sentinel-1 constellation. These interferometric methods are much more precise, but are more sensitive to a series of undesirable factors to take into account:

- First, before the release of REMA, high-resolution DEMs relied on TanDEM-X generated DEMs which are sparse around Antarctica, and difficult to access. In the thesis, we used the DEM produced by the Alfred Wegener Institute.
- Second, the temporal decorrelation is a strong source of artifacts in interferometric signals. Through a request directly to ESA, the RBIS is now part of the 6-day acquisition plan in Extra Wide-swath mode. This has the consequence of drastically improving the estimated coherence. Unfortunately, only a few areas around Antarctica benefit from this type of acquisition plan. In consequence, we redeveloped the coherence tracking technique and its adaptation to the specific case of the Sentinel-1 TOPSAR acquisition mode. We show that coherence tracking can retrieve displacements-induced coherence loss. This coherence recovery is drastically improved in fast-moving areas, enhancing the displacement accuracy. In addition, local corrections produce estimations of 2D displacement. From bidimensional displacements estimated from coherence tracking, we could compute the different strain rates of the RBIS. From these, we can observe the compressive and tensile regions, as well as buttressing effects from shear stresses. Even with all these corrections, DInSAR is still limited by meteorological events (surface melt or snow deposits).
- Third, as ice shelves are afloat, there are sensitive to sea-level variations from tides and atmospheric pressure changes. In this thesis, we presented an empirical technique using double-difference interferograms and regional models to estimate and remove this bias. This correction matters as tides and IBE have a strong impact on measurements, especially with the reduced revisit time. The method should be considered as a first-order correction, assuming the ice shelf to have elastic properties and regional models to have their own uncertainties. We can also use the visible influence of tides in interferograms to extract the grounding line location. This allowed us to produce grounding line mapping at high temporal and spatial resolution from 2017 to 2020 over the RBIS. In this period, we observe no particular grounding line advance or retreat.

The dual polarimetry of Sentinel-1 images can also be exploited. When relatively stable sea ice is present against the ice shelf, this sea ice is coherent on co-polarized signals, but not in cross-polarizations. Using this property, we developed a stable sea ice detection algorithm from multiple polarization coherence differences.

Contrary to offset tracking, DInSAR is only sensitive to displacements in the across-track direction. We overcame this limitation using Multiple Aperture Interferometry and Burst Overlapping Interferometry, allowing the measurements of along-track displacements from the spectral diversity of an interferometric signal. In the thesis, we adapted the Multiple Aperture Interferometry for the TOPSAR acquisition mode. While results are in concordance with offset tracking results, the coarse azimuthal resolution implies a low signal to noise ratio in the MAI phase, making it difficult to exploit. On contrary, burst overlapping interferometry does not imply subbanding approaches, preserving a high estimated number of looks and so an increased signal quality. In the thesis, we managed to extract a coherent BOI phase. In addition, we developed a variant of the Goldstein phase filtering to obtain an improved phase quality. The limitation of the BOI

approach lies in the strongly limited area of application, which is a small fraction of the Sentinel-1 SAR image. In that domain, Prats-Iraola et al. (2016) proposed TOPSAR-based acquisition mode where BOI could be applied on the whole scene.

On top of ice-motion estimation, other ice-shelves characteristics were studied. We already discussed the cases of strain rates, grounding line positions, or sea ice, which are based on measured displacements. We can also investigate surface structural properties from the analysis of spatial patterns in SAR amplitude images. Based on the exploitation of local second-order partial derivatives, we developed a method based on edge-detection techniques to extract and analyze important surface features. In particular, we focused the study on the presence of crevasses and their spatial/temporal variations over the Pine Island Glacier from 2017 to 2021. In addition, a precise delineation of the calving front and icebergs is also possible. The method is interesting because this field of research is still mainly focused on visual inspection. However, the method still suffers from a series of false detection in presence of pressure ridges (e.g. over the Brunt ice shelf).

Finally, we employed the SAR amplitude temporal anomalies to determine the presence of liquid content at the surface of the ice shelf. In the case of surface melt, we assume, from backscattering theory, a strong decrease in the value of sigma naught in SAR images. We can extract melt event maps by thresholding calibrated SAR images. These detections were then compared to a regional climate model. In the end, we observed a strong correlation between both products, even if particular places are causing issues, such as blue ice areas.

In conclusion, Sentinel-1 has completely revolutionized the studies of geophysical processes in many areas, such as land cover usage, oceanography, seismic activities, and emergency management. This is particularly true for the monitoring aspect, as Sentinel-1 produces high-resolution images on each continental place on Earth, with a revisit time of 6 to 12 days, free-of-charge. During four years, we tried to understand if the Sentinel-1 mission is a major step towards an improved Monitoring of Antarctic ice shelves dynamics. May the results produced in the thesis, and the plethora of peer-reviewed articles on the subject, serve as a demonstration proving this assertion.

Nevertheless, the Sentinel-1 acquisition geometry and specifications do not entirely fulfill requirements established for cryospheric contexts. For offset tracking techniques, azimuthal resolution is the main issue encountered. This issue is also met for Multiple Aperture Interferometry, where the azimuthal split-band digital signal processing approach further worsens the azimuthal resolution. For interferometric studies, the major issue of Sentinel-1 is its revisit time. With a revisit time of 6 days in coarse resolution mode (Extended Wide-swath), we are unfortunately higher than the recommended 4 days at high resolution for the cryosphere domain. It results in important temporal decorrelation mainly due to important displacements between different dates, but also meteorological events. If coherence tracking can retrieve a part of coherence from displacements, it remains limited by the resolution of the sensor. Surface melt, calving front, or crevasses propagation are neither impacted by the revisit time nor the spatial resolution. Nevertheless, an increase in their refresh rate would improve their integration into atmospheric models, especially for melt extend.

We are glad to hear that the major Sentinel-1 limitations enumerated in the last paragraph will partly be solved in short- and long-term by ESA Earth Observation department strategies. First, the near-future launch of Sentinel-1 C (scheduled in 2022), will drastically improve the revisit time issues. The adopted strategy is not fixed yet. It could be a total reorganization of the orbit, with a 4-day revisit time using an evenly-spaced constellation (configuration 4-4-4), to an asymmetrical acquisition geometry where Sentinel-1 C is inserted between the Sentinel-1 A and B 6-day repeat pass, reducing it to 1, 2, 3 days (configurations 1-5-6, 2-4-6, or 3-3-6). We regret that this asymmetrical acquisition geometry was not retained in the current Sentinel-1 constellation. Indeed, adopting from the start an acquisition geometry where Sentinel-1 B follows Sentinel-1 A

by 1 or 2 days would resolve almost all the exposed problems in SAR studies belonging to the cryosphere field. This strategy was already developed by the Tandem mission in 1995, where ERS-1 and -2 were separated by one day, enabling important studies in Antarctica (Derauw, 1999a; Pattyn & Derauw, 2002). In mid to long term, Sentinel-1 NG (next generation - launch scheduled in 2028) will further reduce the current Sentinel-1 limitations by drastically improving the azimuthal resolution of the sensor using new antennas systems, as well as increasing the duty cycle of the sensor, allowing Sentinel-1 to acquire more images per orbit.

Bibliography

- Adusumilli, S., Fricker, H. A., Medley, B., Padman, L., & Siegfried, M. R. (2020). Interannual variations in meltwater input to the southern ocean from antarctic ice shelves. *Nature Geoscience*, *13*(9), 616-620. Retrieved from <https://doi.org/10.1038/s41561-020-0616-z> doi: 10.1038/s41561-020-0616-z
- Alley, K. E., Scambos, T. A., Anderson, R. S., Rajaram, H., Pope, A., & Haran, T. M. (2018). Continent-wide estimates of antarctic strain rates from landsat 8-derived velocity grids. *Journal of Glaciology*, *64*(244), 321–332. doi: 10.1017/jog.2018.23
- Andersen, J. K., Kusk, A., Boncori, J. P. M., Hvidberg, C. S., & Grinsted, A. (2020). Improved ice velocity measurements with sentinel-1 tops interferometry. *Remote Sensing*, *12*(12). Retrieved from <https://www.mdpi.com/2072-4292/12/12/2014> doi: 10.3390/rs12122014
- Arrhenius, S. (1897, feb). On the influence of carbonic acid in the air upon the temperature of the earth. *Publications of the Astronomical Society of the Pacific*, *9*, 14. Retrieved from <https://doi.org/10.1086/121158> doi: 10.1086/121158
- Baessler, M., Rosenau, R., Dietrich, R., Shibuya, K., & Doi, K. (2012). Utilizing insar for the measurement of ice flow velocities and ocean tide induced height changes of ice shelves at their grounding zones and surroundings. In *2012 IEEE international geoscience and remote sensing symposium, IGARSS 2012, munich, germany, july 22-27, 2012* (pp. 3249–3252). IEEE. Retrieved from <https://doi.org/10.1109/IGARSS.2012.6350731> doi: 10.1109/IGARSS.2012.6350731
- Bamler, R., & Hartl, P. (1998, aug). Synthetic aperture radar interferometry. *Inverse Problems*, *14*(4), R1–R54. Retrieved from <https://doi.org/10.1088/0266-5611/14/4/001> doi: 10.1088/0266-5611/14/4/001
- Baran, I., Stewart, M., Kampes, B., Perski, Z., & Lilly, P. (2003). A modification to the goldstein radar interferogram filter. *IEEE Transactions on Geoscience and Remote Sensing*, *41*(9), 2114-2118. doi: 10.1109/TGRS.2003.817212
- Bechor, N. B. D., & Zebker, H. A. (2006). Measuring two-dimensional movements using a single insar pair. *Geophysical Research Letters*, *33*(16). Retrieved from <https://agupubs.onlinelibrary.wiley.com/doi/abs/10.1029/2006GL026883> doi: <https://doi.org/10.1029/2006GL026883>
- Benn, D. I., Warren, C. R., & Mottram, R. H. (2007). Calving processes and the dynamics of calving glaciers. *Earth-Science Reviews*, *82*(3), 143-179. Retrieved from <https://www.sciencedirect.com/science/article/pii/S0012825207000396> doi: <https://doi.org/10.1016/j.earscirev.2007.02.002>
- Berardino, P., Fornaro, G., Lanari, R., & Sansosti, E. (2002). A new algorithm for surface deformation monitoring based on small baseline differential sar interferograms. *IEEE Transactions on Geoscience and Remote Sensing*, *40*(11), 2375-2383. doi: 10.1109/TGRS.2002.803792

- Berger, S., Drews, R., Helm, V., Sun, S., & Pattyn, F. (2017). Detecting high spatial variability of ice shelf basal mass balance, roi baudouin ice shelf, antarctica. *The Cryosphere*, 11(6), 2675–2690. Retrieved from <https://tc.copernicus.org/articles/11/2675/2017/> doi: 10.5194/tc-11-2675-2017
- Berry, P., Pinnock, R., Hilton, R., & Johnson, C. (2000, 01). Ace: A new global digital elevation model incorporating satellite altimeter derived heights. *European Space Agency, (Special Publication) ESA SP*, 783-791.
- Bindschadler, R. (1998). Monitoring ice sheet behavior from space. *Reviews of Geophysics*, 36(1), 79-104. Retrieved from <https://agupubs.onlinelibrary.wiley.com/doi/abs/10.1029/97RG02669> doi: <https://doi.org/10.1029/97RG02669>
- Brancato, V., Rignot, E., Milillo, P., Morlighem, M., Mouginot, J., An, L., ... Prats-Iraola, P. (2020). Grounding line retreat of denman glacier, east antarctica, measured with cosmo-skymed radar interferometry data. *Geophysical Research Letters*, 47(7), e2019GL086291. Retrieved from <https://agupubs.onlinelibrary.wiley.com/doi/abs/10.1029/2019GL086291> (e2019GL086291 10.1029/2019GL086291) doi: <https://doi.org/10.1029/2019GL086291>
- Buchelt, S., Skov, K., & Ullmann, T. (2021). Sentinel-1 time series for mapping snow cover and timing of snowmelt in arctic periglacial environments: Case study from the zackenbergl valley, greenland. *The Cryosphere Discussions, 2021*, 1–24. Retrieved from <https://tc.copernicus.org/preprints/tc-2021-78/> doi: 10.5194/tc-2021-78
- Bulthuis, K., Arnst, M., Sun, S., & Pattyn, F. (2019). Uncertainty quantification of the multi-centennial response of the antarctic ice sheet to climate change. *The Cryosphere*, 13(4), 1349–1380. Retrieved from <https://tc.copernicus.org/articles/13/1349/2019/> doi: 10.5194/tc-13-1349-2019
- Casu, F., Manconi, A., Pepe, A., & Lanari, R. (2011). Deformation time-series generation in areas characterized by large displacement dynamics: The sar amplitude pixel-offset sbas technique. *IEEE Transactions on Geoscience and Remote Sensing*, 49(7), 2752-2763. doi: 10.1109/TGRS.2010.2104325
- Choi, Y., Morlighem, M., Wood, M., & Bondzio, J. H. (2018). Comparison of four calving laws to model greenland outlet glaciers. *The Cryosphere*, 12(12), 3735–3746. Retrieved from <https://tc.copernicus.org/articles/12/3735/2018/> doi: 10.5194/tc-12-3735-2018
- Cook, S., Galton-Fenzi, B. K., Ligtenberg, S. R. M., & Coleman, R. (2018). Brief communication: widespread potential for seawater infiltration on antarctic ice shelves. *The Cryosphere*, 12(12), 3853–3859. Retrieved from <https://tc.copernicus.org/articles/12/3853/2018/> doi: 10.5194/tc-12-3853-2018
- Crosetto, M., Monserrat, O., Cuevas-González, M., Devanthéry, N., & Crippa, B. (2016). Persistent scatterer interferometry: A review. *ISPRS Journal of Photogrammetry and Remote Sensing*, 115, 78-89. Retrieved from <https://www.sciencedirect.com/science/article/pii/S0924271615002415> (Theme issue 'State-of-the-art in photogrammetry, remote sensing and spatial information science') doi: <https://doi.org/10.1016/j.isprsjprs.2015.10.011>
- Dangendorf, S., Hay, C., Calafat, F. M., Marcos, M., Piecuch, C. G., Berk, K., & Jensen, J. (2019, Sep 01). Persistent acceleration in global sea-level rise since the 1960s. *Nature Climate Change*, 9(9), 705-710. Retrieved from <https://doi.org/10.1038/s41558-019-0531-8> doi: 10.1038/s41558-019-0531-8
- Derauw, D. (1999a). Dinsar and coherence tracking applied to glaciology : The example of shirase.. Paper session presented at FRINGE 99 Workshop Advancing ERS-SAR interferometry from applications towards operations.
- Derauw, D. (1999b). *Phasimétrie par radar à synthèse d'ouverture; théorie et applications* (Unpublished doctoral dissertation). Université de Liège.
- De Zan, F., & Monti Guarnieri, A. (2006). Topsar: Terrain observation by progressive scans.

- IEEE Transactions on Geoscience and Remote Sensing*, 44(9), 2352-2360. doi: 10.1109/TGRS.2006.873853
- De Zan, F., Prats-Iraola, P., Scheiber, R., & Rucci, A. (2014, June). Interferometry with tops: coregistration and azimuth shifts. In *European conference on synthetic aperture radar (eusar)* (pp. 949–952). VDE Verlag GmbH. Retrieved from <https://elib.dlr.de/89463/>
- Ding, X.-l., Li, Z.-w., Zhu, J.-j., Feng, G.-c., & Long, J.-p. (2008). Atmospheric effects on insar measurements and their mitigation. *Sensors*, 8(9), 5426–5448. Retrieved from <https://www.mdpi.com/1424-8220/8/9/5426> doi: 10.3390/s8095426
- Dinniman, M. S., Asay-Davis, X. S., Galton-Fenzi, B. K., Holland, P. R., Jenkin, A., & Timmermann, R. (2016, December). Modeling ice shelf/ocean interaction in antarctica: A review. *Oceanography*. Retrieved from <https://doi.org/10.5670/oceanog.2016.106>
- Dirscherl, M., Dietz, A. J., Dech, S., & Kuenzer, C. (2020). Remote sensing of ice motion in antarctica – a review. *Remote Sensing of Environment*, 237, 111595. Retrieved from <https://www.sciencedirect.com/science/article/pii/S0034425719306157> doi: <https://doi.org/10.1016/j.rse.2019.111595>
- Drews, R. (2015). Evolution of ice-shelf channels in antarctic ice shelves. *The Cryosphere*, 9(3), 1169–1181. Retrieved from <https://tc.copernicus.org/articles/9/1169/2015/> doi: 10.5194/tc-9-1169-2015
- Drews, R., Matsuoka, K., Martín, C., Callens, D., Bergeot, N., & Pattyn, F. (2015). Evolution of derwael ice rise in dronning maud land, antarctica, over the last millennia. *Journal of Geophysical Research: Earth Surface*, 120(3), 564-579. Retrieved from <https://agupubs.onlinelibrary.wiley.com/doi/abs/10.1002/2014JF003246> doi: <https://doi.org/10.1002/2014JF003246>
- Drews, R., Schannwell, C., Ehlers, T. A., Gladstone, R., Pattyn, F., & Matsuoka, K. (2020). Atmospheric and oceanographic signatures in the ice shelf channel morphology of roi baudouin ice shelf, east antarctica, inferred from radar data. *Journal of Geophysical Research: Earth Surface*, 125(7), e2020JF005587. Retrieved from <https://agupubs.onlinelibrary.wiley.com/doi/abs/10.1029/2020JF005587> (e2020JF005587 10.1029/2020JF005587) doi: <https://doi.org/10.1029/2020JF005587>
- Dupont, T. K., & Alley, R. B. (2005). Assessment of the importance of ice-shelf buttressing to ice-sheet flow. *Geophysical Research Letters*, 32(4). Retrieved from <https://agupubs.onlinelibrary.wiley.com/doi/abs/10.1029/2004GL022024> doi: <https://doi.org/10.1029/2004GL022024>
- Díaz, A., Marrero, G. A., Puch, L. A., & Rodríguez, J. (2019). Economic growth, energy intensity and the energy mix. *Energy Economics*, 81, 1056-1077. Retrieved from <https://www.sciencedirect.com/science/article/pii/S0140988319301768> doi: <https://doi.org/10.1016/j.eneco.2019.05.022>
- Edwards, T. L., Nowicki, S., Marzeion, B., Hock, R., Goelzer, H., Seroussi, H., ... Zwinger, T. (2021, May 01). Projected land ice contributions to twenty-first-century sea level rise. *Nature*, 593(7857), 74-82. Retrieved from <https://doi.org/10.1038/s41586-021-03302-y> doi: 10.1038/s41586-021-03302-y
- Euillades, L. D., Euillades, P. A., Riveros, N. C., Masiokas, M. H., Ruiz, L., Pitte, P., ... Balbarani, S. (2016). Detection of glaciers displacement time-series using sar. *Remote Sensing of Environment*, 184, 188-198. Retrieved from <https://www.sciencedirect.com/science/article/pii/S0034425716302607> doi: <https://doi.org/10.1016/j.rse.2016.07.003>
- Farinotti, D., Huss, M., Fürst, J. J., Landmann, J., Machguth, H., Maussion, F., & Pandit, A. (2019, Mar 01). A consensus estimate for the ice thickness distribution of all glaciers on earth. *Nature Geoscience*, 12(3), 168-173. Retrieved from <https://doi.org/10.1038/s41561-019-0300-3> doi: 10.1038/s41561-019-0300-3
- Favier, L., Durand, G., Cornford, S. L., Gudmundsson, G. H., Gagliardini, O., Gillet-Chaulet,

- F., ... Le Brocq, A. M. (2014, Feb 01). Retreat of pine island glacier controlled by marine ice-sheet instability. *Nature Climate Change*, 4(2), 117-121. Retrieved from <https://doi.org/10.1038/nclimate2094> doi: 10.1038/nclimate2094
- Favier, L., & Pattyn, F. (2015, Jun 16). Antarctic ice rise formation, evolution, and stability. *Geophysical Research Letters*, 42(11), 4456-4463. Retrieved from <https://doi.org/10.1002/2015GL064195> doi: 10.1002/2015GL064195
- Ferretti, A., Monti-Guarnieri, A., Prati, C., Rocca, F., & Massonnet, D. (2007). InSAR principles. In (pp. 9–71). ESA Publications.
- Ferretti, A., Prati, C., & Rocca, F. (2000). Nonlinear subsidence rate estimation using permanent scatterers in differential sar interferometry. *IEEE Transactions on Geoscience and Remote Sensing*, 38(5), 2202-2212. doi: 10.1109/36.868878
- Fraser, A. D., Massom, R. A., Ohshima, K. I., Willmes, S., Kappes, P. J., Cartwright, J., & Porter-Smith, R. (2020). High-resolution mapping of circum-antarctic landfast sea ice distribution, 2000–2018. *Earth System Science Data*, 12(4), 2987–2999. Retrieved from <https://essd.copernicus.org/articles/12/2987/2020/> doi: 10.5194/essd-12-2987-2020
- Frederikse, T., Landerer, F., Caron, L., Adhikari, S., Parkes, D., Humphrey, V. W., ... Wu, Y.-H. (2020, Aug 01). The causes of sea-level rise since 1900. *Nature*, 584(7821), 393-397. Retrieved from <https://doi.org/10.1038/s41586-020-2591-3> doi: 10.1038/s41586-020-2591-3
- Fretwell, P., Pritchard, H. D., Vaughan, D. G., Bamber, J. L., Barrand, N. E., Bell, R., ... Zirizzotti, A. (2013). Bedmap2: improved ice bed, surface and thickness datasets for antarctica. *The Cryosphere*, 7(1), 375–393. Retrieved from <https://tc.copernicus.org/articles/7/375/2013/> doi: 10.5194/tc-7-375-2013
- Frey, O., Santoro, M., Werner, C. L., & Wegmuller, U. (2013). Dem-based sar pixel-area estimation for enhanced geocoding refinement and radiometric normalization. *IEEE Geoscience and Remote Sensing Letters*, 10(1), 48-52. doi: 10.1109/LGRS.2012.2192093
- Friedl, P., Weiser, F., Fluhrer, A., & Braun, M. H. (2020). Remote sensing of glacier and ice sheet grounding lines: A review. *Earth-Science Reviews*, 201, 102948. Retrieved from <https://www.sciencedirect.com/science/article/pii/S0012825219300832> doi: <https://doi.org/10.1016/j.earscirev.2019.102948>
- Fürst, J. J., Durand, G., Gillet-Chaulet, F., Tavard, L., Rankl, M., Braun, M., & Gagliardini, O. (2016, May 01). The safety band of antarctic ice shelves. *Nature Climate Change*, 6(5), 479-482. Retrieved from <https://doi.org/10.1038/nclimate2912> doi: 10.1038/nclimate2912
- Fyke, J., Sergienko, O., Löfverström, M., Price, S., & Lenaerts, J. T. M. (2018). An overview of interactions and feedbacks between ice sheets and the earth system. *Reviews of Geophysics*, 56(2), 361-408. Retrieved from <https://agupubs.onlinelibrary.wiley.com/doi/abs/10.1029/2018RG000600> doi: <https://doi.org/10.1029/2018RG000600>
- Gardner, A. S., Moholdt, G., Scambos, T., Fahnestock, M., Ligtenberg, S., van den Broeke, M., & Nilsson, J. (2018). Increased west antarctic and unchanged east antarctic ice discharge over the last 7 years. *The Cryosphere*, 12(2), 521–547. Retrieved from <https://tc.copernicus.org/articles/12/521/2018/> doi: 10.5194/tc-12-521-2018
- Glaude, Q., Amory, C., Berger, S., Derauw, D., Pattyn, F., Barbier, C., & Orban, A. (2020). Empirical removal of tides and inverse barometer effect on dinsar from double dinsar and a regional climate model. *IEEE Journal of Selected Topics in Applied Earth Observations and Remote Sensing*, 13, 4085-4094. doi: 10.1109/JSTARS.2020.3008497
- Goel, V., Matsuoka, K., Berger, C. D., Lee, I., Dall, J., & Forsberg, R. (2020). Characteristics of ice rises and ice rumples in dronning maud land and enderby land, antarctica. *Journal of Glaciology*, 66(260), 1064–1078. doi: 10.1017/jog.2020.77
- Goldberg, D., Holland, D. M., & Schoof, C. (2009, Dec 01). Grounding line movement and

- ice shelf buttressing in marine ice sheets. *Journal of Geophysical Research: Earth Surface*, 114(F4). Retrieved from <https://doi.org/10.1029/2008JF001227> doi: 10.1029/2008JF001227
- Goldberg, D. N., Gourmelen, N., Kimura, S., Millan, R., & Snow, K. (2019). How accurately should we model ice shelf melt rates? *Geophysical Research Letters*, 46(1), 189-199. Retrieved from <https://agupubs.onlinelibrary.wiley.com/doi/abs/10.1029/2018GL080383> doi: <https://doi.org/10.1029/2018GL080383>
- Goldstein, R. M., Engelhardt, H., Kamb, B., & Frolich, R. M. (1993). Satellite radar interferometry for monitoring ice sheet motion: Application to an antarctic ice stream. *Science*, 262(5139), 1525-1530. Retrieved from <https://www.science.org/doi/abs/10.1126/science.262.5139.1525> doi: 10.1126/science.262.5139.1525
- Goldstein, R. M., & Werner, C. L. (1998). Radar interferogram filtering for geophysical applications. *Geophysical Research Letters*, 25(21), 4035-4038. Retrieved from <https://agupubs.onlinelibrary.wiley.com/doi/abs/10.1029/1998GL900033> doi: <https://doi.org/10.1029/1998GL900033>
- Gomba, G., Parizzi, A., De Zan, F., Eineder, M., & Bamler, R. (2016). Toward operational compensation of ionospheric effects in sar interferograms: The split-spectrum method. *IEEE Transactions on Geoscience and Remote Sensing*, 54(3), 1446-1461. doi: 10.1109/TGRS.2015.2481079
- Gourmelen, N., Escorihuela, M., Shepherd, A., Foresta, L., Muir, A., Garcia-Mondéjar, A., ... Drinkwater, M. (2018). Cryosat-2 swath interferometric altimetry for mapping ice elevation and elevation change. *Advances in Space Research*, 62(6), 1226-1242. Retrieved from <https://www.sciencedirect.com/science/article/pii/S0273117717308098> (The CryoSat Satellite Altimetry Mission: Eight Years of Scientific Exploitation) doi: <https://doi.org/10.1016/j.asr.2017.11.014>
- Grandin, R. (2015, March). Interferometric Processing of SLC Sentinel-1 TOPS Data. In *FRINGE'15: Advances in the Science and Applications of SAR Interferometry and Sentinel-1 InSAR Workshop, Frascati, Italy, 23-27 March 2015*. Frascati, Italy. Retrieved from <https://hal.archives-ouvertes.fr/hal-01621519> doi: 10.5270/Fringe2015.pp116
- Grandin, R., Klein, E., Métois, M., & Vigny, C. (2016). Three-dimensional displacement field of the 2015 mw8.3 illapel earthquake (chile) from across- and along-track sentinel-1 tops interferometry. *Geophysical Research Letters*, 43(6), 2552-2561. Retrieved from <https://agupubs.onlinelibrary.wiley.com/doi/abs/10.1002/2016GL067954> doi: <https://doi.org/10.1002/2016GL067954>
- Greene, C. A., Blankenship, D. D., Gwyther, D. E., Silvano, A., & van Wijk, E. (2017). Wind causes totten ice shelf melt and acceleration. *Science Advances*, 3(11), e1701681. Retrieved from <https://www.science.org/doi/abs/10.1126/sciadv.1701681> doi: 10.1126/sciadv.1701681
- Gudmundsson, G. H. (2006, Dec 01). Fortnightly variations in the flow velocity of rutford ice stream, west antarctica. *Nature*, 444(7122), 1063-1064. Retrieved from <https://doi.org/10.1038/nature05430> doi: 10.1038/nature05430
- Gudmundsson, G. H., Paolo, F. S., Adusumilli, S., & Fricker, H. A. (2019). Instantaneous antarctic ice sheet mass loss driven by thinning ice shelves. *Geophysical Research Letters*, 46(23), 13903-13909. Retrieved from <https://agupubs.onlinelibrary.wiley.com/doi/abs/10.1029/2019GL085027> doi: <https://doi.org/10.1029/2019GL085027>
- Haasnoot, M., Winter, G., Brown, S., Dawson, R. J., Ward, P. J., & Eilander, D. (2021). Long-term sea-level rise necessitates a commitment to adaptation: A first order assessment. *Climate Risk Management*, 34, 100355. Retrieved from <https://www.sciencedirect.com/science/article/pii/S221209632100084X> doi: <https://doi.org/10.1016/j.crm.2021.100355>

- Han, H., & Lee, H. (2014). Tide deflection of campbell glacier tongue, antarctica, analyzed by double-differential sar interferometry and finite element method. *Remote Sensing of Environment*, 141, 201-213. Retrieved from <https://www.sciencedirect.com/science/article/pii/S0034425713004082> doi: <https://doi.org/10.1016/j.rse.2013.11.002>
- Han, H., & Lee, H. (2015). Tide-corrected flow velocity and mass balance of campbell glacier tongue, east antarctica, derived from interferometric sar. *Remote Sensing of Environment*, 160, 180-192. Retrieved from <https://www.sciencedirect.com/science/article/pii/S0034425715000322> doi: <https://doi.org/10.1016/j.rse.2015.01.014>
- He, P., Wen, Y., Xu, C., & Chen, Y. (2019, Apr 01). High-quality three-dimensional displacement fields from new-generation sar imagery: application to the 2017 ezgeleh, iran, earthquake. *Journal of Geodesy*, 93(4), 573-591. Retrieved from <https://doi.org/10.1007/s00190-018-1183-6> doi: 10.1007/s00190-018-1183-6
- Herráez, M. A., Burton, D. R., Lalor, M. J., & Gdeisat, M. A. (2002, Dec). Fast two-dimensional phase-unwrapping algorithm based on sorting by reliability following a noncontinuous path. *Appl. Opt.*, 41(35), 7437-7444. Retrieved from <http://www.osapublishing.org/ao/abstract.cfm?URI=ao-41-35-7437> doi: 10.1364/AO.41.007437
- Hogg, A. E., & Gudmundsson, G. H. (2017, Aug 01). Impacts of the larsen-c ice shelf calving event. *Nature Climate Change*, 7(8), 540-542. Retrieved from <https://doi.org/10.1038/nclimate3359> doi: 10.1038/nclimate3359
- Howat, I. M., Porter, C., Smith, B. E., Noh, M.-J., & Morin, P. (2019). The reference elevation model of antarctica. *The Cryosphere*, 13(2), 665-674. Retrieved from <https://tc.copernicus.org/articles/13/665/2019/> doi: 10.5194/tc-13-665-2019
- Huang, Y., & van Genderen, J. L. (1997, March). Comparison of Several Multi-Look Processing Procedures in Insar Processing for ERS-1&2 Tandem Mode. In T. D. Guyenne & D. Danesy (Eds.), *Ers sar interferometry* (Vol. 406, p. 215).
- IPCC. (2014). Climate change 2013 – the physical science basis: Working group i contribution to the fifth assessment report of the intergovernmental panel on climate change. In (p. 1-30). Cambridge: Cambridge University Press. Retrieved from <https://www.cambridge.org/core/books/climate-change-2013-the-physical-science-basis/summary-for-policymakers/356E277FD1FBC887845FB9E8CBC90CCD> doi: 10.1017/CBO9781107415324.004
- IPCC. (2019). Ipcc special report on the ocean and cryosphere in a changing climate. In T. Stocker et al. (Eds.), (p. 1-45). In press. Retrieved from <https://www.ipcc.ch/srocc/>
- Jiang, H., Feng, G., Wang, T., & Bürgmann, R. (2017). Toward full exploitation of coherent and incoherent information in sentinel-1 tops data for retrieving surface displacement: Application to the 2016 kumamoto (japan) earthquake. *Geophysical Research Letters*, 44(4), 1758-1767. Retrieved from <https://agupubs.onlinelibrary.wiley.com/doi/abs/10.1002/2016GL072253> doi: <https://doi.org/10.1002/2016GL072253>
- Jiang, H. J., Pei, Y. Y., & Li, J. (2017, feb). Sentinel-1 TOPS interferometry for along-track displacement measurement. *IOP Conference Series: Earth and Environmental Science*, 57, 012019. Retrieved from <https://doi.org/10.1088/1755-1315/57/1/012019> doi: 10.1088/1755-1315/57/1/012019
- Johnson, A., Fahnestock, M., & Hock, R. (2020). Evaluation of passive microwave melt detection methods on antarctic peninsula ice shelves using time series of sentinel-1 sar. *Remote Sensing of Environment*, 250, 112044. Retrieved from <https://www.sciencedirect.com/science/article/pii/S0034425720304144> doi: <https://doi.org/10.1016/j.rse.2020.112044>
- Joughin, I., Rignot, E., Rosanova, C. E., Lucchitta, B. K., & Bohlander, J. (2003). Timing of recent accelerations of pine island glacier, antarctica. *Geophysical Research Letters*, 30(13). Retrieved from <https://agupubs.onlinelibrary.wiley.com/doi/abs/10.1029/2003GL017609> doi: <https://doi.org/10.1029/2003GL017609>

- Joughin, I., Smith, B. E., & Abdalati, W. (2010). Glaciological advances made with interferometric synthetic aperture radar. *Journal of Glaciology*, *56*(200), 1026–1042. doi: 10.3189/002214311796406158
- Jung, H.-S., Lee, W.-J., & Zhang, L. (2014). Theoretical accuracy of along-track displacement measurements from multiple-aperture interferometry (mai). *Sensors*, *14*(9), 17703–17724. Retrieved from <https://www.mdpi.com/1424-8220/14/9/17703> doi: 10.3390/s140917703
- Jung, H.-S., Lu, Z., & Zhang, L. (2013). Feasibility of along-track displacement measurement from sentinel-1 interferometric wide-swath mode. *IEEE Transactions on Geoscience and Remote Sensing*, *51*(1), 573–578. doi: 10.1109/TGRS.2012.2197861
- Jung, H.-S., Won, J.-S., & Kim, S.-W. (2009). An improvement of the performance of multiple-aperture sar interferometry (mai). *IEEE Transactions on Geoscience and Remote Sensing*, *47*(8), 2859–2869. doi: 10.1109/TGRS.2009.2016554
- King, M. A., Murray, T., & Smith, A. M. (2010). Non-linear responses of rutford ice stream, antarctica, to semi-diurnal and diurnal tidal forcing. *Journal of Glaciology*, *56*(195), 167–176. Retrieved from <https://www.cambridge.org/core/article/nonlinear-responses-of-rutford-ice-stream-antarctica-to-semidiurnal-and-diurnal-tidal-forcing/A1CB062D6B6F92345B34E6646121E675> doi: 10.3189/002214310791190848
- King, M. D., Howat, I. M., Candela, S. G., Noh, M. J., Jeong, S., Noël, B. P. Y., ... Negrete, A. (2020, Aug 13). Dynamic ice loss from the greenland ice sheet driven by sustained glacier retreat. *Communications Earth & Environment*, *1*(1), 1. Retrieved from <https://doi.org/10.1038/s43247-020-0001-2> doi: 10.1038/s43247-020-0001-2
- Konrad, H., Shepherd, A., Gilbert, L., Hogg, A. E., McMillan, M., Muir, A., & Slater, T. (2018, Apr 01). Net retreat of antarctic glacier grounding lines. *Nature Geoscience*, *11*(4), 258–262. Retrieved from <https://doi.org/10.1038/s41561-018-0082-z> doi: 10.1038/s41561-018-0082-z
- Koskinen, J., Pulliainen, J., & Hallikainen, M. (1997). The use of ers-1 sar data in snow melt monitoring. *IEEE Transactions on Geoscience and Remote Sensing*, *35*(3), 601–610. doi: 10.1109/36.581975
- Kuipers Munneke, P., Luckman, A. J., Bevan, S. L., Smeets, C. J. P. P., Gilbert, E., van den Broeke, M. R., ... Kulesa, B. (2018). Intense winter surface melt on an antarctic ice shelf. *Geophysical Research Letters*, *45*(15), 7615–7623. Retrieved from <https://agupubs.onlinelibrary.wiley.com/doi/abs/10.1029/2018GL077899> doi: <https://doi.org/10.1029/2018GL077899>
- Kulp, S. A., & Strauss, B. H. (2019, Oct 29). New elevation data triple estimates of global vulnerability to sea-level rise and coastal flooding. *Nature Communications*, *10*(1), 4844. Retrieved from <https://doi.org/10.1038/s41467-019-12808-z> doi: 10.1038/s41467-019-12808-z
- Larour, E., Seroussi, H., Adhikari, S., Ivins, E., Caron, L., Morlighem, M., & Schlegel, N. (2019). Slowdown in antarctic mass loss from solid earth and sea-level feedbacks. *Science*, *364*(6444), eaav7908. Retrieved from <https://www.science.org/doi/abs/10.1126/science.aav7908> doi: 10.1126/science.aav7908
- Lenaerts, J. T. M., Lhermitte, S., Drews, R., Ligtenberg, S. R. M., Berger, S., Helm, V., ... Pattyn, F. (2017, Jan 01). Meltwater produced by wind–albedo interaction stored in an east antarctic ice shelf. *Nature Climate Change*, *7*(1), 58–62. Retrieved from <https://doi.org/10.1038/nclimate3180> doi: 10.1038/nclimate3180
- Lhermitte, S., Sun, S., Shuman, C., Wouters, B., Pattyn, F., Wuite, J., ... Nagler, T. (2020). Damage accelerates ice shelf instability and mass loss in amundsen sea embayment. *Proceedings of the National Academy of Sciences*, *117*(40), 24735–24741. Retrieved from <https://www.pnas.org/content/117/40/24735> doi: 10.1073/pnas.1912890117
- Liang, C., Agram, P., Simons, M., & Fielding, E. J. (2019). Ionospheric correction of insar

- time series analysis of c-band sentinel-1 tops data. *IEEE Transactions on Geoscience and Remote Sensing*, 57(9), 6755-6773. doi: 10.1109/TGRS.2019.2908494
- Liang, D., Guo, H., Zhang, L., Cheng, Y., Zhu, Q., & Liu, X. (2021). Time-series snowmelt detection over the antarctic using sentinel-1 sar images on google earth engine. *Remote Sensing of Environment*, 256, 112318. Retrieved from <https://www.sciencedirect.com/science/article/pii/S0034425721000365> doi: <https://doi.org/10.1016/j.rse.2021.112318>
- Liao, H., Meyer, F. J., Scheuchl, B., Mouginot, J., Joughin, I., & Rignot, E. (2018). Ionospheric correction of insar data for accurate ice velocity measurement at polar regions. *Remote Sensing of Environment*, 209, 166-180. Retrieved from <https://www.sciencedirect.com/science/article/pii/S0034425718300580> doi: <https://doi.org/10.1016/j.rse.2018.02.048>
- Lipovsky, B. P. (2020). Ice shelf rift propagation: stability, three-dimensional effects, and the role of marginal weakening. *The Cryosphere*, 14(5), 1673-1683. Retrieved from <https://tc.copernicus.org/articles/14/1673/2020/> doi: 10.5194/tc-14-1673-2020
- Lüttig, C., Neckel, N., & Humbert, A. (2017). A combined approach for filtering ice surface velocity fields derived from remote sensing methods. *Remote. Sens.*, 9(10), 1062. Retrieved from <https://doi.org/10.3390/rs9101062> doi: 10.3390/rs9101062
- Mancon, S., Guarnieri, A. M., Giudici, D., & Tebaldini, S. (2017). On the phase calibration by multisquint analysis in topsar and stripmap interferometry. *IEEE Transactions on Geoscience and Remote Sensing*, 55(1), 134-147. Retrieved from <https://doi.org/10.1109/TGRS.2016.2598686> doi: 10.1109/TGRS.2016.2598686
- Marsh, O. J., Fricker, H. A., Siegfried, M. R., Christianson, K., Nicholls, K. W., Corr, H. F. J., & Catania, G. (2016, Jan 16). High basal melting forming a channel at the grounding line of ross ice shelf, antarctica. *Geophysical Research Letters*, 43(1), 250-255. Retrieved from <https://doi.org/10.1002/2015GL066612> doi: 10.1002/2015GL066612
- Marsh, O. J., Rack, W., Floricioiu, D., Gollledge, N. R., & Lawson, W. (2013). Tidally induced velocity variations of the beardmore glacier, antarctica, and their representation in satellite measurements of ice velocity. *The Cryosphere*, 7(5), 1375-1384. Retrieved from <https://tc.copernicus.org/articles/7/1375/2013/> doi: 10.5194/tc-7-1375-2013
- Massonnet, D., Rossi, M., Carmona, C., Adragna, F., Peltzer, G., Feigl, K., & Rabaute, T. (1993, Jul 01). The displacement field of the landers earthquake mapped by radar interferometry. *Nature*, 364(6433), 138-142. Retrieved from <https://doi.org/10.1038/364138a0> doi: 10.1038/364138a0
- Mastro, P., Serio, C., Masiello, G., & Pepe, A. (2020). The multiple aperture sar interferometry (mai) technique for the detection of large ground displacement dynamics: An overview. *Remote Sensing*, 12(7). Retrieved from <https://www.mdpi.com/2072-4292/12/7/1189> doi: 10.3390/rs12071189
- Matsuoka, K., Hindmarsh, R. C., Moholdt, G., Bentley, M. J., Pritchard, H. D., Brown, J., ... Whitehouse, P. L. (2015). Antarctic ice rises and rumples: Their properties and significance for ice-sheet dynamics and evolution. *Earth-Science Reviews*, 150, 724-745. Retrieved from <https://www.sciencedirect.com/science/article/pii/S0012825215300416> doi: <https://doi.org/10.1016/j.earscirev.2015.09.004>
- McMillan, M., Shepherd, A., Gourmelen, N., Park, J.-W., Nienow, P., Rinne, E., & Leeson, A. (2012). Mapping ice-shelf flow with interferometric synthetic aperture radar stacking. *Journal of Glaciology*, 58(208), 265-277. doi: 10.3189/2012JoG11J072
- McMillan, M., Shepherd, A., Muir, A., Gaudelli, J., Hogg, A. E., & Cullen, R. (2018). Assessment of cryosat-2 interferometric and non-interferometric sar altimetry over ice sheets. *Advances in Space Research*, 62(6), 1281-1291. Retrieved from <https://www.sciencedirect.com/science/article/pii/S0273117717308475> (The CryoSat Satellite Altimetry Mission: Eight Years of Scientific Exploitation) doi: <https://doi.org/10.1016/j.asr.2017.11.036>
- McMillan, M., Shepherd, A., Nienow, P., & Leeson, A. (2011). Tide model accuracy in

- the amundsen sea, antarctica, from radar interferometry observations of ice shelf motion. *Journal of Geophysical Research: Oceans*, 116(C11). Retrieved from <https://agupubs.onlinelibrary.wiley.com/doi/abs/10.1029/2011JC007294> doi: <https://doi.org/10.1029/2011JC007294>
- Merryman Boncori, J. P., Langer Andersen, M., Dall, J., Kusk, A., Kamstra, M., Bech Andersen, S., ... Strozzi, T. (2018). Intercomparison and validation of sar-based ice velocity measurement techniques within the greenland ice sheet cci project. *Remote Sensing*, 10(6). Retrieved from <https://www.mdpi.com/2072-4292/10/6/929> doi: 10.3390/rs10060929
- Mestre-Quereda, A., Lopez-Sanchez, J. M., Selva, J., & Gonzalez, P. J. (2018). An improved phase filter for differential sar interferometry based on an iterative method. *IEEE Transactions on Geoscience and Remote Sensing*, 56(8), 4477-4491. doi: 10.1109/TGRS.2018.2820725
- Minchew, B. M., Simons, M., Riel, B., & Milillo, P. (2017). Tidally induced variations in vertical and horizontal motion on rutford ice stream, west antarctica, inferred from remotely sensed observations. *Journal of Geophysical Research: Earth Surface*, 122(1), 167-190. Retrieved from <https://agupubs.onlinelibrary.wiley.com/doi/abs/10.1002/2016JF003971> doi: <https://doi.org/10.1002/2016JF003971>
- Miranda, N., & Hajduch, G. (2017, 01). *Definition of the tops slc deramping function for products generated by the s-1 ipf* (Tech. Rep.).
- Mohajan, H. (2019). The first industrial revolution: Creation of a new global human era. *Journal of Social Sciences and Humanities*, 5, 1377-387.
- Moon, T., Ahlström, A., Goelzer, H., Lipscomb, W., & Nowicki, S. (2018, Sep 01). Rising oceans guaranteed: Arctic land ice loss and sea level rise. *Current Climate Change Reports*, 4(3), 211-222. Retrieved from <https://doi.org/10.1007/s40641-018-0107-0> doi: 10.1007/s40641-018-0107-0
- Moreira, A., Prats-Iraola, P., Younis, M., Krieger, G., Hajnsek, I., & Papathanassiou, K. P. (2013). A tutorial on synthetic aperture radar. *IEEE Geoscience and Remote Sensing Magazine*, 1(1), 6-43. doi: 10.1109/MGRS.2013.2248301
- Mouginot, J., Rignot, E., Bjørk, A. A., van den Broeke, M., Millan, R., Morlighem, M., ... Wood, M. (2019). Forty-six years of greenland ice sheet mass balance from 1972 to 2018. *Proceedings of the National Academy of Sciences*, 116(19), 9239-9244. Retrieved from <https://www.pnas.org/content/116/19/9239> doi: 10.1073/pnas.1904242116
- Mouginot, J., Rignot, E., & Scheuchl, B. (2019). Continent-wide, interferometric sar phase, mapping of antarctic ice velocity. *Geophysical Research Letters*, 46(16), 9710-9718. Retrieved from <https://agupubs.onlinelibrary.wiley.com/doi/abs/10.1029/2019GL083826> doi: <https://doi.org/10.1029/2019GL083826>
- Mouginot, J., Rignot, E., Scheuchl, B., & Millan, R. (2017). Comprehensive annual ice sheet velocity mapping using landsat-8, sentinel-1, and radarsat-2 data. *Remote Sensing*, 9(4). Retrieved from <https://www.mdpi.com/2072-4292/9/4/364> doi: 10.3390/rs9040364
- Mouginot, J., Scheuchl, B., & Rignot, E. (2012). Mapping of ice motion in antarctica using synthetic-aperture radar data. *Remote Sensing*, 4(9), 2753-2767. Retrieved from <https://www.mdpi.com/2072-4292/4/9/2753> doi: 10.3390/rs4092753
- Nagler, T., Rott, H., Hetzenecker, M., Wuite, J., & Potin, P. (2015). The sentinel-1 mission: New opportunities for ice sheet observations. *Remote Sensing*, 7(7), 9371-9389. Retrieved from <https://www.mdpi.com/2072-4292/7/7/9371> doi: 10.3390/rs70709371
- Nagler, T., Rott, H., Ripper, E., Bippus, G., & Hetzenecker, M. (2016). Advancements for snowmelt monitoring by means of sentinel-1 sar. *Remote Sensing*, 8(4). Retrieved from <https://www.mdpi.com/2072-4292/8/4/348> doi: 10.3390/rs8040348
- Nitti, D. O., Hanssen, R. F., Refice, A., Bovenga, F., & Nutricato, R. (2011). Impact of dem-assisted coregistration on high-resolution sar interferometry. *IEEE Transactions on Geoscience and Remote Sensing*, 49(3), 1127-1143. doi: 10.1109/TGRS.2010.2074204

- Ouchi, K. (2013). Recent trend and advance of synthetic aperture radar with selected topics. *Remote Sensing*, 5(2), 716–807. Retrieved from <https://www.mdpi.com/2072-4292/5/2/716> doi: 10.3390/rs5020716
- Padman, L., Fricker, H. A., Coleman, R., Howard, S., & Erofeeva, L. (2002). A new tide model for the antarctic ice shelves and seas. *Annals of Glaciology*, 34, 247–254. doi: 10.3189/172756402781817752
- Padman, L., King, M., Goring, D., Corr, H., & Coleman, R. (2003). Ice-shelf elevation changes due to atmospheric pressure variations. *Journal of Glaciology*, 49(167), 521–526. doi: 10.3189/172756503781830386
- Padman, L., Siegfried, M. R., & Fricker, H. A. (2018). Ocean tide influences on the antarctic and greenland ice sheets. *Reviews of Geophysics*, 56(1), 142–184. Retrieved from <https://agupubs.onlinelibrary.wiley.com/doi/abs/10.1002/2016RG000546> doi: <https://doi.org/10.1002/2016RG000546>
- Paolo, F. S., Fricker, H. A., & Padman, L. (2015). Volume loss from antarctic ice shelves is accelerating. *Science*, 348(6232), 327–331. Retrieved from <https://www.science.org/doi/abs/10.1126/science.aaa0940> doi: 10.1126/science.aaa0940
- Pattyn, F. (2017). Sea-level response to melting of antarctic ice shelves on multi-centennial timescales with the fast elementary thermomechanical ice sheet model (f.tetish v1.0). *The Cryosphere*, 11(4), 1851–1878. Retrieved from <https://tc.copernicus.org/articles/11/1851/2017/> doi: 10.5194/tc-11-1851-2017
- Pattyn, F. (2018, Jul 16). The paradigm shift in antarctic ice sheet modelling. *Nature Communications*, 9(1), 2728. Retrieved from <https://doi.org/10.1038/s41467-018-05003-z> doi: 10.1038/s41467-018-05003-z
- Pattyn, F., & Derauw, D. (2002). Ice-dynamic conditions of shirase glacier, antarctica, inferred from ers sar interferometry. *Journal of Glaciology*, 48(163), 559–565. doi: 10.3189/172756502781831115
- Pattyn, F., Matsuoka, K., Callens, D., Conway, H., Depoorter, M., Docquier, D., ... Tison, J.-L. (2012, 10). Melting and refreezing beneath roi baudouin ice shelf (east antarctica) inferred from radar, gps, and ice core data. *Journal of Geophysical Research*, 117. doi: 10.1029/2011JF002154
- Pattyn, F., Ritz, C., Hanna, E., Asay-Davis, X., DeConto, R., Durand, G., ... van den Broeke, M. (2018, Dec 01). The greenland and antarctic ice sheets under 1.5 °c global warming. *Nature Climate Change*, 8(12), 1053–1061. Retrieved from <https://doi.org/10.1038/s41558-018-0305-8> doi: 10.1038/s41558-018-0305-8
- Payne, A. J., Vieli, A., Shepherd, A. P., Wingham, D. J., & Rignot, E. (2004, Dec 16). Recent dramatic thinning of largest west antarctic ice stream triggered by oceans. *Geophysical Research Letters*, 31(23). Retrieved from <https://doi.org/10.1029/2004GL021284> doi: 10.1029/2004GL021284
- Pepe, A., & Calò, F. (2017). A review of interferometric synthetic aperture radar (insar) multi-track approaches for the retrieval of earth’s surface displacements. *Applied Sciences*, 7(12). Retrieved from <https://www.mdpi.com/2076-3417/7/12/1264> doi: 10.3390/app7121264
- Power, S. B., & Delage, F. P. D. (2019, Jul 01). Setting and smashing extreme temperature records over the coming century. *Nature Climate Change*, 9(7), 529–534. Retrieved from <https://doi.org/10.1038/s41558-019-0498-5> doi: 10.1038/s41558-019-0498-5
- Prats-Iraola, P., Nannini, M., Yague-Martinez, N., Scheiber, R., Minati, F., Vecchioli, F., ... Desnos, Y.-L. (2016). Sentinel-1 tops interferometric time series results and validation. In *2016 IEEE International Geoscience and Remote Sensing Symposium (IGARSS)* (p. 3894–3897). doi: 10.1109/IGARSS.2016.7730011
- Pritchard, H. D., Arthern, R. J., Vaughan, D. G., & Edwards, L. A. (2009, Oct 01). Extensive dynamic thinning on the margins of the greenland and antarctic ice sheets. *Nature*, 461(7266), 971–975. Retrieved from <https://doi.org/10.1038/nature08471> doi: 10.1038/nature08471

- 10.1038/nature08471
- Pritchard, H. D., Ligtenberg, S. R. M., Fricker, H. A., Vaughan, D. G., van den Broeke, M. R., & Padman, L. (2012, Apr 01). Antarctic ice-sheet loss driven by basal melting of ice shelves. *Nature*, *484*(7395), 502-505. Retrieved from <https://doi.org/10.1038/nature10968> doi: 10.1038/nature10968
- Rack, W., King, M. A., Marsh, O. J., Wild, C. T., & Floricioiu, D. (2017). Analysis of ice shelf flexure and its insar representation in the grounding zone of the southern mcmurdo ice shelf. *The Cryosphere*, *11*(6), 2481–2490. Retrieved from <https://tc.copernicus.org/articles/11/2481/2017/> doi: 10.5194/tc-11-2481-2017
- Reese, R., Albrecht, T., Mengel, M., Asay-Davis, X., & Winkelmann, R. (2018). Antarctic sub-shelf melt rates via pico. *The Cryosphere*, *12*(6), 1969–1985. Retrieved from <https://tc.copernicus.org/articles/12/1969/2018/> doi: 10.5194/tc-12-1969-2018
- Rich, R. S., Alessandro, S., Beatriz, P.-M., van Wijk Esmee, Mark, R., Stevens, G. J., & D., B. D. (2021, 2021/12/21). Ocean heat drives rapid basal melt of the totten ice shelf. *Science Advances*, *2*(12), e1601610. Retrieved from <https://doi.org/10.1126/sciadv.1601610> doi: 10.1126/sciadv.1601610
- Richards, M. A. (2007). A beginner’s guide to interferometric sar concepts and signal processing [aess tutorial iv]. *IEEE Aerospace and Electronic Systems Magazine*, *22*(9), 5-29. doi: 10.1109/MAES.2007.4350281
- Rignot, E., Casassa, G., Gogineni, P., Krabill, W., Rivera, A., & Thomas, R. (2004). Accelerated ice discharge from the antarctic peninsula following the collapse of larsen b ice shelf. *Geophysical Research Letters*, *31*(18). Retrieved from <https://agupubs.onlinelibrary.wiley.com/doi/abs/10.1029/2004GL020697> doi: <https://doi.org/10.1029/2004GL020697>
- Rignot, E., Mouginot, J., & Scheuchl, B. (2011a). Antarctic grounding line mapping from differential satellite radar interferometry. *Geophysical Research Letters*, *38*(10). Retrieved from <https://agupubs.onlinelibrary.wiley.com/doi/abs/10.1029/2011GL047109> doi: <https://doi.org/10.1029/2011GL047109>
- Rignot, E., Mouginot, J., & Scheuchl, B. (2011b). Ice flow of the antarctic ice sheet. *Science*, *333*(6048), 1427-1430. Retrieved from <https://www.science.org/doi/abs/10.1126/science.1208336> doi: 10.1126/science.1208336
- Rintoul, S. R., Chown, S. L., DeConto, R. M., England, M. H., Fricker, H. A., Masson-Delmotte, V., . . . Xavier, J. C. (2018, Jun 01). Choosing the future of antarctica. *Nature*, *558*(7709), 233-241. Retrieved from <https://doi.org/10.1038/s41586-018-0173-4> doi: 10.1038/s41586-018-0173-4
- Ritchie, P. D. L., Clarke, J. J., Cox, P. M., & Huntingford, C. (2021, Apr 01). Overshooting tipping point thresholds in a changing climate. *Nature*, *592*(7855), 517-523. Retrieved from <https://doi.org/10.1038/s41586-021-03263-2> doi: 10.1038/s41586-021-03263-2
- Ritz, C., Edwards, T. L., Durand, G., Payne, A. J., Peyaud, V., & Hindmarsh, R. C. A. (2015, Dec 01). Potential sea-level rise from antarctic ice-sheet instability constrained by observations. *Nature*, *528*(7580), 115-118. Retrieved from <https://doi.org/10.1038/nature16147> doi: 10.1038/nature16147
- Robel, A. A. (2017, Mar 01). Thinning sea ice weakens buttressing force of iceberg mélange and promotes calving. *Nature Communications*, *8*(1), 14596. Retrieved from <https://doi.org/10.1038/ncomms14596> doi: 10.1038/ncomms14596
- Rodriguez-Cassola, M., Prats-Iraola, P., De Zan, F., Scheiber, R., Reigber, A., Geudtner, D., & Moreira, A. (2015). Doppler-related distortions in tops sar images. *IEEE Transactions on Geoscience and Remote Sensing*, *53*(1), 25-35. doi: 10.1109/TGRS.2014.2313068
- Rosen, P., Hensley, S., Joughin, I., Li, F., Madsen, S., Rodriguez, E., & Goldstein, R. (2000). Synthetic aperture radar interferometry. *Proceedings of the IEEE*, *88*(3), 333-382. doi: 10.1109/5.838084

- Rosier, S. H. R., & Gudmundsson, G. H. (2016). Tidal controls on the flow of ice streams. *Geophysical Research Letters*, *43*(9), 4433-4440. Retrieved from <https://agupubs.onlinelibrary.wiley.com/doi/abs/10.1002/2016GL068220> doi: <https://doi.org/10.1002/2016GL068220>
- Rosier, S. H. R., & Gudmundsson, G. H. (2020). Exploring mechanisms responsible for tidal modulation in flow of the filchner–ronne ice shelf. *The Cryosphere*, *14*(1), 17–37. Retrieved from <https://tc.copernicus.org/articles/14/17/2020/> doi: 10.5194/tc-14-17-2020
- Rosier, S. H. R., Gudmundsson, G. H., & Green, J. A. M. (2015). Temporal variations in the flow of a large antarctic ice stream controlled by tidally induced changes in the subglacial water system. *The Cryosphere*, *9*(4), 1649–1661. Retrieved from <https://tc.copernicus.org/articles/9/1649/2015/> doi: 10.5194/tc-9-1649-2015
- Rosier, S. H. R., Marsh, O. J., Rack, W., Gudmundsson, G. H., Wild, C. T., & Ryan, M. (2017). On the interpretation of ice-shelf flexure measurements. *Journal of Glaciology*, *63*(241), 783-791. Retrieved from <https://www.cambridge.org/core/article/on-the-interpretation-of-iceshelf-flexure-measurements/A765A16F6574F60689B78923C97123EF> doi: 10.1017/jog.2017.44
- Rott, H., Abdel Jaber, W., Wuite, J., Scheiblauer, S., Floricioiu, D., van Wessem, J. M., ... van den Broeke, M. R. (2018). Changing pattern of ice flow and mass balance for glaciers discharging into the larsen a and b embayments, antarctic peninsula, 2011 to 2016. *The Cryosphere*, *12*(4), 1273–1291. Retrieved from <https://tc.copernicus.org/articles/12/1273/2018/> doi: 10.5194/tc-12-1273-2018
- Rückamp, M., Neckel, N., Berger, S., Humbert, A., & Helm, V. (2019). Calving induced speedup of petermann glacier. *Journal of Geophysical Research: Earth Surface*, *124*(1), 216-228. Retrieved from <https://agupubs.onlinelibrary.wiley.com/doi/abs/10.1029/2018JF004775> doi: <https://doi.org/10.1029/2018JF004775>
- Sansosti, E., Berardino, P., Manunta, M., Serafino, F., & Fornaro, G. (2006). Geometrical sar image registration. *IEEE Transactions on Geoscience and Remote Sensing*, *44*(10), 2861-2870. doi: 10.1109/TGRS.2006.875787
- Sato, Y., Nakajima, S., Shiraga, N., Atsumi, H., Yoshida, S., Koller, T., ... Kikinis, R. (1998). Three-dimensional multi-scale line filter for segmentation and visualization of curvilinear structures in medical images. *Medical Image Analysis*, *2*(2), 143-168. Retrieved from <https://www.sciencedirect.com/science/article/pii/S1361841598800091> doi: [https://doi.org/10.1016/S1361-8415\(98\)80009-1](https://doi.org/10.1016/S1361-8415(98)80009-1)
- Scambos, T., Bell, R., Alley, R., Anandakrishnan, S., Bromwich, D., Brunt, K., ... Yager, P. (2017). How much, how fast?: A science review and outlook for research on the instability of antarctica's thwaites glacier in the 21st century. *Global and Planetary Change*, *153*, 16-34. Retrieved from <https://www.sciencedirect.com/science/article/pii/S092181811630491X> doi: <https://doi.org/10.1016/j.gloplacha.2017.04.008>
- Scambos, T., Hulbe, C., & Fahnestock, M. (2003, 01). Climate-induced ice shelf disintegration in the antarctic peninsula. *Antarctic Research Series*, *79*, 79–92. doi: 10.1029/AR079p0079
- Scheiber, R., Jäger, M., Prats-Iraola, P., De Zan, F., & Geudtner, D. (2015). Speckle tracking and interferometric processing of terrasars-x tops data for mapping nonstationary scenarios. *IEEE Journal of Selected Topics in Applied Earth Observations and Remote Sensing*, *8*(4), 1709-1720. doi: 10.1109/JSTARS.2014.2360237
- Scheiber, R., & Moreira, A. (2000). Coregistration of interferometric sar images using spectral diversity. *IEEE Transactions on Geoscience and Remote Sensing*, *38*(5), 2179-2191. doi: 10.1109/36.868876
- Schmeltz, M., Rignot, E., & MacAyeal, D. R. (2001). Ephemeral grounding as a signal of ice-shelf change. *Journal of Glaciology*, *47*(156), 71–77. doi: 10.3189/172756501781832502
- Schoof, C. (2007). Ice sheet grounding line dynamics: Steady states, stability, and hysteresis. *Journal of Geophysical Research: Earth Surface*, *112*(F3). Retrieved from <https://>

- agupubs.onlinelibrary.wiley.com/doi/abs/10.1029/2006JF000664 doi: <https://doi.org/10.1029/2006JF000664>
- Schröder, L., Horwath, M., Dietrich, R., Helm, V., van den Broeke, M. R., & Ligtenberg, S. R. M. (2019). Four decades of antarctic surface elevation changes from multi-mission satellite altimetry. *The Cryosphere*, *13*(2), 427–449. Retrieved from <https://tc.copernicus.org/articles/13/427/2019/> doi: 10.5194/tc-13-427-2019
- Seroussi, H. (2019, Feb). Fate and future climatic role of polar ice sheets. *Nature*, *566*, 48+. Retrieved from <https://link.gale.com/apps/doc/A573274310/AONE?u=anon~95ba6079&sid=googleScholar&xid=82b324b6>
- Shen, Q., Wang, H., Shum, C. K., Jiang, L., Hsu, H. T., & Dong, J. (2018, Mar 14). Recent high-resolution antarctic ice velocity maps reveal increased mass loss in wilkes land, east antarctica. *Scientific Reports*, *8*(1), 4477. Retrieved from <https://doi.org/10.1038/s41598-018-22765-0> doi: 10.1038/s41598-018-22765-0
- Shepherd, A., Fricker, H. A., & Farrell, S. L. (2018, Jun 01). Trends and connections across the antarctic cryosphere. *Nature*, *558*(7709), 223–232. Retrieved from <https://doi.org/10.1038/s41586-018-0171-6> doi: 10.1038/s41586-018-0171-6
- Shepherd, A., Gilbert, L., Muir, A. S., Konrad, H., McMillan, M., Slater, T., ... Engdahl, M. E. (2019). Trends in antarctic ice sheet elevation and mass. *Geophysical Research Letters*, *46*(14), 8174–8183. Retrieved from <https://agupubs.onlinelibrary.wiley.com/doi/abs/10.1029/2019GL082182> doi: <https://doi.org/10.1029/2019GL082182>
- Shepherd, A., Ivins, E. R., A, G., Barletta, V. R., Bentley, M. J., Bettadpur, S., ... Zwally, H. J. (2012). A reconciled estimate of ice-sheet mass balance. *Science*, *338*(6111), 1183–1189. Retrieved from <https://www.science.org/doi/abs/10.1126/science.1228102> doi: 10.1126/science.1228102
- Siegfried, M. R., Fricker, H. A., Carter, S. P., & Tulaczyk, S. (2016). Episodic ice velocity fluctuations triggered by a subglacial flood in west antarctica. *Geophysical Research Letters*, *43*(6), 2640–2648. Retrieved from <https://agupubs.onlinelibrary.wiley.com/doi/abs/10.1002/2016GL067758> doi: <https://doi.org/10.1002/2016GL067758>
- Slater, T., Lawrence, I. R., Ootosaka, I. N., Shepherd, A., Gourmelen, N., Jakob, L., ... Nienow, P. (2021). Review article: Earth’s ice imbalance. *The Cryosphere*, *15*(1), 233–246. Retrieved from <https://tc.copernicus.org/articles/15/233/2021/> doi: 10.5194/tc-15-233-2021
- Slater, T., & Shepherd, A. (2018, Dec 01). Antarctic ice losses tracking high. *Nature Climate Change*, *8*(12), 1025–1026. Retrieved from <https://doi.org/10.1038/s41558-018-0284-9> doi: 10.1038/s41558-018-0284-9
- Slater, T., Shepherd, A., McMillan, M., Muir, A., Gilbert, L., Hogg, A. E., ... Parrinello, T. (2018). A new digital elevation model of antarctica derived from cryosat-2 altimetry. *The Cryosphere*, *12*(4), 1551–1562. Retrieved from <https://tc.copernicus.org/articles/12/1551/2018/> doi: 10.5194/tc-12-1551-2018
- Small, D. (2011). Flattening gamma: Radiometric terrain correction for sar imagery. *IEEE Transactions on Geoscience and Remote Sensing*, *49*(8), 3081–3093. doi: 10.1109/TGRS.2011.2120616
- Smith, A. M. (1991). The use of tiltmeters to study the dynamics of antarctic ice-shelf grounding lines. *Journal of Glaciology*, *37*(125), 51–58. doi: 10.3189/S0022143000042799
- Steig, E. J. (2019). How fast will the antarctic ice sheet retreat? *Science*, *364*(6444), 936–937. Retrieved from <https://www.science.org/doi/abs/10.1126/science.aax2626> doi: 10.1126/science.aax2626
- Strozzi, T., Luckman, A., Murray, T., Wegmuller, U., & Werner, C. (2002). Glacier motion estimation using sar offset-tracking procedures. *IEEE Transactions on Geoscience and Remote Sensing*, *40*(11), 2384–2391. doi: 10.1109/TGRS.2002.805079
- Sun, S., Hattermann, T., Pattyn, F., Nicholls, K. W., Drews, R., & Berger, S. (2019). To-

- pographic shelf waves control seasonal melting near antarctic ice shelf grounding lines. *Geophysical Research Letters*, 46(16), 9824-9832. Retrieved from <https://agupubs.onlinelibrary.wiley.com/doi/abs/10.1029/2019GL083881> doi: <https://doi.org/10.1029/2019GL083881>
- Swart, N. C., Gille, S. T., Fyfe, J. C., & Gillett, N. P. (2018, Nov 01). Recent southern ocean warming and freshening driven by greenhouse gas emissions and ozone depletion. *Nature Geoscience*, 11(11), 836-841. Retrieved from <https://doi.org/10.1038/s41561-018-0226-1> doi: 10.1038/s41561-018-0226-1
- Sánchez-Gómez, P., & Navarro, F. J. (2017). Glacier surface velocity retrieval using d-insar and offset tracking techniques applied to ascending and descending passes of sentinel-1 data for southern ellesmere ice caps, canadian arctic. *Remote Sensing*, 9(5). Retrieved from <https://www.mdpi.com/2072-4292/9/5/442> doi: 10.3390/rs9050442
- Tapley, B. D., Watkins, M. M., Flechtner, F., Reigber, C., Bettadpur, S., Rodell, M., ... Velicogna, I. (2019, May 01). Contributions of grace to understanding climate change. *Nature Climate Change*, 9(5), 358-369. Retrieved from <https://doi.org/10.1038/s41558-019-0456-2> doi: 10.1038/s41558-019-0456-2
- Tsai, Y.-L. S., Dietz, A., Opelet, N., & Kuenzer, C. (2019). Remote sensing of snow cover using spaceborne sar: A review. *Remote Sensing*, 11(12). Retrieved from <https://www.mdpi.com/2072-4292/11/12/1456> doi: 10.3390/rs11121456
- Wild, C. T., Marsh, O. J., & Rack, W. (2017). Viscosity and elasticity: a model intercomparison of ice-shelf bending in an antarctic grounding zone. *Journal of Glaciology*, 63(240), 573-580. doi: 10.1017/jog.2017.15
- Wild, C. T., Marsh, O. J., & Rack, W. (2019). Differential interferometric synthetic aperture radar for tide modelling in antarctic ice-shelf grounding zones. *The Cryosphere*, 13(12), 3171-3191. Retrieved from <https://tc.copernicus.org/articles/13/3171/2019/> doi: 10.5194/tc-13-3171-2019
- Wolovick, M. J., & Moore, J. C. (2018). Stopping the flood: could we use targeted geoengineering to mitigate sea level rise? *The Cryosphere*, 12(9), 2955-2967. Retrieved from <https://tc.copernicus.org/articles/12/2955/2018/> doi: 10.5194/tc-12-2955-2018
- Wright, T. J., Parsons, B. E., & Lu, Z. (2004). Toward mapping surface deformation in three dimensions using insar. *Geophysical Research Letters*, 31(1). Retrieved from <https://agupubs.onlinelibrary.wiley.com/doi/abs/10.1029/2003GL018827> doi: <https://doi.org/10.1029/2003GL018827>
- Yague-Martinez, N., De Zan, F., & Prats-Iraola, P. (2017). Coregistration of interferometric stacks of sentinel-1 tops data. *IEEE Geoscience and Remote Sensing Letters*, 14(7), 1002-1006. doi: 10.1109/LGRS.2017.2691398
- Yague-Martinez, N., Prats-Iraola, P., Pinheiro, M., & Jaeger, M. (2019). Exploitation of burst overlapping areas of tops data. application to sentinel-1. In *Igarss 2019 - 2019 ieee international geoscience and remote sensing symposium* (p. 2066-2069). doi: 10.1109/IGARSS.2019.8900644
- Yague-Martinez, N., Prats-Iraola, P., & Wollstadt, S. (2018). The 2-looks tops mode: Enhanced sensitivity to ground displacement in azimuth direction with burst-mode sar systems. demonstration with terrasars-x. In *Igarss 2018 - 2018 ieee international geoscience and remote sensing symposium* (p. 72-75). doi: 10.1109/IGARSS.2018.8518954
- Yagüe-Martínez, N., Prats-Iraola, P., Rodríguez González, F., Brcic, R., Shau, R., Geudtner, D., ... Bamler, R. (2016). Interferometric processing of sentinel-1 tops data. *IEEE Transactions on Geoscience and Remote Sensing*, 54(4), 2220-2234. doi: 10.1109/TGRS.2015.2497902
- Zakeri, F., & Mariethoz, G. (2021). A review of geostatistical simulation models applied to satellite remote sensing: Methods and applications. *Remote Sensing of Environment*, 259, 112381. Retrieved from <https://www.sciencedirect.com/science/article/pii/S0926641021001123>

S0034425721000997 doi: <https://doi.org/10.1016/j.rse.2021.112381>

Zebker, H., & Villasenor, J. (1992). Decorrelation in interferometric radar echoes. *IEEE Transactions on Geoscience and Remote Sensing*, 30(5), 950-959. doi: 10.1109/36.175330

Glossary

ACE Altimeter Corrected Elevations.

AIS Antarctic Ice Sheet.

AWI Alfred-Wegener-Institut Helmholtz-Zentrum für Polar-und Meeresforschung.

BOI Burst Overlapping Interferometry.

CPOD Copernicus Precise Orbit Determination.

DC Doppler Centroid.

DDInSAR Double Differential SAR Interferogram.

DEM Digital Elevation Model.

DInSAR Differential SAR Interferometry.

DML Dronning Maud Land.

ESA European Space Agency.

ESD Extended Spectral Diversity.

ESR Earth and Space Research.

EW Extra Wideswath.

GHG GreenHouse Gases.

GRD Ground Range Detected.

IBE Inverse Barometer Effect.

LOS Line-Of-Sight.

MAI Multiple Aperture Interferometry.

MAR Modèle Atmosphérique Régional.

mCDW modified Circumpolar Deep Water.

MISI Marine Ice Sheet Instability.

NCC normalized cross-correlation.

OSU Oregon State University.

PSI Persistent Scatterer Interferometry.

RBIS Roi Baudouin Ice Shelf.

RCP representative Concentration Pathways.

REMA Reference Elevation Model of Antarctica.

SAR Synthetic Aperture Radar.

SBAS Small BAseline Subset.

SLC Single-Look Complex.

SLR Sea-Level Rise.

SRTM Shuttle Radar Topography Mission.

TMD Tide Model Driver.

TOPS Terrain Observation by Progressive Scans (equivalent to TOPSAR).

TOPSAR Terrain Observation by Progressive Scans (equivalent to TOPS).